Proceedings of the 4th BSME-ASME International Conference on Thermal Engineering
27-29 December, 2008, Dhaka, Bangladesh

ANALYSIS OF HEAT TRANSFER OF THE REFRIGERATOR-FREEZER

Md. Hasanuzzaman, Saidur Rahman and Masjuki Hj. Hassan

Department of Mechanical Engineering, University of Malaya
50603 Kuala Lumpur, Malaysia.
E-mail: hasan492@yahoo.com

ABSTRACT

This paper presents the heat transfer analysis of a refrigerator-freezer during the open door operation. Conduction, convection, radiation, sensible and latent heat impose in the cabinet of the refrigerator-freezer. The Rayleigh number varies from 4.2×10^8 to 5.4×10^8 in the freezer cabinet and from 3.1×10^8 to 4.9×10^8 in the fresh food cabinet that is proved the laminar flow. Energy loss due to the heat transfer is about 46.2% through the walls conduction, 10% convection and radiation that is more affected by the number of door opening and cabinet load.

KEYWORDS: *Energy loss; Thermal load; Heat transfer; Thermal resistance.*

1. INTRODUCTION

Refrigerator-freezer is one of the essential appliances to preserve perishable foods in a household. The number of refrigerator-freezer has increased from 175,842 units in 1970 to 4,196,486 units in 2000 in Malaysia [1]. The function of the refrigeration system is to maintain the desired temperature of the cabinet. As its temperature is very low, the heat is transferred always from the ambient to the cabinet. As a result, thermal load is imposed on the cabinet. Cabinet thermal loads of the 530 liter top-mount refrigerator-freezer are investigated and found the combine radiation and convective heat transfer coefficient were 6.87 $W/m^2.K$, 6.70 $W/m^2.K$ and 6.41$W/m^2.K$ for the exterior, interior freshfood and intrerior freezer compartment respectively [2]. The Rayleigh number based on the width of the refrigerating compartment and the temperature difference between the evaporator and the other walls is equal to 1.43×10^8. Thus, the air flow inside the refrigerator is laminar [3]. Most of the users keep refrigerator-freezers inside the kitchen and near the heat source (i.e. oven, heater) in some cases that is increased heat transfer as well as energy consumption. The aim of the work is to analyze the heat transfer and energy losses of the refrigerator-freezer.

2. RESEARCH METHODOLOGY

2.1 Test conditions

In the open door operation test, the considering variables were the number of fresh food and freezer door openings, duration of each door remains open, ambient temperature, cabinet load, thermostat setting position. In general the environmental controlled chamber was maintained at temperature 25 ºC and relative humidity 70±5 %. The thermostat setting was set at the setting point 3. The cabinet load during the experiment was 2 liter of fresh water in the freezer and 4 liter of fresh water in the fresh food cabinet. The door opening duration was 30 min for fresh food compartment and 60 min for the freezer and the duration of both door remains open 20 seconds. During the experiment, only one variable was changed and the other variables were kept constant. Number of door opening was varied from 8 to 32 of the fresh food cabinet and from 4 to 16 of the freezer cabinet. Duration of each door remain open varied from 10 second to 30 second. Ambient temperature was varied from 18 ºC to 30 ºC. Fresh food and freezer cabinets load was varied from 0 kg to 8 kg and 0 kg to 4 kg of fresh water in the fresh food and freezer cabinet respectively. The thermostat setting position was changed from 1(warm) to 5(coldest) to reveal the effect of cabinet temperature.

2.2 Test unit and Instrumentation

The refrigerator-freezer used was volume 460 liter, top mount freezer section, two doors and both doors hinged at right hand side. T-type thermocouples were used to measure temperature. Humidity sensor was used to monitor the relative humidity with range of 3% to 95% and accuracy of ± 5%. Heat pump was used to maintain the required temperature in side controlled chamber of range from 16 ºC to 32 ºC. Dehumidifier was used to maintain relative humidity with range from 0% to 90%. Electronic balance was used to weight the mass of evaporated water with weighing capability of 0.01g up to 2 kg. Data logger was used to store the data from the test unit to personal computer. Energy consumption was measured by power meter with the accuracy ± 0.2% of the reading. Automatic door opening mechanism was used to open and close the doors of the fresh food and freezer cabinet that is shown in Fig. 1. Programmable Logic Controller was used to control the door opening and closing.

2.3 Location of thermocouples, humidity sensor, water pan and load

The location of thermocouples and humidity sensor are shown in the Fig. 2. Four thermocouples were attached at the middle position of both walls to measure wall temperatures (positions 2-5) and one at the middle (position 1) of cabinet separator in the freezer cabinet [4]. Similarly, six thermocouples were used in fresh food cabinet that was placed at both side of walls (positions 8-11) and the cabinet separators (positions 6-7). To measure temperatures at the outside of the walls and doors of refrigerator-freezer, the other six thermocouples were used (positions 13-15). Five thermocouples are set to monitor the ambient temperature inside the controlled chamber. Humidity sensor was used to measure the relative humidity of the fresh food cabinet and the controlled chamber.

Fig. 1 Automatic door opening mechanism

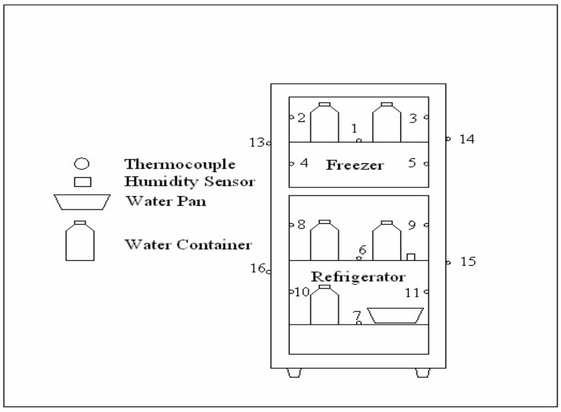

Fig. 2 Location of thermocouple and relative humidity sensor and load

3 FORMULATION OF HEAT TRANSFER MECHANISM

In the case of a refrigerator-freezer, heat is transferred from warm ambient to the cabinet. Heat transfer of the interior and exterior surfaces of the refrigerator-freezer is divided into conduction, convection and radiation. Sensible and latent heat transfer is occurred due to the moisture transfer and cabinet load.

3.1 Thermal resistance

The thermal resistance of a medium depends on the geometry and the thermal properties the medium. There are three basic resistances: external, wall and internal that is shown in Fig. 3 [5].

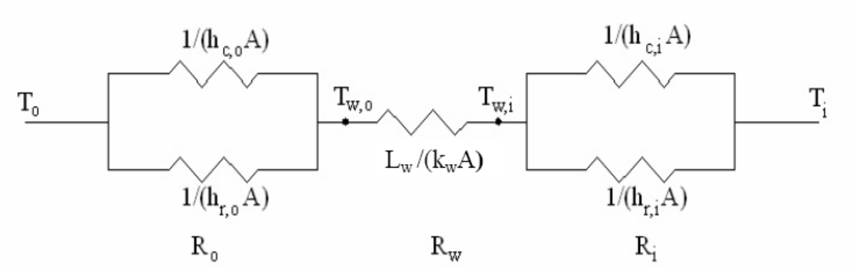

Fig. 3 Thermal resistance network of the refrigerator-freezer

The overall thermal resistance of the refrigerator-freezer can be expressed as:

$$R_{ov} = R_o + R_w + R_i \tag{1}$$

The overall heat transfer (Q_{ov}) is calculated by the Equation (2).

$$Q_{ov} = \frac{T_o - T_i}{R_{ov}} \tag{2}$$

3.2 Convective heat transfer

Convective heat transfer is calculated base on the Nusselt number using an area (height × width) weighted average walls of the refrigerator-freezer. The out side of the wall and door is considered as a vertical flat plate. On the other hand, the fresh food and freezer cabinet are considered as a closed rectangular cavity.

3.2.1 Convective heat transfer coefficient of vertical flat plate

The heat transfer in a refrigerator-freezer is examined on the theory of natural convection between the surrounding air and vertical plates. The empirical correlations have been summarized and developed for common external flow geometries that are suitable for most of the engineering calculations [6]. The general form of the empirical equation is:

$$Nu = cRa^n \tag{3}$$

where the Rayleigh number can be expressed as:

$$Ra = \frac{g\beta \Delta T L^3}{v\alpha} \tag{4}$$

The author also proposed the values of "c" and "n" are as follows,

$c = 0.59$ and $n = \frac{1}{4}$ for laminar flow; $c = 0.10$ and $n = \frac{1}{3}$ for turbulent flow.

The convective heat transfer coefficient can be expressed as:

$$h_c = \frac{Nuk}{L} \tag{5}$$

3.2.2 Convective heat transfer coefficient of closed rectangular cavity

The rectangular cavity is probably the simplest enclosure geometry. The aspect ratio of a typical refrigerator-freezer is $1 < \frac{H}{L} < 2$. The following correlation is used for calculating the convective heat transfer of a refrigerator-freezer [3].

$$Nu = 0.18\left(\frac{\Pr}{0.2+\Pr} Ra\right)^{0.29} \tag{6}$$

where

$1 < \frac{H}{L} < 2$; $10^{-3} < \Pr < 10^{5}$ and $10^{3} < \frac{Ra \Pr}{0.2+\Pr}$

3.3 Conduction heat transfer

All vertical walls are considered as isothermal and exchanges heat with the external ambient air. The horizontal walls are considered as perfectly insulated as heat is transferred from freezer cabinet to fresh food cabinet [3]. In this research, the thermal conductivity and thickness of the wall of refrigerator-freezer are used 0.02 W/m-K and 4.5 cm respectively.

3.4 Radiation heat transfer

The radiation heat transfer occurs between ambient air and external referring walls, internal referring walls and the cabinet air. The radiation heat transfer coefficient depends on the emissivity of the surface and temperature of the wall and ambient air. In this work, emisivity of the surface is considered as 0.7 [7]. The radiation heat transfer coefficient can be expressed as [8]:

$$h_{rad} = \varepsilon \times \sigma \times (T_i^2 + T_w^2) \times (T_i + T_w) \tag{7}$$

3.5 Sensible heat transfer

The sensible heat transfer occurred due to the moisture transfer and cabinet load of the refrigerator-freezer. The sensible heat transfer is expressed as:

$$Q_{sen} = m_{wr} \times S \times \Delta T \tag{8}$$

3.6 Latent heat transfer

Latent heat loss is due to the phase change of freezing and defrosting of water and the cabinet load of the refrigerator-freezer. The latent heat transfer is expressed as:

$$Q_{lat} = m_{wr} \times l_{wr} \tag{9}$$

3.7 Heat and mass transfer analogy of a refrigerator-freezer

When the refrigerator-freezer door is opened, warm ambient air enters into the cabinet. If the compressor and fans are off during a door opening, warm ambient air descends into the upper part of the cabinet filling the void left by the cooler air which flows out near the bottom of the cabinets. During this process, heat is transferred to the cold surfaces inside the cobinets and moisture condenses out of the air to these surfaces. This imposes an additional cooling load on the refrigeration system. Nusselt number and convective heat transfer coefficient is calculated by using the Equation 10 and 11.

$$Nu = \frac{h_{conv} H}{k} \tag{10}$$

$$Nu = 0.091 Ra_H^{1/3} \tag{11}$$

The Rayleigh number is calculated by using the Equation 12 (where the characteristic H height is calculated base on the interior parameter of the cabinet).

$$Ra_H = \frac{g\beta(T_{amb} - T_{cab})H^3}{v\alpha} \tag{12}$$

Analogy for heat and mass transfer is valid and used the Equation 16 to calculate the mass transfer coefficient for the open door convective mass transfer coefficient [9].

$$h_{mass} = 0.00626 \times \rho_a \times h_{conv} \times \frac{D_{ab}^{2/3} \times \alpha^{1/3}}{k_{air}} \tag{13}$$

The mass transfer from the ambient air condensing on the inside a surface of the refrigerator is characterized in the Equation 14.

$$q_{mass} = h_{mass} \times A_{surf} \times (C_{amb} - C_{surf}) \tag{14}$$

The convective heat transfer associated with door opening of the refrigerator is expressed as:

$$q_{conv} = h_{conv} \times A_{surf} \times (T_{amb} - T_{surf}) \tag{15}$$

4. RESULTS AND DISCUSSIONS

Heat is transferred through the walls and the bulk air exchange to the cabinets. ASHRAE Handbook [10] reported that about 60-70% of the total cabinet load comes through the heat conduction through the walls.

4.1 Nondimensional number analysis of the open door heat transfer

An empty refrigerator is considered as a rectangular cavity in order to approximate the heat transfer and heat transfer occurs from the warm ambient to cabinets [3]. When the door is opened, natural convection heat transfer is occurred from the warm ambient to the cabinet. The Rayleigh number is an important non-dimensional number to describe the characteristics of the flow laminar or turbulent. In general, the critical Rayleigh number, which distinguishes the transition from laminar to turbulent flows, is approximately 10^9 [11]. The Rayleigh number varies from 4.2×10^8 to 5.4×10^8 in the freezer cabinet and from 3.1×10^8 to 4.9×10^8 in the fresh food cabinet of the refrigerator-freezer. Laguerre *et al.* [12] carried out two experiments in the refrigerator cavity while the entire cold wall was maintained at -10 ˚C and 0 ˚C. The authors explained by the fact that the temperature variation between the cold wall and ambient air is higher in the case of -10 ˚C. Thus, there is more air circulation by natural convection near the cold wall. The Nusselt number is an important dimensionless parameter that represents the temperature gradient at a surface where heat transfer by convection takes place. The Nusselt number represents the enhancement of heat transfer through a fluid layer as a result of convective to conduction across the same fluid layer. The larger the Nusselt number the more effective the convection. The Nusselt number is calculated that is varied from 68.2 to 74.5 in the freezer cabinet and from 61 to 72.2 in the fresh food cabinet.

4.2 Heat transfer coefficients

Heat transfer by radiation between internal walls of the cavity is as important as natural convection and this should be taken into account [12]. Radiation increases in comparison with convection as the size of the enclosure increases. The convective heat transfer coefficient during the door opening varies from 3.8 W/m^{2}K to 4.2 W/m^{2}K in the freezer cabinet and from 3.5 W/m^{2}K to 4.1 W/m^{2}K in the fresh food cabinet of the refrigerator-freezer. Radiation heat transfer coefficient varies from 3.3 W/m^{2}K to 3.6 W/m^{2}K in the freezer cabinet and from 3.6 W/m^{2}K to 3.9 W/m^{2}K in the fresh food cabinet.

5. CONCLUSIONS

From the comparative evaluation of the experimental results for the different operating conditions, it is revealed that the flow is laminar. Heat is transferred mostly through the wall that is about 46.2 %. It is found that the different environmental operating conditions have a significant influence on heat transfer. The average energy loss due to the heat transfer is about 60 % of the total energy consumption.

REFERENCES

[1] Mahlia, T.M.I., Masjuki, H.H., Saidur, R., Amalina M.A., Cost-benefit analysis of implementing minimum energy efficiency standards for household refrigerator-freezers in Malaysia, *Energy Policy*, 32, 2004, 1819-1824.

[2] Boughton, B.E., Clousing, A.M.,Newell, T.A., An investigation of household refrigerator cabinet loads, *HVAC&R Research*, 2(2), 1996,135-148.

[3] Laguerre,O., Flick, D., Heat transfer by natural convection in domestic refrigerators, *Journal of Food Engineering*, 62, 2004,79-88.

[4] Afonso, C., Matos, J., The effect of radiation shields around the air condenser and compressor of a refrigerator on the temperature distribution inside it, *International Journal of Refrigeration*, 29, 2006, 1144-1151.

[5] Williams, T.L., Clausing, A.M., Newell, T.A, An experimental investigation of natural convection heat transfer in a refrigerator during closed door conditions, *ACRC TR-54,* Urbana, IL, May .1994, 1-109.

[6] Incropera, F.P., Dewitt, D.P., Fundamentals of heat and mass transfer, 5th Edition, 2002.

[7] Hessami, M.A., Calculating energy rating of domestic refrigerators through laboratory heat transfer measurements and computer simulations, *International Network for Information on Ventilation and Energy Performance*, 1997, 1-19.

[8] Boughton, B.E., Clausing, A.M.,Newell, T.A, An investigation of household refrigerator cabinet loads, *ACRC TR-21*, Urbana, IL, May.1992, 1-92.

[9] Inan, C., Egrican, N., Bullard, C., Newell, T.A., Moisture transport in domestic refrigerator, *ASHRAE Transaction*, 108(1), 2002, 801-806.

[10] ASHRAE Handbook (equipment). Household refrigerators and freezers, Atlanta (GA), ASHRAE, 1988.

[11] Incropera, F. P., Dewitt, D. P., Fundamentals of heat and mass transfer. 4th edition, John Wiley and Sons, 1996.

[12] Laguerre, O., Amara, B., Flick, D., Experimental study of heat transfer by natural convection in a closed cavity: application in a domestic refrigerator, *Journal of Food Engineering*, 70, 2005, 523-537.

Proceedings of the 4th BSME-ASME International Conference on Thermal Engineering
27-29 December, 2008, Dhaka, Bangladesh

HYDROMAGNETIC FLOW AND HEAT TRANSFER WITH VARIABLE TEMPERATURE, VISCOUS DISSIPATION AND INTERNAL HEAT GENERATION OVER A STRETCHING SURFACE

Ifte Khairul Islam[1], M Ferdows[1], M Alam[2], S. Sivasankaran[3]

[1]Department of Mathematics, University of Dhaka, Dhaka -1000, Bangladesh,
[2]Mathematics Discipline, Khulna University, Khulna, Bangladesh,
[3]Department of Mechanical Engineering, National Cheng Kung University, Tainan,Taiwan.
e-mail: ifteki@hotmail.com

ABSTRACT

Steady hydromagnetic (MHD) flow and heat transfer over a stretching surface is considered in the presence of an exponential form of internal heat generation (IHG). We consider temperature varies as $T_w - T_\infty = bx^n$ *. The governing boundary layer equations are solved to find the effects of Magnetic field* M^2 *, Stretching parameter* β*, Prandtl number* Pr*, Index of power law variation of wall temperature n, on velocity and temperature profiles and physical properties of skin friction and rate of heat transfer.*

KEYWORDS: *Hydromagnetic flow, Viscous dissipation, Internal heat generation, Stretching surface*

1. INTRODUCTION

Flow and heat transfer over a stretching surface in a fluid is important in many scientific and engineering applications. Some of the typical applications of such study are the polymer sheet extrusion from a dye, glass fiber and paper production, drawing of plastic films, etc. The steady hydromagnetic (MHD) flow and heat transfer of a viscous fluid over a stretching surface with variable temperature and internal heat generation may find application to polymer technology and metallurgy.

Chakrabarti and Gupta [1] examine the flow and heat transfer of an electrically conducting incompressible fluid over a stretching sheet. An analytical solution for the flow and the numerical solution for heat transfer were presented by their work. The skin friction and heat transfer on a continuous flat surface moving in a parallel free stream was investigated numerically by Abdelhafez[2]. Anderson [3] analytically solved the two dimensional Navier–Stokes equations for the MHD fluid over a stretching sheet without applying to boundary layer theory. Chaim [4] reported solutions for steady hydromagnetic flow over a surface with a power law velocity with the distance along the surface. Recently S.P Anjali Devi and M. Thiyagarajan [5] studied the steady hydormagnetic flow of an incompressible, viscous and electrically conducting fluid with heat transfer over a surface of variable temperature stretching with a power-law velocity in the presence of a variable transverse magnetic field.

In the present paper, the steady hydromagnetic (MHD) flow and heat transfer with variable temperature, viscous dissipation and internal heat generation (IHG) over a stretching surface are analyzed. The boundary layer equations are numerically solved by using the Six-order Runge–Kutta shooting method [6] using similarity transformation.

2. FLOW ANALYSIS

Consider a flat surface issuing from a very thin slit at x=0, y=0 and subsequently being stretched. The speed of a point on the surface is proportional to the power of its distance from the slit is also assume. In the energy equation we added the viscous dissipation and Ohomic heating. The boundary layer equations are:

Continuity equation $$\frac{\partial u}{\partial x} + \frac{\partial v}{\partial x} = 0 \tag{1}$$

Momentum equation $$u\frac{\partial u}{\partial x} + v\frac{\partial u}{\partial y} = \nu\frac{\partial^2 u}{\partial y^2} - \frac{\sigma B^2(x)}{\rho}u \tag{2}$$

Energy Equation $$\rho C_p\left(u\frac{\partial T}{\partial x} + v\frac{\partial T}{\partial y}\right) = \kappa\frac{\partial^2 T}{\partial y^2} + \mu\left(\frac{\partial u}{\partial y}\right)^2 + \sigma B^2 u^2 + q''' \tag{3}$$

The relevant boundary conditions are

$y = 0$: $u = U(x) = ax^m$, $v = v_0(x)$, $T = T_w(x)$

$y = \infty$: $u = 0$, $T = T_\infty$ (4)

3. SIMILARITY ANALYSIS

Introducing the following similarity variables as in Banks [7] and Afzal [8]:

$$\eta(x,y) = \left[\frac{(1+m)U(x)}{2\nu x}\right]^{\frac{1}{2}} y,\ \psi(x,y) = \left[\frac{2\nu x U(x)}{(1+m)}\right]^{\frac{1}{2}} f(\eta),\ u = \frac{\partial\psi}{\partial y},\ v = -\frac{\partial\psi}{\partial x},\ \theta(\eta) = \frac{T-T_\infty}{T_w-T_\infty} \tag{5}$$

Define $B(x) = B_0^2\ x^{\frac{m-1}{2}}$, $T_w(x) = T_\infty + bx^n$ (where b is a dimensional constant)

We consider IHG in the form of $q''' = \frac{\kappa(1+m)(T_w-T_\infty)U(x)}{2\nu x}e^{-\eta}$,

With the help of Equations (5) we can transform Equation (1) to (4) and finally we get the following similarity equations.

$$f''' + f f'' - \beta(f')^2 - M^2 f' = 0 \tag{6}$$

$$\theta'' - \frac{2n}{(1+m)}\Pr\theta f' + \Pr f\theta' + \Pr Ec\left(f''\right)^2 + M^2\Pr Ec(f')^2 + e^{-\eta} = 0 \tag{7}$$

The transformed boundary conditions are

$$f(0) = \frac{2}{m+1}S,\quad f'(0) = 1,\quad \theta(0) = 1 \qquad \text{at}\quad \eta = o \tag{8}$$

$$f'(\infty) = 0,\quad \theta(\infty) = 1 \qquad \text{at}\quad \eta = \infty,$$

The dimensionless parameters appeared into the above equations are defined as follows:

$M^2 = \frac{2\,\sigma B_0^2}{\rho a(1+m)}$ is the manetic interaction parameter.

$\beta = \frac{2m}{1+m}$ is the stretching parameter.

$\Pr = \frac{\mu C_p}{\kappa}$ is the Prandtl number.

$Ec = \frac{U^2(x)}{c_p(T_w-T_\infty)}$ is Eckert number

$S = -v_0\left(\frac{(1+m)x}{2\nu U(x)}\right)^{\frac{1}{2}}$ is suction or injection parameter

4. RESULTS AND DISCUSSION FOR THE FLOW PROFILES

The numerical results are present in the form of non-dimensional velocity and temperature profiles. The following considerations are made:

1. The Prandtl number Pr is chosen from 0.71 to 7, where 0.7 and7 corresponds to air and water.
2. The wall temperature variation n is taken 0, 1/3, 1 at the first instance where $n = 0$ is isothermal plate, $n = \frac{1}{3}$ is uniform heat flux independent of x but surface temperature gradient depend only and $n = 1$ is uniform heat flux independent of x. n also chose 2 and 3.
3. The value of Magnetic interaction parameter$M^2$and stretching parameter β are chosen arbitrarily.
4. The value of suction or injection parameter S is chosen arbitrary, where $S > 0$ is suction and $S < 0$ is injection.

Figure 1 and Figure 2 represents the dimensionless velocity profiles $f'(\eta)$ and temperature profile $\Theta(n)$ respectively for different values of magnetic interaction parameter $M^{2,}$ where $\mathrm{Pr} = 7.0, \beta = 1.5, n = 1.0, L = \mathrm{PrEc} = 1.0, m = 3.0, S = 1.0$ with the present of internal heat generation. From the figure we remark that the velocity profile decreases with the increasing value of magnetic interaction parameter M^2. Due to this increasing value of M^2 boundary layer thickness decreases. It is noticed that for increasing values of magnetic interaction parameter M^2, the temperature profile rises.

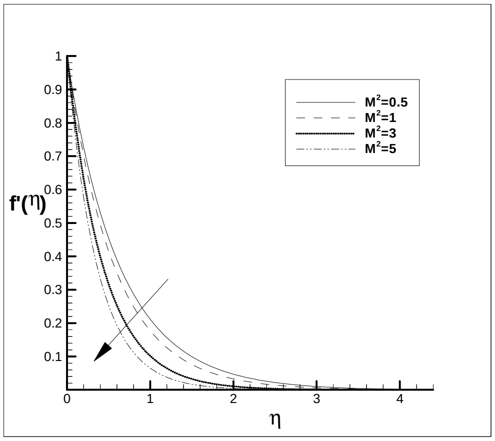

Fig1: **Velocity Porfiles for different M^2**

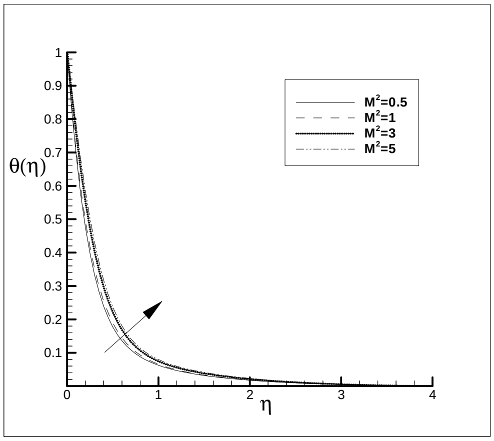

Fig2: **The temperature profiles for different M^2**

Figure 3 and Figure 4 depicts the variation of velocity and temperature profiles for the different value of stretching parameter β with the present of internal heat generation, where $\mathrm{Pr} = 7.0,\ M^2 = 1.0, n = 1.0, m = 3, L = \mathrm{PrEc} = 1.0, S = 1.0$. As the stretching parameter β increases, velocity profiles decreases. It means that the effect of stretching of the wall is to decelerate the velocity. The increasing value of β increases the temperature profiles. This effect is minimum.

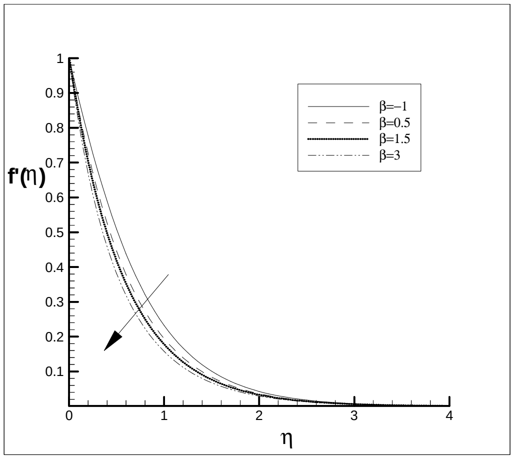

Fig 3 : The velocity profiles for different β

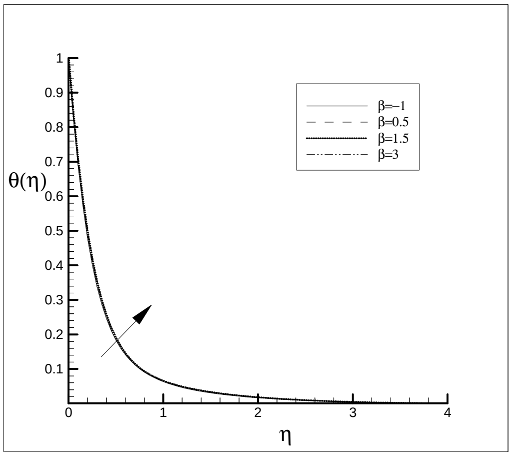

Fig 4: The temperature profiles for different β

Figure 5 is drawn for temperature profile for the different values of n where $\mathrm{Pr} = 7, \mathrm{M}^2 = 1, \beta = 1.5, \mathrm{m} = 3, \mathrm{L} = \mathrm{PrEc} = 1.0, \mathrm{S} = 1$ with the presence of internal heat generation. It is observed that the temperature profile decrease if the value of n is increased.

Figure 6 illustrates the influence of Prandtl number on temperature profile with existing of internal heat generation for the values of $\beta = 1.5, \mathrm{M}^2 = 1.0, \mathrm{n} = 1.0, \mathrm{m} = 3, \mathrm{L} = \mathrm{PrEc} = 1.0, \mathrm{S} = 1.0$. It is seen that the effect of rising value of Prandtl number is to decrease the temperature profiles. The boundary layer thickness decreases due to the effect of Prandtl number. Large Pr represents the flow is approaching the fluid boundary.

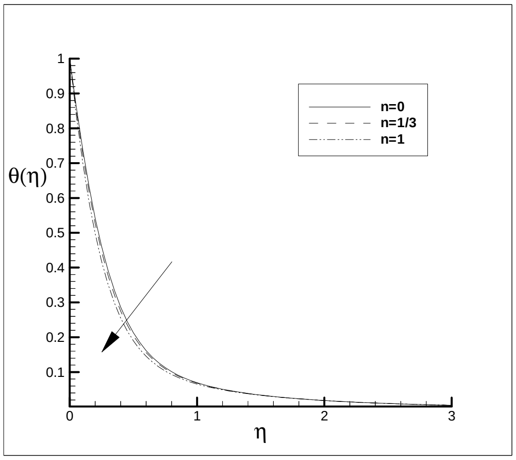

Fig 6: The temperature profiles for different n

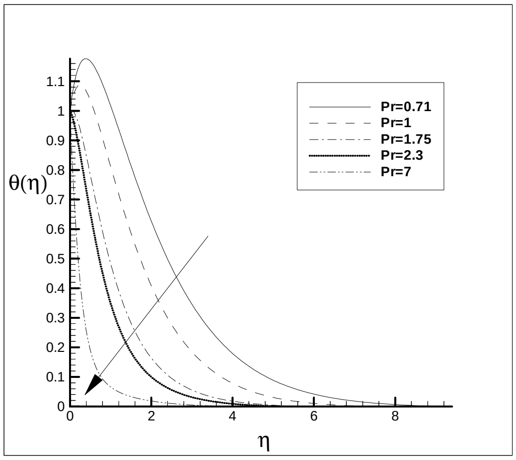

Fig 6: The temperature profiles for different Pr

Table 1 is constructed for skin friction $f''(0)$ and rate of heat transfer $\theta'(0)$ for different values of the governing parameter a stretching parameter β, index of power law variation of wall temperature n, and suction or injection parameter S. The skin friction decreases and rate of heat transfer increase for increasing value of β. For increasing value of n the heat transfer is decreased. For raising value of suction or injection parameter S both skin friction and rate of heat transfer are decreased.

Table 1: Numerical values of skin friction coefficients and rate of heat transfer for different values of $\boldsymbol{\beta}, \mathbf{n}$ and S with IHG where $\mathbf{Pr = 7.0, M^2 = 1.0, m = 3,}$ $\mathbf{L = PrEc = 1.0}$

β	n	S	$f''(0)$	$\theta'(0)$
-1	1	1	-1.1827359	-3.6904554
0	1	1	-1.4559418	-3.5795209
0.5	1	1	-1.5752469	-3.5287676
1.5	1	1	-1.7901086	-3.4345931
3	1	1	-2.0703241	-3.3076073
1.5	0	1	-1.7901086	-2.8343815
1.5	1/3	1	-1.7901086	-3.0405137
1.5	1	1	-1.7901086	-3.4345931
1.5	2	1	-1.7901086	-3.9708997
1.5	3	1	-1.7901085	-4.4564318
1.5	1	-1.5	-1.2050370	-0.0954309
1.5	1	-1	-1.3018602	-0.2078988
1.5	1	-0.5	-1.4084622	-0.5687246
1.5	1	0.5	-1.6524797	-2.2425538
1.5	1	1	-1.7901086	-3.4345931
1.5	1	1.5	-1.9379208	-4.7643975

5. CONCLUSIONS

In the presence of internal heat generation the steady hydromagnetic (MHD) flow and heat transfer with variable temperature, viscous dissipation are studied in this paper. The following conclusion can be drawn:

1. With the presence of internal heat generation the effect of magnetic field is to decrease the velocity and increases the temperature .
2. The velocity and skin friction are reduced because of the increasing value of streching parameter β . Its effect is very small in temperature profile. The stretching parameter also increase the rate of heat transfer.
3. The rising value of n is to decrease the termperature and rate of heat transfer. The velocity profile and skin friction does not change for the effect of n.
4. The Prandtl Pr number has no effect in velocity profile with the attendence of internal heat generaton but for increasing Prandtl number the temperature profile is decreased.
5. Due to increase of both Prandtl number and n, the flow of heat becomes slow.
6. For increasing value of suctoin or injection parameter skin friction and rate of heat transfer is decreased.

6. REFERENCES

[1] Chakrabarti A, Gupta AS, (1979), Hydromagnetic flow and heat transfer over a stretching sheet. Quart Appl Math 37:73–78.

[2] Abdelhafez TA, (1985), Skin friction and heat transfer on a continuous flat surface moving in a parallel free stream, Int J Heat Mass Transfer 28:1234–1237.

[3] Andersson HI, (1995), An exact solution of the Navier–Stokes equations for magneto hydrodynamic flow. Acta Mechanica 113:241–244.

[4] Chiam TC, (1995), Hydromagnetic flow over a surface stretching with a power-law velocity. Int J Eng Sci 33(3):429–435.

[5] S. P. Anjali Devi, M. Thiyagarajan, (2006), Steady nonlinear hydromagnetic flow and heat transfer over a stretching surface of variable temperature, Heat Mass Transfer 42:
671–677.

[6] Philip R. Nachtsheim and Paul Swigert, (1965), Satisfaction of Asymptotic Boundary Condition s in numerical solution of systems of nonlinear equations of boundary layer type, National aeronautics and space administration, Washington, D. C.

[7] Banks WHH, (1983), Similarity solutions of the boundary layer equations for stretching wall. J Mecan Theo Appl 2:375–392.

[8] Afzal N, (1993), Heat transfer from a stretching surface. Int J Heat Mass Transfer 36:1128–1131.

[9] R.Kandasamy, Abd. Wahid B. Md. Raj Azme B. Khamis, (2006), Effects of chemical reaction, heat and mass transfer on boundary layer in the presence of suction or injection. Theoret. Appl. Mech. Vol.33. No-2 pp. 123-148, belgrade.

[10] Frank M. white, (2006), Viscous fluid flow, Third international edition.

“Proceedings of the 4th BSME-ASME International Conference on Thermal Engineering
27-29 December 2008, Dhaka, Bangladesh”

EFFECT OF INLET TO CAVITY WIDTH RATIO ON MIXED CONVECTION IN A MICROSTRUCTURE FILLED VENTED CAVITY

Shama Farabi Barna, Arafat Ahmed Bhuiyan, M H Banna, A. K. M. Sadrul Islam

Department of Mechanical and Chemical Engineering, IUT,
Board Bazar, Gazipur-1704, Dhaka Bangladesh

Email: farabibd@gmail.com

ABSTRACT: *This investigation has been carried out considering enclosures filled with fluid saturated porous medium with four of its wall are isothermal at constant temperatures. Due to the temperature difference between the isothermal wall and the fluid, Natural convection takes place. By providing an inlet at the bottom surface, and a vent at the top, facing the inlet, forced convection is induced. Using the modified Darcy flow model and energy equation for five different Rayleigh Numbers (1, 50, 100, 500, and 1000) and seven different Peˊclet Numbers (0.1, 1, 5, 10, 20, 50 and 100 the problem is solved. Considering three different Aspect Ratios of the cavity (AR=H/W=0.5, 1, 2), the equations are solved using standard Finite Element method for. By means of the numerical analysis, effect of inlet to cavity width ratio I/W on mixed convection is observed.*

KEYWORDS: *Porous medium, Mixed Convection, Peclet Number, Bejan Number.*

1. INTRODUCTION

Convective heat transfer in saturated porous media has been widely studied in heat transfer due to its fundamental importance & wide range of applications. Fundamental studies related to thermal convection in porous media have increased significantly due to the requirement for energy, the necessity to develop effective technologies for nuclear waste management, transpiration cooling, separation processes in chemical industries, building thermal insulations, winding structure for high-power density in electric machines, packed-bed catalytic reactors and numerous other applications have led to a considerable interest in convective heat transport through porous media.

The fundamental nature and the growing volume of works in this area are amply documented in the books by Nield and Bejan [1], Ingham and Pop [2–4], Vafai [5,6], Pop and Ingham [7], Bejan and Kraus [8], Ingham et al. [9] and Bejan et al. [10], and the review articles by Hadim and Vafai [11], and Vafai and Hadim [12].

A rich variety of important analytical, numerical, and experimental results have been published on this topic and they are important to better understand the thermal convection inside porous cavities. The technical issues of mixed convection flow in porous media have been concerned mainly with situations in which buoyancy effects are substantial, if not entirely dominant. So the flow regime of interest is clearly the flow situations where buoyancy effects are substantial or dominant.

In this paper our attention has been focused on a problem of mixed convection .By providing an inlet and a square vent, forced convection condition can be imposed inside an enclosure filled with porous medium. All the walls of the enclosure are at constant temperature. The interaction between the buoyancy stemming from one or more heated elements inside the enclosure and the imposed forced flow forms the topic of our investigation. In this numerical analysis, different aspect ratios of enclosure, different inlet outlet ratios, different inlet width to cavity width ratios, boundary conditions are considered. The performance of the enclosure is determined by flow visualization and by analyzing different parameters such as Bejan Number, Nusselt Number, and Entropy Generation Number.The results will help to find out most effective Inlet –cavity Width Ratios.

2. BASIC EQUATIONS

The fluid flow takes place through an enclosure where all of its walls are considered as isothermal at a temp T_w. There is an inlet at the left corner of the bottom wall and the vent is on the left corner of the top wall. The widths of the inlet and vent are I and O respectively as shown in figure 1, and in this study we have considered I/O=0.5. Buoyancy effects are induced due to the difference in temperature between the left vertical wall, T_w, and the through-stream temperature, T_0, which has a constant velocity, V_0, at the inlet of the enclosure. The inlet forced flow is fixed at the inlet and the temperature difference (T_w - T_0) considered here is positive which means it is an aiding flow.

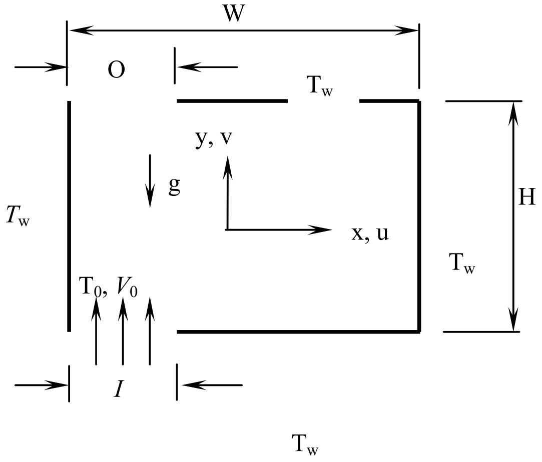

Fig. 1: Physical model and the coordinate system of the cavity

The assumptions made for porous media to prepare mathematical model are: the fluid and the porous medium are in local thermal equilibrium; the properties of the fluid and the porous media are constant; the viscous drag and inertia terms of the momentum equations are negligible, and the Darcy and Boussinesq approximations are valid. Under these assumptions, the conservation equation for mass becomes:

$$\frac{\partial u}{\partial x}+\frac{\partial v}{\partial y}=0 \qquad \dots \quad \dots \quad \dots \quad \dots \dots \dots \dots \dots. \qquad (1)$$

The momentum flow inside the enclosure can be modeled by the Darcy flow model [1], by using the assumptions. This constructs a relationship between the flow velocities at a certain direction to the pressure gradient in that direction in vector form is,

$$\mathbf{v}=\frac{K}{\mu}(-\,\mathbf{grad}\,p+\rho\ \mathbf{g}) \qquad \dots \quad \dots \quad \dots \quad \dots \dots. \dots.. \qquad (2)$$

where, **v**, K, μ, p, and **g** are the velocity vector, permeability, viscosity, pressure, and gravity vector, respectively. The permeability K is an empirical constant which may define a length scale squared of pores. The Darcy flow model is applicable where the order of magnitude of the local pore Reynolds number, based on the local volume averaged speed ($|\mathbf{v}|^{1/2}$) and $K^{1/2}$ is smaller than 1. Taking **curl** on the both side of Eq. (2) with the assumption, $\mathbf{v} = u\boldsymbol{i} + v\boldsymbol{j} + 0\mathbf{k}$ and $\mathbf{g} = 0\boldsymbol{i} + g_y\boldsymbol{j} + 0\boldsymbol{k}$, we can get

$$\frac{\partial u}{\partial y} - \frac{\partial v}{\partial x} = -\frac{g\beta K}{\nu}\frac{\partial T}{\partial x} \tag{3}$$

where $g = g_y$. Eq. (3) has no pressure term. Finally, the energy equation, according to Nield and Bejan [1], is

$$\sigma\frac{\partial T}{\partial t} + u\frac{\partial T}{\partial x} + v\frac{\partial T}{\partial y} = \alpha_m\left(\frac{\partial^2 T}{\partial x^2} + \frac{\partial^2 T}{\partial y^2}\right) \tag{4}$$

Without any external or internal source, the equation of entropy generation according to Mahmud, S., and Fraser, [13] is

$$S'''_{gen} = HTI + FFI = \frac{k}{T_0^2}\left[\left(\frac{\partial T}{\partial x}\right)^2 + \left(\frac{\partial T}{\partial y}\right)^2\right] + \frac{\mu}{KT_0}\left(u^2 + v^2\right) \tag{5}$$

where, $HTI = \dfrac{k}{T_0^2}\left[\left(\dfrac{\partial T}{\partial x}\right)^2 + \left(\dfrac{\partial T}{\partial y}\right)^2\right]$ … … … … …… (6)

and $FFI = \dfrac{\mu}{T_0 K}\left(u^2 + v^2\right)$ … … … … … … … … .. (7)

Finally, the equation of energy flux density vector according to Mahmud, S., and Fraser [13] is

$$\mathbf{E} = E_x\mathbf{i} + E_y\mathbf{j} = \rho\mathbf{v}\left[\frac{1}{2}|v|^2 + C_P(T-T_0)\right] - k\,\mathbf{grad}(T) \tag{8}$$

where x, y are the Cartesian coordinates measured in the horizontal and vertical directions, u, v are the velocity components along x- and y-axes, and T is the fluid temperature, respectively,

We define the stream function, ψ, in the usual way as

$$u = \frac{\partial \psi}{\partial y} \tag{9}$$

$$v = -\frac{\partial \psi}{\partial x} \tag{10}$$

Substituting Eqs. (9) and (10) into Eqs. (3) and (4), the following equations are obtained:

$$\frac{\partial^2 \psi}{\partial x^2} + \frac{\partial^2 \psi}{\partial y^2} = -\frac{g\beta k}{\nu}\frac{\partial T}{\partial x} \tag{11}$$

$$\frac{\partial T}{\partial t} + \frac{\partial \psi}{\partial y}\frac{\partial T}{\partial x} + \frac{\partial \psi}{\partial x}\frac{\partial T}{\partial y} = \alpha_m\left(\frac{\partial^2 T}{\partial x^2} + \frac{\partial^2 T}{\partial x^2}\right) \tag{12}$$

where Ra and Pe are the Rayleigh and Pe´clet numbers for a porous medium which are defined by

$$Ra = \frac{gK\beta(T_w - T_0)H}{\alpha_m \nu}, \qquad Pe = \frac{V_0 H}{\alpha_m} \tag{13}$$

2.1 Boundary Conditions

It is mentioned before that the walls are isothermal and their temperature, T_w is assumed to be 1K. The temperature of the flow passing through the inlet, T_0, is considered to be 0K above the freezing point of water. So, the boundary conditions of Eqs. (11) and (12) are

Left isothermal wall: $\psi = 0$, $T = T_w = 1$ on $x = 0$, $0 \le y \le H$, …… 14(i)
Inlet: $\psi = -xV_0$, $T = T_0 = 0$ on $y = 0$, $0 \le x \le I$, …… 14(ii)
Bottom Isothermal wall: $\psi = 0$, $T = T_w = 1$ on $y = 0$, $I \le x \le W$, …… 14(iii)
Right Isothermal wall: $\psi = 0$, $T = T_w = 1$ on $x = W$, $0 \le y \le H$, … … 14(iv)
Top Isothermal wall: $\psi = 0$, $T = T_w = 1$ on $y = H$, $O \le x \le W$, ………14(v)
Outlet: $\frac{\partial \psi}{\partial y} = 0$, $\frac{\partial T}{\partial y} = 0$ on $y = H$, $0 \le x \le O$ …… … 14(vi)

3. RESULTS AND DISCUSSION

Figure 2 shows the isothermal lines for different Aspect Ratio, I/O=0.5 and different Rayleigh Number and Peclet Number. The variation of isothermal line with the change of inlet to cavity width ratio (I/W) is observed. It can be observed from the figure that at low I/W isothermal lines are confined near the left isothermal wall and spread towards right with the increase of I/W. Thus it can be concluded that the rate of change of temperature decreases with the increase of I/W ratio. Again the isothermal lines cover more area of the porous media with the increase of I/W ratio. This tendency of isothermal lines to spread are higher at low aspect ratio (for AR=0.5 in the figure). But for higher values of aspect ratio the tendency of the isotherms to spread with increasing I/W gradually decreases. The variation of isothermal line with the change of aspect ratio is also observed. For same I/W it can be observed from the figure that the spread of isothermal lines decreases with the increase of aspect ratio. Thus it can be concluded that the rate of change of temperature increases with the increase of aspect ratio. The isothermal lines cover less area of the porous media with the increase of aspect ratio.

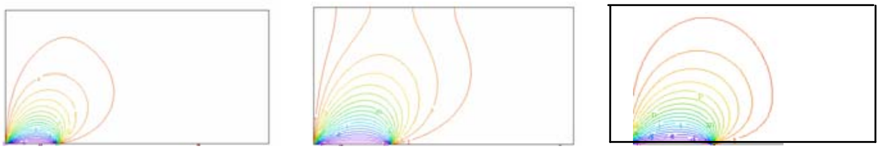
I/W=0.1 I/W=0.3 I/W=0.5

(a) AR=0.5


I/W=0.1 I/W=0.3 I/W=0.5

(b) AR=2.0

Figure 2: Isothermal Line for I /O=0.5 Ra=1 Pe=0.1

Figure 3 shows the streamlines for different aspect ratio, I/O=0.5 and different Rayleigh Number and Peclet Number. The variation of streamline with the change of I/W is observed. One of the significant phenomenons found in this observation is the formation of vortex and its increase in growth & number with increase of I/W. As a result resistance to convection also increases due to energy dissipation by the vortex .This trend is fairly detectable at low aspect ratio. As aspect ratio increases, the trend exists but vortex growth rate becomes slower than it does at a lower aspect ratio. Also, for same I/W, as the aspect ratio increases size of the vortex formed gets smaller .These characteristics can be fairly noticed from streamlines of I/W= 0.5 for different aspect ratio.

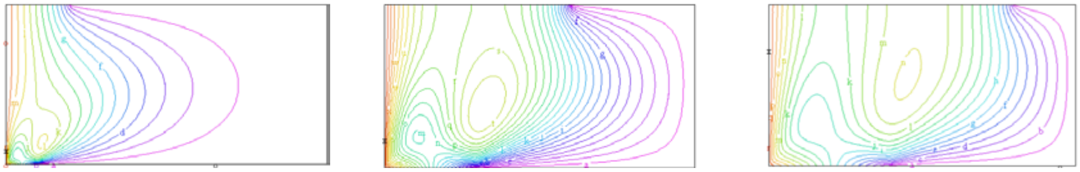
I/W=0.1 I/W=0.3 I/W=0.5

(a) AR=0.5


I/W=0.1 I/W=0.3 I/W=0.5

(b) AR=2

Figure 3: Streamlines for I /O=0.5 Ra=1 Pe=0.1

Figure 4 shows the constant Bejan Number line for different I/W, I/O=0.5 and different Rayleigh Number and Peclet Number. Bejan number does not show any significant change with inlet to cavity width ratio (I/W).

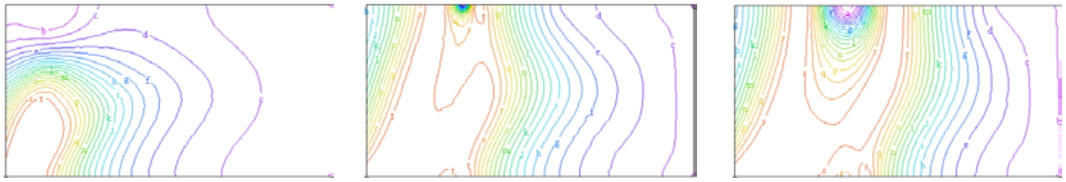
I/W=0.1 I/W=0.3 I/W=0.5

(a)AR=0.5

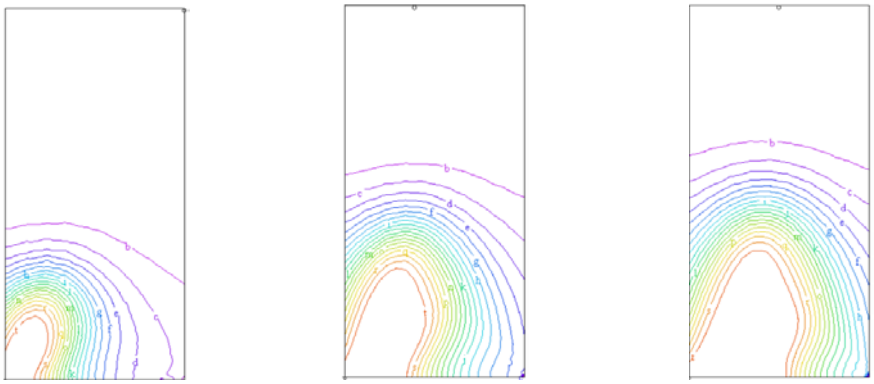

I/W=0.1 I/W=0.3 I/W=0.5

(b) AR=2.0

Figure 4: Constant Bejan Number line for I /O=0.5 Ra=1 Pe=0.1

Figure 5 shows the variation of Average Nusselt Number with I/W for different Pe. It is evident from these figures that Nu_{av} increases with the increase of I/W. From figure 3.4 (a) it is observed that the value of Nu_{av} increases by 327%, 348%, 442%, 553%, 713%, 622%, 295% for Pe= 0.1, 1, 5, 10, 20, 50, 100 respectively when I/W increases from 0.1 to 0.5 for I/W=0.1, I/O=0.5, Ra=50. The graph increases linearly & get into a parabolic shape before it approaches a steady state. Thus it indicates that Nu_{av} will move towards a steady value after certain I/W.

Figure 6shows the variation of Average Entropy Generation Number with inlet to cavity width ratio for different Pe. It is evident from these figures that Ns_{av} increases with the increase of Aspect Ratio. From figure 3.4(b) it is observed that the value of Ns_{av} increases by 108%,112%, 135.2%, 176.4%, 279.15%, 872%, 1619% for Pe= 0.1, 1, 5, 10, 20, 50, 100 respectively when I/W increases from 0.1 to 0.5 for AR=1, I/O=0.5, Ra=1000.The rate of increase decreases at high I/W

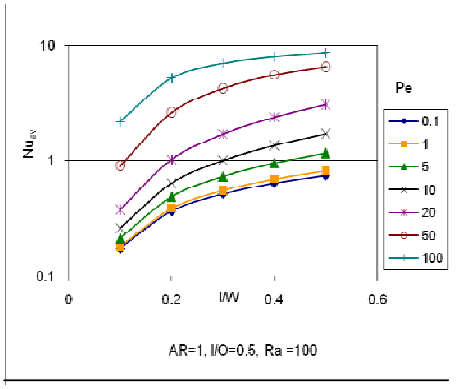

Figure 5: Variation of Nu_{av} with I/W for different Pe

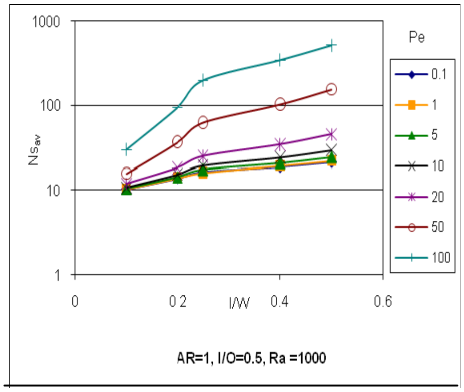

Figure 6: Variation of Ns_{av} with I/W for different Pe

Figure 7 shows the variation of Average Bejan Number with inlet to cavity width for different Pe. It is evident from these figures that Be_{av} decreases with the increase of I/W. It is apparent from figure 3.5(a) that the value of Be_{av} increases by 32.2%, 34.9%, 50.27%, 66.9%, 79.3%, 83.7%, 81.5% for Pe= 0.1, 1, 5, 10, 20, 50, 100 respectively when I/W increases from 0.1 to 0.5 for AR=1, I/O=0.5, Ra=100.

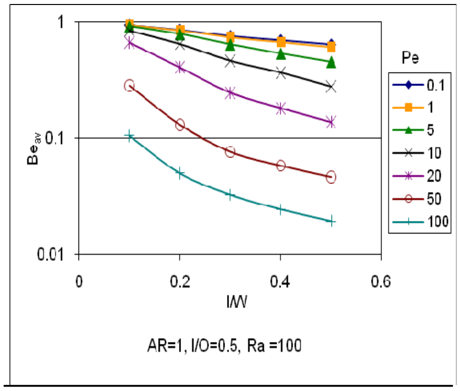

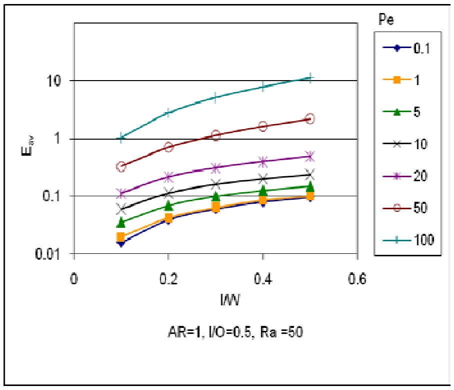

Figure 7: Variation of Be_{av} with I/W for different Pe

Figure 8: Variation of E_{av} with I/W for different Pe

Figure 8 shows the variation of Average Energy Flux Density with Aspect Ratio for different Pe. It is evident from these figures that E_{av} increases significantly with the increase of I/W. This rate of increase is higher at low I/W, but it reduces as I/W move towards higher values. It is observed from figure 3.5(b) that the value of E_{av} increases by 504.7%, 412%, 318%, 296% ,331.7%, 565% & 977% for Pe= 0.1, 1, 5, 10, 20, 50 and 100 respectively when I/W increases from 0.1 to 0.5 for AR=0.1, I/O=1, Ra=50.

4. CONCLUSION

The present numerical study examined and explained two-dimensional, steady mixed convection flow in a porous square vented cavity with all walls being isothermal surfaces. The transformed equations of Darcy and energy in non-dimensional form have been solved numerically using the finite-volume method. Governing parameters chosen are Pe , Ra, I/W, AR which are varied in the range $0.1 \leq Pe \leq 100$, $1< Ra <5000$, $0.1\leq$ I/W $\leq$ 0.5, $0.5\leq AR \leq 2$ .It is clear from the results that the I/W has considerable influence on the flow and heat transfer characteristics in the cavity. Isotherms, streamlines show substantial variation in their pattern or magnitude in response to changing values of I/W whereas constant bejan number lines remain unaffected. , Average nusselt number, average entropy generation number, average bejan number, average energy flux density either increases or decreases. But as the I/W is increased ,the amount of increase or decrease becomes less .So it can be concluded that increasing I/W leads these parameters to a steady value after a certain I/W.

ACKNOWLEDGMENTS

The authors are indebted to members of Department of Mechanical & Chemical Engineering ,Islamic University of Technology(IUT).The authors are specially grateful to Dr. Md. Abdur Razzaq Akhanda ,Head, Department of Mechanical & Chemical Engineering, IUT. They also wish to express their appreciation to various colleagues who through their continued interest & intellectual input have indirectly contributed to the work reported. The list includes Sakib Bin Lutful Mahmud, Md. Raju Hossain & numerous others.

REFERENCES

[1] D.A. Nield, A.Bejan, Convection in Porous Media, second ed.,Springer, New York, 1999.
[2] D.B.Ingham,I.Pop (Eds.),Transport Phenomena in Porous Media,Pergamon,Oxford, 1998.
[3] D.B.Ingham,I.Pop (Eds.),Transport Phenomena in Porous Media,Pergamon,Oxford, 2002.
[4] D.B. Ingham,I.Pop (Eds.), Transport Phenomena in Porous Media,Elsevier, Oxford, 2005.
[5] K. Vafai (Ed.), Handbook of Porous Media, Marcel Dekker, NewYork, 2000.
[6] K.Vafai (Ed.), Handbook of Porous Media, second ed.,Taylor & Francis,New York, 2005.
[7] I. Pop, D.B. Ingham, Convective Heat Transfer: Mathematical and Computational Modeling of Viscous Fluid Porous Media, Pergamon, Oxford, 2001.
[8] A. Bejan, A.D. Kraus (Eds.), Heat Transfer Handbook, Wiley, New York, 2003.
[9] D.B. Ingham, A. Bejan, E. Mamut, I. Pop (Eds.), Emerging Technologies and Techniques in Porous Media,Kluwer, Dordrecht,2004.
[10] A. Bejan, I. Dincer, S.Lorente, A.F. Miguel, A.H. Reis, Porous and Complex Flow Structures in Modern Technologies, Springer, New York, 2004.
[11] H. Hadim, K. Vafai, Overview of current computational studies of heat transfer in porous media and their applications—forced convection and multiphase heat transfer, in: W.J. Minkowycz, E.M.Sparrow (Eds.), Advances in Numerical Heat Transfer, vol. II, Taylorand Francis, New York, 2000, pp. 291–329.
[12] K. Vafai, H. Hadim, Overview of current computational studies ofheat transfer in porous media and their applications-natural and mixed convection, in: W.J. Minkowycz, E.M. Sparrow (Eds.), Advances in Numerical Heat Transfer, vol. II, Taylor and Francis, New York, 2000, pp. 331–369.
[13] S. Mahmud, R.A. Fraser, Magnetohydrodynamic free convection and entropy generation in a square porous cavity Int J. Heat Mass Transfer 47 (2004) 3245–3256.

Proceedings of the 4th BSME-ASME International Conference on Thermal Engineering
27-29 December, 2008, Dhaka, Bangladesh

EFFECT OF THERMAL RADIATION ON CONVECTIVE FLOW PAST A UNIFORMLY HEATED VERTICAL PLATE IN THE PRESENCE OF MAGNETIC FIELD

Tamanna Sultana[1], Goutam saha[2], Sumon Saha[3]

[1]Institute of Natural Science,
United International University (UIU), Dhaka-1209, Bangladesh
[2]Department of Mathematics,
University of Dhaka, Dhaka-1000, Bangladesh
[3]Department of Energy and Environmental Engineering, Interdisciplinary Graduate School of Engineering Sciences, Kyushu University, 6-1 Kasuga-koen, Kasuga-shi, Fukuoka 816-8580, Japan
E-mail: labsachin@gmail.com

ABSTRACT

The effect of radiation parameters on convection flow along a uniformly heated vertical flat plate in the presence of a magnetic field has been investigated numerically. The nonlinear governing equations with associate boundary conditions for this analysis are transferred to simultaneous nonlinear differential equations and solved numerically using Multi-segment integration technique. The main objective of this work is to analyze the effect of radiation and magnetic field on the temperature profiles. Numerical results for the details of the temperature are shown graphically for different values of the parameters entering into the problem.

Key words: *Convection, Electrically conducting fluid, Porous medium, Radiation.*

1. INTRODUCTION

The radiation effect on convective flow and heat transfer problems has become more important industrially. Many processes in engineering areas occur at high temperatures and knowledge of radiation heat transfer becomes very important for the design of pertinent equipment. Nuclear power plants, gas turbines and the various propulsion devices for aircraft, missiles, satellites and space vehicles are examples of such engineering areas. The similarity solution of natural convection along vertical isothermal plate has been presented by Ostrach [1]. The thermal radiation of a gray fluid, which is emitting and absorbing radiation in a non-scattering medium has been examined by Ali *et al.* [2], Ibrahim [3], Mansour [4], Hossain *et al.* [5] and Elbashbeshy and Dimian [6]. In the aspect of both convection and radiation, Viskanta and Grosh [7] considered the effects of thermal radiation on the temperature distribution and the heat transfer in an absorbing and emitting media flowing over a wedge by using the Rosseland diffusion approximation. Hossain *et al.* [8] investigated the natural convection–radiation interaction on a boundary layer flow along a vertical plate with uniform suction. Ibrahim *et al.* [9] investigated similarity reductions for problems of radiative and magnetic field effects on free convection and mass transfer flow past a semi-infinite flat plate. In the present paper, we investigate the effect of thermal radiation interaction of the boundary layer flow of electrically conducting fluid past a uniformly heated vertical plate embedded in a porous medium. The governing equations are converted into a set of nonlinear system of coupled differential equations and solved numerically using Multi-segment integration technique. The normalized similarity solutions are then obtained numerically for various governing parameters considering into the problem and explained their nature of variation from the physical point of view.

2. MATHEMATICAL FORMULATION OF THE PROBLEM

Let us consider a steady two-dimensional flow of a viscous, incompressible and electrically conducting fluid at ambient temperature, T_∞ past a semi-infinite heated vertical plate having constant temperature T_w (where $T_w > T_\infty$). A magnetic field of uniform strength is applied perpendicular to the plate. The magnetic Reynolds number is taken to be small enough so that the induced magnetic field can be neglected. The flow is assumed to be in the x-direction, which is taken along the plate in the upward direction and y-axis is normal to it. The flow configuration and the coordinate system are shown in the Fig. 1.

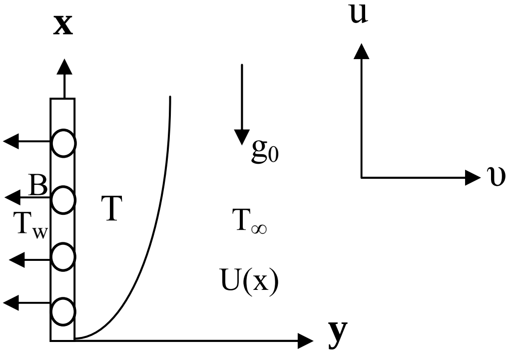

Fig. 1 Flow configuration and co-ordinate system

The fluid is considered to be gray, absorbing-emitting radiation but non-scattering medium and the Rosseland approximation is used to describe the radiative heat flux in the energy equation. The radiative heat flux in the *x*-direction is considered negligible in comparison to the *y*-direction. Within the framework of the above-noted assumptions, we assume that the Bousssinesq and boundary layer approximations hold and the governing equations relevant to the problem in the presence of radiation are given by:

Continuity equation

$$\frac{\partial u}{\partial x}+\frac{\partial \upsilon}{\partial y}=0 \tag{1}$$

Momentum equation

$$u\frac{\partial u}{\partial x}+\upsilon\frac{\partial u}{\partial y}=\nu\frac{\partial^2 u}{\partial y^2}+U\frac{\partial U}{\partial x}+\frac{\sigma B^2}{\rho}(U-u)-\frac{\nu}{K'}(U-u) \tag{2}$$

Energy equation

$$u\frac{\partial T}{\partial x}+\upsilon\frac{\partial T}{\partial y}=\frac{\kappa}{\rho c_p}\frac{\partial^2 T}{\partial y^2}-\frac{1}{\rho c_p}\frac{\partial q_r}{\partial y} \tag{3}$$

where, u and υ are the velocity components along x and y coordinates respectively, $U(x)$ is the free stream velocity, $\nu = \mu / \rho$ is the kinematic viscosity, μ is the coefficient of dynamic viscosity, ρ is the mass density of the fluid, σ is the electrical conductivity of the fluid, B is the magnetic induction, K' is the Darcy permeability, T is the temperature of the fluid in the boundary layer, T_∞ is the temperature of the fluid outside the boundary layer, c_p is the specific heat of the fluid at constant pressure, κ is the thermal conductivity and q_r is the radiative heat flux.

We assume that the velocity of the free stream is of the form

$$U\left(x\right)=a\,x+c\,x^2 \tag{4}$$

where, a and c are constants.

By using Rosseland approximation q_r for radiation for an optically thick layer (Ali *et al.* [8]), we can write

$$q_r = -\frac{4\sigma^*}{3\kappa^*}\frac{\partial T^4}{\partial y} \tag{5}$$

where, σ^* is the Stefan-Boltzmann constant and κ^* is the mean absorption coefficient.

We assume that the temperature differences within the flow are sufficiently small such that T^4 may be expressed as a linear function of temperature. This is accomplished by expanding T^4 in a Taylor's series about T_∞ and neglecting higher-order terms, thus

$$T^4 \cong T_\infty^4 + (T - T_\infty).4T_\infty^3 = 4T_\infty^3 T - 3T_\infty^4 \tag{6}$$

By using (5) and (6) Eq. (3) gives

$$u\frac{\partial T}{\partial x} + \upsilon\frac{\partial T}{\partial y} = \frac{k}{\rho c_p}\frac{\partial^2 T}{\partial y^2} + \frac{16\sigma^* T_\infty^3}{3\rho c_p \kappa^*}\frac{\partial^2 T}{\partial y^2} \tag{7}$$

The corresponding boundary conditions for the above problem are given by,

$$\left.\begin{array}{ll} u = 0,\ \ \upsilon = 0,\ \ T = T_w & \text{at } \mathrm{y} = 0, \\ u \to U(x),\ \ T \to T_\infty & \text{as } \mathrm{y} \to \infty. \end{array}\right\} \tag{8}$$

3. NON-DIMENSIONALISATION

In order to obtain a solution of equations (1), (2) and (7), we introduce the following transformations:

$$\eta = \sqrt{\frac{a}{\nu}}\,y\,,\quad u = axf'(\eta) + cx^2 g'(\eta)\,,$$

$$\upsilon = -\sqrt{a\nu}\,f(\eta) - \frac{2cx}{\sqrt{\frac{a}{\nu}}}g(\eta)\,,\ T = T_w + (T_\infty - T_w)\left[T_0(\eta) + \frac{2cx}{a}T_1(\eta)\right]$$

Then Eqs. (2) and (7) reduces to,

$$f''' + ff'' - f'^2 + N(1 - f') - Mf' + 1 = 0, \tag{9}$$

$$g''' + fg'' - 3f'g' + 2f''g + N(1 - g') - Mg' + 3 = 0, \tag{10}$$

$$T_0'' + Pn(fT_0' + T_0) = 0, \tag{11}$$

$$T_1'' + Pn(-f'T_1 + fT_1' + gT_0') = 0, \tag{12}$$

where,

$P = \dfrac{\rho\nu c_p}{\kappa}$ is the Prandtl number,

$N = \dfrac{\sigma B^3}{a\rho}$ is the Magnetic parameter,

$M = \dfrac{\nu}{aK'}$ is the Darcy parameter,

$Pn = \dfrac{3KP}{3K + 4}$ is the Radiative Prandtl number and

$K = \dfrac{\kappa^*\kappa}{4\sigma^* T_\infty^3}$ is the Radiation parameter.

The corresponding boundary conditions (10) becomes,

$$\left.\begin{array}{ll} f = 0, f' = 0, g = 0, g' = 0, T_0 = 0, T_1 = 0 & \text{at } \eta = 0 \\ f' = 1, g' = 1, T_0 = 1, T_1 = 0 & \text{as } \eta \to \infty \end{array}\right\} \tag{13}$$

4. RESULTS AND DISCUSSION

The non-linear system of coupled differential equations (9)-(12) together with the boundary conditions (13) are solved numerically using Multi-segment integration technique. To assess the accuracy of our code, we have plot the graphs of similarity temperatures $T_0(\eta)$ and $T_1(\eta)$ for K = 3 and 30 where the Prandtl number and magnetic parameter are taken fixed at 0.71 and 0.8 respectively. We have compared these graphs with that of Raptis *et al.* [10]. Fig. 2 shows the comparison of the temperature profiles T_0 and T_1 for P = 0.71 and N = 0.8 produced by the present code and that of Raptis *et al.* [10]. In fact the results show a close agreement, hence an encouragement for the use of the present code. Hence, the numerical scheme used in this paper is found both stable and accurate.

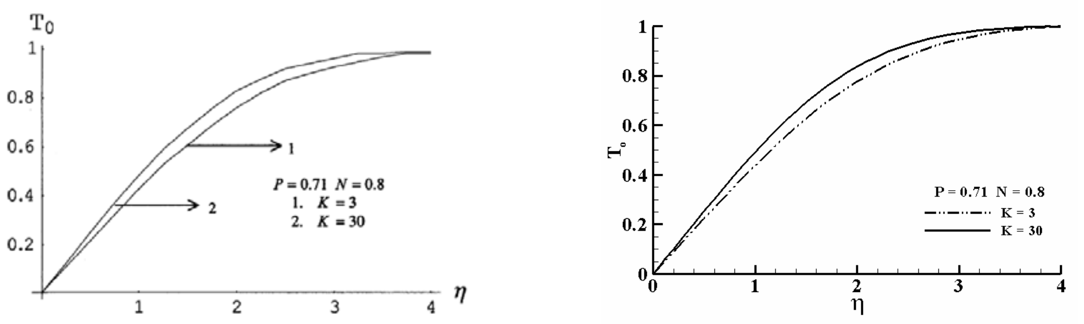

(a) Raptis *et al.* [10] **(b) Present Work**

Fig. 2 Comparison of the temperature profiles T_0 and T_1 for P = 0.71 and N = 0.8

Our aim is to determine the effects of different parameters on the normalized similarity temperatures, $T_0(\eta)$ and $T_1(\eta)$. In the calculations, the values of Magnetic parameter (N), Darcy parameter (M), Prandtl number (P) and radiation parameter (K) are chosen arbitrarily.

Figure 3 shows the effect of magnetic field parameter (N), on the temperature profiles. This figure reveals that the normalized similarity temperature, $T_0(\eta)$ shows no effect for variation of magnetic field parameter but similarity temperatures, $T_1(\eta)$ increases with the increase of N. This is due to the fact that the magnetic field tends to retard the velocity field which in turn induces the temperature field resulting to the increase of the temperature profiles. The magnetic field can therefore be used to control the flow characteristics.

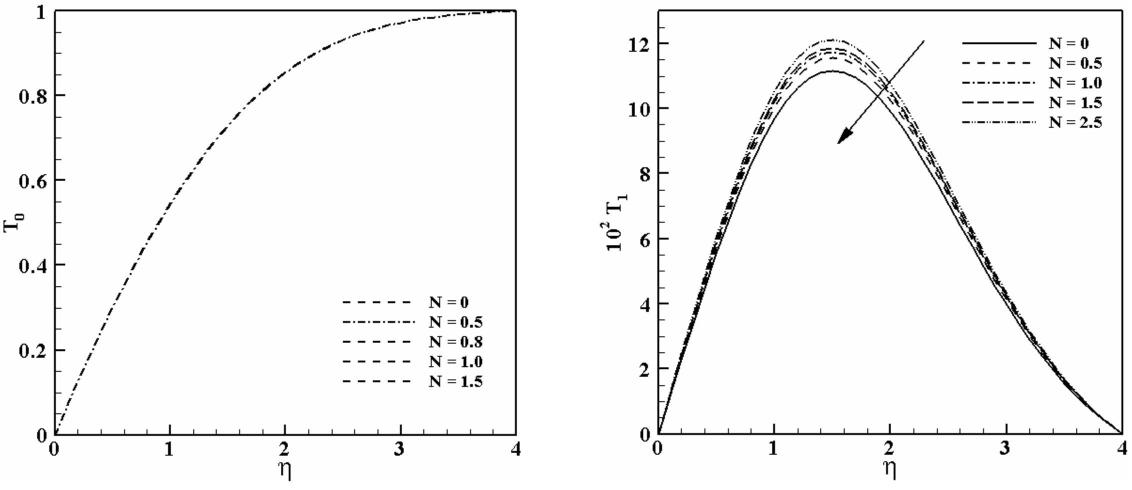

Fig. 3 Temperature profiles with the variation of N for P = 0.71 and M = 0.5

For different values of Prandtl number (P), we get significant changes on temperature profiles, which is shown in Fig. 4. From this figure, we see that for cooling of the plate, normalized similarity temperature, $T_0(\eta)$ increases as P increases and similarity temperatures $T_1(\eta)$ also increases near the plate surface. It is apparent that the peak region of each profile move far away from the plate as P increases and after a short distance from the plate, these profiles overlap and decreases monotonically.

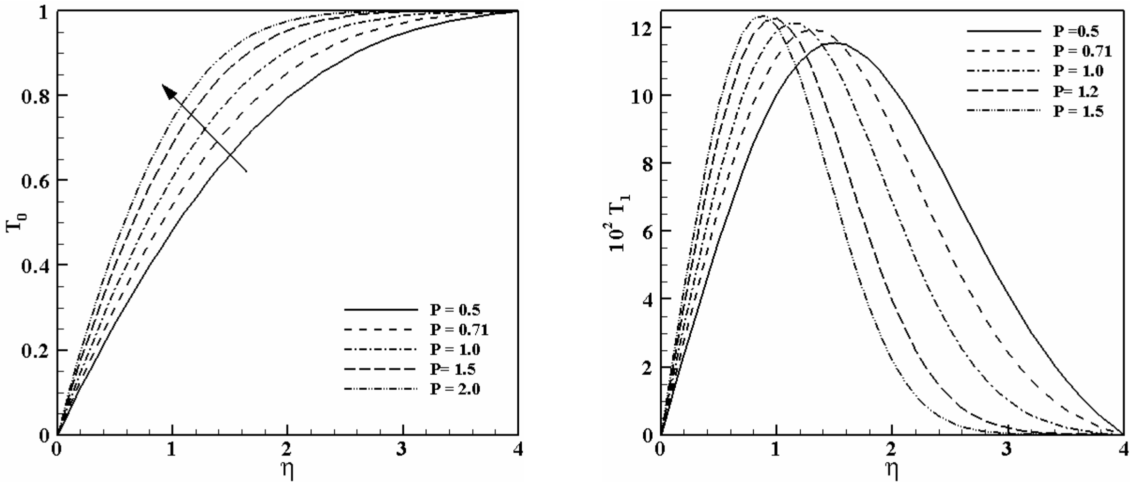

Fig. 4 Temperature profiles with the variation of P for M = 0.5 and N = 0.5

All the above calculations have been carried out for a fixed radiation parameter, K. Therefore, the effects of radiation parameter (K) on temperature profiles are not clear from the earlier discussions. Figure 5 shows the effect of radiation parameter (K) on the temperature profiles. We observe that the temperature increases as K increases for both normalized similarity temperatures, $T_0(\eta)$ and $T_1(\eta)$. It is apparent from the figure that for large values of K, the profiles have less significant effect.

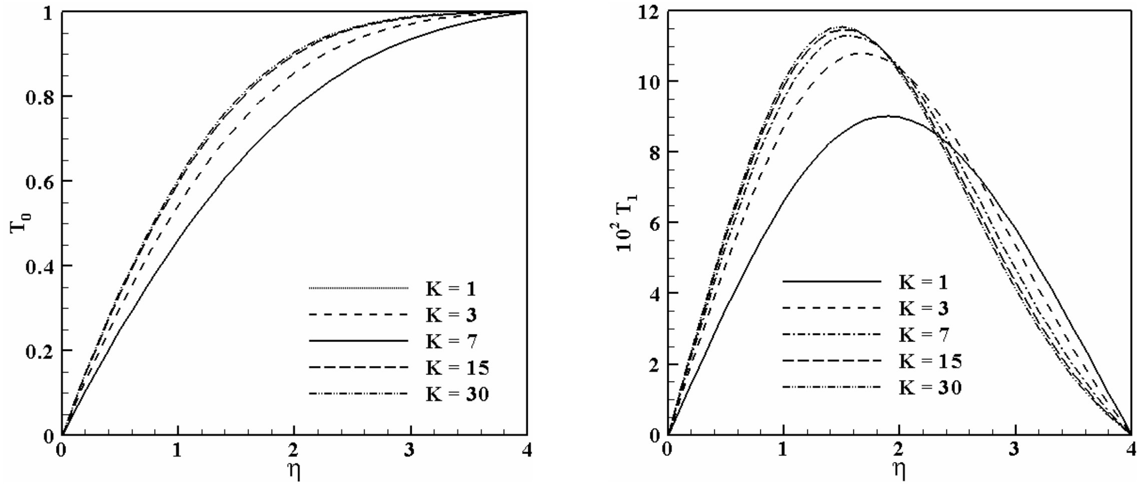

Fig. 5 Temperature profiles with the variation of K for P = 0.71, M = 0.5 and N = 0.5

6. CONCLUSIONS

In this paper, we have investigated numerically the solutions for the temperature field of an electrically conducting fluid past a semi-infinite stationary plate in the presence of radiation. Attention is focused on how the normalized similarity temperatures, $T_0(\eta)$ and $T_1(\eta)$ are effected by variations of different parameters. From the present calculation, we may conclude that magnetic field parameter have increasing effect on the temperature profiles. Radiation has significant effects on the temperature profiles.

NOMENCLATURE

B	Magnetic field intensity
c_p	Specific heat at constant pressure
g_o	Gravitational acceleration
K'	Darcy permeability
k^*	Mean absorption coefficient
K	Radiation parameter
M	Darcy number
N	Magnetic parameter
P	Prandtl number
Pn	Radiative Prandtl number
q_r	Radiative heat flux
T	Temperature within boundary layer
T_w	Temperature at the plate
T_∞	Temperature of the ambient fluid
u	Velocity along x-axis
$U(x)$	Free stream velocity
υ	Velocity along y-axis
x, y	Cartesian co-ordinate

Greek Letters

ρ	Density of the fluid
μ	Coefficient of dynamic viscosity
ν	Kinematic viscosity
k	Thermal conductivity
η	Similarity parameter
σ	Electrical conductivity
σ^*	Stefan-Boltzmann constant

REFERENCES

[1] Ostrach, S., An analysis of laminar free convective flow and heat transfer about a flat plate parallel to direction of the generating body force, NACA Technical Report 1111, 1952.

[2] Ali, M. M., Chen, T. S. and Armaly, B. F., Natural convection–radiation interaction in boundary-layer flow over horizontal surfaces, *AIAA Journal*, 22 (1984), pp. 1797–1803.

[3] Ibrahim, F. S., Mixed convection–radiation interaction in boundary-layer flow over horizontal surfaces, *Astrophysics and Space Science*, 168 (1990), pp. 263–276.

[4] Mansour, M. A., Radiative and free-convection effects on the oscillatory flow past a vertical plate, *Astrophysics and Space Science*, 166 (1990), pp. 269–275.

[5] Hossain, M. A., Khanafer, K. and Vafai, K., The effect of radiation on free convection flow of fluid with variable viscosity from a porous vertical plate, *International Journal of Thermal Science*, 40 (2001), pp. 115–124.

[6] Elbashbeshy, E. M. A. and Dimian, M. F., Effect of radiation on the flow and heat transfer over a wedge with variable viscosity, *Applied Mathematics and Computation*, 132 (2002), pp. 445–454.

[7] Viskanta, R. and Grosh, R. J., Boundary layer in thermal radiation absorbing and emitting media, *International Journal of Heat and Mass Transfer*, 5 (1962), pp. 795–806.

[8] Hossain, M. A., Alim, M. A. and Rees, D. A. S., The effect of radiation on free convection from a porous vertical plate, *International Journal of Heat and Mass Transfer*, 42 (1999), pp. 181–191.

[9] Ibrahim, F. S., Mansour, M. A. and Hamad, M. A. A., Lie-group analysis of radiative and magnetic field effects on free convection and mass transfer flow past a semi-infinite vertical flat plate, *Electronic Journal of Differential Equation*, 39 (2005), pp. 1–17.

[10] Raptis, A., Perdikis, C. and Takhar, H. S., Effect of thermal radiation on MHD flow, *Applied Mathematics and Computation*, 153 (2004), pp. 645-649.

Proceedings of the 4th BSME-ASME International Conference on Thermal Engineering
27-29 December, 2008, Dhaka, Bangladesh

TEMPERATURE DEPENDENCE OF SINGLE-BUBBLE SONOLUMINENCES (SBSL)

Mohammad Mashud, Md. Ilias Inam and Takuma Endo*
Department of Mechanical Engineering
Khulna University of Engineering & Technology (KUET)
Khulna-9203, Bangladesh.
*Department of Aerospace Engineering, Nagoya University, Japan.
(E-mail: mdmashud@yahoo.com)

ABSTRACT

This paper presents an experimental documentation of production of Single-bubble Sonoluminescence (SBSL) and its temperature dependence. The sonoluminescent bubble experiences continuous rapid contractions and expansions with precise regularity. The intensity of light emitted by bubble is depending on the bubble size. The main purposes of this research are to investigate the luminescence intensity and the maximum bubble size with variation of water temperature. In this study it has been observed that the luminescence intensity and the bubble size are inversely proportional to the water temperature. The size of the bubble was measured by Mie-scattering and light intensity measured by Photo-Multiplier Tube (PMT).

Key words: *Sonoluminescence, Single-bubble Sonoluminescence (SBSL) and Temperature dependence.*

1. INTRODUCTIONS

Sonoluminescence (SL) is the production of visible light by a gas bubble that is suspended in fluid (normally water) by an acoustic standing-wave field. Presently understanding if the phenomena suggested that Sonoluminescence may result in temperatures of over 10^5 K (which approaches the temperature found in the solar corona), such a high temperatures makes the study of Sonoluminescence especially interesting for the possibility that it might be a means to achieve thermonuclear fusion. If the bubble is hot enough, and the pressures in it high enough, fusion reactions like those that occur in the Sun could be produced within these tiny bubbles. Pressure of over 10^{12} Pa (close to the pressure at the center of the planet Jupiter), the wavelength of the emitted light is short – the spectrum extends well into the ultraviolet i.e. light emission of less than 10^9 s duration and the concentration of mechanical energy of up to 10^{12}, The mystery of how a low –energy-density sound wave can concentrate enough energy in a small volume to cause the emission of light is still unsolved. In Sonoluminescence, a 10μm diameter of bubble (i.e. a bubble with a diameter of about 1/10 the width of a human hair) oscillating in an audio frequency, ultrasonic field synchronously emits on the order of a million photons in a short pulse each acoustic period. The mechanism for the light emission is still not completely understood and is being investigated by research groups around the world. There is general agreement that the violent collapse of a micron size bubble to its hard core limit is at the heart of the light emission process.

There are two types of Sonoluminescence that have been discovered to date. There are: (1) Multiple- bubble Sonoluminescence (MBSL), and (2) Single-bubble Sonoluminescence (SBSL). First, Multiple-bubble Sonolumiensecece involved the emission of light from not one, but many bubbles of air trapped in water. Typically, the light obtained from multiple-bubble Sonoluminescence was much weaker that single –bubble Sonoluminescence, which meant that it was not possible to observe the glow in daylight. The complexity of a system which involved many bubbles caused many problems in the formulation of theoretical models of Sonoluminescence, and it is probably this which leads to the lack of interest in futher research. Another one is single-bubble Sonoluminescence (SBSL), a single bubble of air is acoustically levitated in water which is bombarded with sound waves. The bubble is seen to emit light which is visible in a lit room. The bubble varies in size with the pressure of the applied sound field, and the light is emitted as flashes which occur so rapidly that it appears as if the bubble is emitting light continuously.

In 1896 Henri Becquerel discovered that a uranium Salt could darken a photographic plate, and from this effect he went on to discover radioactivity. In 1934 H. Frenzel and H. Schultes expose a photographic plate to acoustic waves generated in a water bath and also observed a darkening of the plate. They attributed that result to luminescence from the sound field-an effect that has come to be known as Sonoluminescence. The luminescence they observed did not result from the sound field directly but arose through a process called cavitation, in which voids filled with gas and vapor are generated within the liquid during the tensile portion of the pressure variation. Single-bubble sonoluminescence was discovered in 1989 by Felipe Gaitan, then a gradute student at the University of Mississippi working with Larry Crum. Crum had seen hints of light emission from a single bubble in 1985, and Gaitan's objective for his thesis was to search systematically for it. Gaitan was carrying out a set of experiments on the oscillation and collapse of bubbles, using a flask of liquid lined with transducers tuned to set up an acoustic standing wave at the resonant frequency at the jar. When the pressure amplitude of the sound waves is larger than the ambient pressure, the pressure in the flask becomes negative, putting the liquid under tension. At large enough tension, the liquid breaks apart (cavitation),creating unstable bubble clouds collapse with enormous force, powerful enough to do serious damage to the surfaces of solid bodies in their vicinity.

2. SONOLUMINESCENCE PROCESS

Sonoluminecence is the conversion of sound into light. Ultrasonic waves are aimed at an air bubble in a small water cylinder. In this process the bubble is trapped at a pressure node which is located at an antinode of sound. Once this bubble is trapped, it is driven at a great enough amplitude to cause the bubble to swell and shirk at regular cycles corresponding to the cycle of the sound wave. During this cycles, 50 ps light flashes are emitted about every 30 μs. The bubble swells without the addition of any molecules so at the point of greatest radii the pressure inside the bubble to violently collapse. It has been measured that at the point of greatest size, the bubble is approximately 50 microns and the collapses to only about 0.5 microns. Putterman states that this is the smallest size the bubble can become because at this point the repulsion forces between the gas atoms is great enough to prevent further collapse. Putterman further explains that the minimum size of the bubble is determined by the van der waals forces of the atoms at the core of the bubble. It is during this collapse that the light is emitted. This is due to the adiabatic compression of the gas trapped inside of the bubble.

A simple Schamatic diagram is shown in Fig. 1 to understand the Sonoluminescence process.

(a) The bubble starts out at a size around 5 microns (millionths of meter);
(b) Then it expands to a maximum size (not to scale) of about 50 microns. At this larger size there is a near-vacuum inside the bubble because of the relatively few air molecules present. This low-pressure near-vacuum region is surrounded outside the bubble by a much higher-pressure region, which causes.
(c) A catastrophic collapse of the bubble to between 0.1 and 1 micron. During this compression phase a flash of light.
(d) Emerges from the bubble.

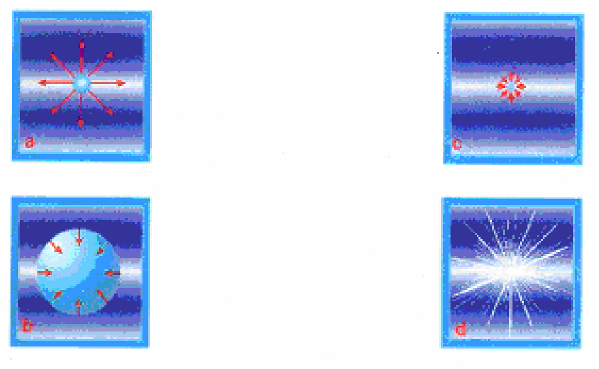

Figure 1: Schematic diagram of Sonoluminescence Process.

3. EXPERIMENTAL SET-UP AND PROCEDURE

The experiments were carried out in the Gas-dynamics Laboratory, Department of Aerospace Engineering, Nagoya University, Japan. The experimental set-up is shown in Fig. 2 (Schematic) and Fig.3 (Photograph).

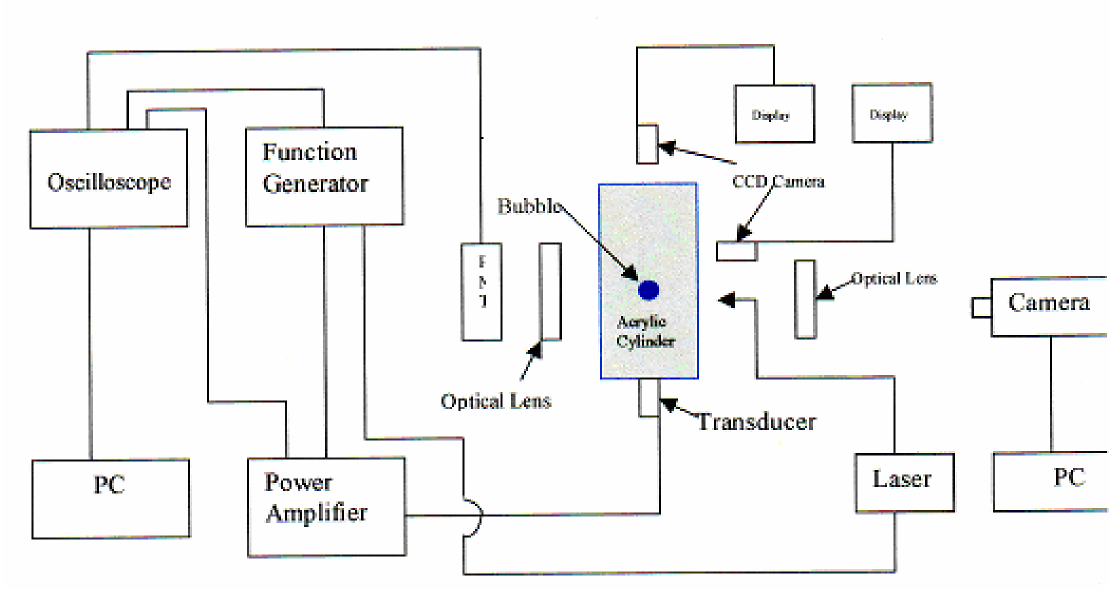

Figure 2: Schematic diagram of experimental set-up.

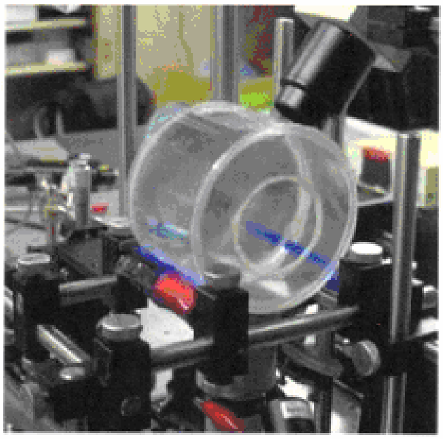

Figure 3: Photograph of Experimental set-Up

For conducting the experiment the following procedure were followed.

De-gas the water: This process is commonly known as degassing. In this experiment the water was boiling for 20-30 minutes and sealing the container as soon as the boiling stopped. And pour the de-gassed water into the acrylic cylinder. And turn on the temperature controller, fix-up the working temperature and wait until the working temperature reach to the inside acrylic cylinder water. Then turn on all electronic device i.e. Function generator, Power amplifier, PC and Oscilloscope. Insert air into cylinder water by syringe and create bubble, trap it, adjusting frequency and amplitude and see it glow. When looking at the cylinder for the bubble, it is convenient to be in a dark place with a light source behind the flask. This makes the finding of the bubble easier. Once the bubble is found, it can easily be found at other times. Adjust the frequency and amplitude for bubble stability. When the bubble is stable and luminescence, make the experimental from room dark and turn on Photo-Multiplier tube, the Oscilloscope will show the luminescence intensity in graphical from and transferring data from oscilloscope to PC and save it.

4. EXPERIMENTAL RESULTS

The initial goal of this study was to investigate the intensity of Single Bubble Sonoluminscence (SBSL) with variation of liquid (water) temperature and the final goal was to measure the maximum bubble size at different liquid (water) temperature, i.e. temperature dependence of Single Bubble Sonoluminescence (SBSL). The goals were achieved by measure the luminescence intensity as a function of voltage (Photograph of Bubble). Typical outputs of PMT and bubble photograph are shown in Fig. 4 and Fig. 5.

During the first experiment, it was found that the luminescence intensity depends on liquid (water) temperature and it is about inversely proportional to square root of liquid (water) temperature, i.e. as the liquid (water) temperature was increasing the intensity of light emission from bubble decreased which is shown in Figure 6 and it follows the following fitted curve.

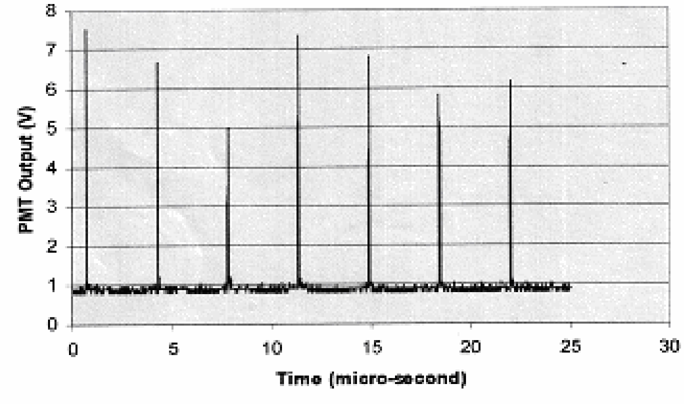

Figure 4: Typical PMT Output in Oscilloscope at 8.2°C water temperature.

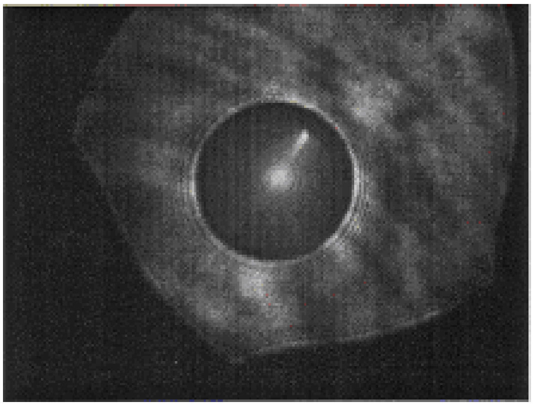

Figure 5: Maximum Bubble Size Photograph at 7.5° water temperature.

During the second experiment, it was also found that the maximum bubble size depends on liquid (water) temperature and it is about inversely proportional to the cubic root square of liquid (water) temperature, i.e. as the liquid (water) temperature was increasing the maximum bubble size decreased which is shown in Figure 7 and it follows the following fitted curve.

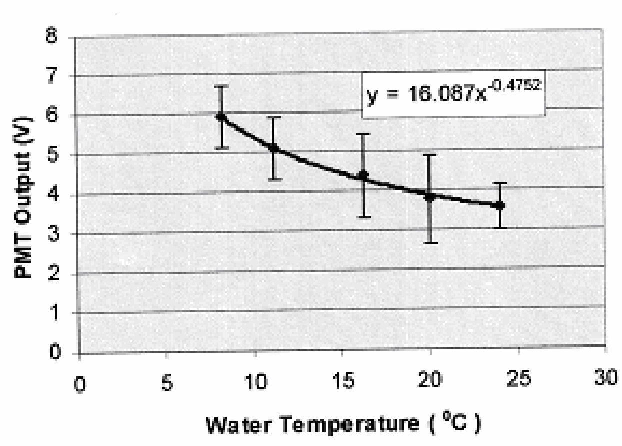

Figure 6: Water Temperature Vs Luminescence Intensity Curve.

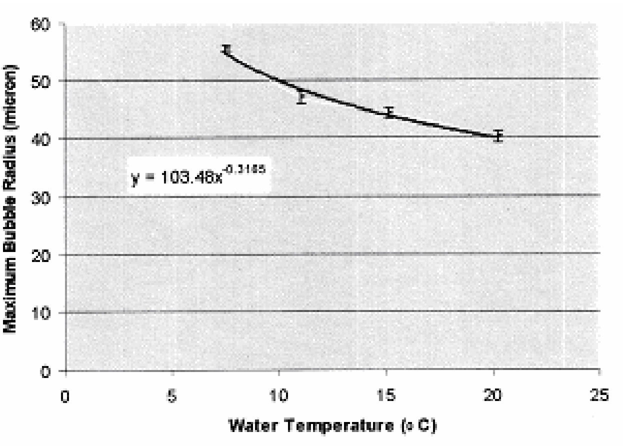

Figure 7: Water Temperature Vs Maximum Bubble Radius Curve.

5. DISCUSSIONS

From this study it has been shown that the Sonoluminescence intensity decrease with increasing the liquid (water) temperature, i.e. the bubble is brighter at low water temperature than higher temperature. The luminescence intensity is the function of temperature of the bubble (I_t=I_t(T_{bubble})) and it is directly proportional to the inside bubble temperature. If the inside temperature of the bubble increases, the emission of light from bubble will be increased. At low water temperature the bubble contains less air gases, such as Nitrogen, Oxygen, Carbon dioxide etc., expect noble gas (Ar), compare tohigher water temperature. Because at low water temperature most of the air gases, such as Nitrogen, Oxygen, Carbon dioxide etc., are dissolved into water. So in the same bubble the ratio of noble gas (Ar) increases but decreases the ratio of the others air gases (such as Nitrogen, Oxygen, Carbon dioxide etc.). As the bubble compressions and expansions are adiabatic, the change in temperature of bubble is depends on the degree of freedom of presence air gases inside the bubble at the same internal energy. This change in temperature is inversely proportional to the degree of freedom, i.e. increase the degree of freedom decrease the bubble inside temperature. The degree of freedom of noble gas (Ar) is 3 and others air gases (such as Nitrogen, Oxygen, Carbon dioxide etc.) are 5. So, at the same internal energy the temperature of Ar. is higher than others. For this reason the bubble is brighter at low water temperature than higher water temperature.
As the bubble collapses, the pressure does work on the decreasing volume, which energy goes to increasing the kinetic energy of moving fluid. The bubble is a spherical cavity and let its initial radius R_0 in an infinite reservoir of water at pressure P.
When the bubble collapsed to radius R its volume changed by amount

$$v = \frac{4\pi}{3}(R_0^3 - R^3) \text{ ………………………………………………………..(1)}$$

So the work done is

$$KE = W = Pv = \frac{4\pi}{3}(R_0^3 - R^3) \approx \frac{4?ïR_o^3P}{3}$$

Where the approximation holds once $R \ll R_o$
Kinetic Energy of Bubble

$$KE = \frac{1}{2}kT^2 \text{ ……………………………………………………………(2)}$$

Where T is the inside temperature of bubble.

In the second experiment is has been found that the maximum bubble radius decreases with increases the water temperature because from equation 2 and 3 it is clear that the maximum bubble radius is proportional to the inside bubble temperature with some constants. Previously it has discussed that the inside bubble temperature is a function of water temperature, inversely proportional, i.e. if the water temperature increases then the inside bubble temperature will be decreased. So, it can say that the maximum bubble radius is also a function of water temperature and it's inversely proportional. For this reason the maximum bubble radius decreases water temperature.

As the maximum bubble radius decrease with increasing water temperature, from equation 2, it is easy to understand that the kinetic energy must decrease with increasing water temperature. Suppose that all the kinetic energy of the collapsing bubble is converted to photons with the spectrum $\mathrm{dN}\,?\{\frac{dE}{E}$. (Bremsstrahlung-like spectrum), Where E is the kinetic energy. The emitted photons are proportional to kinetic energy and kinetic energy is inversely proportional to water temperature. So the emitted photons are inversely proportional to water temperature, i.e. if the water temperature increases, emitted photons will decrease that means the luminescence intensity decrease with increase water temperature as light is emitted in the from of photons.

In whole of the experiments in this study, liquid (water) temperature considered ±0.1°C.

6. CONCLUSIONS

The following conclusions can be made after summarizing the present study:

(a) The luminescence intensity depends on the water temperature which is $y = 16.087x^{-0.4752}$.

(b) The maximum bubble radius also depend on the water temperature which is fitted by $y = 103.48x^{-0.316}$.

REFERENCS

[1] D.Felipe Ganiten, Lawrence A. Crum, Charles C. Church, and Ronald A.Roy. “Sonoluminescence and bubble dynamics for single, stable, cavitation bubble.” Journal of Acoustic Society of America, Vol. 91, No. 6. p.3166 (1992).

[2] Lowrence A. Crum (1994). “Sonoluminescence” Physics Todoy, American Instituent of Physics. P .22 (1994).

[3] L.D.Landau and E.M.Lifshitz, Courses of Theoretical Physics, Vol.6, Fluid Mechanics, 2nd Edition, Pergamon Press, Tokyo, Japan. (1987).

[4] C.Ray Wylie, Advanced Engineering Mathematics, International Student Edition, McGraw-Hill Kogakusha, Ltd. Tokoy, Japan (1975).

[5] Helen M. Walker and Joseph Lev, Elementary Statistical Methods, Third Edition, Holt, Rinehart and Winston, Inc. New York. (1969).

[6] R.S. Burington and Donald Curtis May, Hand Book of Probability and Statistics with Tables, Handbook Publishers, Inc., Sandusky, Ohio.

[7] B.S.Grew, Higher Engineering Mathematics, Thirty Fourth Edition, Third Print, Khanna Publishers (1999).

Proceedings of 4th BSME-ASME International Conference on Thermal Engineering
27-29 December, 2008, Dhaka Bangladesh

PARALLEL PERFORMANCE OF PRECONDITIONED DOMAIN DECOMPOSITION METHOD FOR LARGE SCALE HEAT TRANSFER PROBLEM

*A.M.M.Mukaddes, **Masao Ogino and **Atsushi Uragami
*Department of Industrial and Production Engineering, Shahjalal University of Science and Technology,
**Department of Intelligent Machinery and Systems, Kyushu University, Japan
Email: mukaddes-ipe@sust.edu

ABSTRACT

Domain decomposition is a well known parallel finite element method for distributed parallel computing environment. Incorporation of a suitable preconditioner like balancing domain decomposition (BDD) method makes the method more efficient due to its excellent convergence rate. Several studies have considered applications of the BDD method to various phenomena and improvement of its convergence rate. However, in applying the BDD method to large-scale problems, it is difficult to solve the coarse problem since the size of the coarse problem increases in proportion to the number of subdomains. In this work, domain decomposition technique with an incomplete balancing preconditioner has been adapted to the distributed parallel environment of networked workstations and the supercomputer. Using the developed code, several heat transfer model problems are solved and the parallel performances are analyzed on the network of eight Pentium IV PC cluster and GP7000F workstations. Finally, very large size of problem over 11 million DOFs has been solved using 1024 SR8000 supercomputer.

KEYWORDS: *parallel computing, finite element, balancing domain decomposition, domain decomposition, finite element.*

1. INTRODUCTION

Large scale problem, particularly those defined in three dimensional domain, often need substantial computation time and memory to run on ordinary sequential computers. Even if they can be solved, powerful computation capability is required to obtain the accurate and precise results within a reasonable time. Parallel computing can meet requirements of high performance computation [1]. Among the various parallel computing algorithms, domain decomposition method has become much popularity in the recent years [2]. In this method, the whole domain to be solved is first decomposed into a number of subdomains without overlapping. Finite Element Analysis (FEA) is defined and solved in each subdomain in parallel and then partial solutions are assembled together to get the global solution.

This method is exclusively implemented on structural analysis [3], heat conduction problem [4] and fluid analysis [5]. Most of the papers emphasizes only on the implementation of the method without analyzing the parallel performance as well as taking the necessary advantages of the parallel computing environment. Again incorporation of a suitable preconditioner like balancing domain decomposition method (BDD) [6] makes the method more efficient due to its excellent convergence rate. The BDD method includes the Neumann-Neumann preconditioner and a coarse grid correction. Several studies have considered applications of the BDD method to various phenomena and improvement of its convergence rate. However, in applying the BDD method to large-scale problems, it is difficult to solve the coarse problem since the size of the coarse problem increases in proportion to the number of subdomains.

In this research, the two parallel approaches (dynamic load distribution [7] and static load distribution) of domain decomposition method with an incomplete balancing preconditioner [8] have been adapted to the distributed parallel environment of networked workstations [9] and the supercomputer.

Using the developed code several heat transfer models are solved and the performances are measured in different computing environments. The important factors affecting the performance of parallel computing using the domain decomposition method are found and analyzed.This analysis will be useful as a guideline for the user of the domain decomposition based software in the parallel computing environment.

2. DOMAIN DECOMPOSITION METHOD

***Main method**:*

Consider a linear system of algebraic equations,

$$[K]\{u\} = \{f\} \tag{1}$$

arising from a finite element discretization of a linear elliptic boundary value problem in the domain Ω, where K is the global stiffness matrix, u is an unknown vector and f is a known vector. The domain Ω to be solved is first decomposed into N number of subdomains, $\{\Omega^{(i)}\}_{i=1,\dots,N}$, for which the union of all subdomains boundaries is

$$\Gamma = \bigcup_{i=1}^{N} \Gamma^{(i)}. \tag{2}$$

Let $K^{(i)}$ be the local stiffness matrix corresponding to subdomain $\Omega^{(i)}$. Then as usual the global stiffness matrix K can be generated by subassembling:

$$K = \sum_{i=1}^{N} R^{(i)} K^{(i)} R^{(i)T} \tag{3}$$

where $R^{(i)T}$ is the 0-1 matrix which translates the global indices of the nodes into local numbering. Let $u^{(i)}$ be the vector corresponding to the variables in $\Omega^{(i)}$ and it can be expressed as $u^{(i)} = R^{(i)T}u$. Each $u^{(i)}$ is split into degrees of freedom $u_B^{(i)}$, which correspond to $\partial\Omega^{(i)} \setminus \Gamma_u$, called interface degrees of freedom and the remaining interior degrees of freedom $u_I^{(i)}$. The subdomain stiffness matrices $K^{(i)}$, the vector $u^{(i)}$ and the 0-1 matrices $R^{(i)T}$ are then split accordingly:

$$K^{(i)} = \begin{pmatrix} K_{II}^{(i)} & K_{IB}^{(i)} \\ K_{IB}^{(i)T} & K_{BB}^{(i)} \end{pmatrix}, \tag{4}$$

$$u^{(i)} = \begin{pmatrix} u_I^{(i)} \\ u_B^{(i)} \end{pmatrix}, \tag{5}$$

$$\text{and } R^{(i)T} = \begin{pmatrix} R_I^{(i)T} & 0 \\ 0 & R_B^{(i)T} \end{pmatrix}. \tag{6}$$

$$u_B^{(i)} = R_B^{(i)T} u_B, \quad i = 1, \ldots, N \tag{7}$$

The unknown in the interior of the subdomain $\Omega^{(i)}$ is eliminated by Gaussian elimination according to the equation (8) using an initial value of $u_B^{(i)}$,

$$u_I^{(i)} = K_{II}^{(i)-1}\left(f_I^{(i)} - K_{IB}^{(i)} u_B^{(i)}\right). \tag{8}$$

Then, after elimination of the interior degrees of freedom, the problem (1) reduces to a problem on the interface,

$$Su_B = g \tag{9}$$

where S is the Schur complement matrix:

$$S = \sum_{i=1}^{N} R_B^{(i)} S^{(i)} R_B^{(i)T}, \tag{10}$$

$$S^{(i)} = K_{BB}^{(i)} - K_{IB}^{(i)T}\left(K_{II}^{(i)}\right)^{-1} K_{IB}^{(i)}. \tag{11}$$

The problem (9) is solved using the preconditioned conjugate gradient method which requires the solution of the following auxiliary problem in each iteration.

$$Mz = r \tag{12}$$

where, M is a preconditioning matrix, z is a preconditioned vector and r is the residual of the interface problem.

Preconditioners [6, 8]:

The present domain decomposition method includes the following preconditioning techniques [8]

Simplified diagonal scaling:

$$M_{DIAG} = \sum_{i=1}^{N} R_B^{(i)} \left(diag\left(K_{BB}^{(i)}\right)\right)^{-1} R_B^{(i)T} \tag{13}$$

Balancing domain decomposition (BDD):

This preconditioning matrix is defined as

$$M_{BDD}^{-1} = Q_c + \left(I - Q_c S\right) Q_l \left(I - SQ_c\right) \tag{14}$$

where Q_l is the local level part and Q_c is the coarse level part of the preconditioner.

Balancing domain decomposition with diagonal scaling:

$$M_{BDD-DIAG}^{-1} = (I - Q_c S) Q_{DIAG} \tag{15}$$

Incomplete balancing domain decomposition (IBDD):

$$M_{IBDD}^{-1} = \widetilde{Q}_c + \left(I - \widetilde{Q}_c S\right) Q_l \left(I - S\widetilde{Q}_c\right) \tag{16}$$

where $\widetilde{Q}_c$ is constructed from the incomplete factorized coarse operator.

Incomplete balancing domain decomposition with simplified diagonal scaling (IBDD-DIAG):

$$M_{IBDD-DIAG}^{-1} = \widetilde{Q}_c + \left(I - \widetilde{Q}_c S\right) Q_{DIAG} \left(I - S\widetilde{Q}_c\right) \tag{17}$$

3. PARALLELISM OF THE DOMAIN DECOMPOSITION METHOD

Constructing the DDM algorithms for parallel computers, a good principle is to divide the original domain into parts, which are further decomposed into smaller subdomains. In this research we adopt Hierarchical Domain Decomposition Method

(HDDM) [6] which is a well known parallel DDM. This hierarchically structured DDM classifies processors in two different following ways.

Dynamic load distribution (h-mode):

The h-mode classifies processors into 3 groups, 'Grand Parent', 'Parent' and 'Child'. Fig. 1 illustrates the practical implementation of hierarchical organized processors in the present method. The role of Grand Parent is to organize all processor communications (i.e. message passing) which occur between all processors. Parents prepare mesh data, manage FEA (Finite Element Analysis) results, and coordinate the CG iteration, including convergence decision for the CG iteration. Parents send data to Child processors, where FEA is performed in parallel. After the FEA, Child processors send the results to Parents. This computation will be repeated until the CG iteration is convergent.

Static load distribution (p-mode):

However, because almost all computation is performed in Child processors and the most communication time is taken between Parent processors and Child processors, so the communication speed becomes important. In recent years although the communication performance has also been improving by improvement in network technology, the high-speed network is still expensive. On the other hand, for the PC cluster generally used, the network speed becomes a bottleneck to the processing performance of CPU. Moreover, when a parallel processing performance is considered, it is important to reduce the amount of communication time as much as possible. Therefore, the Parent-Only type (static load distribution: p-mode) is useful than the conventional Grand-Parent-Child type (dynamic load distribution: h-mode).

Fig. 4 shows the parallel processor scheme of p-mode. In the p-mode, the Parent processors perform the FEA by themselves, which is computed by the Child processors in the h-mode. In the h-mode, although Parent processors store some of the subdomain analysis data and coordinate the CG iteration as the main work, the idling time of CPU increases because of less computation in Parent processors.

4. PARALLEL PERFORMANCE

Speed up:

The key issue in the parallel processing in a single application is the speed up achieved, specially its dependence on the number of processors used. For simplicity speed up with n processors, S_n is defined as follows:

$$S_n = \frac{t_1(A)}{t_n(A)} \tag{18}$$

where $t_1(A)$ and $t_n(A)$ are total time for solving the problem using one processor and n processors, respectively. Also scaled speed up S_n' is defined as follows:

$$S_n' = \frac{n \times t_1(A)}{t_n(nA)} \tag{19}$$

where $t_n(nA)$ is the total time for solving the problem of size nA.

Sequential processing and parallel processing:

The program might be sequential, parallel or combination of sequential and parallel. The execution time to solve a problem of size n having the sequential processing is given by the equation (20)

$$T(n) = T_{calc}(n) + T_{i/o}(n) \tag{20}$$

where $T(n)$, $T_{calc}(n)$, $T_{i/o}(n)$ are the total execution time, calculation time and input/output time. Again the execution time to solve a problem of size n, having the parallel processing also is given by the equation (21)

$$T(n,p) = T_{calc}(n,p) + T_{i/o}(n,p) + T_{comm}(n,p) \tag{21}$$

where $T(n,p)$, $T_{calc}(n,p)$, $T_{i/o}(n,p)$ and $T_{comm}(n,p)$ are the execution time, calculation time input/output time and time for communication respectively.

The ratio of the calculation time, input/output time and communication time over the total execution time is defined as follows

$$R_{calc} = \frac{T_{calc}(n,p)}{T(n,p)}\ ,\ R_{i/o} = \frac{T_{i/o}(n,p)}{T(n,p)}\ ,\ R_{comm} = \frac{T_{comm}(n,p)}{T(n,p)} \tag{22}$$

and

$$R_{calc} + R_{i/o} + R_{comm} = 1 \tag{23}$$

5. NUMERICAL RESULTS AND DISCUSSIONS

A. Physical model and computational environment:

Using the developed code, two heat transfer models [4] are analyzed here. Models are High Temperature Test Reactor (HTTR) and Advanced Boiling Water Reactor (ABWR) which are shown in fig. 2.The calculations are performed in three different computational environments shown in Table 1.

B. scalability and speed-up:

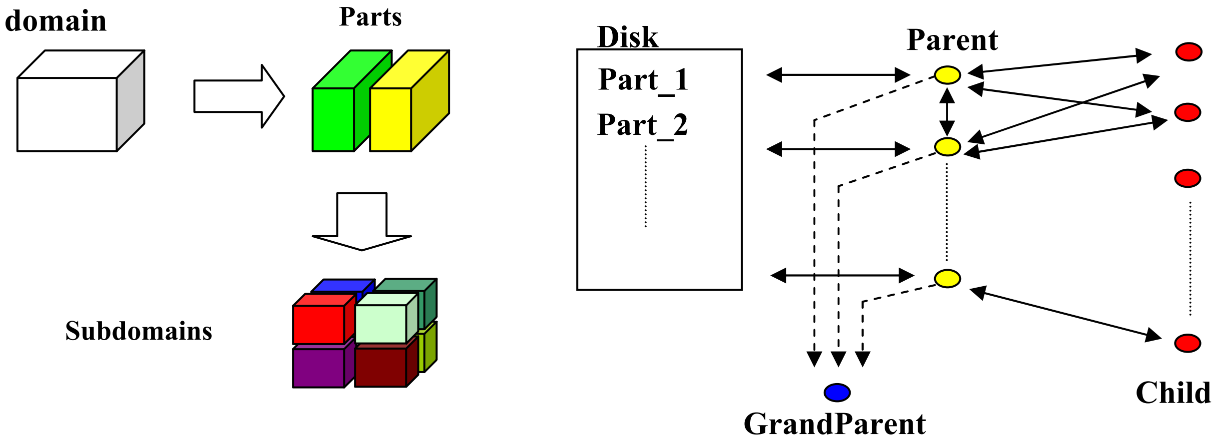

Fig. 1 Hierarchical domain decomposition method (left), dynamic load distribution (right)

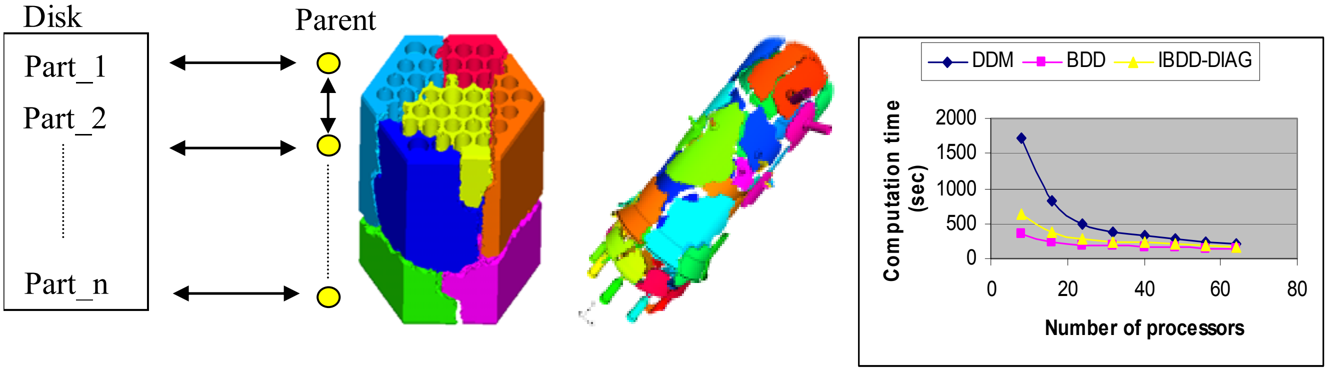

Fig. 2 Left- Parallel processor scheme (p-mode), middle- HTGR and ABWR , right- computation time in different process

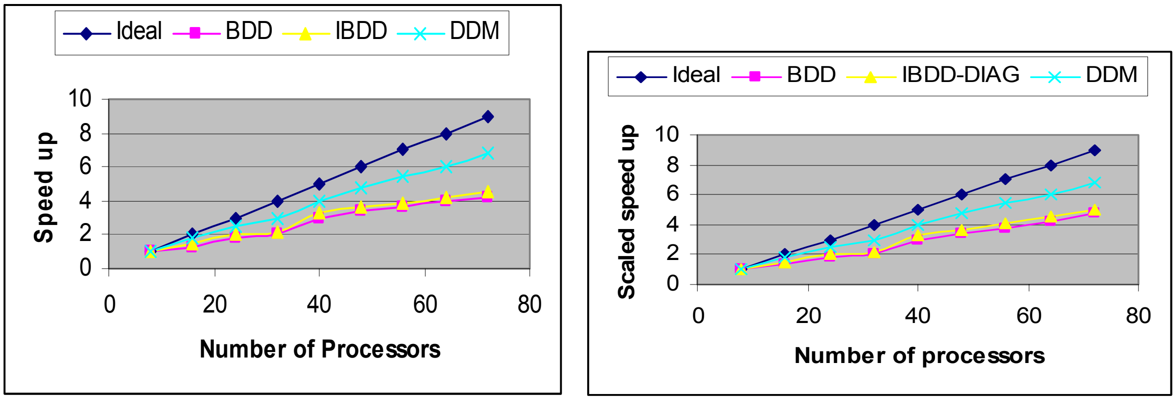

Fig. 3 Speed up (left) and scaled speed-up in different number of processors for HTGR model.

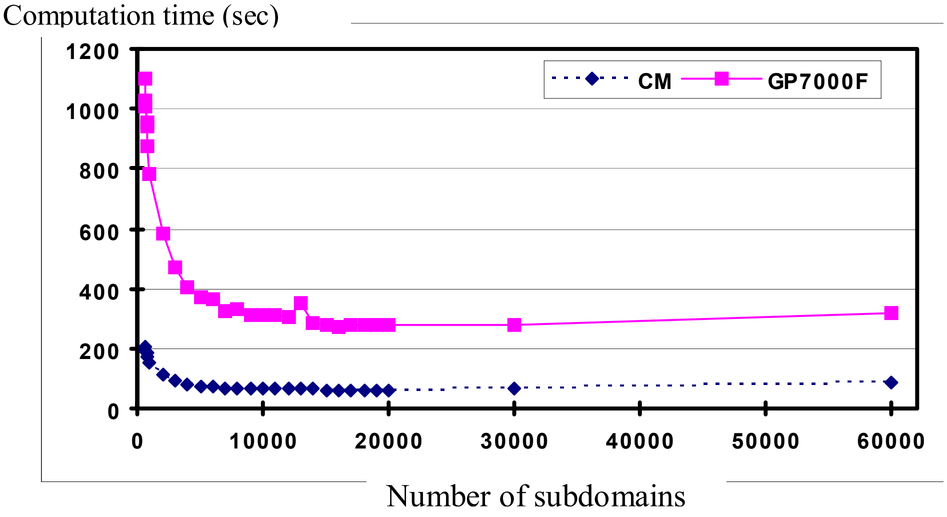

Fig. 4 Computation time in two different computational environment

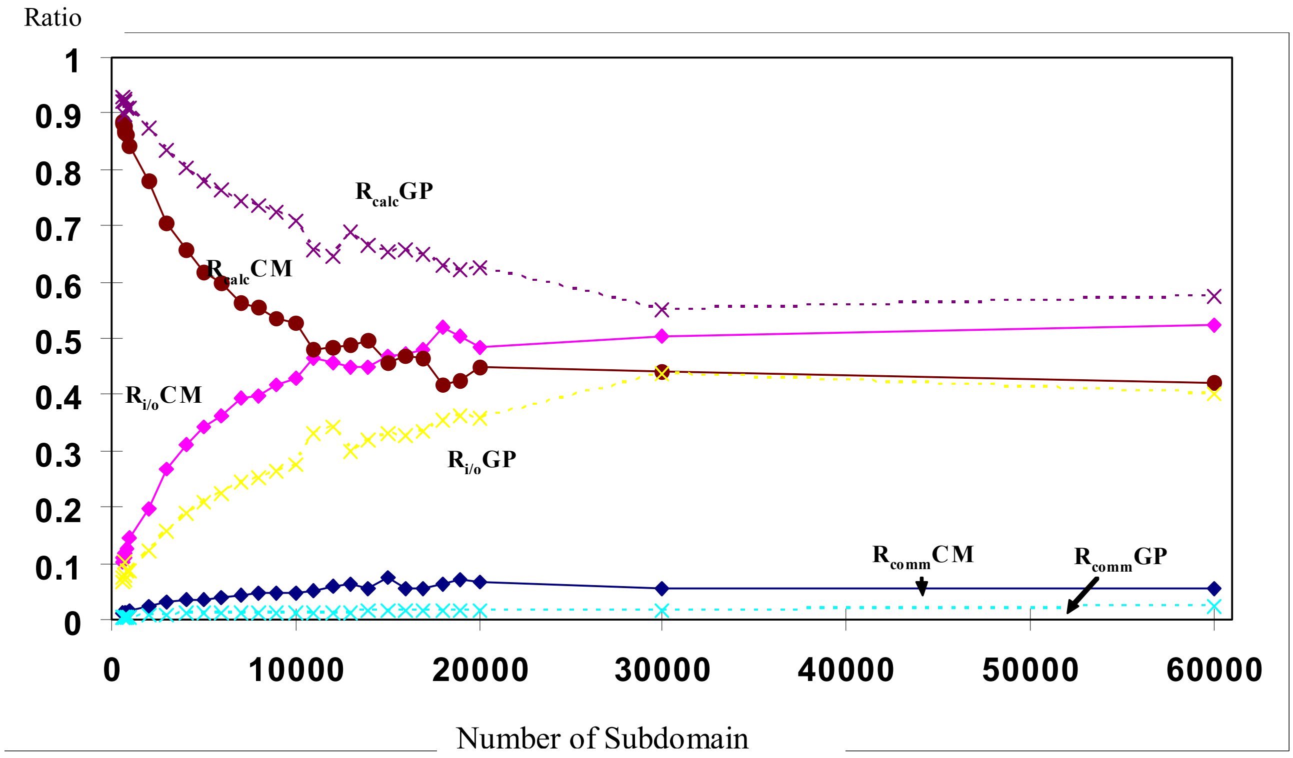

Fig. 5. Ratio of calculation, input/output and communication time (p-mode)

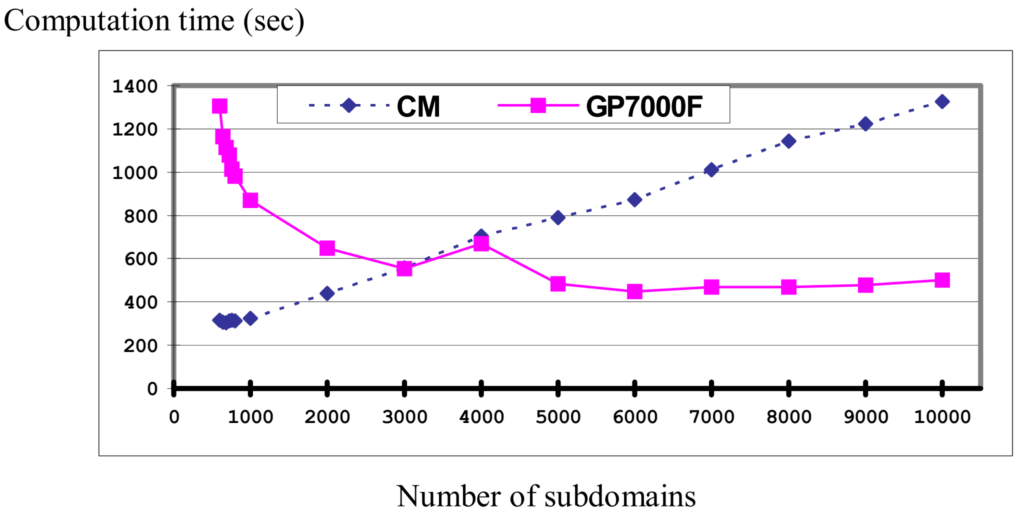

Fig. 6. Execution time in two different computational environments (h-mode)

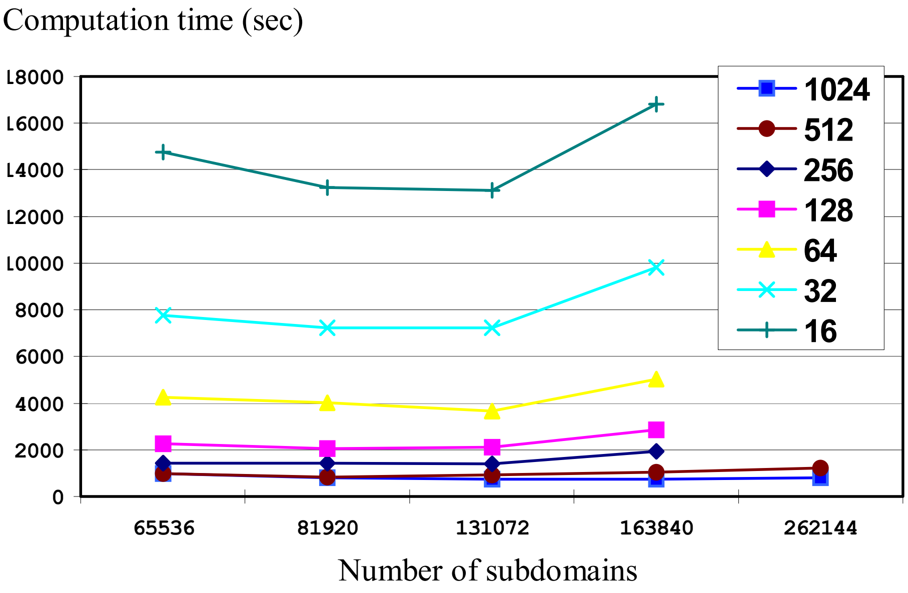

Fig. 7 Computation time vs number of subdomains in different number of processors

Table 1 Parallel Computational environments

	CPU	Memory	Network
PC Cluster	Pentium4, 2.0GHz	1GB/CPU	Ethernet (100Mbp)
GP7000F	SPARC64 ,333MHz	1GB/CPU	Ethernet (1Gbps)
Hitachi SR8000	250 MHz	1 GB/CPU	

We evaluate the parallel scalability of the BDD and IBDD-DIAG preconditioner, varying the number of processors employed. Such evaluation is performed using the HITACHI SR8000. The results are shown in Fig.2 (right). Fig. 2 (right) reports that BDD and IBDD-DIAG can compute faster solutions of a fixed mesh problem when the number of processors is increased. The speed-up and scaled speed-up are bothe compared with the number of processors, referring the value for using 8 processors in Fig. 3 The results shown in figures confirm the parallel scalability properties of the BDD and IBDD-DIAG preconditioners. Since the program has both parallelable and nonparallelable portion, results are too far from ideal one. For the parallelable portion, parallel computing with n processors can shorten computation time to $1/n$ in ideal.

C. Results concerning the number of subdomains:

The number of subdomains is the major concern in the domain decomposition method. We compare the computation time (for IBDD-DIAG) in two different computational environments corresponding to the number of subdomains and results are shown in Fig. 4. CM shows better performance than GP7000F. The ratio of the calculation time, time for input/output data and communication time corresponding to the number of subdomains are shown in the Fig. 5. With the increase of number of subdomains, ratio of calculation time decreases while ratio of input/output time and communication time increases. Since the network speed of GP7000F is faster than the CM, the communication takes less time compared to the CM clustures. The Fig. 6 shows the computation time for h-mode in two different computation environments, which shows that when the number of subdomain is 3000 the computation time increases in CM cluster compared to the GP7000F. This is because, in the h-mode the more communication takes place between the Parents and Childs as the number of subdomains increases thereby in CM it takes more time for the communication. So in the parallel computing environment having low performance it is better to use the static load distribution mode and having high performance it is better to use the dynamic load distribution mode.

ABWR model is analyzed in the vector type supercomputer SR8000 changing number of processors.

Fig. 7. shows the variation of the computation time using the different number of processors in SR8000. As the number processor increases, the difference decreases. As a result, the difference between the time required using 512 processors and 1024 processors is too small. So it is not necessary to use more than 1024 processors for this model.

6. CONCLUSION

Two parallel approaches, static load distribution and dynamic load distribution of the domain decomposition method are adapted to the parallel computing environment and their parallel performances are analyzed. Static load distribution seems to be more efficient in the parallel computer having low the network speed while dynamic load distribution shows good performance in the high speed networked parallel computers. By the performance test, the effectiveness of the domain decomposition method in the parallel computer is verified. Important factors affecting the performance of the distributed parallel computing are found and analyzed. By using workstation cluster, a huge size of problem having over 11 million DOFs is solved successfully.

7. REFERENCES

[1] Almasi G S and Gottlieb A, Highly Parallel Computing [M]. The Benjamin/Cummings Publishing Company, Inc., Redwood City, Ca, 1990

[2] Farhat, C., Chen, P.S. and Mandel, J., A Scalable Lagrange Multiplier Based Domain Decomposition Method for Time-Dependent Problems, *International Journal for Numerical Methods in Engineering,* Vol. 38 (1995), p. 3831-3853.

[3] Shioya, R., Ogino, M., Kanayama, H. and Tagami, D., Large Scale Finite Element Analysis with a Balancing Domain Decomposition Method, *Key Eng. Mate.,* 243-244 (2003), p.21-26.

[4] A.M..M..Mukaddes, M. Ogino, H. Kanayama and R. Shioya, A Scalable Balancing Domain Decomposition Based Preconditioner for Large Scale Heat Transfer Problems. *JSME Inter. Journal, Series B,* vol 49, No. 2 pp-533-540 ,2006

[5] Kanayama, H., Ogino, M., Takesue, N and A.M.M.Mukaddes, Finite Element Analysis for Statinary Incompressible Viscous Flows Using Balancing Domain Decomposition, *Theoretical and Applied Mechanics,* 54(2005), p.211-219.

[6] Mandel, J., Balancing Domain Decomposition, *Comm. on Num. Meth. in Eng.*, Vol. 9 (1993), p. 223-241.

[7] Yagawa, G. and Shioya, R., Parallel Finite Elements on a Massively Parallel Computer with Domain Decomposition, *Computing Systems in Engineering* 4:4-6 (1993), p.495-503.

[8] Ogino, M, Shioya, R and Kanayama H., An inexact balancing precondition for large scale structural analysis, *Journal of computational science and technology,* 2 (2008) No.1, p.150-161

[9] Kim S J, Kim J H. Large-scale structural analysis using domain decomposition method on distributed parallel computing environment. *Proceedings of High-Performance Computing in the Information Superhighway.* HPC-Asia, 1997, 573-678.

Proceedings of the 4th BSME-ASME International Conference on Thermal Engineering
27-29 December, 2008, Dhaka, Bangladesh

THERMAL PERFORMANCE OF COPPER PERFORATED-PLATES FOR USE AS HEAT ECHANGER CORE SURFACES

F. Farhani
Iranian Research Organization for Science and Technology (I.R.O.S.T.),
P.O. Box 15815 – 3538, Tehran, Iran.
ffarhani@yahoo.com

ABSTRACT

In this paper thermal performance of copper perforated-plates has been studied. The single-blow transient test technique, and a single-blow test setup has been used to study the heat transfer coefficients of stacks of copper perforated-plates and stainless steel spacers used as heat transfer elements in compact heat exchangers. Analytical techniques have been used to reduce the experimental data of the single-blow transient test. The analytical results have been presented in terms of Nusselt number, given as function of Reynolds number and geometrical parameters. The results of this study have been used in the development of compact heat exchangers.

KEYWORDS: *Compact heat exchanger, Perforated-plates, Heat transfer coefficient, Single blow test, Maximum slope technique*

1. INTRODUCTION

No satisfactory theory exists to predict the overall heat transfer coefficient for a perforated-plate, and this coefficient must be measured experimentally, under varying geometrical and operating parameters. Two techniques namely steady state method [1] and single-blow transient method [2] are usually used for this purpose. However, the transient method is preferred, because it requires less time, effort and expense than the steady state procedure. In this paper we have used single-blow transient test technique, and a single-blow test setup to study the heat transfer coefficients of stacks of copper perforated-plates and stainless steel spacers used as heat transfer elements in compact heat exchangers. The experimental data has been analyzed using maximum slope technique [3]. According to this technique, in the absence of axial conduction, the maximum slope of the dimensionless outlet fluid temperature vs. time curve is a unique function of exchanger N_{tu}, given as:

$$\textit{Max. Slope}= \left(\frac{d\chi}{d\zeta}\right)_{\max} = f(N_{tu}) \tag{1}$$

Here ζ is a dimensionless time, and χ is a dimensionless parameter defined as $\chi = 1-\theta_{out}$, where θ_{out} is the dimensionless outlet temperature of the fluid from the exchanger bed. For a single channel perforated-plate exchanger core, N_{tu} is a dimensionless number defined as [4]:

$$N_{tu} = \frac{hA}{\dot{m}c_p} \tag{2}$$

In the single blow transient test, the exchanger bed is initially maintained at a constant temperature, and at time zero, a step change is applied to the inlet temperature of the fluid flowing through the bed, and the response at the exit is monitored. If the exchanger core consists of *n* plates, then total N_{tu} is given as $N_{tu} = n * N_{tu,f}$, where $N_{tu,f}$, the number of heat transfer units per plate, is defined as following:

$$N_{tu,f} = \frac{hA_p}{\dot{m}c_p} \tag{3}$$

In the above equation *h* is the average heat transfer coefficient between the plate and the fluid, A_p is the heat transfer area of a single plate. Eq.(1) can be recast in terms of $N_{tu,f}$ as:

$$Max.\ Slope = \left(\frac{d\chi}{d\zeta}\right)_{\max} = f(n, N_{tu,f}) \tag{4}$$

2. THE THEORETICAL MODEL USED

We have developed a theoretical model for processing the experimental data from the single-blow test of perforated-plates, taking into account the discrete nature of the heat exchanger core.

Let the test exchanger core consist of *n* plates, separated by $(n-1)$ insulating spacers (fig. 1). The fluid inlet temperature, t_{in} is constant, and at time $\xi = 0^-$, the matrix is at a uniform temperature, T_0. At time $\xi = 0$, a step change, $\Delta T = t_{in} - T_0$, is applied to the fluid inlet temperature, and thereafter this temperature is maintained constant at t_{in}. Temperature of the *j*th plate is denoted by T_j. Fluid temperatures at inlet and outlet of the *j*th plate, are given by t_j and t_{j+1}, respectively.

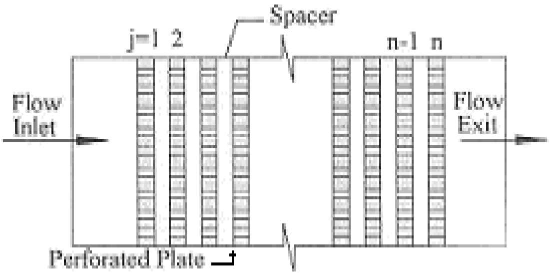

Fig.1 Schematic of the theoretical model used

Certain simplifying assumptions have been made such as: negligible axial conduction through the spacers, temperature independent fluid and matrix properties, negligible heat capacity of the fluid contained in the plate perforations, and adiabatic matrix boundaries.

The governing equations for the exchanger core are obtained by the energy balance over a control volume containing a single plate. The serial number of the plate is designated by *j*:

$$MC\frac{dT_j}{d\xi} = \dot{m}c_p\left(t_j - t_{j+1}\right) \tag{5}$$

where M is mass of a single plate, C is specific heat of plate material, T_j is temperature of the jth plate, t_j is Fluid temperature at entrance to *j*th plate, t_{j+1} is Fluid temperature leaving *j*th plate, ξ is time coordinate, $\dot{m}$ is mass flow rate, and c_p is fluid specific heat.

If a single perforated-plate is considered as a heat exchanger of effectiveness ε_p, the fluid inlet and outlet temperatures are related to the plate temperature as:

$$\varepsilon_p = \frac{t_{j+1} - t_j}{T_j - t_j} \tag{6}$$

where, $\varepsilon_p = 1 - e^{-N_{tu,f}}$, and $N_{tu,f}$ is the N_{tu} of a single plate defined by Eq.(3).

Defining a dimensionless time coordinate ζ , as $\zeta = (\frac{\dot{m}c_p}{MC})\,\xi$, and dimensionless fluid temperature θ and plate temperature τ , as $\theta = \frac{t - t_{in}}{T_0 - t_{in}}$ and $\tau = \frac{T - t_{in}}{T_0 - t_{in}}$, respectively, governing equations of the exchanger, Eqs.(5) and (6), can be rephrased in terms of the dimensionless fluid inlet temperature as follows:

$$\frac{d\tau_j}{d\zeta} + \varepsilon_p \tau_j = \varepsilon_p \theta_j \tag{7}$$

$$\theta_{j+1} = \theta_j + \varepsilon_p(\tau_j - \theta_j) \tag{8}$$

Equations (7) and (8), extended over all plates of stack $(1 \le j \le n)$, constitute the governing equations of the single-blow transient test of an MHE. Solving the differential Eq.(7), gives:

$$\tau_j(\zeta) = e^{-\varepsilon_p \zeta}\left[1 + \varepsilon_p \int_0^{\zeta} \theta_j e^{\varepsilon_p \zeta}\, d\zeta\right] \tag{9}$$

where $e^{\varepsilon_p \zeta}$ is an integrating factor. The algebraic Eqs.(8) and (9) now describe the dimensionless temperatures of the plate as a function of the dimensionless time ζ .

The plates and the fluid remain at uniform temperature T_0, till a step change in fluid inlet temperature is introduced. Therefore, the initial temperature condition ($\zeta = 0$) in dimensionless form for $1 \le j \le n$ is given as:

$$\tau_j = \theta_j = 1 \tag{10}$$

After the initial step change, the fluid inlet temperature is maintained constant, at $\theta_1 = 0$. Therefore, the boundary conditions in dimensionless form are stated as:

$$\theta_{in} = \theta_1 = 0 \qquad \text{for} \qquad \zeta > 0 \tag{11}$$

3. SOLUTION OF THE GOVERNING EQUATIONS

The sequence for solution of governing equations of the stack, Eqs.(8) and (9), to yield the temperature histories of all the plates $1 \le j \le n$ is as follows:

1. Starting with $j = 1$, Eq.(9) is solved using the initial and boundary conditions, Eqs. (10) and (11), to get the dimensionless temperature of the first plate, τ_1, for $\zeta \ge 0$.
2. Substitution of τ_1 in Eq.(8) gives temperature of fluid leaving the first plate, θ_2, for $\zeta \ge 0$.
3. Solving Eqs.(8) and (9) for the remaining plates successively, we finally get τ_n for the *n*th plate , and θ_{n+1}, the temperature of the fluid leaving the bed, for $\zeta \ge 0$.

3.1 Plate and Fluid Temperatures

$$\tau_1 = e^{-\varepsilon_p \zeta} \tag{12}$$

$$\tau_2 = e^{-\varepsilon_p \zeta} (\varepsilon_p{}^2 \zeta + 1) \tag{13}$$

$$\tau_3 = e^{-\varepsilon_p \zeta} \left[\varepsilon_p{}^2 \zeta \left(\frac{1}{2} \varepsilon_p{}^2 - \varepsilon_p + 2 \right) + 1 \right] \tag{14}$$

$$\theta_2 = \varepsilon_p e^{-\varepsilon_p \zeta} \tag{15}$$

$$\theta_3 = \varepsilon_p \left(\varepsilon_p{}^2 \zeta - \varepsilon_p + 2 \right) e^{-\varepsilon_p \zeta} \tag{16}$$

$$\theta_4 = \varepsilon_p \left[\begin{array}{c} (1 - \varepsilon_p)\left(\varepsilon_p{}^2 \zeta - \varepsilon_p + 2 \right) + \\ \frac{1}{2} \varepsilon_p{}^2 \zeta \left(\varepsilon_p{}^2 \zeta - 2\varepsilon_p + 4 \right) + 1 \end{array} \right] e^{-\varepsilon_p \zeta} \tag{17}$$

3.2 Maximum Slope - the Special Case of $N_{tu,f} \to \infty$ ($\varepsilon_p \to 1$)

When mass flow rate through the bed is very small, $N_{tu,f}$ approaches infinity, and ε_p approaches unity. In this case, plate and fluid outlet temperatures take the following forms:

$$\theta_2 = \tau_1 = e^{-\zeta} \tag{18}$$

$$\theta_3 = \tau_2 = (\zeta + 1) e^{-\zeta} \tag{19}$$

$$\theta_4 = \tau_3 = \left(\frac{1}{2} \zeta^2 + \zeta + 1 \right) e^{-\zeta} \tag{20}$$

A general expression for plate and fluid outlet temperatures can be written as:

$$\theta_{n+1} = \tau_n = e^{-\zeta} \sum_{i=1}^{n} \frac{1}{(n-i)!} \zeta^{(n-i)} \tag{21}$$

On using Locke's analysis [3] and Eq.(5), the maximum slope of the exit temperature response curve for the first three plates can be written as follows:

$$n = 1 : \left(\frac{d\chi_1}{d\zeta} \right)_{\max} = e^0 = 1.0 \quad at\ \zeta = 0$$

$$n = 2 : \left(\frac{d\chi_2}{d\zeta} \right)_{\max} = e^{-1} = 0.3678 \quad at\ \zeta = 1$$

$$n = 3 : \left(\frac{d\chi_3}{d\zeta} \right)_{\max} = 2e^{-2} = 0.2706 \quad at\ \zeta = 2$$

The general analytical expression for the maximum slope of the exit temperature response curve in the transient test of a MHE core with *n* plates and zero axial conduction and $N_{tu,f} \to \infty$, is:

$$\left(\frac{d\chi}{d\zeta} \right)_{\max} = \frac{(n-1)^{(n-1)}}{(n-1)!} e^{-(n-1)} \tag{22}$$

Using the Stirling formula [5], the above relation can be rewritten in a simple form:

$$\text{Max. Slope} \approx \frac{1}{\sqrt{2\pi (n-1)}} \quad for \ \ n \succ 10 \tag{23}$$

Equation (22) shows the dependence of the maximum slope of the exit temperature response curve on the finite number of plates in a test of the heat exchanger core. The maximum slope remains finite even for $N_{tu,f}$ approaching infinity. For the above case, the maximum slope occurs at $\zeta = n - 1$, and for the case of finite $N_{tu,f}$, the maximum slope occurs at $\zeta \succ (n-1)$.

4. NUMERICAL SOLUTION OF THE GOVERNING EQUATIONS

Numerical techniques have been used for solving the governing equations of the exchanger matrices consisting of 1, 7, 10, 20, 40 and 60 plates. In each case the number of transfer units per plate $N_{tu,f}$, was varied between 0.2 and 4.0, and axial conduction effects were neglected. Figure 2, presents the time response of dimensionless plate temperature for some $N_{tu,f}$ values. The time response of dimensionless temperature of different plates for $N_{tu,f}=1$ is shown in fig. 3, and the maximum slope versus time for different plates, as a function of $N_{tu,f}$ is presented in fig. 4. The effect of number of plates on relationship between exchanger N_{tu} ($N_{tu}=n*N_{tu,f}$) and maximum slope of the fluid exit temperature, for zero axial conduction is given in fig. 5. The figure shows the error incurred when using the continuous exchanger formalism to process experimental data for a perforated plate heat exchanger.

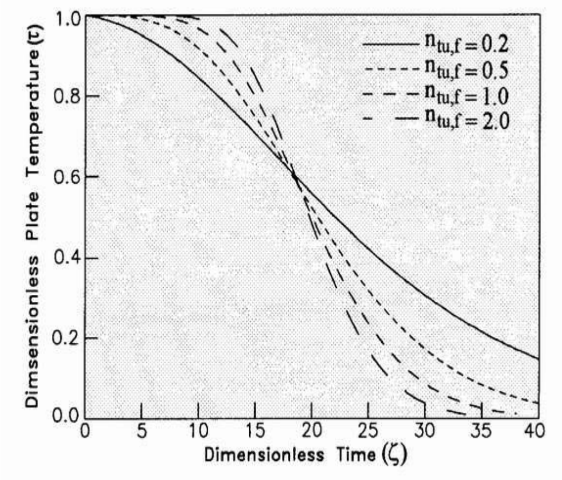

Fig.2 Dimensionless plate temperature *vs.* dimensionless time and $N_{tu,f}$, for plate #7

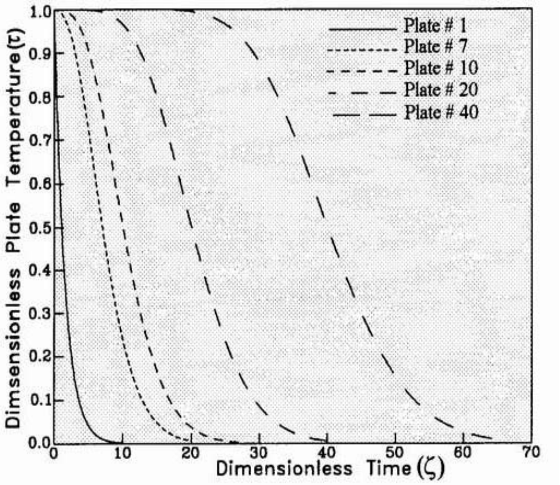

Fig.3 Dimensionless plate temperature, as a function of dimensionless time for $N_{tu,f}=1$

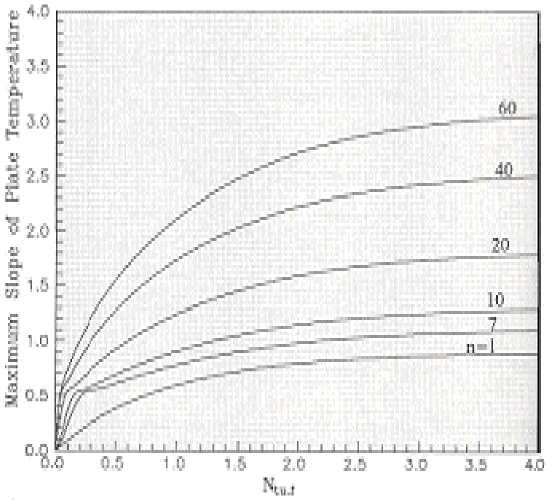

Fig.4 Maximum slope of dimensionless plate temperature *vs.* time

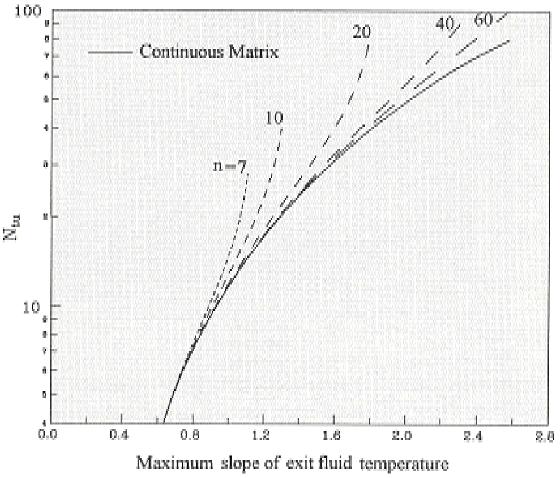

Fig.5 N_{tu} *vs.* maximum slope of dimensionless fluid exit temperature and number of plates

5. EXPERIMENTAL STUDIES

The heat transfer and flow friction characteristics of the perforated-plates determine the performance of the heat exchanger. Convective heat transfer coefficients with gas flow through perforated copper plates have been experimentally determined for a few cases, and the data has been compared with the results of the above model.

The copper perforated-plates and the stainless steel spacers, shown in fig. 6, were produced using photochemical milling (PCM) technique. The perforated-plates are circular, 50.4 mm in diameter, 0.4 mm thick with 0.8 mm perforations, and a porosity of about 43%.

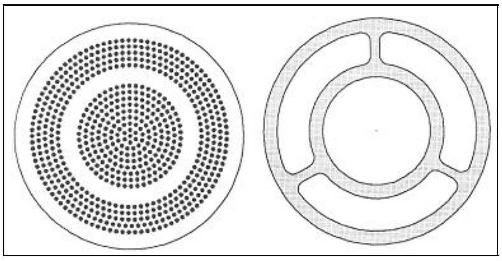

Fig.6 Copper perforated plate and stainless steel spacer configurations

5.1 Experimental Setup and Procedure

A simple experiment, shown in fig. 7, based on the design of Ravikumar et al. [2], has been used to evaluate the performance of the perforated-plates.

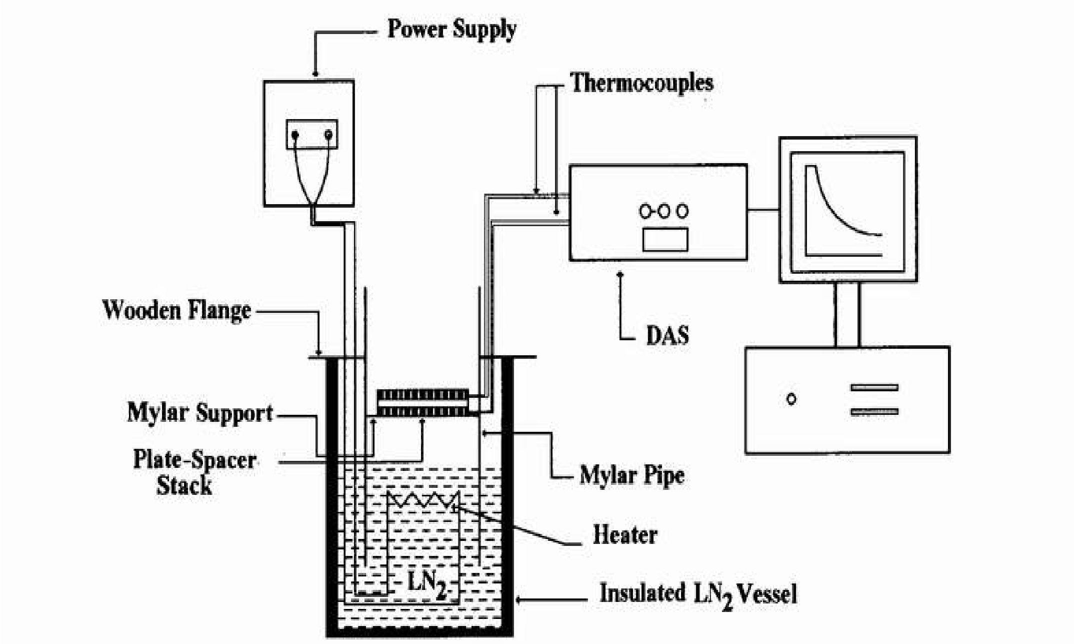

Fig.7 The single-blow transient test technique experimental setup

The set up consists of an insulated Dewar, filled with liquid nitrogen to a sufficient height. The stack of perforated-plates and spacers are arranged inside a short cylindrical pipe made of a thin Mylar® sheet. The stacks are separated from the pipe walls, and are supported centrally by a thin annular ring, approximately 2 cm wide, which rests on an annular Mylar® flange inside the pipe. This unit, supported by another annular flange made of thin plywood, is placed vertically in the insulated Dewar. The Mylar® pipe is immersed in the liquid nitrogen bath, remaining a centimeter or two above the bottom of the Dewar. A heater is placed inside the immersed portion of the Mylar® pipe, to generate saturated nitrogen vapor, which flows through the perforated-plates. Thermocouples, placed inside the plates by drilling small holes in their rims, and connected to a data acquisition system, are used to measure temperatures of plates.

The experiments are carried out by placing the plate assembly on top of the liquid nitrogen and switching on the heater simultaneously, to generate and force nitrogen vapor through the plates. Temperatures of the plates fall as the nitrogen vapor passes through them, and these temperatures sensed by the thermocouples are transmitted to the computer via the data acquisition system. The current and voltage across the heater are also noted to calculate the power input to the heater. The mass flow rate of the nitrogen vapor through the stack of plates is then estimated from this power input.

6. RESULTS AND DISCUSSION

The analytical procedure developed in previous sections, has been used to study the experimental data from single-blow tests on a stack of 7 plates. Figure 8 presents typical cool down response curves for different mass flow rates.

On using fig. 4 and the experimentally determined value of maximum slopes of the dimensionless plate temperatures curves from fig. 8, $N_{tu,f}$ of the stacks of plates is calculated. The heat transfer coefficients are then calculated from the definition of $N_{tu,f}$. Figure 9 presents the heat transfer coefficients in terms of Nusselt number versus Reynolds number.

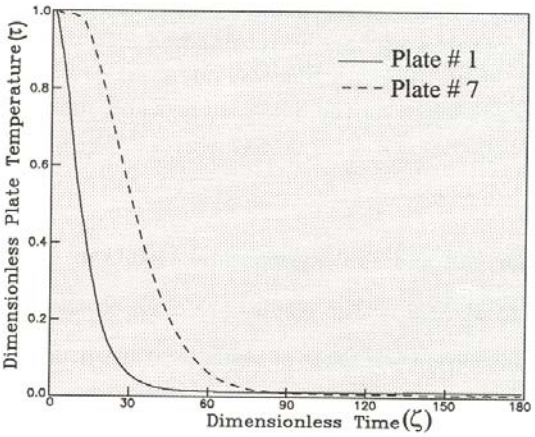

Fig.8 Cool down response of the plates: nitrogen gas flow rate = 0.5980 g/s, number of plates = 7

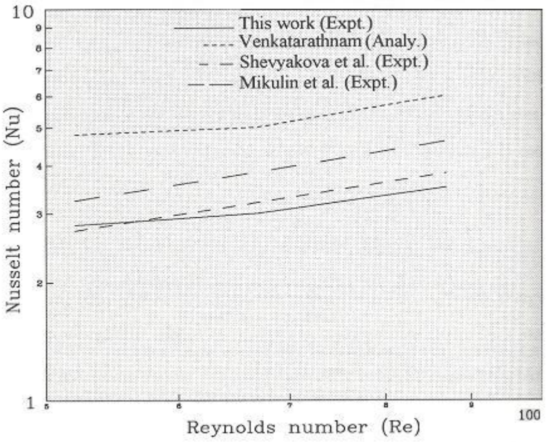

Fig.9 Nusselt number *vs.* Reynolds number, calculated for a stack of 7 plates

From the experimental data, the following correlation, representing the relationship between Nusselt number and Reynolds number, has been obtained as:

$$Nu = 0.492.\mathrm{Re}^{0.436}$$

The Reynolds number range considered is 50-100. The Nusselt number and Reynolds number are based on the hole diameter and superficial velocity. The results of present work has been compared with the analytical results of Venkatarathnam [6] and the experimental results of Mikulin et al. [7] and Shevyakova et al. [8]. Our results are close to those of Mikulin and Shevyakova, but are lower than those of Venkatarathnam.

7. CONCLUSIONS

A single-blow transient test setup has been used to determine the heat transfer coefficients of stacks of perforated-plates. An analytical technique has been developed to reduce the experimental data of single-blow transient test of discrete plate-spacer pairs. The analytical results have been presented in terms of Nusselt number, given as function of Reynolds number and geometrical parameters. The results presented provide a good prior estimate of heat transfer coefficients for design and development of matrix type compact heat exchangers for cryogenic applications.

8. REFERENCES

[1] Farhani, F., Venkatarathnam, G., Sarangi, S., Evaluation of Heat Transfer and Flow Friction Characteristics of Matrix Heat Exchangers, 14th Annual (International) Mechanical Engineering Conference, Isfahan University of Technology, Isfahan, Iran, May 2006.

[2] Ravikumar, K.V., Frederking, T.H.K., On the Thermal Performance of Perforated Heat Exchanger Plates, *Advances in Cryogenic Engineering*, 39B (1994).

[3] Locke, G.L., Heat Transfer and Flow Friction Characteristics of Porous Solids, Technical Report TR No. 10, Stanford University, June 1950, California, USA.

[4] Kays, W.M., London, A.L., Compact Heat Exchangers, McGraw-Hill, New York, Third Edition, 1983.

[5] Spiegel, M.R., Mathematical Handbook of Formulas and Tables, Schaum's Outline Series, McGraw Hill, 1968.

[6] Venkatarathnam, G., Matrix Heat Exchangers, Ph.D. Thesis, Cryogenic Engineering Centre, Indian Institute of Technology, Kharagpur, India, 1991.

[7] Mikulin, E.I, et al., Study of Matrix-type Heat Exchangers Made of Perforated Plates, *Khim. Neft. Mashin (In Russian)*, 9 (1980).

[8] Shevyakova, S.A., Orlov, V.K., Study of Hydraulic Resistance and Heat Transfer in Perforated-Plate Heat Exchangers, *Inzhenerno Fizicheskii Zhurnal (In Russian)*, 45 (1983).

Proceedings of the 4th BSME-ASME International Conference on Thermal Engineering
27-29 December, 2008, Dhaka, Bangladesh

CALCULATION OF HEAT TRANSFER AND TEMPERATURE DISTRIBUTION IN AN ELECTRONIC BOX USING THERMAL DESKTOP AND SINDA/FLUINT SOFTWARE

Mehran Shahryari[1], **Foad Farhani**[2]

[1]Iranian Space Agency, Tehran, Iran.
[2]Department of Mechanical Engineering
Iranian Research Organization for Science and Technology (I.R.O.S.T),
P.O. Box 15815 – 3538, Tehran, Iran.
e-mail: a_mshahryari@yahoo.com

ABSTRACT

Electronic cooling and thermal control is an important branch of thermal engineering. A thermal designer should use available software tools for the design and evaluation of his thermal design to ensure the operation of electronic instruments under suitable working conditions. In this research work we have used such software for the stated purpose. In the paper we have presented the transient heat transfer calculations and temperature distribution in an electronic box under forced convection conditions, using Thermal Desktop (TDT) and SINDA/FLUINT software. The geometrical mathematical model (GMM) and thermal mathematical model (TMM) of the electronic box, consisting of two electronic boards have been built. Different flow options and links between flow network and thermal network have been modeled with FloCAD. To simulate the working conditions of the electronic box, constant and periodic heat dissipations have been allocated to the electronic boards, and transient heat transfer calculations have been performed. Convection coefficients are obtained from numerical simulation of flow field in the electronic box. Temperature distribution for all parts and elements of electronic box has been determined. The ease of modeling and analysis of the problem at hand goes to indicate the suitability of the software for tackling complex electronic thermal control applications.

KEYWORDS: *Forced convection, Transient heat transfer, Thermal desktop, SINDA/FLUINT software*

1. INTRODUCTION

Thermal control of electronic devices used in aerospace applications and computer industry is an important consideration for optimum operation of these devices. In recent years, miniaturization of the electronic circuits has resulted in reduction of the available area for transfer of dissipated heat in these elements, further complicating the cooling requirements. Hence, a thermal designer should use available software tools for the design and evaluation of his design to ensure the operation of electronic instruments under allowable working conditions. Thermal desktop [1] is a program that allows the user to quickly build, analyze, and postprocess sophisticated thermal models. RadCAD®, a subset of the Thermal Desktop, is a module to calculate radiation exchange factors and orbital heating rates (for space applications). FloCAD, another module of the Thermal Desktop, generates flow networks and calculates convective heat transfer factors. The outputs from Thermal Desktop, RadCAD and FloCAD are automatically combined for input into SINDA/FLUINT software [2, 3], a comprehensive software package, used for design and simulation of heat transfer and fluid flow problems. SINDA is a network-style (resistor-capacitor circuit analogy) thermal simulator and FLUINT is a network-style fluid flow simulator.

In this research work we have used thermal desktop and SINDA/FLUINT software to study the transient heat transfer in an electronic box under forced convection conditions and determine the temperature distribution in the electronic box. The electronic box contains two electronic boards, dissipating heat at different rates. Cooling of the electronic box using a fan of given size and flow rate has been investigated.

2. MODELING PROCESS

The modeling process results in construction of a geometrical mathematical model (GMM) and a thermal mathematical model (TMM) [4]. The GMM is a mathematical representation of physical surfaces of the components, and is used to calculate blackbody radiation couplings between surfaces. The GMM is analyzed using thermal desktop software to calculate the convection conductors, capacitances, and so on. The calculated radiation interchange couplings are usually used in construction of the TMM. The output data, in the form of arrays, can then be merged directly into the TMM file.

The TMM consists of nodes representing parts of the components, conduction and radiation conductors between nodes, blocks of arrays, and constants for storing inputs, which are previously calculated, and logic blocks for controlling the execution of the program. Thermal mathematical model includes a network representation of the thermal mass and conduction and radiation couplings of the components and is used to predict temperatures of the components. TMM model is built using SINDA/FLUINT soft ware.

To calculate the capacitances and various convection conductors, a simple geometrical model, representing the electronic box has been constructed. Each surface of the electronic box is assigned the appropriate thermophysical properties like conductivity, density, specific heat and etc. The main structure of the electronic box consists of a cubic case of 20 cm sides. The model structure is aluminum with K=237 W/m-K, ρ=2702 kg/m^3, and C_P=900 j/kg-k. Two electronic boards are placed in the box. The electronic boards are 20 cm × 24 cm, and have been simulated as flat plates of 2 mm thickness.

As shown in fig. 1 each lateral plate has been modeled with 3 diffusion nodes. These nodes are connected to each other with conductive conductors. Also two nodes each are specified for the bottom and top plates of the electronic box. Plates are connected to each other by contact conductors. According to the number of heat sources in the electronic boards, these plates have been broken down to nodes. Nodes presenting the electronic boards have been linked to each other using conductive links. Electronic boards are connected to lateral plates by contact conductors. At the front side of the box, a fan of 15 cm diameter has been installed to cool the electronic boards by blowing outside cool air. To discharge the warm air from the electronic box, an opening has been considered in the opposite side.

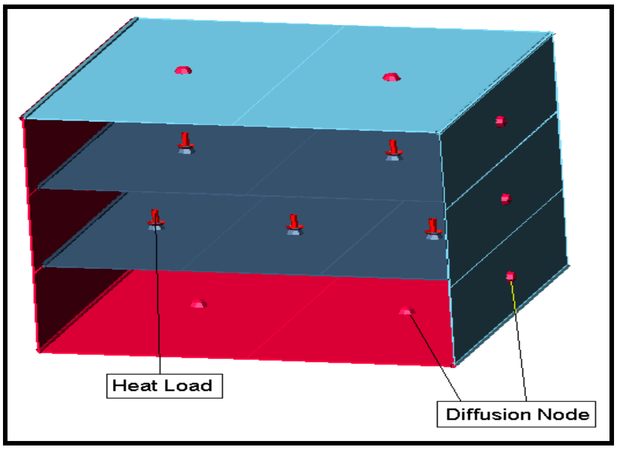

Fig.1 The thermal nodal network

Fluid network specified for the model is illustrated in fig. 2. A plenum lump is specified on the external surface of the box case, before the cooling fan. Three junction lumps are located in the inlet of each air passage in the box. In order to model exhaust condition of each passage, three plenum lumps have been considered at the end of each passage, outside the electronic box. Mass transfer paths (paths describe the means by which fluid flows from one lump to another. Each path has a single characteristic mass flow rate) have been considered between different lumps. In addition, lumps and diffusion nodes of thermal network convective heat transfer links (ties, which describe the means by which heat flows between FLUINT lumps (representing the fluid) and SINDA nodes) have been considered between the tank lump (lumps represent a point at which energy and mass are conserved).

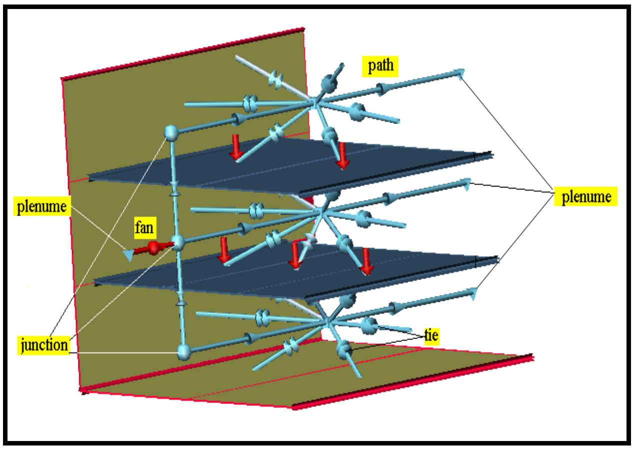

Fig.2 Representation of the flow network

Heater elements have been defined in order to specify heat dissipation of electronic boards. Accordingly, on basis of the heat dissipations, two constant and three periodic heat loads have been assigned to heater elements. Heat dissipation variation with time is shown in fig. 3. As it is evident in this figure a constant heat load (52 W) has been specified for each heater element of the upper board, and a periodic heat load with frequency of 0.025 Hz has been applied to each heater element of lower board.

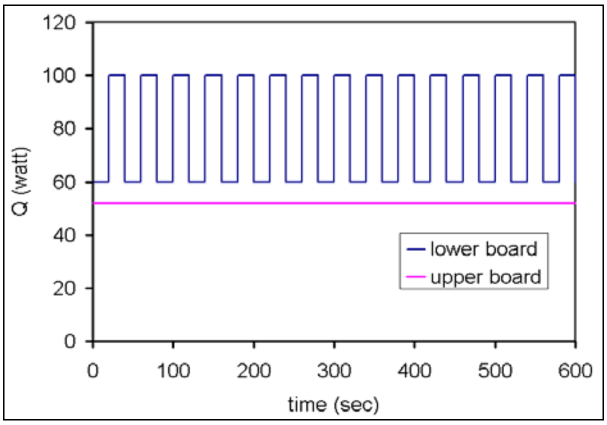

Fig.3 Variation in the heat dissipation of electronic boards

Conduction conductors were calculated in a straight forward manner using the KA/L relationship. The contact conduction between nodes was based on screw conduction terms. Linear conductors transport the heat according to the difference of absolute temperatures of two nodes.

$$Q_{1-2} = GR_{1-2}(T_1 - T_2) \tag{1}$$

$$GR_{1-2} = \frac{KA}{\Delta X} \tag{2}$$

where K is the conduction heat transfer coefficient ($\frac{W}{m\,k}$). A is the heat transfer area between the two nodes (m^2), and ΔX is the distance between two nodes (m).

Contact conductors transport heat according to the difference of temperature between two nodes.

$$Q_{1-2} = GR_{1-2}(T_1 - T_2) \tag{3}$$

$$GR_{1-2} = hA \tag{4}$$

where h is the contact heat transfer factor ($\frac{W}{m^2\,k}$), and A is the area of contact surface (m^2).

Since the convective process of heat transfer is so closely linked to fluid motion, it is first required to establish whether the fluid flow is laminar or turbulent. Additionally, to apply the relationship for forced convection coefficient in the passage, it is necessary to calculate the hydraulic diameter and Reynolds number. Physical properties such as density (ρ), dynamic viscosity (μ), thermal conductivity (k), Prandtle number (Pr), and specific heat (Cp) must be determined at film temperature ($T_f = (T_{wall} + T_{fluid})/2$). The flow regime is determined on the basis of calculated Reynolds number. For the case under study, the calculated Reynolds number is greater than 10^4, and so the flow in this passage is turbulent.

Thermo physical properties of aluminum electronic box and electronic boards are presented in tab. 1. Allowable temperature limits of electronic boards and box case are given in tab. 2.

Table 1. Thermo physical properties

Material/ Item	**Conductivity [W/m-K]**	**Specific Heat [J/kg-k]**	**density [kg/m^3]**
Aluminium	237	900	2702
Electronic boards	15.1	837.32	2000

Table 2. Allowable temperature limits

Unit	Min. Temperatue [K]	Max. Temperatue [K]
Electronic board	263	300
Eelectronic box (case)	263	320

2.1 Simulation of Flow Field in the Electronic Box

In order to thermally couple the air flow and elements of the electronic box case and external surfaces, the flow pattern must be determined and local thermal convection coefficients calculated. To obtain the flow pattern and determine the flow velocity and pressure distribution within the electronic box, the fluid flow has been analyzed numerically. Towards this end, the geometrical and numerical networks have been constructed using Gambit software, and modeling and analysis has been performed using FLUENT software. Mass, momentum and energy equations for incompressible air flow have been analyzed numerically and through trial and error. The analysis results have been used for determination of Reynolds number *Re* and Nusselt number *Nu*, used in determination of the local thermal convection coefficients. The elemental networks have been constructed using Hex/Hybrid elements of Tgrid type.

A three dimensional segregated solver and steady state condition with absolute formulation has been used for this analysis. The ideal gas state, incompressible flow and viscosity effects have been considered in the numerical simulation of the flow. Continuity, momentum and energy equations and ideal state have coupled and solved. In order to discretize the pressure terms in these equations, we have used the standard method, and to couple pressure and velocity field the SIMPLE algorithm has been used [5, 6]. For modeling the turbulence we have used the k-ε RNG turbulence model, and standard wall function [7]. To discretize the momentum and energy equations, and also equations for turbulence kinetic energy (*k*) and turbulence dissipation energy (*ε*), *Second Order Upwind* has been used.

Figures 4 and 5 show the flow and velocity field lines for fans rotating at 18500 and 30000 rpm. The increased air flow velocity over the electronic boards is due to increase in the rotational speed of the fans. As one end of the electronic box is closed and only some opening for passage of air have been considered, the flow inside the box experiences rotational motion and small and big vortices are formed inside the box and between the electronic boards. Increase in fans' speed increased the local velocities inside the electronic box, which results in increased convective heat transfer and hence drop in temperatures of the electronic boards.
Considering the obtained velocity field and heat transfer relations, it is possible to determine the coefficient of convection heat transfer. For this purpose, the relation for forced convection on a flat surface and Reynolds number in the range of $2\times10^5 \leq \mathrm{Re} \leq 5\times10^5$, has been used for Nusselt number [8].

$$Nu_L = 0.0370\,\mathrm{Re}_L^{0.8}\,\mathrm{Pr}^{0.43} \tag{5}$$

In the above equation, $\mathrm{Re}_L = \frac{U_\infty L}{\upsilon}$ is the Reynolds number defined on basis of the free velocity U_∞ on a flat surface of length *L*, and μ is dynamic viscosity, and *Pr* is Prandtle number defined for the air flow.

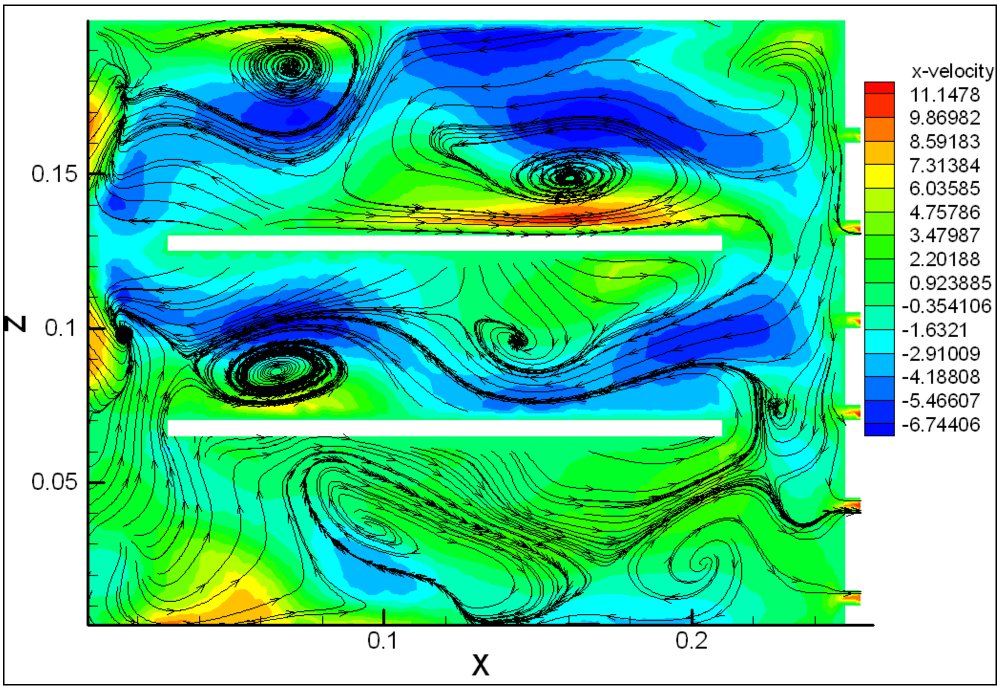

Fig.4 Flow and velocity field lines for fans rotating at 18500 rpm

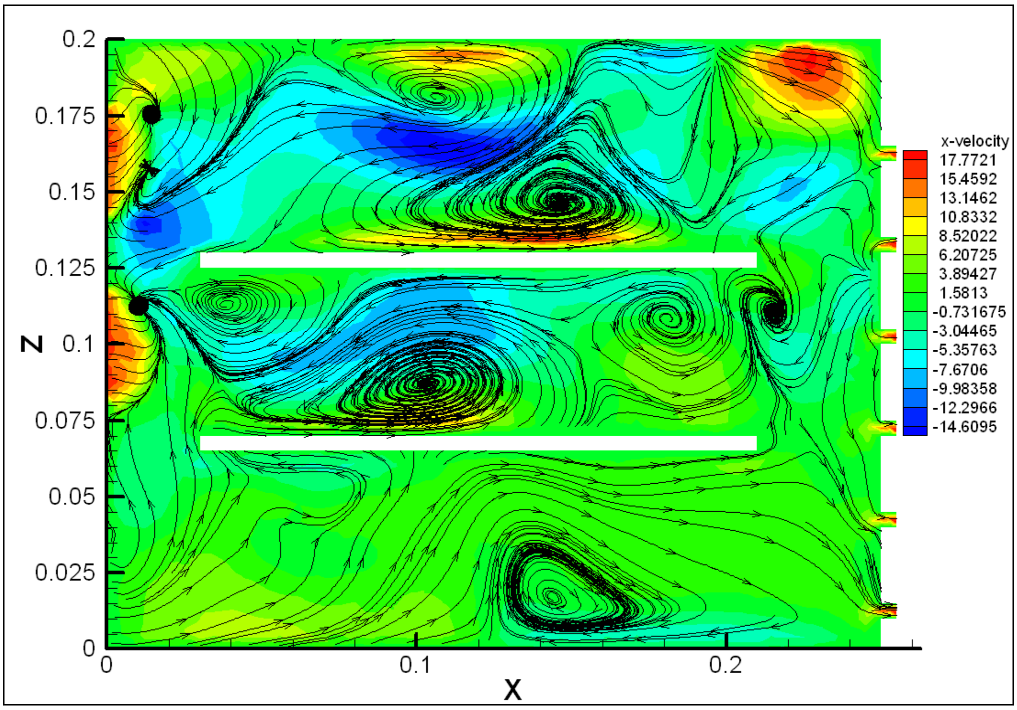

Fig.5 Flow and velocity field lines for fans rotating at 30000 rpm

3. RESULTS AND DISCUSSIONS

Temperature variations of thermal nodes for various parts of the electronic box are shown in figs. 6 through 8. After a relatively steep increase, temperatures of all thermal nodes reach thermal equilibrium except for the condition arising from variable applied thermal loads. Figure 6 shows temperature variations for a thermal node on the electronic box case. Increase in fan's rotational speed, from 5000 rpm to 30000 rpm, has resulted in a temperature drop from 302 °C to 300 °C. Figure 7 presents variation in temperature of a thermal node on the upper electronic board. As shown an increase in fan's rotational speed has resulted in decrease in temperature from 305 °C to 301.3 °C. Variation in temperature of one of the thermal nodes on the lower electronic board is shown in fig. 8. Here again, increase in fan's rotational speed has resulted in a temperature drop of about 6 °C.

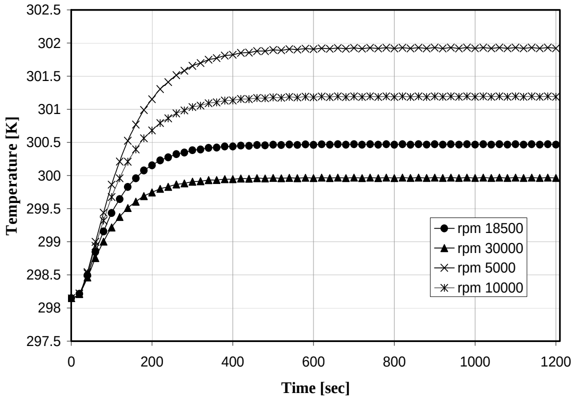

Fig.6 Temperature variations of a thermal node on the electronic box case

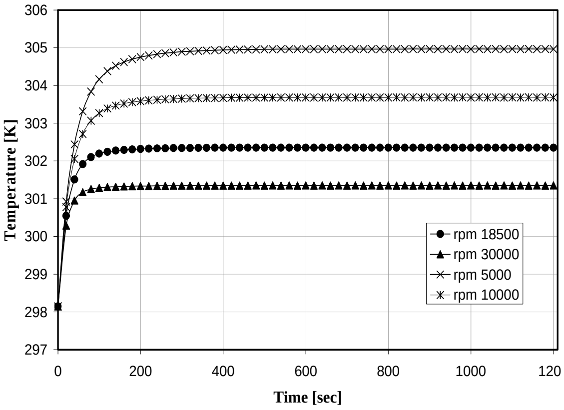

Fig.7 Temperature variations of a thermal node on the upper electronic board

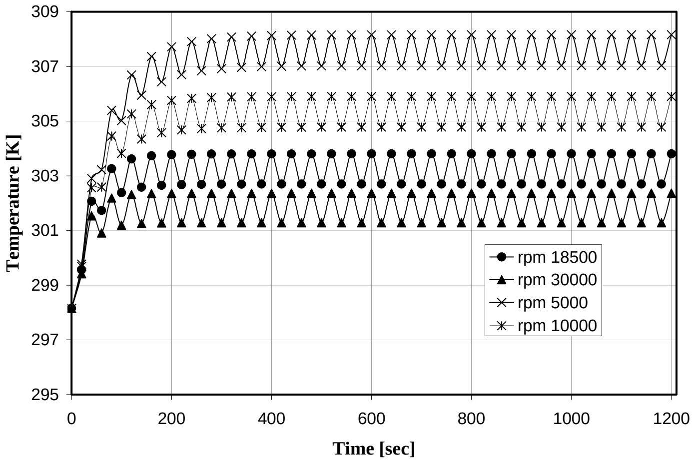

Fig.8 Temperature variations of a thermal node on the lower electronic board

4. CONCLUSIONS

- Increase in fan's rotational speed, increases air flow rate through the electronic box, resulting in higher thermal convection inside the box and cooling of its internal components.
- The effect of higher fan rotational speeds is more pronounced for high dissipating electronic boards.
- The effect of increase in fan's rotational speed is more pronounced for lower speed ranges. For example, increasing fan's speed from 5000 rpm to 10000 rpm results in 1.4 °C drop in the working temperature of the upper electronic board, while increase from 18500 rpm to 30000 rpm produces a temperature drop of about 1.1 °C.
- For fan rotational speed of 18500 rpm, all the electronic boards are maintained at allowable temperature levels (see tab. 2).

- The ease of modeling and analysis of the problem presented in this paper, using Thermal Desktop and SINDA/FLUINT software, indicates their suitability for tackling complex thermal control applications such as electronic cooling in computer industry and aerospace applications.

5. REFERENCES

[1] Panczak, T., et al., Thermal Desktop, Version 4.4, Cullimore and Ring Technologies, Inc., 2001.
[2] Introduction to SINDA, Version 4.4, Cullimore and Ring Technologies, Inc, 2001.
[3] SINDA/FLUINT User's Manual, Version 4.4, Cullimore and Ring Technologies, Inc., 2001.
[4] Thermal Network Modeling Handbook, Version 97.003, K&K Associates, 1999-2000.
[5] Lomax, H., Pulliam, T.H., Zingg, D.W., Fundamentals of Computational Fluid Dynamics, 1999.
[6] White, F.M., Fluid Mechanics, 4th Edition, McGraw-Hill, 1998.
[7] Ferziger, J.H., Peric, M., Computational Methods for Fluid Dynamics, 3rd Edition, Springer, 2001.
[8] Thermal Network Modeling Handbook, K&K Associates, http://www.tak2000.com, visited during 1999-2000.

Proceedings of the 4th BSME-ASME International Conference on Thermal Engineering
27-29 December, 2008, Dhaka, Bangladesh

VISCOUS DISSIPATION EFFECTS ON NATURAL CONVECTION FLOW ALONG A SPHERE WITH RADIATION HEAT LOSS

M. A. Alim[1], M. M. Rahman[2] and Salina Aktar[2]

[1]Department of Mathematics, Bangladesh University of Engineering and Technology,
Dhaka-1000, Bangladesh,
[2]Department of Natural Science, Stamford University, Bangladesh.
e-mail: maalim@math.buet.ac.bd

ABSTRACT

The present work describes the effects of viscous dissipation on the natural convection flow of incompressible fluid along a uniformly heated sphere with radiation heat loss. The governing boundary layer equations are first transformed into dimensionless non-similar equations by using set of suitable transformations and solved numerically by implicit finite difference method known as Keller-box technique. Numerical results are presented in the form of velocity profiles, temperature profiles, local shear stress and local rate of heat transfer for selected values of parameters set consisting of viscous dissipation parameter Vd, radiation parameter R_d, and the Prandlt number Pr.

KEYWORDS: *Natural convection, viscous dissipation, radiation, skin-friction, Nusselt number.*

1. INTRODUCTION

Along with the free convection flow, the phenomenon of the boundary layer flow of an incompressible fluid along a sphere in presence of viscous dissipation and radiation heat loss is also very common because of their applications in nuclear engineering in connection with the cooling of reactors. The influence and importance of viscous stress work effects in laminar flows have been examined by Gebhart [1] and Gebhart and Mollendorf [2]. In both of the investigations special flows over semi-infinite flat surfaces parallel to the direction of body force were considered. Gebhart [1] has shown that the viscous dissipation effect plays an important role in natural convection in various devices which are subjected to large deceleration or which operate at high rotational speeds and also in strong gravitational field processes on large scales (on large planets) and in geological processes. Gebhart and Mollendorf [2] considered flows generated by plate surface temperature. Zakerullah [3] has been investigated the viscous dissipation and pressure work effects in axisymmetric natural convection flows. The effect of pressure stress work and viscous dissipation in natural convection flow along vertical flat plate with heat conduction due to plate thickness has been studied by Alam *et al.* [4].

In the present study, effects of viscous dissipation on laminar free convection flow along a uniformly heated sphere with radiation heat loss have been investigated. The governing boundary layer equations are first transformed into dimensionless non-similar equations by adopting appropriate transformations. The transformed equations are then solved numerically using implicit finite difference method known as Keller box technique [5,6]. The solutions are obtained in terms of velocity profiles, temperature profiles, local shear stress and local rate of heat transfer for various values of relevant parameters and displayed on graphs.

2. MATHEMATICAL FORMULATIONS

Free convective flow past an isothermal sphere of radius a has been considered. The physical co-ordinates $(\hat{x}, \hat{y})$ are chosen such that $\hat{x}$ is measured along the surface of the sphere and $\hat{y}$ is normal to the sphere. The co-ordinate system and the flow configuration are shown in Figure 1.

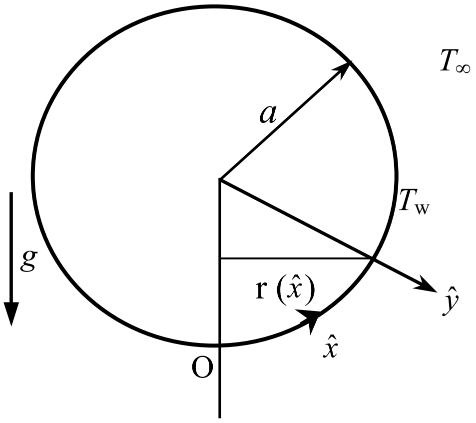

Fig. 1: Physical model and coordinate system

Under the usual Boussinesq and boundary layer approximation, the equations for mass of continuity, momentum and energy take the following form:

$$\frac{\partial}{\partial \hat{x}}(r\hat{u}) + \frac{\partial}{\partial \hat{y}}(r\hat{v}) = 0 \tag{1}$$

$$\hat{u}\frac{\partial \hat{u}}{\partial \hat{x}} + \hat{v}\,\frac{\partial \hat{u}}{\partial \hat{y}} = \nu\frac{\partial^2 \hat{u}}{\partial \hat{y}^2} + g\beta(T\text{-}T_\infty)\,\sin\left(\frac{\hat{x}}{a}\right) \tag{2}$$

$$\hat{u}\frac{\partial T}{\partial \hat{x}} + \hat{v}\frac{\partial T}{\partial \hat{y}} = \frac{k}{\rho C_p}\left[\frac{\partial^2 T}{\partial \hat{y}^2} - \frac{1}{k}\frac{\partial q_r}{\partial \hat{y}}\right] + \frac{\nu}{\rho C_P}\left(\frac{\partial \hat{u}}{\partial \hat{y}}\right)^2 \tag{3}$$

where $r(\hat{x}) = a\sin\left(\hat{x}/a\right)$ is the radial distance from the centre of the sphere, g is the acceleration due to gravity, β is the coefficient of thermal expansion, ν is the kinematics viscosity, T is the local temperature, C_p is the specific heat at constant pressure, ρ is the density and q_r is the radiative heat flux. In order to reduce the complexity of the problem and to provide a means of comparison with future studies that will employ a more detail representation for the radiative heat flux, the optically thick radiation limit is considered in this study. Thus radiation heat flux term is simplified by the Rosseland diffusion approximation is given by

$$q_r = -\frac{4\sigma}{3(a_r + \sigma_s)}\frac{\partial T^4}{\partial \hat{y}}$$

Where, a_r is the Rosseland mean absorption co-efficient, σ_s is the scattering co-efficient and σ is the Stephan-Boltzman constant.

The boundary conditions for the equations (1) - (3) are

$$\begin{aligned} &\hat{u} = \hat{v} = 0,\ T = T_w \ \text{ at } \hat{y} = 0 \\ &\hat{u} \to 0,\ T \to T_\infty \ \text{ as } \hat{y} \to \infty \end{aligned} \tag{4}$$

Where, T_w is the surface temperature of the sphere and T_∞ is the ambient temperature of the fluid with $T_{\mathrm{w}} > T_\infty$.

To transform the above equations into non-dimensional form, the following dimensionless variables are introduced:

$$\xi = \frac{\hat{x}}{a},\ \eta = Gr^{\frac{1}{4}}\frac{\hat{y}}{a},\ \mathrm{u} = \frac{\mathrm{a}}{\nu}\mathrm{G}_{\mathrm{r}}^{-\frac{1}{2}}\,\hat{\mathrm{u}}\ ,\ v = \frac{\mathrm{a}}{\nu}\mathrm{G}_{\mathrm{r}}^{-\frac{1}{4}}\,\hat{v},$$

$$\theta = \frac{T - T_\infty}{T_W - T_\infty}, Gr = \frac{g\beta(T_W - T_\infty)a^3}{\nu^2}, \tag{5}$$

$$\theta_W = \frac{T_W}{T_\infty},\ \ \Delta = \theta_W - 1 = \frac{T_W}{T_\infty} - 1 = \frac{T_W - T_\infty}{T_\infty}$$

Where Gr is the Grashof number, θ is the dimensionless temperature and θ_w is the surface temperature parameter. Substituting variables (5) into equations (1) to (3) leads to the following non-dimensional equations

$$\frac{\partial}{\partial\xi}(ru) + \frac{\partial}{\partial\eta}(rv) = 0 \tag{6}$$

$$u\frac{\partial u}{\partial\xi} + v\frac{\partial u}{\partial\eta} = \frac{\partial^2 u}{\partial\eta^2} + \theta\sin\xi \tag{7}$$

$$u\frac{\partial\theta}{\partial\xi} + v\frac{\partial\theta}{\partial\eta} = \frac{1}{Pr}\frac{\partial}{\partial\eta}\left[\left\{1 + \frac{4}{3}R_d\left(1 + (\theta_w - 1)\theta\right)^3\right\}\frac{\partial\theta}{\partial\eta}\right] + Vd\left(\frac{\partial u}{\partial\eta}\right)^2 \tag{8}$$

Where, $\mathrm{Pr} = \dfrac{\nu C_p}{k}$ is the Prandtl number, $Vd = \dfrac{\nu^2 G_r}{\rho a^2 C_p (T_w - T_\infty)}$ is viscous dissipation parameter and $R_d = \dfrac{4\sigma T_\infty^3}{k(a + \sigma_s)}$ is the radiation parameter.

The boundary conditions associated with equations (6) to (8) are

$$\begin{aligned} &u = v = 0,\ \theta = 1 \text{ at } \eta = 0 \\ &u \to 0,\ \theta \to 0 \text{ as } \eta \to \infty \end{aligned} \tag{9}$$

To solve equations (6) to (8) subject to the boundary conditions (9), we assume the following variables

$$\psi = \xi r(\xi) f(\xi,\eta),\quad \theta = \theta(\xi,\eta), r(\xi) = \sin\xi \tag{10}$$

Where, ψ (ξ,η) is the non-dimensional stream function, which is related to the velocity components in the usual way as

$$u = \frac{1}{r}\frac{\partial\psi}{\partial\eta} \ \text{ and } \ v = -\frac{1}{r}\frac{\partial\psi}{\partial\xi} \tag{11}$$

We may proceed to transform the conservation of momentum and energy equations (7) and (8) into the new co-ordinates. To facilitate the transformation, it is useful to have the velocity components explicitly expressed in terms of the new variables. Therefore we obtained

$$\frac{\partial^3 f}{\partial \eta^3}+\left(1+\frac{\xi}{\sin\xi}\cos\xi\right)f\frac{\partial^2 f}{\partial \eta^2}-\left(\frac{\partial f}{\partial \eta}\right)^2+\theta\frac{\sin\xi}{\xi}=\xi\left(\frac{\partial f}{\partial \eta}\frac{\partial^2 f}{\partial \xi\partial \eta}-\frac{\partial f}{\partial \xi}\frac{\partial^2 f}{\partial \eta^2}\right) \tag{12}$$

and

$$\begin{aligned}&\frac{1}{\Pr}\left[\frac{\partial}{\partial \eta}\left\{1+\frac{4}{3}R_d\left(1+(\theta_w-1)\theta\right)^3\right\}\frac{\partial \theta}{\partial \eta}\right]+\left(1+\frac{\xi}{\sin\xi}\cos\xi\right)f\frac{\partial \theta}{\partial \eta}\\&\qquad+Vd\left\{\xi\frac{\partial}{\partial \eta}\left(\frac{\partial f}{\partial \eta}\right)\right\}^2=\xi\left(\frac{\partial f}{\partial \eta}\frac{\partial \theta}{\partial \xi}-\frac{\partial f}{\partial \xi}\frac{\partial \theta}{\partial \eta}\right)\end{aligned} \tag{13}$$

It has been seen that the lower stagnation point of the sphere *or* $\xi \approx 0$, equations (12) and (13) reduce to the following ordinary differential equations:

$$\frac{d^3 f}{d\eta^3}+2f\frac{d^2 f}{d\eta^2}-\left(\frac{df}{d\eta}\right)^2+\theta=0 \tag{14}$$

$$\frac{1}{Pr}\left[\frac{d}{d\eta}\left\{1+\frac{4}{3}R_d\left(1+(\theta_w-1)\theta\right)^3\right\}\frac{d\theta}{d\eta}\right]+2f\frac{d\theta}{d\eta}=0 \tag{15}$$

Subject to the boundary conditions

$$\begin{aligned}&f=f'=0,\ \theta=1 \text{ at } \eta=0\\&f'\to 0,\ \theta\to 0 \text{ as } \eta\to\infty\end{aligned} \tag{16}$$

In practical applications, the physical quantities of principle interest are the wall shearing stress τ_w and the rate of heat transfer, which lead to compute the coefficient of skin-friction C_f and the Nusselt number *Nu* respectively. These can be written in non-dimensional form as

$$C_f=\frac{Gr^{-3/4}a^2}{\mu_\infty \nu_\infty}(\tau_w) \text{ and } Nu=\frac{aGr^{-1/4}}{k\left(T_w-T_\infty\right)}(q_c+q_r) \tag{17}$$

$$\text{where } \tau_w=\mu\left(\frac{\partial \hat{u}}{\partial \hat{y}}\right)_{\hat{y}=0},\quad q_c=-k\left(\frac{\partial T}{\partial \hat{y}}\right)_{\hat{y}=0} \text{ and } q_r=-\frac{4\sigma}{3\left(a_r+\sigma_s\right)}\left(\frac{\partial T^4}{\partial \hat{y}}\right)_{\hat{y}=0} \tag{18}$$

where q_c is conductive heat flux and q_r is the radiative heat flux. Using the variables from equations (5), (10), (11) and the boundary conditions (16) into equations (17) and (18), we have

$$C_f=\xi\left(\frac{\partial^2 f}{\partial \eta^2}\right)_{\eta=0} \text{ and } Nu=-\left(1+\frac{4}{3}R_d\theta_w^3\right)\left(\frac{\partial \theta}{\partial \eta}\right)_{\eta=0} \tag{19}$$

3. RESULTS AND DISCUSSION

Effects of viscous dissipation on laminar free convective flow along an isothermal sphere in presence of radiation heat loss have been investigated. Results are obtained in terms of the local skin friction, the rate of heat transfer, velocity and temperature profiles and presented graphically as well as in tabular form. Fig.2 (a)-2(b) show the effects of viscous dissipation on velocity and temperature. From Fig.2 (a), it can be observed that the velocity goes significantly upward with the increase of the viscous dissipation parameter *Vd* , which indicates that viscous dissipation enhances the fluid motion. In Fig.2 (b), it is shown that the temperature profile *θ(ξ ,η)* is influenced by the increasing values of *Vd* at small values of *η*. The effects of varying Prandtl number (*Pr* = 0.72, 1.0, 2.0, 5.0, 7.0), on the dimensionless velocity, $f'(\xi,\eta)$ and the dimensionless temperature, $\theta\ (\xi,\eta)$ distributions against η for the viscous dissipation parameter Vd =1.0 and radiation parameter R_d =1.0 are shown in Fig. 3(a)-3(b). From these figures, it is observed that both the velocity and temperature profiles decreases with the increasing values of *Pr* . The free laminar boundary shows a sharp decrease for *Pr* = 7.0 compared to the effects for *Pr* = 1.0 and *Pr* = 0.72. It is seen from Fig.4 (a) that increase in the radiation parameter is associate with a considerable increase in velocity. Near the surface of the sphere (small η) the velocity increases, becomes maximum, then decreases and finally (large η) approaches to zero. Fig.4(b) shows the distribution of the temperature profile $\theta(\xi\ ,\eta)$ against η for the same values of radiation parameter R_d and each of which reaches the maximum at the surface. In Figs. 5-7 numerical values of local skin-friction coefficient and the local heat transfer coefficient obtained by finite difference method has been presented for different values of viscous dissipation parameter *Vd*, Prandtl number *Pr* and radiation parameter R_d. Numerical values of the skin -friction coefficient and heat transfer coefficient are depicted graphically in Fig.5 (a)-5(b) respectively against ξ for different values of viscous dissipation parameter (Vd = 0.1, 0.5, 1.0, 2.0, 4.0) for the fluid having Prandtl number Pr = 0.72 and radiation parameter Rd = 1.0. It is seen from Fig.5 (a) that the skin friction C_f increases as the viscous dissipation parameter, Vd increases. It is also observed in Fig.5 (b) that the opposite result holds for heat transfer coefficient. The effect of varying Prandtl number (*Pr* = 0.72, 1.0, 2.0, 5.0, 7.0) on the skin friction and the heat transfer coefficient with *Vd* =1.0 and R_d = 1.0 are displayed in Fig 6(a)-6(b). It is found that values of skin friction coefficient, C_f decreases and the Nusselt number, *Nu* increases for increasing values of Prandtl number *Pr*. According to definition of *Pr*, for increasing values of *Pr* the thermal conductivity of the fluid decreases and the viscosity of the fluid increases.

Then in any one point on the surface, the shearing stress that means the skin-friction coefficient is larger and the heat is not able to conduct easily into the fluid as *Pr* increases and therefore the thermal boundary layer becomes thinner, hence the corresponding temperature gradients are larger and the surface rate of heat transfer increases. In Fig. 7(a), (b), it is depicted that both the skin-friction and heat transfers coefficient are increasing with the increasing values of radiation parameter (R_d = 0.0, 0.5, 1.0, 1.5, 2.0) with other controlling parameters *Vd* = 1.0, *Pr* = 0.72.

4. CONCLUSIONS

The present paper deals with the effects of viscous dissipation on laminar free convection boundary layer flow along an isothermal sphere with radiation heat loss. Numerical solutions of the equations governing the flow have been obtained by using the implicit finite difference method known as Keller-box technique. From the present investigation, the following conclusions may be drawn:

- For higher values of viscous dissipation both the fluid velocity and the temperature increase.
- The skin–friction increases and the rate of heat transfer decreases with the increasing viscous dissipation.
- The fluid velocity and the temperature profiles increase with increasing values of radiation parameter Rd ; which also leads to increase both the skin –friction and the rate of heat transfer.
- An increase in the value of Prandtl number, Pr leads to decrease in the values of skin –friction and to increase the rate of heat transfer.
- The velocity and temperature profiles both decrease with increasing values of the Prandtl number, Pr.

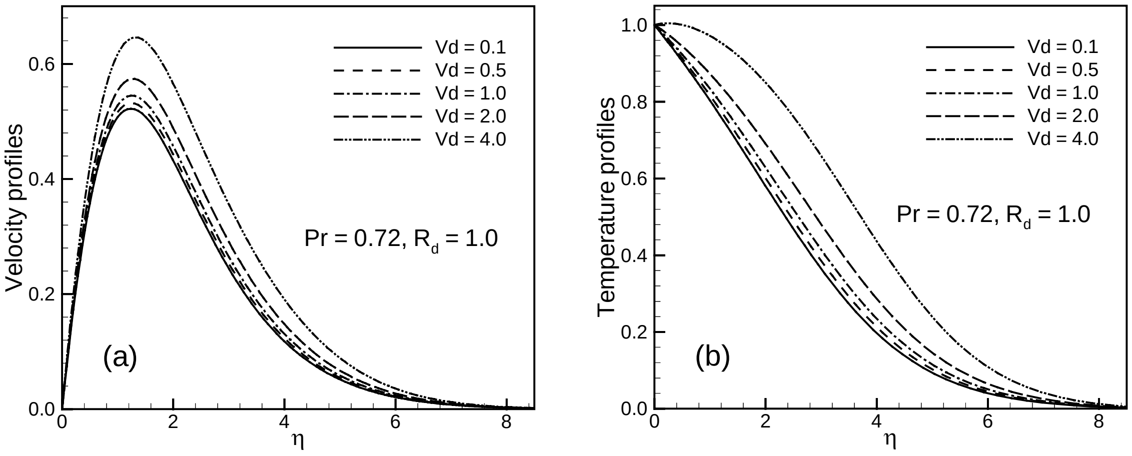

Fig. 2: (a) Velocity and (b) temperature profiles against η for different values of viscous dissipation parameter Vd with $R_d = 1.0$, $Pr = 0.72$.

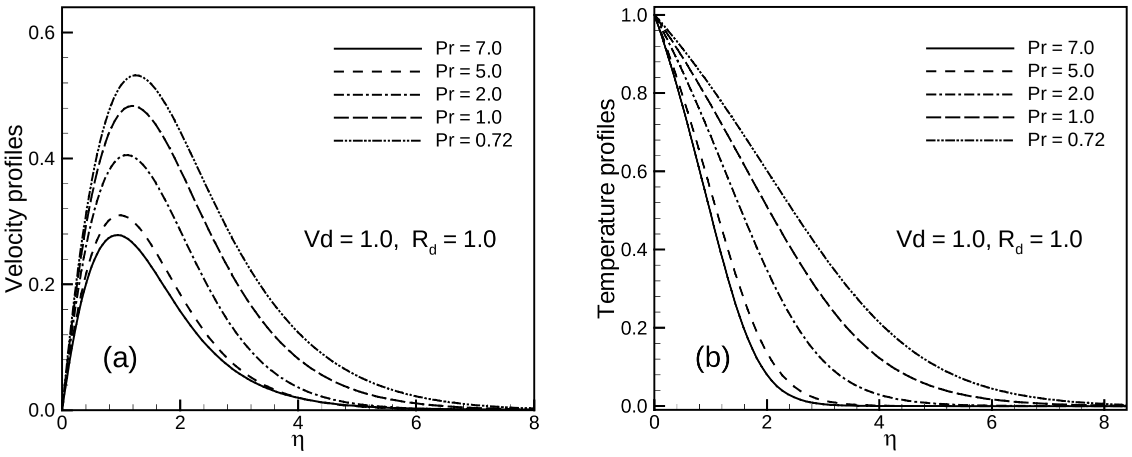

Fig. 3: (a) Velocity and (b) temperature profiles against η for different values of Prandtl number Pr with $Vd = 1.0$, $R_d = 1.0$.

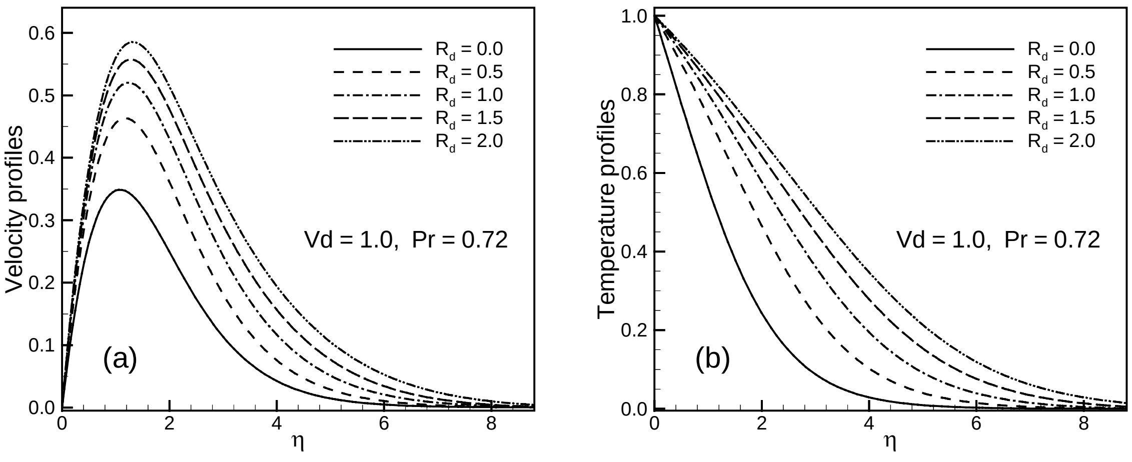

Fig. 4: (a) Velocity and (b) temperature profiles against η for different values of radiation parameter with $Vd = 1.0$, $Pr = 0.72$.

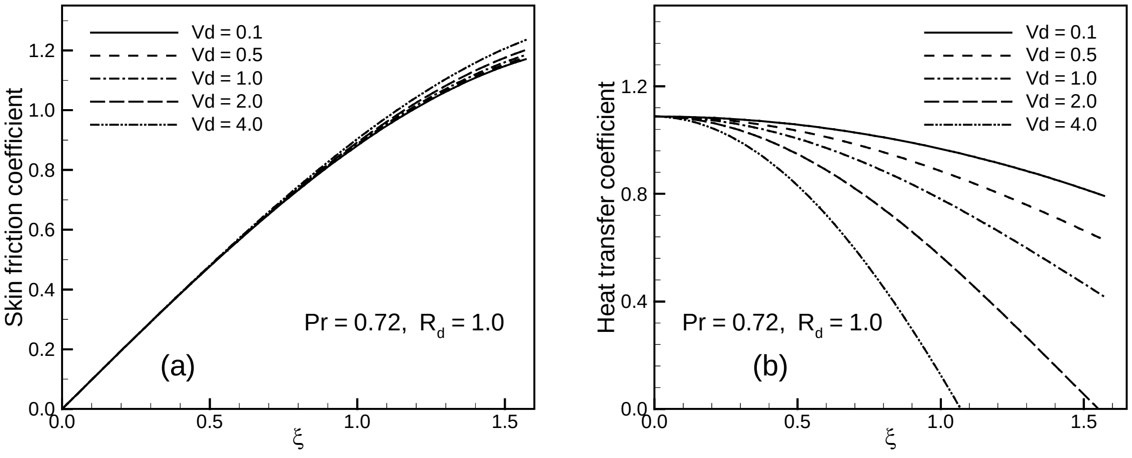

Fig.5: (a) Skin friction and (b) heat transfer coefficients against ξ for different values of viscous dissipation parameter Vd with $Pr = 0.72$, $R_d = 1.0$.

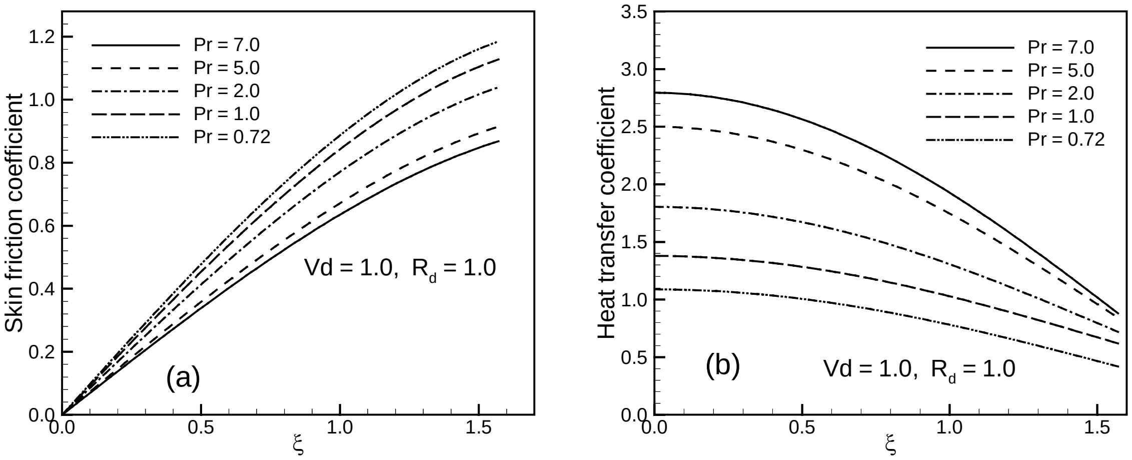

Fig. 6: (a) Skin friction and (b) heat transfer coefficients against ξ for different values of for different values of Prandtl number Pr with $Vd = 1.0$, $R_d = 1.0$.

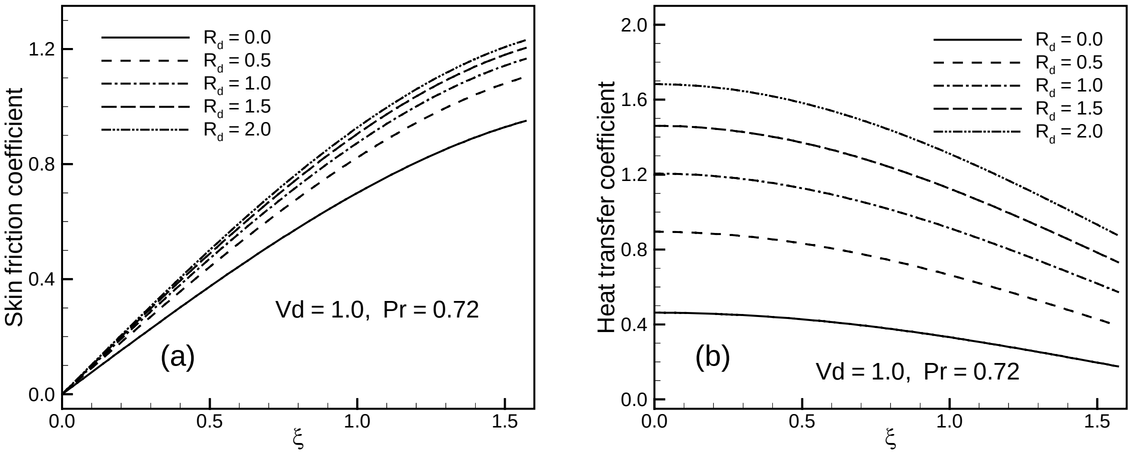

Fig. 7: (a) Skin friction and (b) heat transfer coefficients against ξ for different values of radiation parameter R_d with $Vd = 1.0$, $Pr = 0.72$.

NOMENCLATURE

a	radius of the sphere [m]	T_w	temperature at the surface [K
a_r	Rosseland mean absorption co-efficient [cm^3/s]	$u\ ,v$	dimensionless velocity components along and normal to the surface
C_f	skin-friction coefficient	$\hat{u}$,	velocity components along and normal to the surface [ms^{-1}]
C_p	specific heat at constant pressure [kJ kg^{-1} K^{-1}]	Vd	viscous dissipation parameter
f	dimensionless stream function		coordinates along and normal to the surface [m]
Gr	Grashof number	*Greek symbols*	
g	acceleration due to gravity [ms^{-2}]	β	volumetric coefficient of thermal expansion [K^{-1}]
k	thermal conductivity [$wm^{-1}k^{-1}$]	η	dimensionless coordinates normal to the surface
Nu	Nusselt number	θ	dimensionless temperature
Pr	Prandtl number	μ	viscosity of the fluid [m^2/s]
q_c	conduction heat flux [w/m^2]	ξ	dimensionless coordinates along the surface
q_r	radiation heat flux [w/m^2]	ρ	density of the fluid [kgm^{-3}]
R_d	radiation parameter	σ	Stephan-Boltzman constant
r	radial distance from the symmetric axis to surface [m]	σ_s	scattering coefficient [lm]
T	temperature of the fluid in the boundary layer [K]	τ_w	shearing stress at the wall [$dynes/cm^2$]
T_∞	temperature of the ambient fluid [K]	ψ	stream function [m^2s^{-1}]

REFERENCES

[1] Gebhart, B., Effects of viscous dissipation in natural convection, *J. Fluid Mechanics*, 14 (1962), pp. 225-232.

[2] Gebhart, B. and Mollendorf, J., Viscous dissipation in external natural convection flows. *J. Fluid Mech anics*, 38 (1969), pp. 97-107.

[3] Zakerullah, M., Viscous dissipation and pressure work effects in axisymmetric natural convection flows. *J. Bangladesh Math. Soc. (Ganit*), 2 (1972), 1, pp. 43-51.

[4] Alam, Md. M., Alim, M. A. and Chowdhury, Md .M .K., Effect of pressure stress work and viscous dissipation in natural convection flow along a vertical flat plate with heat conduction, *J. Naval Architecture and Marine Engineering*, 3 (2006) 2, pp. 69-76.

[5] Keller, H. B., Numerical methods in boundary layer theory, *Annual Rev. Fluid Mechanics*, (1978), pp. 417–433.

[6] Cebeci, T. and Bradshaw, P., Physical and Computational Aspects of Convective Heat Transfer, Springer, New York, 1984.

Proceedings of the 4th BSME-ASME International Conference on Thermal Engineering
27-29 December, 2008, Dhaka, Bangladesh

COOLING OF DESKTOP PROCESSOR USING PARALLEL MICRO HEAT PIPES

Ahmed Imtiaz Uddin and Chowdhury Md. Feroz

Department of Mechanical Engineering,
Bangladesh University of Engineering and Technology, BUET.
Dhaka-1000, Bangladesh. E-mail: aimtiaz_me@yahoo.com

ABSTRACT

The present experiment investigates the heat transfer performance of copper parallel micro heat pipes (PMHPs) with acetone as working fluid used for the cooling of desktop processor. PMHPs consists of six single tube micro heat pipes (MHPs) connected by a copper block at the evaporator section and fifteen parallel copper sheets used as external fins at the condenser section. The experimental results are compared with heat transfer performance of miniature heat pipes. Use of smaller diameter heat pipes reduces the maximum and steady state temperature of the processor surface significantly. Much better heat transfer performance is found by using micro heat pipes instead of miniature heat pipes or conventional cooling fan system. The lowest maximum and steady state processor surface temperature is found when a cooling fan is used at the top of the condenser section of the PMHPs.

KEYWORDS: *Parallel Micro Heat Pipe (PMHP), desktop computer, heat transfer performance.*

1. INTRODUCTION

The continuous increase of power density and the decrease of available volume make the thermal management of desktop computers challenging. Traditional desktop computer design has relied on natural convection from a heat sink placed directly on the processor. With the increasing power of today's micro processors, a processor cooling fan is used to these local heat sinks. Mechanical components with moving parts are the most unreliable components in desktop computers. The use of heat pipes may eliminate the use of the processor fans and their inherent reliability concerns. A heat pipe heat sink is a passive cooling device that requires no moving parts, and operates silently, more importantly and reliably. Additionally, heat pipe technology is emerging as a cost-effective thermal design solution for the desktop industry. The development of high-end and compact computers has resulted in a considerable rise in the power dissipation tendency of their microprocessors. At present, heat released by the Central Processing Unit (CPU) of a desktop and server computer is 80 to 130 W and of notebook computer is 25 to 50W [1]. In the latter case, the heating area of the chipset has become as small as 1– 4 cm. This problem is further complicated by both the limited available space and the restriction to maintain the chip surface temperature below 100^{o}C [2]. It is expected that conventional cooling fan system will not be able to meet the futuristic thermal needs of the next generation computers. Other technologies like liquid cooling and thermoelectric coolers have good potential but still create major integration, reliability and cost issues. With the development in the two-phase heat transfer systems and porous media technology, heat pipes have come up as a potential candidate to meet these challenging needs. Notebook computers involved the first high volume use of heat pipes when Intel introduced the Pentium ® TCP packages in 1994 [3]. The main reason for the use of heat pipes is the Pentium ® power dissipation level and the limitation and constraints of space and weight in notebooks. Compared to metal plates or heat sinks, heat pipes offer excellent thermal performance with much less weight and can spread the heat away from the CPU to other areas where the heat can be rejected. The performance of natural convection heat sinks is directly dependent on the effective surface area: more effective surface area results in better performance. To enhance the heat transfer, an additional cooling fan is used with the aluminum heat sink. The increase of the microprocessor speed and number of transistors cramped into the processor core silicon die has continuously driven up its power dissipation. Heat sink sizes have been increasing in personal computers, from the 2”× 2” aluminum extrusion heat sinks for i486 to the 3”× 3” heat sinks for Pentium ® and even large heat sinks for the latest Pentium ® II microprocessors. Heat pipes, as higher level thermal solutions are naturally being investigated as the potential thermal solutions for these systems [4]. Another severe problem of today’s processor cooling fan is the generation of noise. Much effort has been made in recent years to minimize noise generated by CPU cooling fans, a fact that has been demonstrated by the popularity of variable and low speed fans coupled with efficient CPU heat sink designs. Even with the adjustable fans generating lower noise at lower speeds, the main noise sources in a computer system are fans and hard drive. Therefore, the best way to eliminate the noise is to remove these sources. As it is impractical to get rid of the hard drives, it seems like a good idea to cool the CPU without a fan. After looking at products based on heat pipe technology, such as Zalman's graphics card coolers, a good idea could be to try passive CPU cooling utilizing heat pipes [5]-[7].

The heat pipe can, even in its simplest form, provide a unique medium for the study of several aspects of fluid dynamics and heat transfer and it is growing in significance as a tool for use by the practicing engineer or physicist in applications ranging from heat recovery to precise control of electronic equipments. Normally for these equipments heat pipes of diameter 3 to 6 mm and length less than 400 mm are preferred [8]. Most preferable length is 150 mm [9]. The heat pipe applications for cooling computer CPU was started in the last decade and now 98% of notebooks CPU are cooled by using heat pipes. The concept of micro heat pipe (MHP) was introduced by Cotter in 1984 [10]. MHP is a very small heat pipe that has a diameter between about 100 micrometers and 2 millimeters (0.004 and 0.08 inch) and a length of several centimeters. Studies on the application of heat pipes having the diameter of 3 or 4 mm for cooling of the notebook computers CPU has been actively conducted by the American and Japanese enterprises specializing in the heat pipe recently [7], [11], [12]. An experimental study is performed by Tanim *et al.* [13] to investigate the performance of cooling desktop processors using miniature heat pipes of 5.78 mm ID and a length of 310 mm with respect to the normal fanned CPU unit. So far no investigation has been conducted for cooling desktop processor with MHPs. Therefore the objective of the present experiment is an investigation to draw the heat from the CPU into one end of parallel micro heat pipes (PMHPs) while making the other end of the PMHPs as extended fins of copper plate to expel the heat into the air. Finally the performance of the PMHPs in cooling desktop processor is investigated with respect to the miniature heat pipe and conventional fan cooling system.

2. EXPERIMENTAL APPARATUS AND TEST PROCEDURE

The experimental setup for this study is mainly consists of four parts – PMHPs, a desktop computer, temperature measuring system and cooling system. Six MHPs are placed parallel to each other for cooling purpose. Every MHP has an inner diameter of 2.8 mm and outer diameter of 3.8 mm having a length of 150 mm. There are three sections in every MHP: evaporator, adiabatic and condenser. Acetone is used as the working fluid in this experiment.

The condenser sections of PMHPs are made of copper sheets of 67mm×50mm (0.5mm thickness) placed parallel as extended fins at a constant interval of 5 mm as shown in Fig. 1. Plates are welded with the PMHPs for better heat transfer. As there is space constrain inside the CPU, the PMHPs are bend at 90° in adiabatic section. The evaporator sections of PMHPs are inserted in to the grooves of copper blocks shown in Fig. 2, which are placed on the top of the processor to remove the generated heat. Two copper blocks of 67mm×50mm×8mm are made very precisely to mate with the MHPs. Grooves are cut inside the blocks. The blocks are precise in dimension and surfaces are highly finished to reduce the contact resistance as well as to increase the heat transfer rate.

Heat is generated in the processor which is conducted through the copper blocks to the evaporator section of PMHPs where working fluid absorbs heat and rejects it in the condenser sections. Before bending, wick of stainless steel of 200 mesh are inserted into the MHPs. After inserting the wick, MHPs are bent to the desired angle. Different sections of PMHPs are shown in Fig. 3. One end of the MHPs is sealed and working fluid with charge ratio of 0.9 is poured into it. Nine calibrated K-type ($\Phi = 0.18$ mm) thermocouples are attached at the wall of each MHP using adhesive to measure the wall temperature: four units at the evaporator section, one unit at the adiabatic section and four units at the condenser section. Locations of thermocouples connected on different points along the length of the MHP are shown in the Fig. 4. The surface temperature of the processor is also measured by four K-type thermocouples. All thermocouples are connected with a digital temperature indicator (YF-160A, type-K thermometer, Made in Taiwan) through selector switches. Experiment is conducted in two arrangements: Firstly the cooling system by using PMHPs, shown in Fig. 5 and secondly with the PMHPs, an additional cooling fan placed at condenser section as shown in Fig. 6 to enhance heat transfer rate. Processor surface temperature and wall temperatures of PMHPs are recorded for 130 minutes at an interval of 10 minutes. Experimental parameters and configurations of the desktop computer that is used in this experiment are given in Tab. 1 and Tab 2, respectively.

Tab. 1: Experimental Parameters and their ranges

Parameters	Condition
Number of the heat Pipes	6
Diameter of the heat pipe(mm)	ID- 2.8; OD- 3.8
Length of the heat pipe(mm)	150
Length of the evaporator section (mm)	50
Length of the adiabatic section (mm)	30
Length of the condenser section (mm)	70
Working fluid	Acetone
Dimension of the copper block(mm)	67×50×8
Dimension of the copper sheet(mm)	67×50×0.5
Charge ratio	0.9
Wick (SS)	200 mesh

Tab. 2: Configuration of the desktop computer

Components	Specification
Processor	Ali M1542A1
Fan	DC 12 V brushless Fan, Model- L80S12H-1; 0.18A
Ram	16 MB
Hard disk	Seagate; Model ST34321A; 10GB
Power box	115/230 VAC,15 A/ 10 A

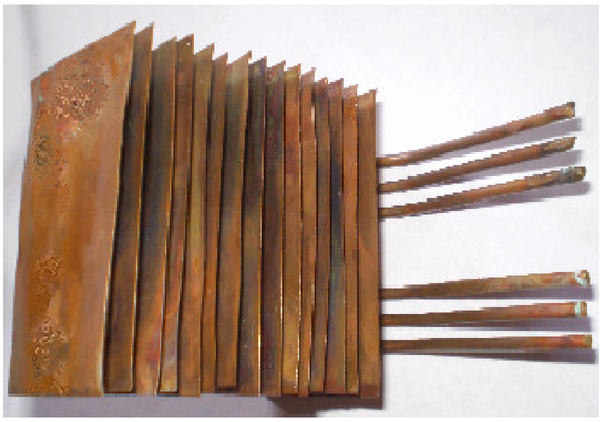

Fig. 1 Extended fins of copper sheet in the condenser section.

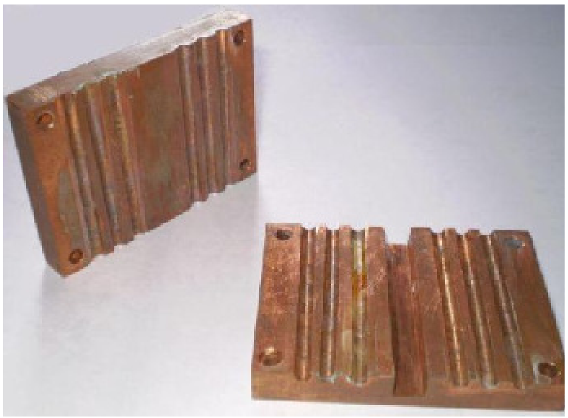

Fig. 2 Grooves cut in the copper blocks for inserting PMHPs in the evaporator section.

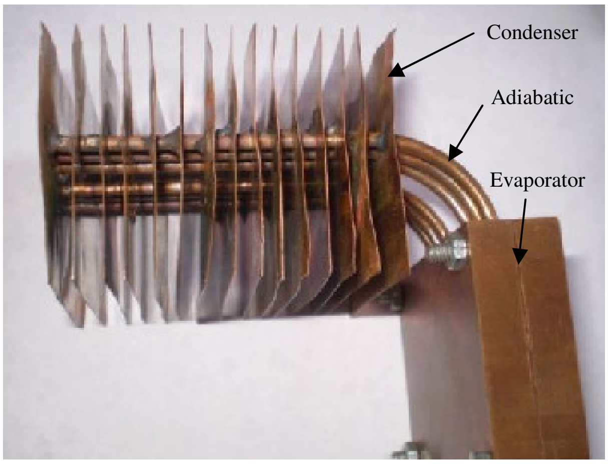

Fig. 3 PMHPs with evaporator, adiabatic and condenser sections for cooling desktop processor.

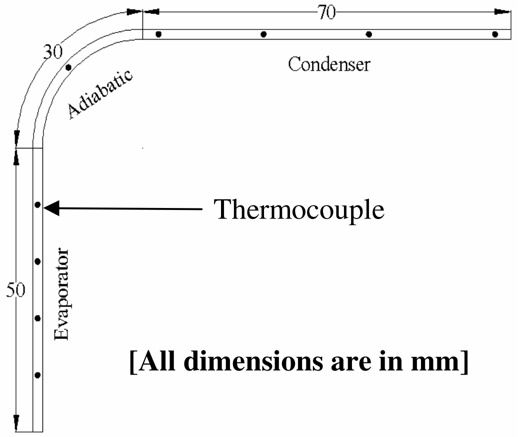

Fig. 4 Locations of thermocouples on the PMHP axial position.

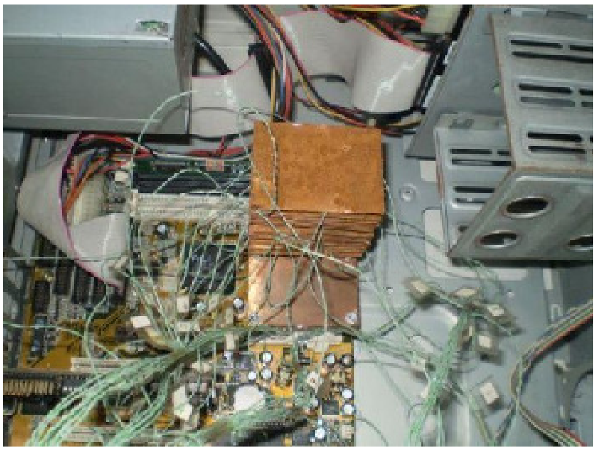

Fig. 5 Experimental setup for cooling desktop processor by using PMHPs.

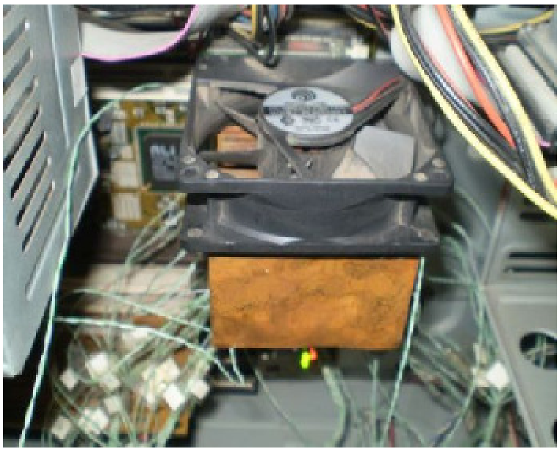

Fig. 6 Experimental setup for cooling desktop by using PMHPs with cooing fan.

3. TEST RESULTS AND DISCUSSIONS

As heat load is applied to the evaporator section, the temperature of the evaporator section rises and results the vaporization of the working fluid. This vaporization of liquid absorbs heat from the evaporator which causes a lower working temperature in the processor surface. Fig. 7 shows the variation of the processor surface temperature with time. Results are compared with miniature heat pipes of 5.78 mm ID [13] and the conventional fan cooling. The figure indicates that the maximum temperature on the processor surface by using conventional cooling fan and aluminum heat sink is found to be 90.7ºC. Replacement of the cooling fan and aluminum heat sink by six PMHPs of 2.8 mm ID reduce the maximum surface temperature to 73.8ºC which shows much lower processor surface temperature than that of 4 miniature heat pipes of 5.78 mm ID with cooling fan at condenser [13]. Addition of a cooling fan in the condenser section with six MHPs gives much better result as it can reduce the processor surface temperature to 70.9ºC.

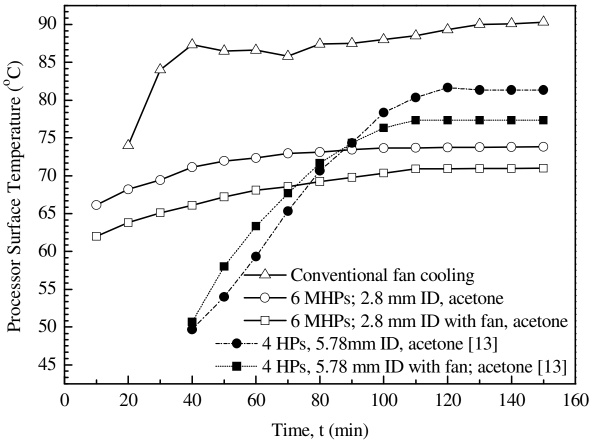

Fig. 7. Variation of processor surface temperature with time.

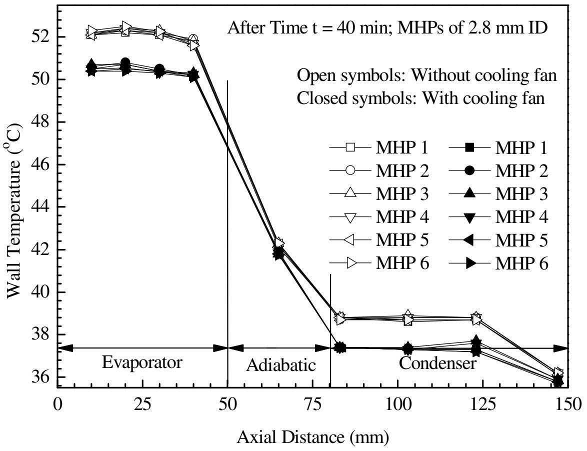

Fig. 8. Temperature profile of the six MHPs along their length after a time t=40 min.

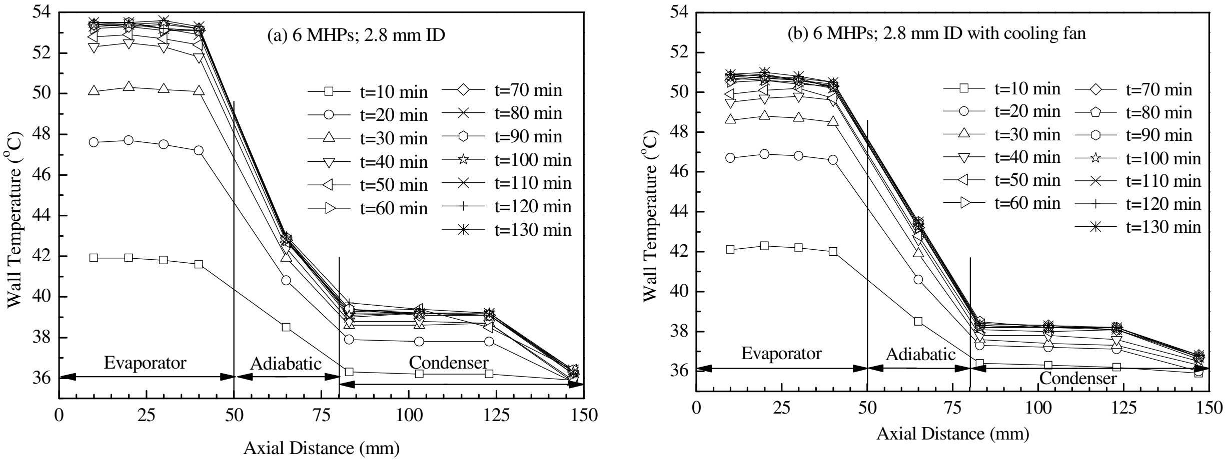

Fig. 9. Temperature profile along the length of the PMHPs used for cooling desktop processor.

Variation of the axial wall temperature along the length of the PMHPs with and without the cooling fan for a transient time t = 40 minutes after the start of CPU is shown in Fig. 8. Uniformity of temperature in the evaporator and condenser sections indicates the reliability of using MHPs for the cooling of desktop processors.

Fig. 9 shows the axial wall temperature distribution along the length of the PMHPs for the time duration of 130 minutes. Maximum wall temperature in the evaporator section is found to be 53.5ºC shown in Fig. 9 (a). The maximum wall temperature in the evaporator section is 50.9ºC, when a cooling fan is used with the PMHPs, shown in Fig. 9 (b). Using PMHPs, the steady state temperature is attained approximately after 60 minutes of the start of the CPU which can be reduced to approximately 50 minutes by using a cooling fan with PMHPs. Result shows that natural convection cooling by using only extended fins in the condenser of PMHPs is not efficient enough to cool the high performance desktop processors.

4. CONCLUSION

The following conclusions can be drawn form the experimental study of the performance test of PMHPs of 2.8 mm ID in the cooling of desktop computer processors:

- Lowest processor surface temperature is found for the use of six PMHPs with a cooling fan in the condenser section.
- The lowest maximum evaporator temperature of the PMHPs is attained by using the cooling fan compared to the use of only PMHPs or miniature heat pipes. The steady state temperature also obtained quickly.
- Uniform temperature distribution in the evaporator and condenser section of PMHPs indicates the reliable of using PMHPs in the cooling of desktop processor.

REFERENCES

[1] Mochizuki M., Saito Y., Nguyen T., Wuttijumnong V., Wu X., and Nguyen T.: Revolution in Fan Heat Sink Cooling Technology to Extend And Maximize Air Cooling For High Performance Processors in Laptop/ Desktop/Server Application, Proceedings, IPACK'05, San Francisco, CA, Jul. 17–22, 2005,CD-ROM.

[2] Saucius I., Prasher R., Chang J., Erturk H., Chrysler G., Chiu C., and Mahajan R.: Thermal Performance and Key Challenges For Future CPU Cooling Technologies, Proceedings, IPACK'05, San Francisco, CA,2005.

[3] Xie H., Aghazadeh M., Lui W. and Haley K.: Thermal Solutions to Pentium Processors in TCP in Notebooks and Sub-notebooks, IEEE Transactions on components, Packaging and Manufacturing Technology, Part A, 19 (1996), 1, pp54-65.

[4] Xie H., Ali A., Bathia R.: The Use of Heat Pipes in Personal Computers, IEEE Inter Society Conference on Thermal Phenomena 1998; pp 442-448.

[5] Babin, B.R. Peterson, G. P., Wu, D.: Steady State Modeling and Testing of a Micro Heat Pipe, ASME J. of Heat Transfer, 112 (1990), 3, pp. 595-601.

[6] Zhou. J., Yao, Z., and Zhu, J.: Experimental Investigation of the Application Characters of Micro Heat Pipe, Proceedings, 8th Int. Heat Pipe Conf., Beijing, China, 1992.

[7] Eguchi, K., Mochizuki, M., Mashiko, K., Goto, K., Saito, Y., Takamiya , A.,Nguyen, T.: Cooling of CPU Using Micro Heat Pipe, Fujikura Co.,Technical Note, 9 (1997), pp. 64~68.

[8] Yoshiaki S., M. Takase, M. Tanabe, Teruo N., I. Kinoshita, Tadashi I., K. Namba and Masahiro S.: A Junction Block Incorporating a Micro Heat-Pipe, Furukawa Review, 18 (1999).

[9] Kim K. S., Moon S. H. and Choi C. Gi.: Cooling Characteristics of Miniature Heat Pipes with Woven Wired Wick, Proceedings, 11th international Heat Pipe Conference, Tokyo 1999, pp 239 – 244.

[10] Cotter T. P.: Principles and prospects for micro heat pipes, Proceedings, 5th International Heat Pipe Conference, Tsukubs, Japan, 1984, pp. 328~335.

[11] Xie , H., Aghazadeh , M., Togh, J.: The Use of Heat Pipes in the Cooling of Portables with High Power Packages, Thermacore Co., Technical Note.

[12] Mochizuki, M., Mashiko , K., Nguyen, T., Saito, Y., Goto, K.: Cooling CPU Using Hinge Heat Pipe, Proceedings, Heat Pipe Technology , Pergamon , 1997,pp. 218~229.

[13] Tanim T. R., Hussain T. and Feroz C. M.: Cooling of Desktop Computer Using Heat Pipes, International Conference on Mechanical Engineering, Dhaka, 29-31 December, 2007; ICME07-TH-01.

ACKNOWLEDGEMENT

This work was supported by Bangladesh University of Engineering and Technology (BUET), Dhaka, Bangladesh. The authors are also grateful to the Department of Mechanical Engineering and Directorate of Advisory Extension and Research Services (DAERS), BUET, Dhaka for providing the facilities to carryout the experiment.

Proceedings of the 4th BSME-ASME International Conference on Thermal Engineering
27-29 December, 2008, Dhaka, Bangladesh

PERFORMANCE CHARACTERISTICS OF A MINIATURE LOOPED PARALLEL HEAT PIPE

C. M. Feroz, Md. Emdadul Hoque, Md. Nahid Andalib

Department of Mechanical Engineering, BUET, Bangladesh, cmferoz@me.buet,ac.bd

ABSTRACT

Thermal designers have widely accepted the MLPHP for their thermal design solution and the utilization as well as area of application of MLPHP has been increased day by day. But MLPHP is relatively a new technology; its data and information are quite scarce. So a thorough comprehension of the heat transfers capability of MLPHP with improved wick structure and factors of influence are indispensable for further development and improvement of its performance. The present study has described test of the heat transfer characteristics of MLPHP of 5.78 mm ID and of 150 mm length at varying coolant flow rate in the condenser and heat flux would be the parameters of prime concern. A miniature looped parallel heat pipe [MLPHP] which consists of two single tube heat pipes connected by two U- tubes of same diameter at the top and bottom ends. For this purpose, the copper tube is used with acetone as the working fluid. Analysis of the experimental data gives that the axial wall temperature of both condenser and evaporator sections increase with increase in heat flux and decrease with the increase in coolant flow rate. The thermal resistance of MLPHP decreases with the increase of both coolant flow rate and thermal load. Overall heat transfer coefficient increases with the increase of both coolant flow rate and heat flux.

KEY WORDS: *Heat pipe, Coolant flow rate, Overall heat transfer coefficient, Thermal Resistance.*

1. INTRODUCTION

The enormous growth of the electronics industry is due mainly to the continued evolution of the microprocessor in personal computers (PC). These microprocessors are now being moved out of the PC and embedded into telecom/data-com equipment, automobiles, medical equipment, and test equipment and consumer electronics. On electronics equipment, market's demand for increasingly powerful product, in smaller and smaller packaging, creates a cooling problem. The integrated circuit (IC) lifetime is dependent upon its operating temperature creating a trade off situation, either to enlarge the package to accept additional cooling or to sacrifice IC lifetime. This is a great challenge in thermal design management. The solution is miniaturization of cooling technique. Among other cooling techniques heat pipes emerged as the most appropriate technology and cost effective thermal design solution due to its excellent heat transfer capability, high efficiency and structural simplicity. Due to space constraint in most of personal computers and telecommunications systems placed constraint on the size of heat pipes, normally miniature looped parallel heat pipes (MLPHPs) of diameter 3 to 6 millimeter and length less than 400 millimeter are preferred[1]. MLPHP has unique physical phenomenon contrary to micro heat pipes (MHPs) and general medium sized heat pipes in view of affects of the operating limit, liquid blocking, and length. That is, while the liquid blocking phenomenon occurs in the MHP of less than 1 mm, the condenser liquids are accumulated at the end of the condenser and heat is not delivered completely. The phenomenon of reducing the vapor temperature and thus reducing the maximum rate of heat transfer occurs in MHP if the condenser is cooled excessively. And there appear significant effects caused by the entire length of a heat pipe, and the effect by the capillary limit among operating limits of a heat pipe is mainly significant[2][3][4]. Studies on the application of miniature heat pipes having the diameter of 3 or 4 mm for cooling of the notebook PC have been actively conducted by the American and Japanese enterprises specializing in heat pipes recently[5][6][7]. Experimental investigations on MHPs[8][9] reported that all structures of wicks have little influence on the heat transfer capability of miniature heat pipe with the aid of gravity. Under condition of antigravity, the structure of wicks has obvious influence on the heat transfer capability of miniature heat pipes. The idea of looped parallel heat pipe[10][11] is developed to minimize several insufficient performances of single tube heat pipe such as low maximum heat transfer rate and non-uniform wall temperature in an evaporator section. Thermal designers have widely accepted MLPHP for their thermal design solution and the area of application is increases day by day. Chowdhury *et al.*[12] experimentally investigated the heat transfer characteristics of a MLPHP and reported that the thermal resistance of MLPHP decreases with the increase of coolant flow rate and thermal load. MLPHP is relatively a new technology; relevant data, information is quite scarce. So, a thorough investigation of heat transfer capability of MLPHP is indispensable for further development and improvement of performance. Therefore, the objective of this present study is to investigate the heat transfer characteristics of a MLPHP.

2. EXPERIMENTAL APPARATUS AND TEST PROCEDURE

The test loop consists of a pair of evaporator, adiabatic, condenser and U-tube sections. Detailed dimensions of the MLPHP are shown in the Figure1. Two evaporator and two condenser sections are located at bottom and top of the loop, respectively. All sections are made of 5.78 mm ID copper tube and stainless steel wicks are inserted into the tube. The length of the evaporator, adiabatic, and condenser sections are 50 mm, 30 mm, and 70 mm, respectively. The both tubes are connected by U-tubes with the same inside diameter at top and the bottom. The U-tube is a half of a circular ring with 31.72 mm inner radius and the total length of the loop is 120mm. The Ni-Cr thermic wires are wound around the wall of the evaporators at a constant interval of The Ni-Cr thermic wires are wound around the wall of the evaporators at a constant interval of 1.5 mm. The heat added to the two evaporator sections of MLPHP is processed in the electrical method by using the two separate DC power supply. The evaporator sections are covered with glass fiber to minimize heat loss. The adiabatic and the condenser sections are also covered with the insulator. The condenser sections are cooled by a constant temperature water coolant circulating in an annular space between the copper tube and jacket. The water coolant is supplied from an elevated water tank and the flow is controlled by the flow meters. Nine calibrated T-type thermocouples are attached at each side of the wall of the MLPHP to measure the wall temperature. Five units in each evaporator section, two units at each adiabatic section, and two units are at each condenser section. The inlet and outlet coolant temperatures are also measured. The thermocouples are attached at the wall surface using adhesive. Temperatures are measured by the digital thermometers. The input power to the heater in each evaporator section is increased stepwise. The measurements are made under a steady state condition at each input power. Acetone is used as the working fluid. The experiment is carried out only at vertical orientation since it is reported by [4] that the heat transfer characteristic of MHP is almost independent on the inclination angle. The experimental parameters and their ranges are indicated in Table1.

In the present study, the performance of MLPHP is evaluated by measuring the thermal resistance, *R*, which is defined in Equation (1)

$$R = \frac{T_e - T_c}{Q} \tag{1}$$

The overall heat transfer coefficient, U_t is obtained from Equation (2) as follows

$$U_t = \frac{Q}{A_e(T_e - T_c)} \tag{2}$$

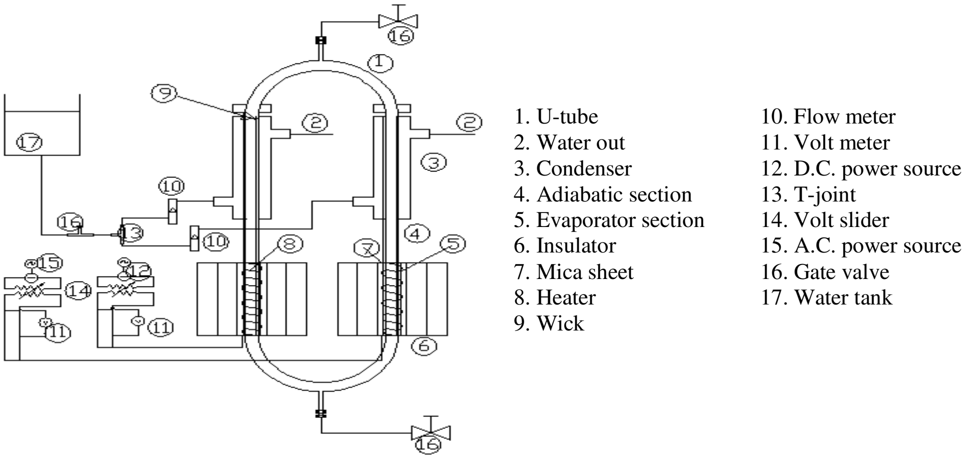

Fig. 1 Experimental set-up of MLPHP

3. RESULTS AND DISCUSSION

3.1 Wall temperature profile along the length of the MLPHP

Figure 2 shows the wall temperature profiles along the axial length on both sides from the bottom of MLPHP at various heat fluxes. It is found that wall temperatures of both the condensers and evaporators sections increase with the increase of heat flux. But the rate of increase for condenser sections is not significant. Figures indicate almost identical temperature profiles on both sides of MPHP at all heat fluxes within our experimental range. At zero coolant flow rate wall temperature in the condenser sections is found very irregular as shown in Fig. 3. This irregularity decreases with the increase of coolant flow rate. The evaporator wall temperature also decreases with the increase in coolant flow rate.

3.2 Effect of coolant flow rates on overall heat transfer coefficient

Figures 4(a) and (b) depict the overall heat transfer coefficient variation with coolant flow rate. Figures indicate that the overall heat transfer rate increases with the increase of coolant flow rate up to 0.3 l/min. But beyond this value overall heat transfer coefficient is almost independent of coolant flow rate at all heat flux conditions. This result is consistent with the findings of Chowdhury, *et al.* [12].

3.3 Effect of coolant flow rate on thermal resistance

Figures 5(a) and 5 (b) show the change in thermal resistance according to the coolant flow rate in the condenser within the stable operational zone where no dry out occurs. It is shown that the thermal resistance is maximum when cooling water flow rate is zero. At a particular heat flux, with the increase of coolant flow rate the thermal resistance remains fairly constant beyond a coolant flow rate of 0.3 l/min.

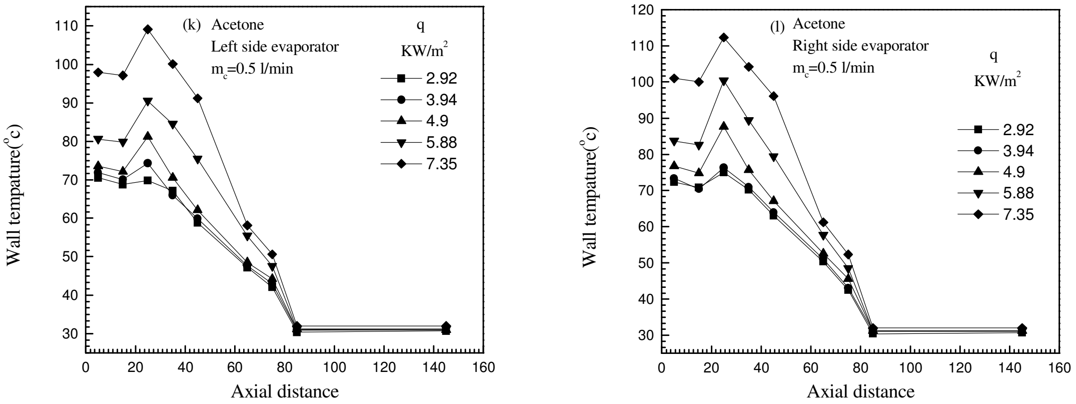

Figure 2. Axial wall temperature distribution along the MLPHP for various power input

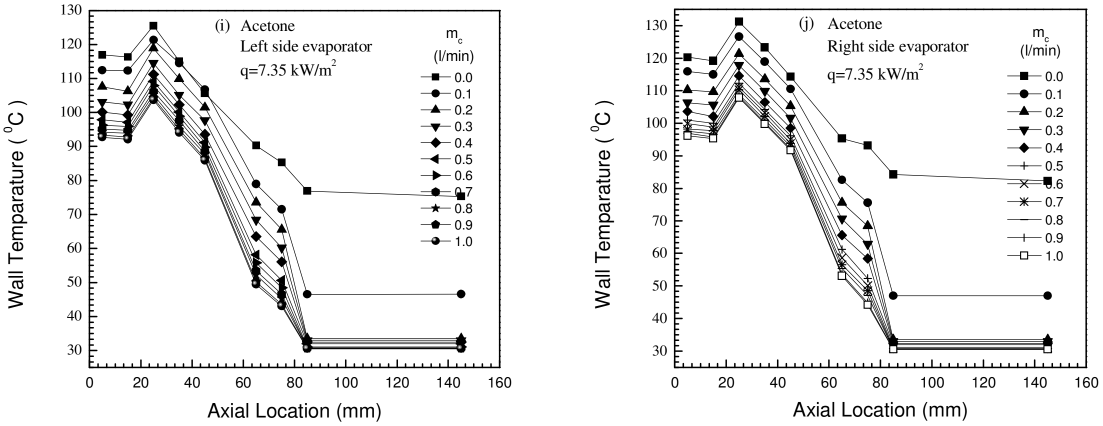

Figure 3. Axial wall temperature distribution along the MLPHP for various coolant flow rate

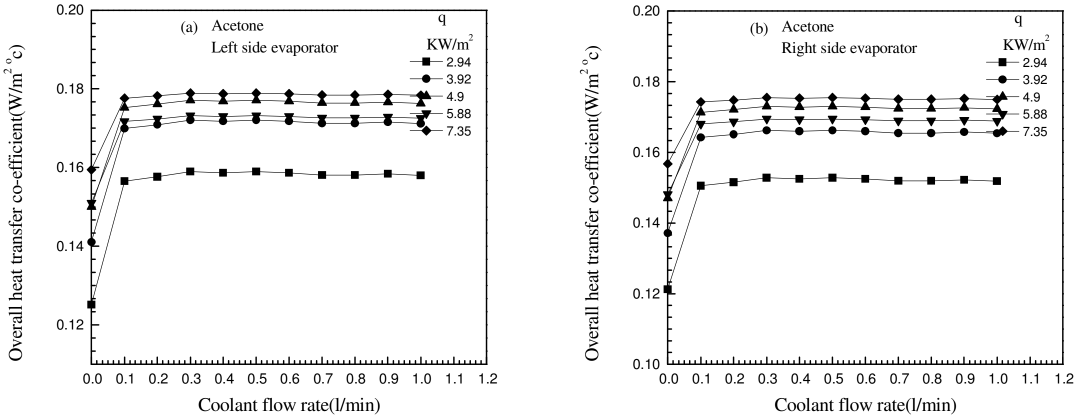

Figure 4. Effect of coolant flow rate on overall heat transfer co-efficient

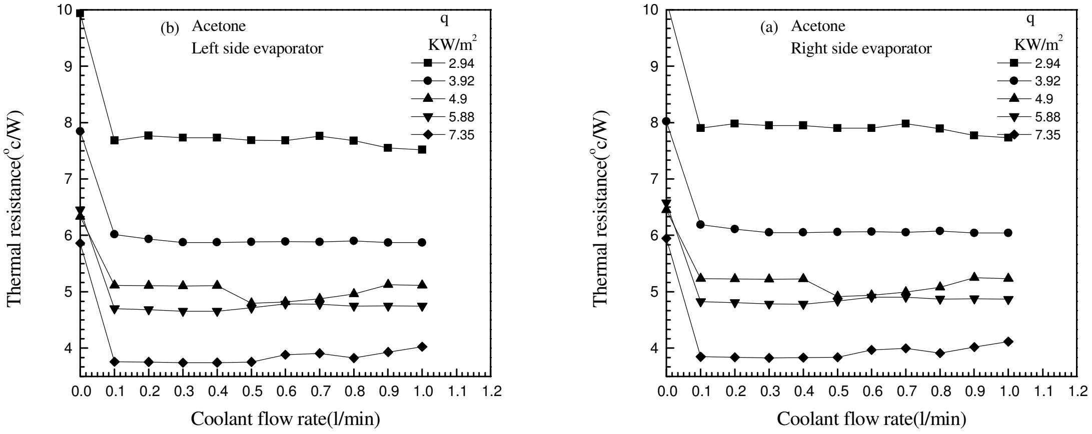

Figure 5. Effect of coolant flow rate on thermal resistance

4. CONCLUSIONS

The results of the performance test for the MLPHP having 5.78 mm ID and length of 150 mm give the following conclusions:

[1] The axial wall temperature distribution of both condenser and evaporator decreases with the increase in coolant flow rate. There is no significant variation in wall temperature between left and right sides of MLPHP.

[2] Overall heat transfer coefficient of the MLPHP increases with the increase of both heat flux and coolant flow rate**.** But beyond a coolant flow rate of 0.3 l/min overall heat transfer coefficient is independent of coolant flow rate at all heat flux conditions.

[3] Thermal resistance of MLPHP decreases with the increase of coolant flow rate but there is no significant change after a flow rate of 0.3 l/min. Thermal resistance of the MLPHP also decreases with the increase in thermal load.

5. NOMENCLATURE

A_e	surface area of evaporator (m^{2})	R	thermal resistance (^{o}C W^{-1})
m_c	coolant flow rate (l min^{-1})	T_c	coolant temperature (^{o}C)
Q	input power (W)	T_e	average evaporator wall temperature(^{o}C)
q	heat flux(W m^{-2})	U_t	overall heat transfer coefficient(Wm^{-2} ^{o}C)

6. REFERENCES

[1] Kim, K. S., Moon, S. H., Choi, C. G., "*Cooling Characteristics of Miniature Heat Pipes with Woven Wired Wick,"* Proc. of the 11th international Heat Pipe Conference, Tokyo, Japan (1999), pp 239 -244.

[2] Babin, B.R. Peterson, G. P., Wu, D., "*Steady State Modeling and Testing of a Micro Heat Pipe.*" ASME J. of Heat Transfer, Vol. 112, No. 3(1990), pp. 595-601.

[3] Zhou. J., Yao, Z., and Zhu, J., "*Experimental Investigation of the Application Characters of Micro Heat Pipe,*"Proc. of the 8th Intl. Heat Pipe Conf., Beijing, China, 1992.

[4]Kim, C. J., Moon, S. H., Kim, J. O., "*Fundamental Study on Performance Characteristics of a Micro Heat Pipe with Triangular Cross Section ,"* Korean J. of Air-Conditioning and Refrigeration Engineering , Vol. 11, No. 2(1999), pp. 176-184.

[5]Eguchi, K., Mochizuki, M., Mashiko, K., Goto, K., Saito, Y., Takamiya , A.,Nguyen, T., *"Cooling of CPU using Micro Heat Pipe,"* Fujikura Co., Technical Note, Vol. 9(1997), pp. 64~68.

[6] Xie , H., Aghazadeh , M., Togh, J., "*The Use of Heat Pipes in the Cooling of Portables with High Power Packages,"* Thermacore Co., Technical Note.

[7]Mochizuki, M., Mashiko , K., Nguyen, T., Saito, Y., Goto, K., *"Cooling CPU Using Hinge Heat Pipe,"* Heat Pipe Technology , Pergamon,(1997), pp. 218~229.

[8]Lanchao Lin et. al *"High Performance Miniature Heat Pipes,"* Thermal Management Research Studies. Volume 1.Page-86.

[9] Zhuang, J., Zhang, H., Liu, J., *"Comparison of Heat Transfer Performance of Miniature Heat Pipes,"* proceedings of the 11th International Heat Pipe Conference- Tokyo(1999), pp.226~229.

[10]Chowdhury, F., Kaminaga, F., Tokuhara, A., Matsumura, K.. "*Study on Heat Transfer Characteristics of Looped Parallel Thermosyphon,"* Proc. of the 4th European thermal science Conf., S10-HPI-2004.

[11] Kaminaga, F., Chowdhury, F., Watanabe, H., Kunihito, M.,"*HeatTtransfer Characteristics in an Evaporator Section of a Looped Parallel Thermosyphon,"* Proc. of the 7th International Heat Pipe Symposium(2003), pp 225-230.

[12]Chowdhury, F., Hoque, M E., Andalib, M N., "*Heat Transfer Characteristics of a Miniature Looped Parallel Heat Pipe,"* Proc. of the 12th Asian Congress of Fluid Mechanics, Daejeon, Korea(2008), M-3C-4, pp 1-4.

Proceedings of the 4th BSME-ASME International Conference on Thermal Engineering
27-29 December, 2008, Dhaka, Bangladesh

EFFECT OF A CENTERED HEAT CONDUCTING SQUARE BODY SIZE ON MIXED CONVECTION IN A VENTED CAVITY

Md. Mustafizur Rahman[1], M. A. Alim[1], Sumon Saha[2], M. K. Chowdhury[1]

[1]Department of Mathematics,
Bangladesh University of Engineering and Technology, Dhaka-1000, Bangladesh
[2]Department of Energy and Environmental Engineering, Interdisciplinary Graduate School of Engineering Sciences, Kyushu University, 6-1 Kasuga-koen, Kasuga-shi, Fukuoka 816-8580, Japan
E-mail: mmustafizurrahman@math.buet.ac.bd

ABSTRACT

This work is focused on the numerical study of steady, laminar mixed convection flow in a vented square cavity filled with a heat conducting square solid body. The solid body is shaped into geometry, namely square rod, which is horizontally placed at the center inside the cavity. The governing mass, momentum and energy equations are solved by employing a finite element scheme based on the Galerkin method of weighted residuals. Fluid flow and heat transfer characteristics in the air filled cavity are examined for a wide range of Richardson number (Ri) and various the body size ratios (D). The results indicate that the average Nusselt number at the heated surface, average temperature of the fluid inside the cavity and the temperature at the body center are dependent on Richardson number as well as the size of the body. Extensive results of the interaction between the forced cold air-stream and the buoyancy-driven flow induced by the heat source are demonstrated by the distributions of streamline and isotherm.

Key words: *Finite element method, Square rod, Vented cavity, Mixed convection.*

1. INTRODUCTION

Efficient convection heat transfers are essential in modern technology and also very important in many industrial areas. Hence, it is necessary to study and simulate these phenomena. Several numerical and experimental methods have been developed to investigate cavities with and without obstacle because these geometries have great practical engineering applications, for example cooling of electronic devices, furnaces, lubrication technologies, chemical processing equipment, drying technologies etc. House *et al.* [1] studied the effect of a centered, square, heat conducting body on natural convection in a vertical enclosure. The same geometry was considered by the numerical study of Oh *et al.* [2], where the conducting body generated heat within the cavity. Later on Roychowdhury *et al.* [3] analyzed the natural convective flow and heat transfer features for a heated body placed in a square enclosure with different thermal boundary conditions. However, Dong and Li [4] studied conjugate effect of natural convection and conduction in a complicated enclosure. Moreover, Bilgen and Yamane [5] examined numerically the effect of conjugate heat transfer by laminar natural convection and conduction in two-dimensional rectangular enclosures with openings. Bhoite *et al.* [6] studied numerically the problem of mixed convection flow and heat transfer in a shallow enclosure with a series of block-like heat generating components for a range of Reynolds numbers and Grashof numbers and block-to-fluid thermal conductivity ratios. Also Braga and de Lemos [7] investigated laminar natural convection within a square cavity filled with a fixed volume of conducting solid material consisting of either circular or square obstacles. The problem of laminar natural convection heat transfer in a square cavity with an adiabatic arc shaped baffle was numerically analyzed by Tasnim and Collins [8]. Recently, conjugate natural convection heat transfer inside an inclined square cavity with an internal conducting block was carried out by Das and Reddy [9]. At the same time, Xu *et al.* [10] experimentally investigated the thermal flow around a square obstruction on a vertical wall in a differentially heated cavity.

In the light of the above literature review, it has been pointed out that there is no significant information about mixed convection processes when a heat conducting square rod exists within a vented cavity having different size. The purpose of the present study is to examine how the sizes of the inner heat conducting body affect the mixed convection phenomena within the vented cavity.

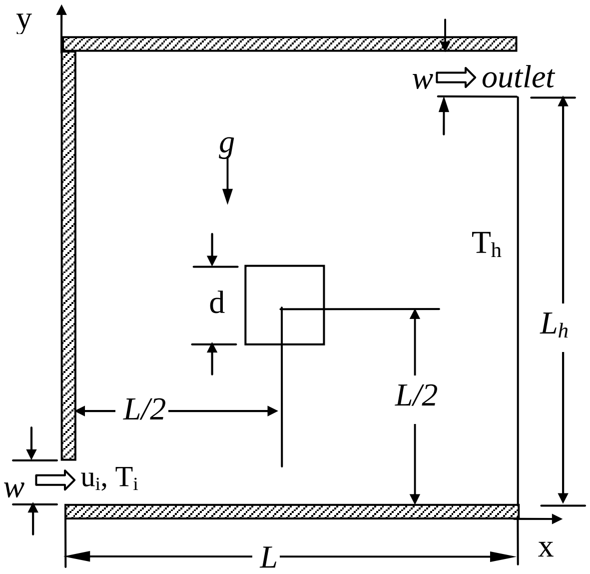

Fig. 1 Schematic of the problem with the domain and boundary conditions

2. PROBLEM DEFINITION

The problem here investigated is schematically presented in Fig. 1, where a square cavity of size, L is considered. A square heat conducting body of size, d and thermal conductivity, k_s is located at the center within the cavity. The top, bottom and left vertical walls of the cavity are kept adiabatic and the right vertical wall is kept at a uniform constant temperature, T_h. The inflow opening located on the bottom of the left wall of size, w and the outflow opening of the same size placed at the top of the opposite heated wall is shown in Fig. 1. For simplicity, the size of the two openings, w is set equal to the one-tenth of the cavity length (L). Cold air flows through the inlet inside the cavity at a uniform velocity, u_i. It is also assumed that the incoming flow is at the ambient temperature, T_i and the outgoing flow is assumed to have zero diffusion flux for all dependent variables i.e. convective boundary conditions (CBC). All solid boundaries are assumed to be rigid no-slip walls.

3. MATHEMATICAL MODEL

The flow is considered to be two dimensional, steady and laminar and the physical properties are assumed to be constant except for the density in the buoyancy term of the momentum equation in the vertical direction, which is treated by using the Boussinesq approximation. The viscous dissipation and joule heating in the energy equation is neglected. Taking into account the above-mentioned assumptions, the governing equations can be written in non-dimensional form as follows:

$$\frac{\partial U}{\partial X}+\frac{\partial V}{\partial Y}=0 \tag{1}$$

$$U\frac{\partial U}{\partial X}+V\frac{\partial U}{\partial Y}=-\frac{\partial P}{\partial X}+\frac{1}{Re}\left(\frac{\partial^2 U}{\partial X^2}+\frac{\partial^2 U}{\partial Y^2}\right) \tag{2}$$

$$U\frac{\partial V}{\partial X}+V\frac{\partial V}{\partial Y}=-\frac{\partial P}{\partial Y}+\frac{1}{Re}\left(\frac{\partial^2 V}{\partial X^2}+\frac{\partial^2 V}{\partial Y^2}\right)+Ri\Theta \tag{3}$$

$$U\frac{\partial \Theta}{\partial X}+V\frac{\partial \Theta}{\partial Y}=\frac{1}{Re\,Pr}\left(\frac{\partial^2 \Theta}{\partial X^2}+\frac{\partial^2 \Theta}{\partial Y^2}\right) \tag{4}$$

For heat conducting rod, the energy equation is

$$\frac{\partial^2 \Theta_s}{\partial X^2}+\frac{\partial^2 \Theta_s}{\partial Y^2}=0 \tag{5}$$

The non-dimensional variables used in the above equations are defined as

$$X=\frac{x}{L},\ Y=\frac{y}{L},\ U=\frac{u}{u_i},\ V=\frac{v}{u_i},\ P=\frac{p}{\rho u_i^2},\ D=\frac{d}{L},\ \Theta=\frac{(T-T_i)}{(T_h-T_i)},\ \Theta_s=\frac{(T_s-T_i)}{(T_h-T_i)}$$

and the parameters *Re, Ri*, *Pr* and *K* are defined as

$$\mathrm{Re}=\frac{u_i L}{\upsilon},\ Ri=\frac{g\beta(T-T_i)L}{u_i^2},\ \mathrm{Pr}=\frac{\upsilon}{\alpha}\ and\ K=\frac{k_s}{k}$$

The average Nusselt number (*Nu*) at the hot wall is defined as

$$Nu=\frac{L}{L_h}\int_0^{L_h/L}\left.\frac{\partial \Theta}{\partial X}\right|_{X=1} dY \tag{6}$$

and the bulk average temperature in the cavity is defined as

$$\Theta_{av}=\frac{1}{\overline{V}}\int \Theta\, d\overline{V} \tag{7}$$

where, L_h is the length of the hot wall and $\overline{V}$ is the cavity volume.

4. NUMERICAL PROCEDURE

The solution of the governing equations along with the boundary conditions is through the Galerkin finite element formulation. In this method, the solution domain is discretized into finite element meshes which are composed of triangular elements. Then the nonlinear governing partial differential equations i.e., mass, momentum and energy equations are transferred into a system of integral equations by applying Galerkin weighted residual method.

5. RESULTS AND DISCUSSION

Mixed convection flow and temperature fields in a vented square cavity filled with a horizontal square solid body are examined. The numerical model developed in the present investigation is used to carry out a number of simulations for the parametric variation of *D* from 0 to 0.6 and *Ri*. The range of *Ri* for this investigation is varied from 0 to 5.0 by changing *Gr* while keeping *Re* fixed at 100 and the working fluid is air with Prandtl number, *Pr* = 0.71.

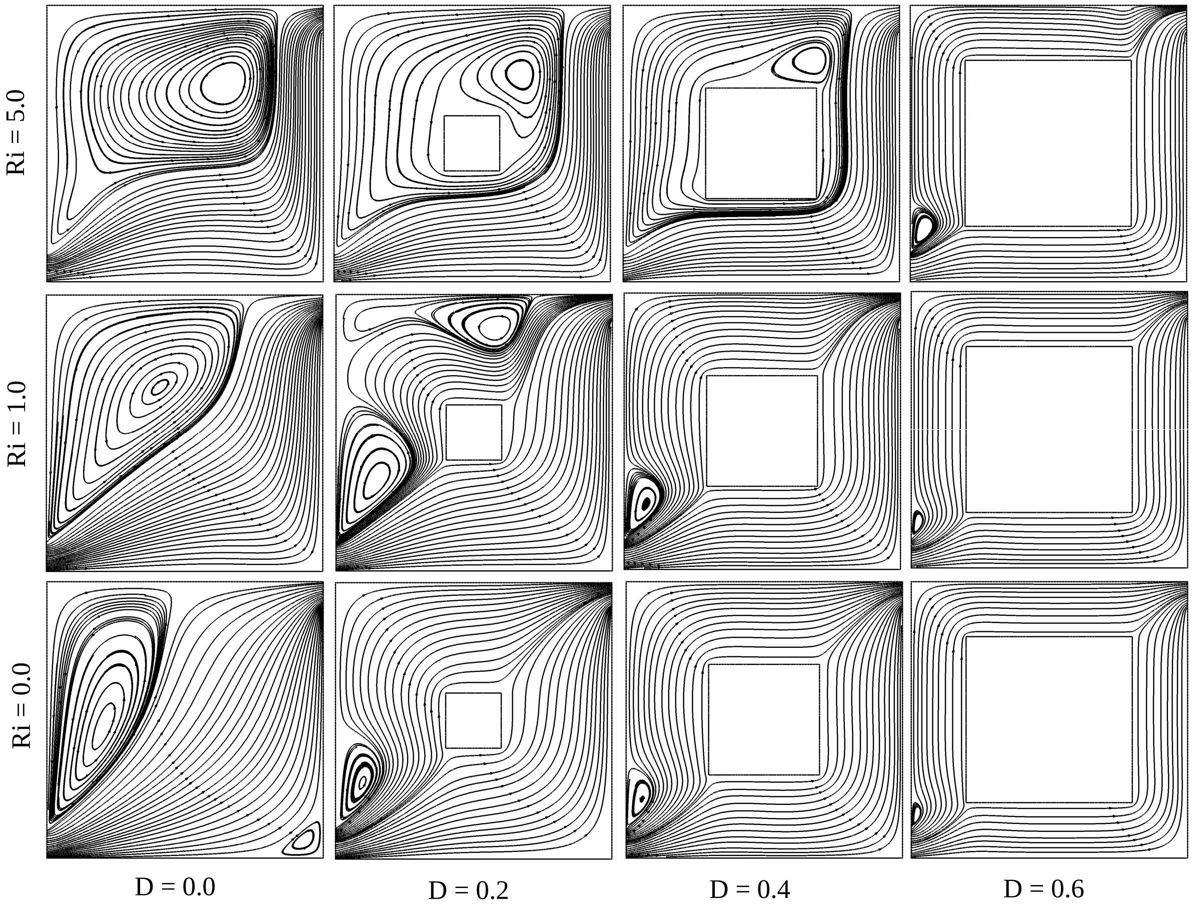

Fig. 2 Streamlines for various Richardson numbers and rod size ratios

The dependence of the flow and thermal fields on the mixed convection parameter *Ri* and the size of the centrally positioned solid body are presented in the Figs. 2 and 3 respectively. Streamline plots for several cases are displayed in Fig. 2. The flow structure in the absence of free convection effect (i.e. for *Ri* = 0) and for the four different values of *D* is shown in the bottom row of Fig. 2. At *Ri* = 0 and *D* = 0, it is seen that a comparatively large uni-cellular vortex appears at the left top corner of the cavity and a very small eddy of very low intensity appears at the right bottom corner of the cavity, which is owing to the effect of share driven flow. Further increase of *D* at fixed *Ri*, the size of the large vortex sharply decreases and the small vortex vanishes. This is due to the increasing size of the solid body which gives rise to a decrease in the space available for the flow induced by the heat source. Again for *Ri* = 1.0 and *D* = 0, it is also seen from the figure that the natural convection effect is present but remains relatively weak at high values of *D*. The reason is that the open lines characterizing the imposed flow are still dominant. Further increase of *Ri* = 5.0 gradually increase the size of the vortex for *D* = 0. This expansion of the size of the vortex squeezes the induced forced flow path resulting almost same kinetic energy in the bulk-induced flow as that of the inlet port. It must be noticed that in this case, the size of the vortex reduced dramatically at the highest value of *D* = 0.6. The isotherms in the absence of body (*D* = 0) and for the three values of *Ri* are shown in the left column of Fig. 3. At *Ri* = 0 and *D* = 0, the high temperature region is concentrated near the hot wall and the isothermal lines are linear and parallel to the heated surface in the cavity, indicating conduction dominant heat transfer. On the other hand, the concentrated temperature region becomes thin and the isothermal lines become nonuniform for *Ri* = 1.0 and various values of *D*. As *Ri* increases to 5.0, the nonlinearity in the isotherms becomes higher and plume formation is profound, indicating the well established natural convection. While comparing the isothermal lines for the case of D = 0.2 to those lines for D = 0 with different Ri, only slight difference in isotherms is observed. Further increase of the size of the body gives the higher nonlinearity in the isothermal lines of the cavity.

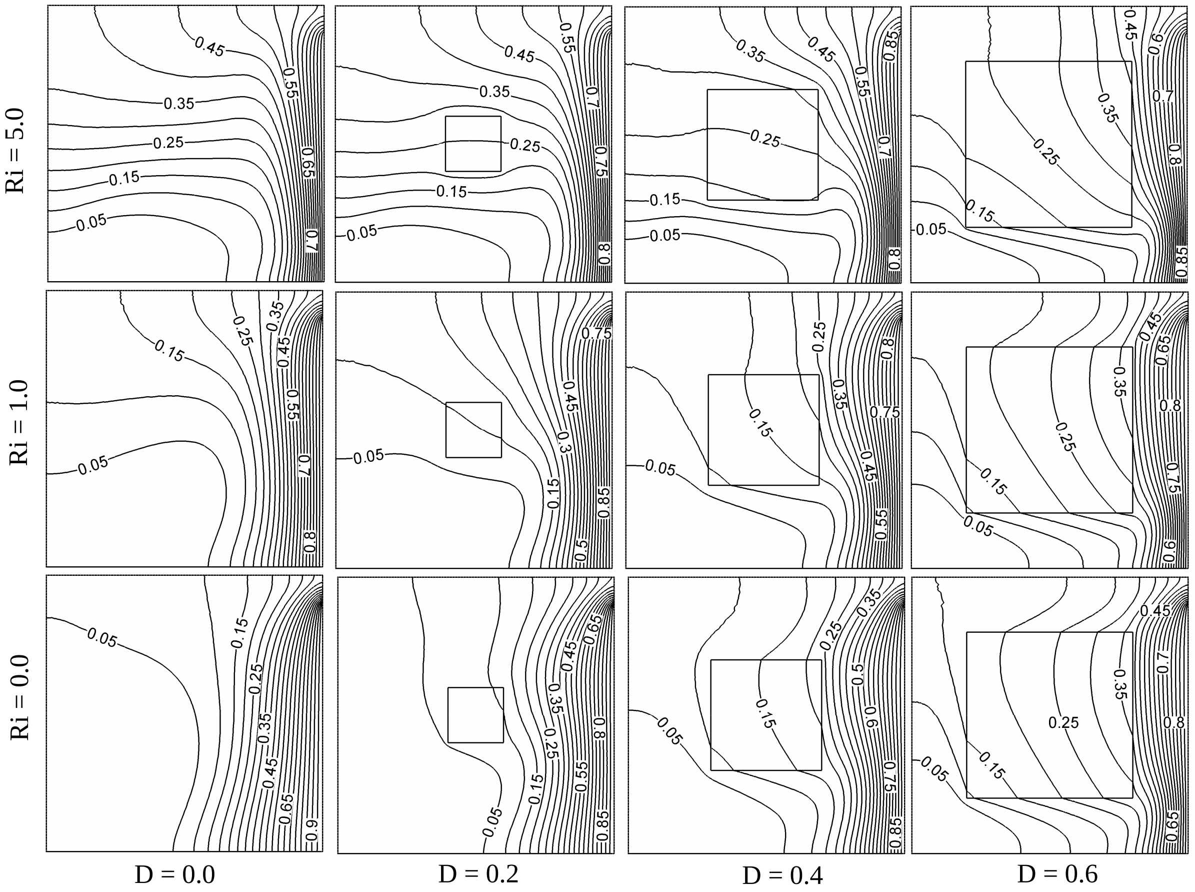

Fig. 3 Isotherms for various Richardson numbers and rod size ratios

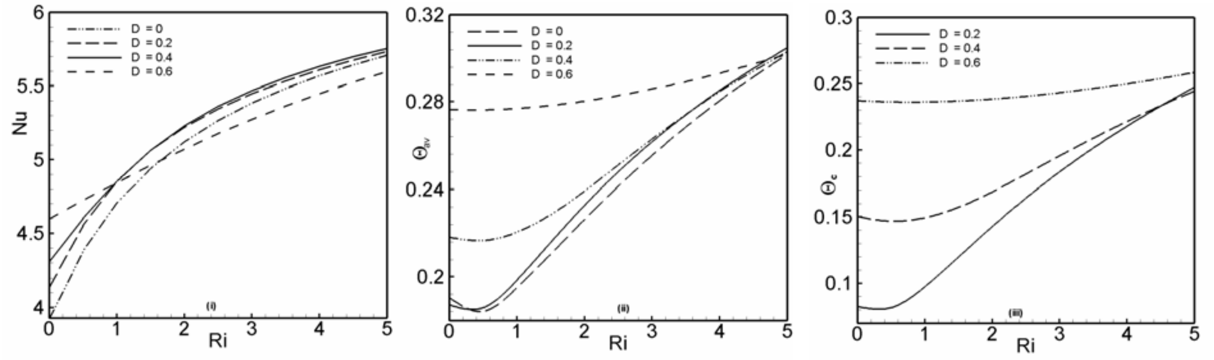

Fig. 4 Effect of different rod size ratios on (i) average Nusselt number, (ii) average temperature and (iii) dimensionless temperature at the cylinder center for various Richardson numbers

Plots of the average Nusselt number (Nu) at the heated wall, average temperature (Θ_{av}) of the fluid in the cavity and the dimensionless temperature (Θ_c) at the body center as a function of Ri and D are shown in Fig. 4. As Ri increases, the values of average Nusselt number (Nu) at the heated wall increases monotonically for all values of D, which is due to increasing Ri enhances convective heat transfer. On the other hand, average Nusselt number (Nu) at the heated wall is the highest for D = 0.6 in the forced convection dominated region ($0 \le Ri \le 1$) and for D = 0.4 in the free convection dominated region (Ri > 1). It is seen that the average temperature (Θ_{av}) of the fluid in the cavity decreases at $Ri \leq 0.5$ for $D = 0.0$, 0.2 and 0.4. However, beyond these values of *Ri*, it is gradually increases. Besides, Θ_{av} is the lowest for $D = 0.2$ at $Ri \leq 0.5$ and beyond these, it the lowest for $D = 0$. It is also seen that the dimensionless temperature (Θ_c) at the body center in the cavity decreases at $Ri \leq 0.5$ for $D = 0.2$ and 0.4 and beyond these values of *Ri*, it is rising. Also Θ_c is the lowest at $D = 0.2$ for almost any particular value of *Ri*.

6. CONCLUSIONS

A numerical study is performed for laminar mixed convection in a vented square cavity containing a centered heat conducting horizontal square body. Results are obtained for a wide range of the governing parameters, Ri and D. The present study illustrates that the patterns of flow and thermal stratification in the cavity as well as the overall heat transfer rate are significantly influenced by these parameters. On the other hand, the average temperature (Θ_{av}) of the fluid inside the cavity and the dimensionless temperature (Θ_c) at the solid body center in the cavity are not monotonic with the increasing values of these parameters.

REFERENCES

[1] House, J. M., Beckermann, C. and Smith, T. F., Effect of a centered conducting body on natural convection heat transfer in an enclosure, *Numerical Heat Transfer, Part A*, 18 (1990), pp. 213–225.

[2] Oh, J. Y., Ha, M. Y. and Kim, K. C., Numerical study of heat transfers and flow of natural convection in an enclosure with a heat generating conducting body, *Numerical Heat Transfer, Part A*, 31 (1997), pp. 289–304.

[3] Roychowdhury, D. G, Das, S. K. and Sundararajan, T. S., Numerical simulation of natural convection heat transfer and fluid flow around a heated body inside an enclosure, *Heat and Mass Transfer*, 38 (2002), pp. 565–576.

[4] Dong, S. F. and Li, Y. T., Conjugate of natural convection and conduction in a complicated enclosure, *International Journal of Heat and Mass Transfer*, 47 (2004), pp. 2233–2239.

[5] Bilgen, E. and Yamane, T., Conjugate heat transfer in enclosures with openings for ventilation, *Heat and Mass Transfer*, 40 (2004), pp. 401–411.

[6] Bhoite, M. T., Narasimham, G. S. V. L., and Murthy, M. V. K., Mixed convection in a shallow enclosure with a series of heat generating components, *International Journal of Thermal Sciences*, 44 (2005), pp. 125–135.

[7] Braga, E. J. and de Lemos, M. J. S., Laminar natural convection in cavities filed with circular and square rods, *International Communication in Heat and Mass Transfer*, 32 (2005), pp. 1289–1297.

[8] Tasnim, S. H. and Collins, M. R., Suppressing natural convection in a differentially heated square cavity with an arc shaped baffle, *International Communication in Heat and Mass Transfer*, 32 (2005), pp. 94–106.

[9] Das, M. K. and Reddy, K. S. K., Conjugate natural convection heat transfer in an inclined square cavity containing a conducting block, *International Journal of Heat and Mass Transfer*, 49 (2006), pp. 4987–5000.

[10] Xu, F., Patterson, J. C. and Lei, C., Experimental observations of the thermal flow around a square obstruction on a vertical wall in a differentially heated cavity, *Experiments in Fluids*, 40 (2006), pp. 364–371.

Proceedings of the 4th BSME-ASME International Conference on Thermal Engineering
27-29 December, 2008, Dhaka, Bangladesh

THERMAL PERFORMANCE OF MICRO HEAT PIPE

R.A. Hossain[1], M.A.K Chowdhuri[2], C. M. Feroz[3]

[1]Lecturer, Primeasia University, Dhaka-1213
[2]Lecturer, [3]Professor
Department of Mechanical Engineering,
Bangladesh University of Engineering & Technology (BUET), Dhaka-1000
e-mail: rifat79_me@yahoo.com

ABSTRACT

Overheating of integrated circuit (IC), microchip etc. is a potential threat to these electronic components. It is very important to facilitate optimum cooling of electronic components in a smaller electronic device because integrated circuit lifetime depends on it. Among other cooling techniques heat pipes emerge as the most appropriate technology and cost effective thermal design solution due to its excellent heat transfer capability, high efficiency and its structural simplicity. Due to the space constraint in most of personal computers and telecommunication devices, application of micro heat pipe (MHP) has been extended gradually. So investigation on MHP is indispensable for further development and improvement of its performance. An experimental study has been performed to investigate the heat transfer characteristics of micro heat pipe (MHP) of circular geometry having inner diameter of 1.8 mm and length of 150 mm. The experimental parameters are inclination angle, coolant flow rate, working fluid and heat input. Taking acetone, ethanol and methanol as working fluids, heat transfer characteristics are determined experimentally for different inclination angles ($30^0 \leq \theta \leq 90^0$), various heat input ($0.612W \leq Q \leq 8.71W$) and coolant flow rates (0.3 lit/min $\leq m_c \leq 1.0$ lit/min). It is observed that MHP with acetone as working fluid shows better performance for an inclination angle of 70^0.

Key words: *Heat transfer characteristics, Micro heat pipe, Inclination angle, Coolant flow rate.*

1. INTRODUCTION

The thermal management problems of microelectronic components will worsen with further miniaturization. The size of microprocessors has been reducing day by day with the development of electronics. Consequently, the number of active semi-conductor devices per unit chip area has been increasing. In the last decade, the number of active semi-conductor devices per unit chip area has almost quadrupled [1]. The minimum feature size in microprocessors has reduced from 0.35 μm in 1990 to 0.25 μm in 1997 and which will go down further to 0.05 μm by the year 2012 [2]. This has increased the heat dissipation density for desktop microprocessors. As an example, heat flux has increased from 2W/cm^2 for an Intel 486 microprocessor to almost 21 W/cm^2 for the Intel P II 300-400 MHz microprocessors [3]. The current heat dissipation rates for some of desktop computers are approximately 25 W/cm^2. It is expected that microprocessor chips for some of the next generation work stations will dissipate 50-100 W/cm^2. Thus reduction in size also brings severe limitations to the conventional cooling techniques [4]. Development of efficient thermal management scheme is essential to dissipate these high heat fluxes and maintain suitable operating temperature of the device. MHP are increasingly filling this role. To keep up with today's thermal solution challenges, MHPs must improve efficiency and integrate remote heat transfer into thermal management solutions. Thus application of micro heat pipe (MHP) has been extended gradually. Jin Zhang [5] studied the heat transfer and fluid flow in an idealized MHP. Yuichi et al. [6] experimentally confirmed steady-state heat transfer characteristics of flat MHP in detail and proposed a method for determining its maximum heat transfer rate. Moon et al. [7] studied performance of a triangular MHP mounted horizontally and found that its heat transport limit 6-15 W/cm^2 for the operating temperature ranging from 45-80^{o}C. Due to high power density and space constraint in most of the electronic devices, especially in personal computers and telecommunications systems placed constraint on the size of heat pipes, MHP of small diameter are preferred. The objectives of this experimental study are to study the heat transfer performance, the wall temperature profile and thermal resistance at various coolant flow, inclination angle (30^0, 50^0, 70^0, and 90^0), heat input and working fluids (Acetone, Ethanol and Methanol) for MHP having diameter of 1.8 mm and length 150 mm.

2. EXPERIMENTAL SET UP

In order to study the heat transfer characteristics of micro heat pipe, an experimental facility has been designed, fabricated and installed. The schematic diagram of the experimental setup is shown in Fig. 1.

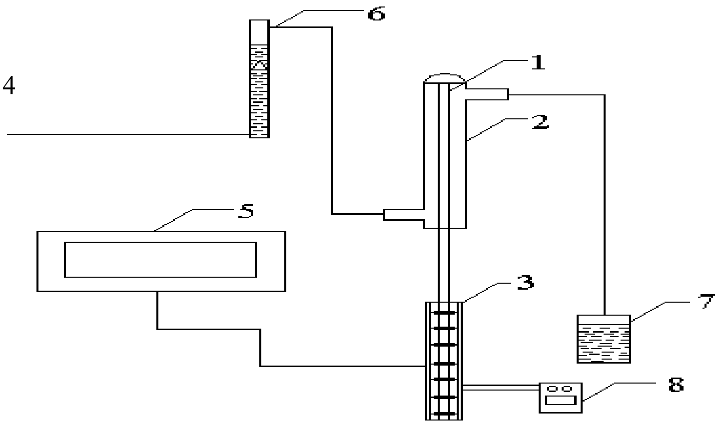

1. Heat pipe 2. Condenser 3. Evaporator 4. Water supply line
5. Temperature indicator 6. Flow meter 7. Container 8. Power supply

Figure 1: Schematic diagram of the experimental setup

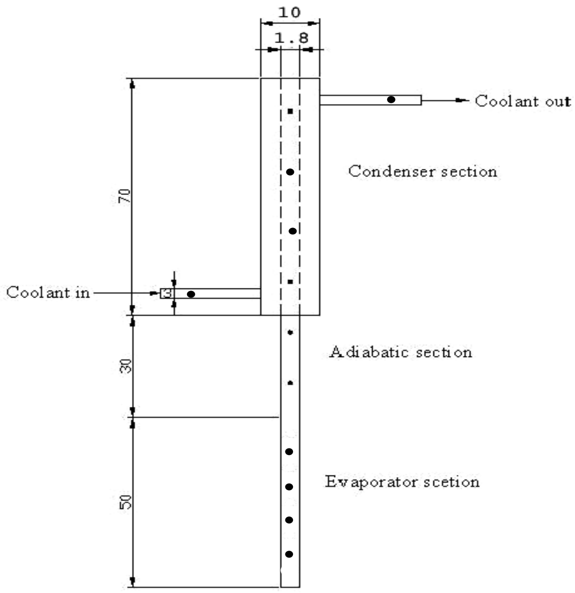

Figure 2: Schematic view of circular MHP

Heat pipe of circular geometry is used in this experiment. The circular one is made of copper tube. The heat pipe consists of three sections as shown in Fig. 2. The sections are evaporator section, adiabatic section and condenser section. Evaporator section is located at the bottom of the heat pipe. Heat is added to the heat pipe through evaporator section. Adiabatic section is located in between the evaporator and condenser section. This section is actually kept with heat pipe to distinguish evaporator section and condenser section. Adiabatic section is thermally insulated using glass wool. Condenser section is the uppermost part of the heat pipe. There is a water jacket around this section which is concentric with the container section. Water flowing through the jacket cools the condenser section of the pipe and thus takes away the latent heat of condenser of vapor. Experimental parameters and their ranges are given in Table. 1.

Table 1: Experimental Parameters and their ranges

Parameters	Condition		Parameters	Condition
Geometry	Circular		Kind of Working fluid	Acetone, Methanol, Ethanol
Diameter of pipe (mm)	1.80		Heat Input (W)	.612 ~ 8.713
Length of Heat Pipe (mm)	150		Coolant flow rate (*l*/min)	0.3 ~ 1.0
Evaporator section (mm)	50		Inclination angle (degree)	$30^0 \sim 90^0$
Adiabatic section (mm)	30		Charge ratio	0.9
Condenser section (mm)	70		Wick (SS)	200 mesh

3. TEST PROCEDURE

Ni-Cr thermic wires are wound around the wall of the evaporator at a constant interval of 1.5 mm. For electrical insulation in the evaporator section, insulation tape is used. The heat added to the evaporator section of MHP is processed in the electric method by using the AC power supply (variac). To minimize heat losses, evaporator section is covered with glass wool. Twelve calibrated thermocouples of K type (Cooper-Constantan, diameter 0.18mm) are glued to the wall of the MHP; four units at the evaporator section, two units at the adiabatic section, four units at the condenser section and two units for measuring the inlet and outlet temperature of the water in condenser section. A digital thermometer (precession 0.05%) is used to measure the wall temperature at various points on MHP. A 12-point selector switch has been used in the experiment to measure the temperature of different points on the heat pipe.

The condenser section is cooled by a constant temperature water coolant, circulating in an annular space between the copper tube and the jacket. The water coolant is taken from supply line trough pipe and the flow is controlled by the flow meter. The inlet and outlet coolant temperatures are measured. An input power to the heater in the evaporator section is increased by using a variac from 0.612 W to 8.71 W. The measurements are made under a steady state condition at each input power. To understand the effects of inclination as well as the change of coolant flow rate in the condenser, the same procedure is followed at each fixed inclination angle and coolant flow rate.

4. MATHEMATICAL EQUATION

One of the methods of evaluating performance of MHP in the present study is measuring the thermal resistance, *R* (^{0}C/W) which is defined in Equation (1)

$$R = \frac{T_e - T_c}{Q} \quad \ldots\ldots\ldots\ldots\ldots\ldots\ldots\ldots\ldots\ldots\ldots\ldots\ldots\ldots (1)$$

The overall heat transfer coefficient, U ($W/m^{2\,0}C$) is obtained from Equation (2)

$$U = \frac{Q}{A_e(T_e - T_c)} \quad \text{…………………….. …………….. (2)}$$

5. RESULTS AND DISCUSSION

Experiment has been carried out with MHP for different working fluids; methanol, ethanol and acetone at different inclination angles, $30^0 \leq \theta \leq 90^0$ for various heat input, $0.612W \leq Q \leq 8.71W$ and coolant flow rates, 0.3 lit/min ≤ m_c ≤ to 1.0 lit/min. To keep the volume of the paper minimum only representative curves (similar nature curves are not shown) are given. Fig. 3 shows the distribution of wall temperature along the length of MHP. From this figure it is seen that in evaporator section temperature remains same, which indicates uniform heating. After that temperature drops in adiabatic section and in condenser section. Again it indicates coolant flow rate has a little effect on wall temperatures. From Fig. 4 it is seen that the nature of the curve in different section of MHP is similar as Fig. 3. Wall temperature is higher for higher heat input in each section of MHP.

From Fig. 5 it is seen that effect of coolant flow rates is insignificant on thermal resistance. From Fig. 5 it is clear that thermal resistance exhibited a decreasing trend as the heat input is increased. It is suspected that as the heat input is raised, heat transfer rate is increased due to the increase of vapor density; this is consistent with the result found by Jon H. B. et al [8] and Kim, K. S. [9]. Thermal resistance decreases slightly with inclination angle up to 50^0 at constant heat input. After that sharp decrease is visible up to 70^0 and then increases (Fig. 6). For this working fluid and heating condition MHP will work better at inclination angle 70^0. Again, coolant flow rate has a little effect on thermal resistance.

Overall heat transfer coefficient is higher for high heat input (Fig. 7). Fig. 8 shows the effect of inclination angle on overall heat transfer coefficient. It is evident that overall heat transfer coefficient is maximum at $\theta = 70^0$ for MHP with ethanol as working fluid when Q = 3.67 W. Figure 9 depicts the variation of overall heat transfer coefficient with heat input for MHP with ethanol as working fluid. The overall heat transfer coefficient is increased with the increase of heat input. Again this figure also shows overall heat transfer coefficient is better for inclination angle 70^0. To find the effect of working fluid, Figure 10 is plotted. This figure is plotted for inclination angle 70^0 and heat input is 3.67W. From the figure it is quite clear that performance of MHP with acetone is better than MHP with methanol or ethanol.

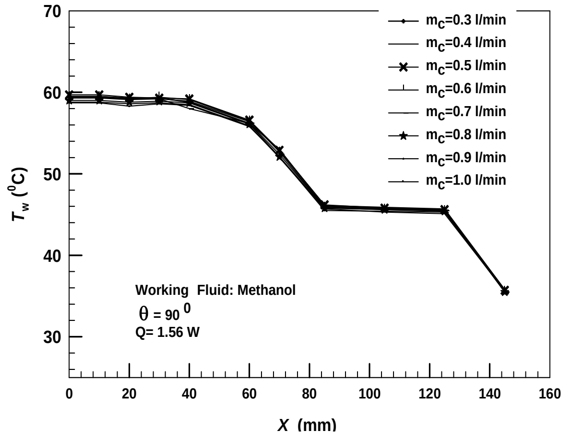

Figure 3: Wall temperature distribution along the length of MHP for various coolant flow rate.

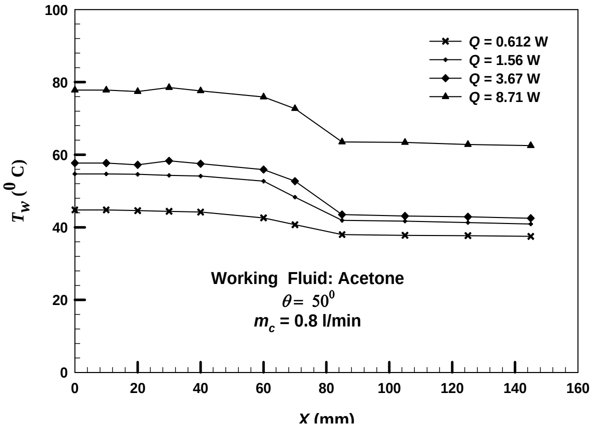

Figure 4: Wall temperature distribution along the length of MHP for various coolant flow rate.

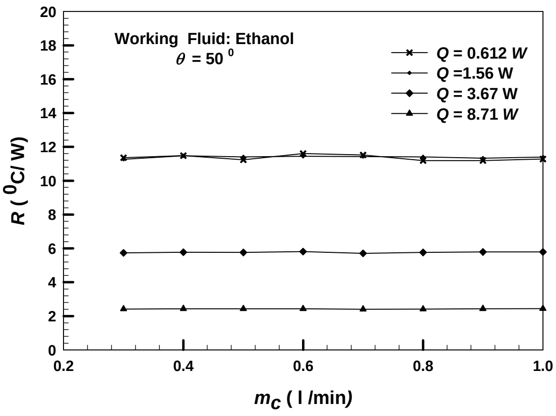

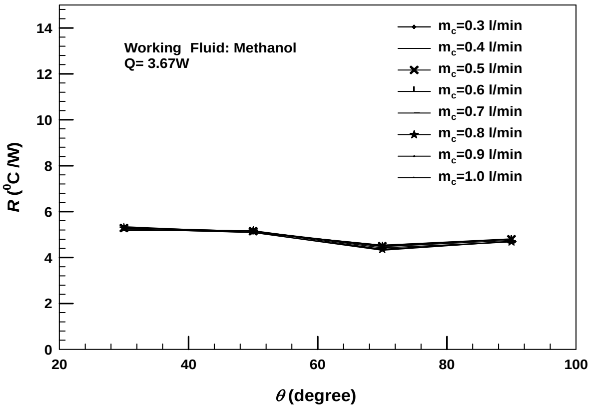

Figure 5: Variation of thermal resistance with coolant flow rate for various heat input.

Figure 6: Variation of thermal resistance with inclination angle for various coolant flow rate.

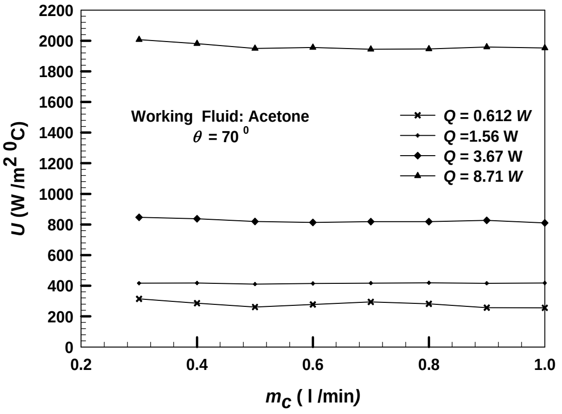

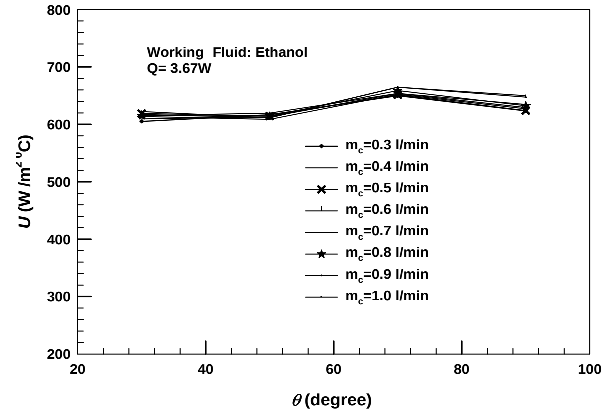

Figure 7: Variation of overall heat transfer coefficient with coolant flow rate for various heat input.

Figure 8: Variation of overall heat transfer coefficient with inclination angle for various coolant flow rate.

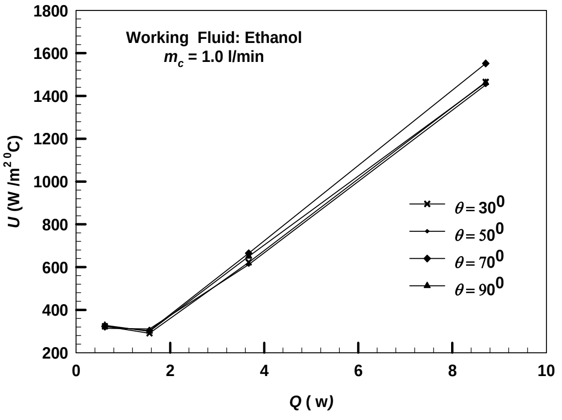

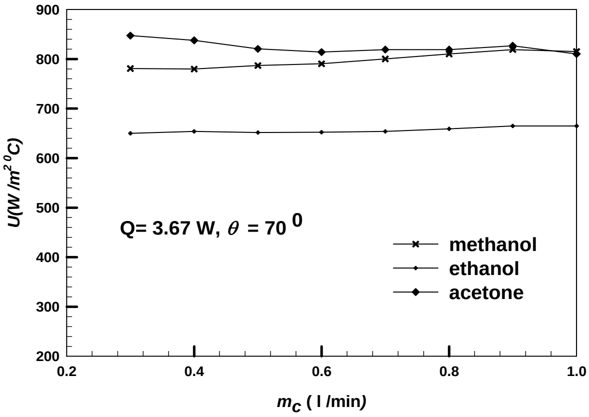

Figure 9: Variation of overall heat transfer coefficient with heat input rate for various inclination angle.

Figure 10: Variation of overall heat transfer coefficient with coolant flow rate for different working fluid.

6. CONCLUSIONS

The experiment of investigating thermal performance of MHP is done by varying the angle of inclination, coolant flow rates, working fluids and heat inputs. The effect of these parameters on the performance are evaluated and presented in above. So from the above discussion the following conclusion can be made.

- Coolant flow rate has an insignificant effect on the performance of MHP.
- Performance of MHP depends upon angle of inclination. Better performance is found for an inclination angle of 70^0.
- Heat input has significant effect on the performance of MHP. It is found that overall heat transfer coefficient is higher for higher heat input.
- It is observed that for the same heat input and inclination angle MHP with acetone as working fluid performs better.

7. NOMENCLATURE

X:	Axial distance	mm	T_w:	Wall temperature	^{0}C
R:	Thermal Resistance	^{0}C/W	Tc:	Average condenser temp	^{0}C
m_c:	Coolant flow rate	lit/min	Te:	Average evaporator temp	^{0}C
Q:	Heat Input	W	Ae:	Surface area of evaporator	mm^2
U:	Overall heat transfer coefficient	W/m^2 ^{0}C	θ:	Inclination angle	Degree

8. REFERENCES

[1] Babin, B.R. Peterson, G. P., Wu, D., "Steady State Modeling and Testing of a Micro Heat Pipe." *ASME J. of Heat Transfer*, 112 (1990), 3, pp. 595-601.

[2] Zhou. J., Yao, Z., and Zhu, J., "Experimental Investigation of the Application Characters of Micro Heat Pipe", Proceedings of the 8th international Heat Pipe Conference, Beijing, China, 1992.

[3] Kim, C. J., Moon, S. H., Kim, J. O., "Fundamental Study on Performance Characteristics of a Micro Heat Pipe with Triangular Cross Section ," *Korean J. of Air-Conditioning and Refrigeration Engineering* , 11 (1999), 2, pp. 176-184.

[4] Luca Rossi, 'Thermal Control of Electronic equipment by Heat Pipes and Two-Phase Thermosyphons'ELBOMEC thermalloy , Via del Tipografo, 440138 Bologna, Italy.

[5] Zhang. J. Heat transfer and fluid flow in idealized Micro heat pipe. Proceedings of the ME Graduate Student Conference, USA, 2002.

[6] Yuichi Kimura, Yoshio Nakamura, Junji Sotani and Masafumi Katsuta, "Steady and Transient Heat TransferCharacteristics of Flat Micro heat pipe", Japan, 2005, Furukawa Review No. 27, pp. 3-8.

[7] Seok Hwan Moon, Chul Ju Kim, Bong Hoon Kim and Sung Lee. An experimental study on the performance limitation of a micro heat pipe with triangular cross-section. Proceedings of the 11th International Heat Pipe Conference-Tokyo, Japan, 1999, pp. 234-238.

[8] Jon H. B., et. al. "An Experimental Study of a Slab-wick Heat Pipe for Medium-high Condenser Temperatures," pp 143-148, Proceedings of the 11th International Heat Pipe Conference –Tokyo 1999.

[9] Kim, K. S. "Cooling Characteristics of Micro Heat Pipes With Woven Wired Wick". pp 239 -244, Proceedings of the 11th international Heat Pipe Conference – Tokyo 1999.

"Proceedings of the 4th BSME-ASME International Conference on Thermal Engineering
27-29 December, 2008, Dhaka, Bangladesh"

COOLING TOWER DESIGN FOR CENTRAL GENERATORS OF CUET, BANGLADESH.

Mohammad Sharif Khan, Golam Mainuddin, Abu Sadat Mohammad Sayem, Nadeem Nafis

Department of Mechanical Engineering,
Chittagong University of Engineering & Technology (CUET)
Chittagong, Bangladesh.
Email: sharif_khan5827@yahoo.com

ABSTRACT:

Cooling tower has a very crucial impact on any kind of power plant like steam power plant, nuclear power plant, gas turbine power plant etc. as the segment of circulating water system. The circulating water system supplies cooling water to the turbine condensers with the assistance of the cooling tower. The system also supplies lesser amounts of auxiliary cooling water for turbine and steam generator buildings, for the fire protection system. Cooling tower is not installed only for a power plant but also in industries of various kinds for cooling purposes like paper mills, garments, chemical industries etc. Our concentration regarding the project and thesis is to design a cooling tower for the central generators of CUET to remove the heat from the generators during operation. There are three gas generators in generator house of CUET each of 120KW rated output. Each generator set is fitted with a radiator engine cooling by cooling water. Radiator is of forced convective type installed with a fan of 15 KW capacities. Thus the three fans consuming about 8% of output power & in addition the fans produce noise. So we have decided to replace this radiator cooling system by an appropriate induced draft wet cooling tower.

.

KEYWORDS: *Power Generator, Wet Cooling Tower, Counter Flow.*

1. INTRODUCTION:

Cooling towers are heat exchangers that are used to dissipate large heat loads to the atmosphere. When water is used as the heat transfer medium, wet, or evaporative, cooling towers may be used. Wet cooling towers rely on the latent heat of water evaporation to exchange heat between the process and the air passing through the cooling tower. Although cooling towers can be classified several ways, the primary classification is into dry towers or wet towers, and some hybrid wet-dry combinations exist. In wet cooling towers, heat transfer is measured by the decrease in the process temperature and a corresponding increase in both the moisture content and the wet bulb temperature of the air passing through the cooling tower. Wet cooling towers typically contain a wetted medium called "fill" to promote evaporation by providing a large surface area and/or by creating many water drops with a large cumulative surface area. Our goal is to design an **induced draft counter flow type wet cooling tower** for three generators of capacity 150KW each. The main advantages of mechanical draft cooling towers are the assurance of moving the required quantity of air at all loads and climate conditions, low initial capital and construction costs and a low physical profile. Counter flow type is more efficient then counter flow and wet cooling tower has greater heat transfer rate than dry cooling tower. Circulating cooling system of water with the help of cooling tower is more efficient than radiator. The present trend in materials for wet – cooling towers favors concrete structures with plastic fill, drift eliminators also with plastic, fan stacks fan blades with galvanized steel, valves and nozzles. The concrete-plastic combination results in longer life and less maintenance.

2. OBJECTIVES:

Although there is a radiator with each generator unit, the cooling tower for these generators circulating water can be a right choice due to following reasons.

- To improve heat transfer from the generator engine.
- To save energy consumption by radiator fan.
- To reduce vibration and hence noise due to radiator fan.

3. METHODOLOGY:

For designing a cooling tower following steps can be followed.

- ➢ To study about the various components and terminology of cooling tower theoretically.
- ➢ To collect related data or information about circulating water system of water jacket of the engine of gas generator.
- ➢ To study for designing suitable cooling tower.
- ➢ To select the appropriate type of cooling tower according to optimal sense.
- ➢ To design the selected cooling tower.

4. COOLING TOWER:

Cooling towers may either use the evaporation of water to reject process heat and cool the working fluid to near the wet-bulb air temperature or rely solely on air to cool the working fluid to near the dry-bulb air temperature. Common applications include cooling the circulating water used in oil refineries, chemical plants, power plants and building cooling. The towers vary in size from small roof-top units to very large hyperboloid structures that can be up to 200 meters tall and 100 meters in diameter, or rectangular structures that can be over 40 meters tall and 80 meters long. Smaller towers are normally factory-built, while larger ones are constructed on site.

4.1 Working Principle of Wet Cooling Tower:

Wet cooling towers have a hot-water distribution system that showers or sprays the water evenly over a lattice network of closely set horizontal slats or bars called fill, or packing. The fill thoroughly mixes the falling water with air moving through the fill as the water splashes down from one fill level to the next by gravity. Outside air enters the tower via louvers in the form of horizontal slats on the side of the tower. The slats usually slope downward to keep the water in the intimate mix between water and air enhances heat and mass transfer, which cools the water. Cold water is then collected in a concrete basin at the bottom of the tower where it is pumped back to the condenser or returned to the natural body of water. Now the hot, moist air leaves the tower at the top.

5. COOLING TOWER DESIGN & CALCULATION:

5.1 Design Layout:

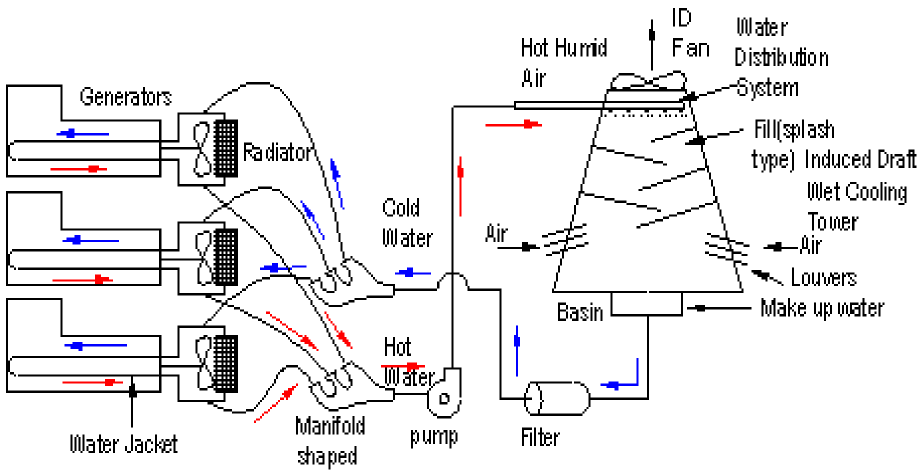

Fig 2: Design Layout

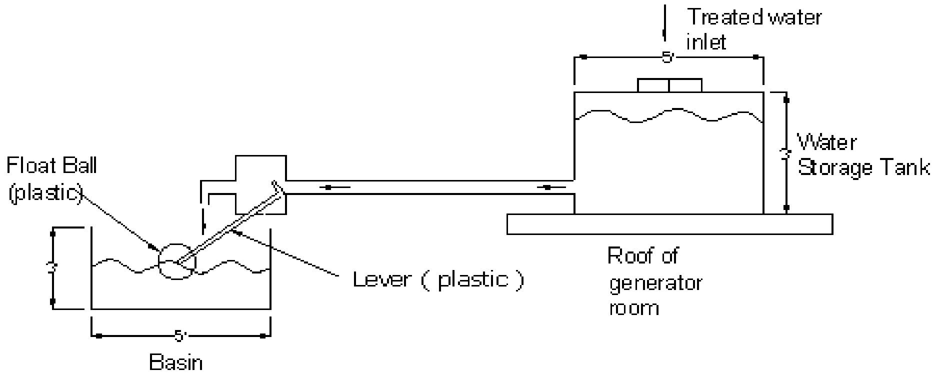

Fig 3: Make up water system

Wet cooling tower calculations involve energy and mass balances. The energy balances will be based on the first law steady state steady flow equation. Three fluids entering and living the system:

1. the cooling water
2. the dry air
3. the water vapor in the air

5.2 Energy Balance:

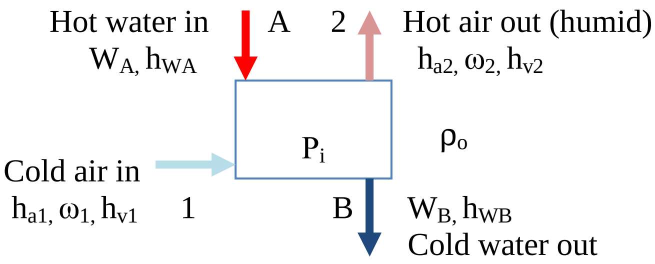

Where,
h_a = Enthalpy of dry air (J/Kg)
ω = absolute humidity, mass of water vapor per unit mass of dry air.
h_v = Enthalpy of water vapor (J/Kg)
W = Mass of circulating water per unit mass of dry air
h_ω = Enthalpy of circulating water(J/Kg)
The subscripts 1 & 2 refer to air inlet and exit and the subscripts A & B refer to circulating – water inlet & exit respectively. The air leaving the system at 2 is often saturated.

$h_v \longrightarrow$ From steam table, saturated vapor at given temperature
$h_\omega \longrightarrow$ From steam table, saturated liquid at given temperature
air = dry air + water vapor
Neglecting the energy of make up water
Energy in = Energy out
Energy in by dry air + Energy in by water vapor + Energy in by circulating water = Energy out by dry air + Energy out by water vapor + Energy out by circulating water.

$$\Rightarrow h_{a1} + \omega_1 h_{v1} + W_A h_{WA} = h_{a2} + \omega_2 h_{v2} + W_B h_{WB} \quad (1)$$

Because of the low pressures and temperatures commonly encountered in towers, the above equation can be simplified with little error by the following approximations. For constant specific heats, $h_{a2} - h_{a1} = c_{pa} (t_{a2} - t_{a1})$ (2)

5.2.1 Mass Balance:

Loss of circulating water = Increase of water vapor in the air = make up water

$$W_A - W_B = \omega_2 - \omega_1 \quad (3)$$

5.2.2 Height of the Cooling Tower:

$$\Delta P_d = (\rho_o - \rho_{i)} \times H \quad (4)$$

Where,
ρ_o = outside air density (at inlet air temperature)
ρ_i = inside air density at the exit of the fill.
H = Height of the cooling tower.
ΔP_d = driving pressure which should equal to the air pressure losses in the tower.

6. CONSIDERATION FOR DESIGN:

- Considering the design for different climate condition (winter, summer and rainy season).
- Neglecting forced convection heat transfer through the pipe.
- Tower may be erected on the roof of the generator room for availability of good flow of air.

6.1 Heat Removal by the Radiator:

Cooling water heat release = 93 KW, Cooling water flow rate = 3.7 Kg/s, Cooling water heat release,
$Q = MC (T_{wi} - T_{wo})$ Where, So, $Q = MC (T_{wi} - T_{wo})$
So water temperature drop by the radiator = 6°C

6.2 Winter Season

Let, the range = 80°C - 70°C = 10°C & the approach = 70°C - 15°C = 55°C

6.2.1 Energy Balance:

From equation (1)
$h_{a1} + \omega_1 h_{v1} + W_A h_{WA} = h_{a2} + \omega_2 h_{v2} + W_B h_{WB} \Rightarrow W_A h_{WA} = C_{pa}(t_{a2} - t_{a1}) + \omega_2 h_{v2} + W_B h_{WB} - \omega_1 h_{v1}$
h_{WA} = 340 KJ/Kg of water (at 50°C) from steam table, v_{WA} = .001 m^3/Kg of water
P_{sat2} = 0.038126 bar (at 28°C) from steam table, h_{v2} = 2552.7 KJ/Kg vapor (at 28°C) from steam table
$W_A h_{WA} = C_{pa}(t_{a2} - t_{a1}) + \omega_2 h_{v2} + W_B h_{WB} - \omega_1 h_{v1}$, $W_A = 1.07 Kgwater/Kgdryair$

6.2.2 Dry Air Required:

= Circulating water inlet flow rate (m^3/sec) / W_A= 3.45 Kg da/sec = 207.47Kg da/min

6.2.3 Make Up Water:

= $\omega_2 - \omega_1$ Kg water/ Kg da = 3.93×10^{-3} m^3/min

6.2.4 Total Outside Air Required:

= Dry air required + water vapor
= Dry air + dry air $\times \omega_1$ = 207.47 + 207.47 × .00527 =208.563 Kg air/ min = 171.09 m^3/min

6.2.5 Air Densities:

$$\rho_o = \frac{P - P_{v1}}{R_a T_1} + \frac{P_{v1}}{R_v T_1} = 1.219 \text{ Kg/m}^3; \ \rho_i = \frac{P - P_{v2}}{R_a T_2} + \frac{P_{v2}}{R_v T_2} = 1.156 \text{ Kg/m}^3$$

6.2.6 Height of the Tower:

From equation (4) H = 4.85; assumption, ΔP_d = 3 N/m^2

6.2.7 Power Requirement of the Pump:

Power, P = $\rho gh \times Q$, h = H_1+ H, Where, H_1 = height of the generator room, H = height of the tower
H_1 = 3.04 m, H = 4.85 m, h = H_1 + H =3.04 + 4.85 = 7.89, hence P = 0.4 hp

6.2.8 Cooling Tower Efficiency:

The efficiency of the cooling tower can be illustrated as
$$\mu = \frac{t_i - t_o}{t_i - t_{wb}} \times 100 = \frac{80-70}{80-5} \times 100 = 13.33\%$$
Where, t_i = water inlet temp^r. t_o = water outlet temp .t_{wb} = wet bulb temp of inlet air,
Similarly the values of different properties can be calculated for summer & winter season. From which values can be tabulated, given below.

Table.1: Values of different parameters in various climatic conditions.

Climatic condition	Dry air required (Kg/min)	Make up water (m^3/min)	Outside air required (m^3/min)	Height of the tower (m)	Power reqd. of the pump (hp)	Cooling tower efficiency μ (%)
Winter	207.47	3.93×10^{-3}	171.09	4.85	0.4	13.33
Summer	62.53	5.19×10^{-3}	58.23	3.15	0.3	25
Rainy season	164.45	2.32×10^{-3}	139.53	6.37	0.5	15.15

The highest values from the table from each column can be taken for consideration of factor of safety in design.

7. CONCLUSION:

The proper design of cooling tower will ensure the longevity of the generator. The design of a cooling tower is really cumbersome task. The basis of my design was to determine basically the height of the tower. The radiator of each generator can lessen maximum of 6°C temperature of circulating water. What should be the maximum height of the tower for reducing temperature of 10-15°C was my goal to find out. Some heat also must be transferred by forced convection, radiation and conduction through the pipe that I neglected from calculation. I have tried my level best to design the cooling tower in optimal sense. Different companies I have visited that I mentioned earlier adopted a heat exchanger for transferring heat from generators circulating hot water to cooling tower cold water. They have adopted the heat exchanger for avoiding natural dust, debris, turbidity etc. and installed for high capacity generator unit (1MW, 2MW) etc. By considering the cost effectiveness I didn’t use the heat exchanger in my design because the heat exchanger is costly (a shell & tube type heat exchanger is cost about Tk.700000). In place of heat exchanger I have used a filter to remove natural fouling. I have also proposed in my design to make the tower wooden structured in place of steel by considering optimal cost sense. Above all whether I have designed properly or not but I have accomplished a deep knowledge about cooling tower design as well as construction that will make me pioneer for engineering.

8. REFERENCES:

[1] M.M. EI Wakil, 1st printed 1985, Power Plant Technology.
[2] Gustaf A.Gaffert, fourth edition, Steam Power Stations.
[3] John Maulbetsch, Maulbetsch Consulting, May 2003, Cooling System Retrofit Costs EPA Workshop on Cooling Water Intake Technologies.
[4] Department of Energy, Office of Fossil Energy's Power Plant Water Management R&D Program.

Proceedings of the 4th BSME-ASME International Conference on Thermal Engineering
27-29 December, 2008, Dhaka, Bangladesh

NATURAL CONVECTION WITHIN AN ENCLOSURE OF SINUSOIDAL CORRUGATED TOP SURFACE

Noman Hasan[1], Sumon Saha[2], Chowdhury Md. Feroz[1]

[1]Department of Mechanical Engineering,
Bangladesh University of Engineering and Technology, Dhaka-1000, Bangladesh
[2]Department of Energy and Environmental Engineering, Interdisciplinary Graduate School of Engineering Sciences, Kyushu University, 6-1 Kasuga-koen, Kasuga-shi, Fukuoka 816-8580, Japan
E-mail: noman.becker@yahoo.com

ABSTRACT

Natural convection of a two-dimensional laminar steady-state incompressible fluid flow in a modified square enclosure having sinusoidal corrugated top surface has been numerically investigated for different inclination angles. A constant flux heat source is flush mounted on the top sinusoidal wall, modeling a wavy tin shaded room exposed to sunlight. The effect of inclination angle on natural convection flow characteristics has been studied to observe the hydrodynamic and thermal behavior for different orientations of the enclosure. The flat bottom surface is considered as adiabatic, while the both flat side walls are symmetric and considered as isothermal maintained at the ambient temperature. The fluid considered inside the enclosure is air. The numerical scheme is based on the finite element method adapted to triangular non-uniform mesh element by a non-linear parametric solution algorithm. The results are obtained for the Rayleigh number, Ra ranging from 10^3 to 10^6 with constant physical properties for the fluid medium considered. The streamlines, isotherms and average Nusselt numbers are presented to observe the presence of the corrugation effect on fluid flow and heat transfer characteristics for the range of governing parameters. The present results show that the convective phenomena are greatly influenced by the variation of the inclination angles.

Key words: *Natural convection; Numerical simulation; Sinusoidal corrugation; Inclination angle.*

1. INTRODUCTION

Natural convection heat transfer and fluid flow in enclosed space or closed cavities is one the most studied thermal phenomena that has considerable attention of engineers because of its great importance in several thermal engineering applications. Cavities with regular geometries like rectangular or triangular enclosures with arrangements like horizontal or vertical have studies in a great extent. Such boundaries are easier to model and the flow patterns and circulations are less complex than an enclosure having complex profile and different orientations like tilted enclosure having sinusoidal surface. Applications of such enclosures can be found in designing solar collectors, electric machinery, cooling systems of micro-electronic devices and so on. Though numerical study of complex cases has not been done in a great extent, Morsi and Das [1] studied the natural convection inside complex enclosures. Investigation of the heat transfer for corrugations are mostly done for vee surfaces Saha *et al.* [2] but study of sinusoidal surfaces are limited due the difficulties associated with the generation of such profiles accurately. Natural convection along vertical wavy surface was studied by Yao [3] and Mahmud *et al.* [4]. Similar studies had been carried out by Mébrouk *et al.* [5] for the case of horizontal wavy enclosure. Most studies on heat transfer for different corrugated enclosures were carried out either vertical or horizontal arrangements. Velocity-pressure formulation for convective flow inside enclosure with top quadratic inclined roof had been investigated by Das and Sahoo [6]. For an inclined wavy enclosure, laminar free convection and entropy generation was studied by Mahmud and Islam [7]. Varol and Oztop [8, 9] studied the thermal and flow characteristics inside of a tilted solar collector having absorber at the wavy bottom surface. The present study focuses on the effect of the inclination for natural convection inside a modified square enclosure with a sinusoidal top surface of fixed corrugation frequency and amplitude that has isoflux heating condition.

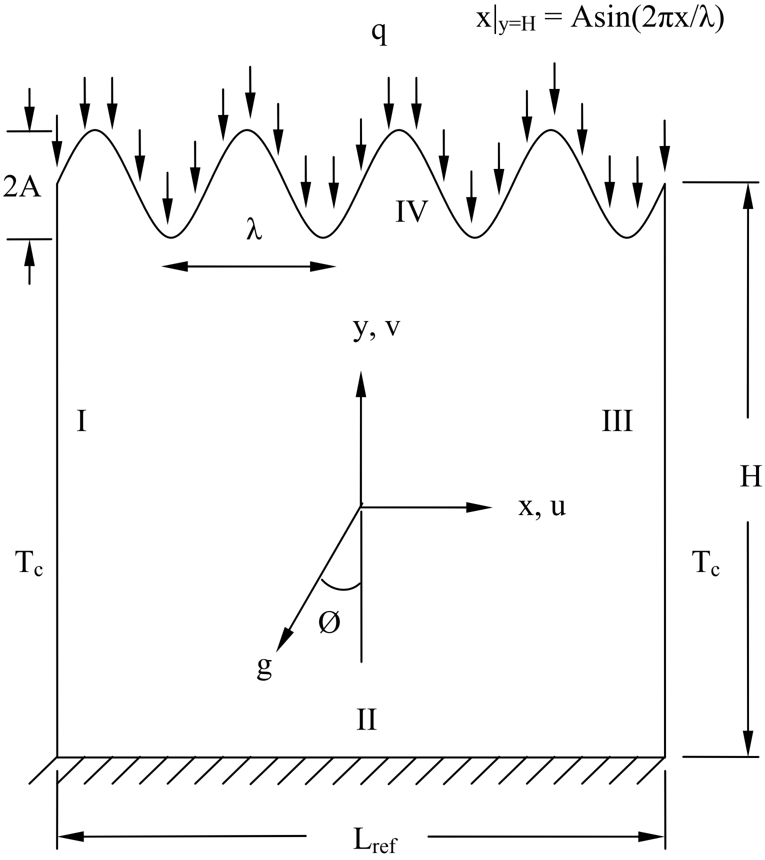

Fig. 1 Schematic physical configuration and boundary conditions of the modified square enclosure with sinusoidal top surface

2. MATHEMATICAL MODEL

A Cartesian co-ordinate system is used with the origin at the bottom left of the considered computational domain (Fig. 1). The considered model is (L_{ref} = H) a modified square enclosure having sinusoidal corrugated top surface of corrugation frequency (L_{ref}/λ) of a value of 3 and non-dimensional corrugation amplitude (A/L_{ref}) is 0.1, inclined at an angle, Ø maintained at uniform heat flux, q. The side walls are maintained at cold (surrounding) temperature, T_c. The bottom surface is considered as adiabatic. No-slip conditions are considered for all the solid boundaries and are assumed to be rigid.

Using the Boussinesq approximation and neglecting the dissipation effect due to the viscous term, the governing equations in non-dimensional form are written as follows:

$$\frac{\partial U}{\partial X}+\frac{\partial V}{\partial Y}=0 \tag{1}$$

$$U\frac{\partial U}{\partial X}+V\frac{\partial U}{\partial Y}=-\frac{\partial P}{\partial X}+Pr\left[\frac{\partial^2 U}{\partial X^2}+\frac{\partial^2 U}{\partial Y^2}\right]+Ra\Pr\Theta\sin\phi \tag{2}$$

$$U\frac{\partial V}{\partial X}+V\frac{\partial V}{\partial Y}=-\frac{\partial P}{\partial Y}+Pr\left[\frac{\partial^2 V}{\partial X^2}+\frac{\partial^2 V}{\partial Y^2}\right]+RaPr\Theta cos\phi \tag{3}$$

$$U\frac{\partial \Theta}{\partial X}+V\frac{\partial \Theta}{\partial Y}=\frac{\partial^2 \Theta}{\partial X^2}+\frac{\partial^2 \Theta}{\partial Y^2} \tag{4}$$

All the above equations are normalized using the following dimensionless scales:

$$(X,Y)=\frac{(x,y)}{L_{ref}},\ (U,V)=\frac{(u,v)L_{ref}}{\alpha},\ P=\frac{pL_{ref}^2}{\rho\alpha^2},\ \Theta=\frac{(T-T_c)}{qL_{ref}/k},\ Ra=\frac{g\beta qL_{ref}^4}{k\eta\alpha},\ \Pr=\frac{\eta}{\alpha}$$

where Ra, Pr, α, β, ρ, η, k, P, p are Rayleigh number, Prandtl number, thermal diffusivity, thermal expansion coefficient, fluid density, kinematic viscosity and thermal conductivity, non-dimensional and dimensional pressure respectively. The average Nusselt number, Nu at the heated surface is a measure of convective heat transfer coefficient, h_{av}. The expression for the average Nusselt number is

$$Nu=\frac{h_{av}L_{ref}}{k}=\int_0^1\frac{1}{\Theta(X,Y=H)}dX \tag{5}$$

3. NUMERICAL PROCEDURE

The numerical procedure used to solve the governing equations for the present work is based on the Galerkin weighted residual method of finite-element formulation. The matrix factorization technique (LU decomposition) is used with partial pivoting. The non-linear parametric solution method is chosen to solve the governing equations. This approach will result in substantially fast convergence assurance. A non-uniform triangular mesh arrangement is implemented in the present investigation especially near the corrugated walls to capture the rapid changes in the dependent variables.

4. RESULTS AND DISCUSSION

The results of the present study are obtained for Pr = 0.71, $H/L_{ref} = 1$, $L_{ref}/\lambda = 3$, and $A/L_{ref} = 0.1$ using non-uniform triangular meshes with the parametric variation of $10^3 \leq Ra \leq 10^6$ and $0° \leq Ø \leq 45°$.

4.1 Flow Field Characteristics:

The streamlines, from Fig. 2, show that there are two vortexes for each case as the two side walls are maintained at cold temperature and the convective currents are separated the main flow into two flows. For a certain Rayleigh number, as the inclination angle increases, the vortex close to the lower cold wall are suppressed and the other vortex dominates the heat transfer. As the Rayleigh number increases, the streamlines become more densely packed and the suppressed lower vortex tends to become stronger and bigger.

4.2 Thermal Field Characteristics:

In Figs. 2 and 3, the effects of the inclination angle are revealed with the help of streamlines and isotherms respectively. Figure 3 shows that for a lower Rayleigh number the isotherms are like elliptical shape and the nature does not change much with the variation of the inclination.

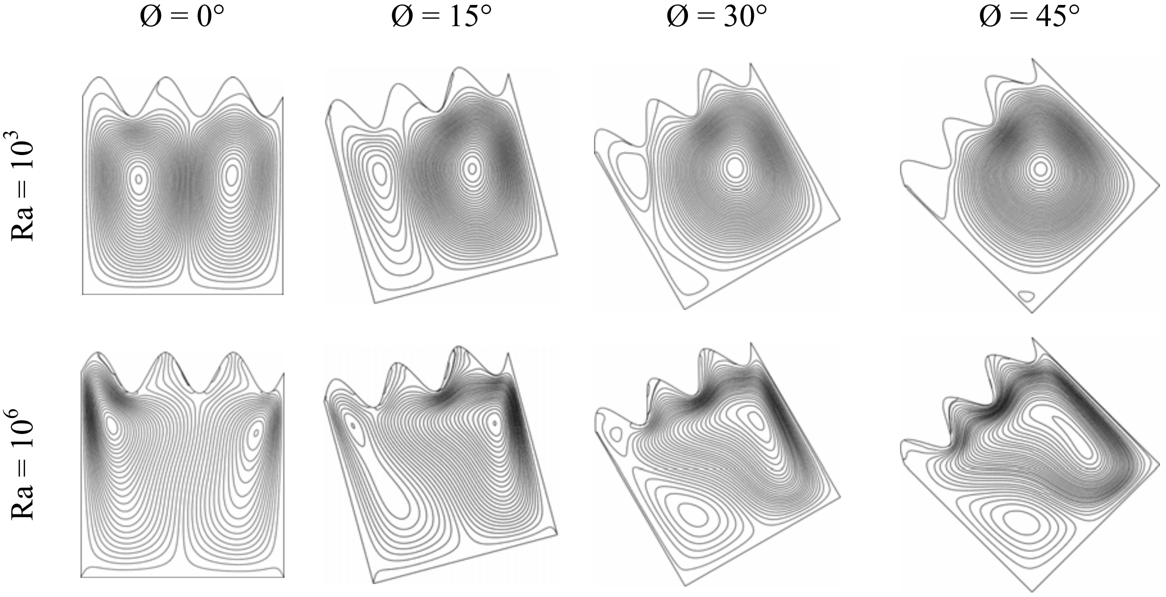

Fig. 2 Streamline patterns for different inclination angles at Ra = 10^3 and 10^6

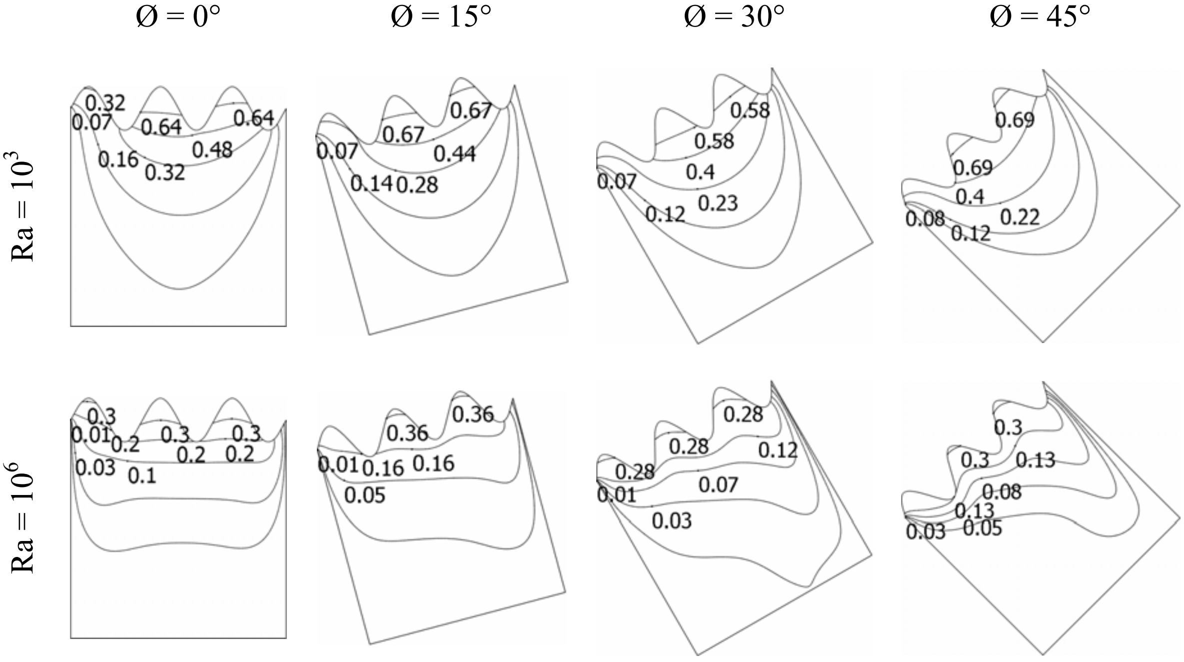

Fig. 3 Isotherm patterns for different inclination angles at Ra = 10^3 and 10^6

4.3 Heat Transfer Characteristics:

From Fig. 4, it is observed that the heat transfer phenomenon is greatly influenced by the change of inclination angle of the cavity. The reason behind this behavior is the interaction of the gravity and the buoyancy force. For lower Rayleigh number, the average Nusselt number is very close up to Ra = 10^4 but as the Rayleigh number increases the average Nusselt number increases linearly. However, the slope remains same but the magnitude of average Nusselt number increases for the higher inclination angle. But as the Rayleigh number increases, the isotherms tend to distort. This is due to the fact that the convective phenomena are greatly enhanced by the increment of Rayleigh number. Another observation shows that the distortion of the isotherm tends to head towards the upper cold wall.

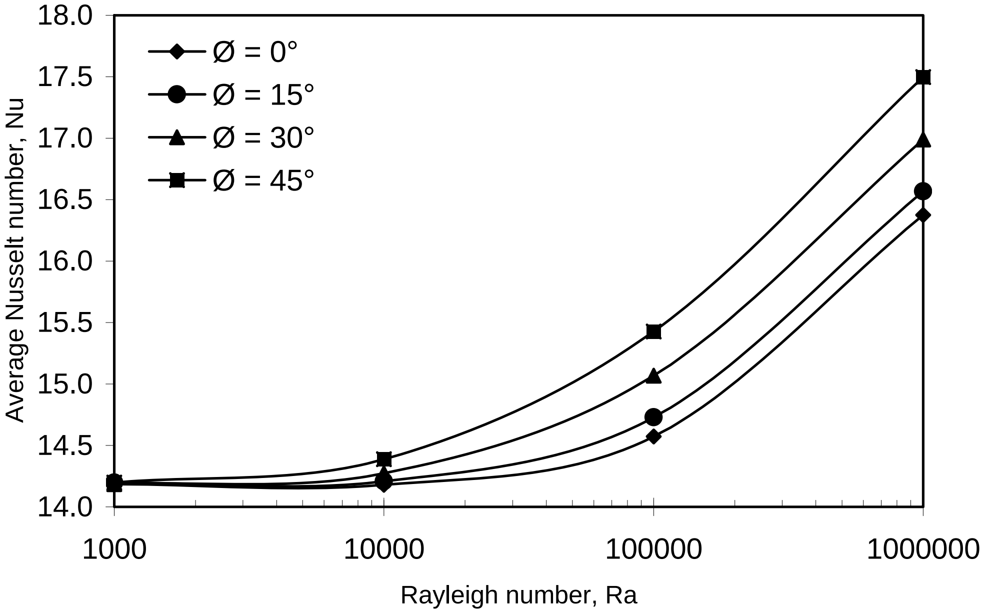

Fig. 4 Variation of average Nusselt number with Rayleigh number for different inclination angles

6. CONCLUSIONS

A numerical study has been carried out for a modified square enclosure with sinusoidal corrugation at the top surface to observe the influence of the inclination angle of the enclosure on the fluid flow and heat transfer phenomena. The important outcomes of the present investigation are as follows:

(i) For a convective fluid having constant value of Prandtl number 0.71 and a range of Rayleigh number from 10^3 to 10^6, representing the domination of convection over diffusion heat transfer as the value of Rayleigh number increases.
(ii) The inclination angle plays a significant role on the convection heat transfer phenomenon. The higher the inclination angle, the more enhanced heat transfers occurs from the heated wall.
(iii) The average Nusselt number for the case of lower Rayleigh number are very close for all inclination angles and the rate of increment of average Nusselt number with the increment of Rayleigh number is higher for higher inclination angle.

NOMENCLATURE

A	Half of the amplitude
g	Gravitational acceleration
H	Cavity height
L_{ref}	Reference length
T	Temperature
u, v	velocity components
U, V	Non-dimensional velocity components
x, y	Cartesian co-ordinate
X, Y	Non-dimensional Cartesian co-ordinate

Greek Letters

λ	Wave length
Θ	Non-dimensional Temperature

REFERENCES

[1] Morsi, Y. S. and Das, S., Numerical investigation of natural convection inside complex enclosures, *Heat Transfer Engineering*, 24(2) (2003), pp. 30-41.

[2] Saha, G., Saha, S., Ali, M. and Islam, M.Q., Natural convection in a vee-corrugated square enclosure with discrete heating from below, *Journal of Engineering and Technology*, 6(1) (2007), pp. 15-27.

[3] Yao, L.S., Natural convection along a vertical wavy surface, *Journal of Heat Transfer*, 105 (1983), pp. 465-468.

[4] Mahmud, S., Das, P.K., Hyder, N. and Islam, A.K.M.S., Free convection in an enclosure with vertical wavy walls, *International Journal of Thermal Sciences*, 41 (2002), pp. 440-460.

[5] Mébrouk, R. Abdellah. B. and Abdelkader, S., Effect of wall waviness on heat transfer by natural convection in a horizontal wavy enclosure, *International Journal of Applied Engineering Research*, 1(2) (2006), pp. 187-201.

[6] Das, S. and Sahoo, R., Velocity-pressure formulation for convective flow inside enclosure with top quadratic inclined roof, *Journal of Energy, Heat and Mass Transfer*, 20 (1998), pp. 55-64.

[7] Mahmud, S. and Islam, A.K.M.S., Laminar free convection and entropy generation inside an inclined wavy enclosure, *International Journal of Thermal Science*, 42 (2003), pp. 1003- 1012.

[8] Varol, Y. and Oztop, H. F., A comparative numerical study on natural convection in inclined wavy and flat-plate solar collectors, *Building and Environment*, 43 (2008), pp. 1535–1544.

[9] Varol, Y. and Oztop, H. F., Buoyancy induced heat transfer and fluid flow inside a tilted wavy solar collector, *Building and Environment*, 42 (2007), pp. 2062–2071.

Proceedings of the 4th BSME-ASME International Conference on Thermal Engineering
27-29 December, 20086, Dhaka, Bangladesh

EXPERIMENTAL INVESTIGATION ON HEAT TRANSFER OF AN OPEN LOOP PULSATING HEAT PIPE

Chowdhury M. Feroz, Md. Imran Khan, Md. Mahmudul Hasan

Department of Mechanical Engineering
Bangladesh University of Engineering and Technology
Dhaka, Bangladesh
E-mail: cmferoz@me.buet.ac.bd

ABSTRACT

An experimental investigation of an open loop pulsating heat pipe (OLPHP) has been presented here, where several issues related to its performance were evaluated. The main objective of this experiment is to discover at which orientation heat transfer performance is better for ethanol as the working fluid. The other objective was to compare the nature of the pulsation of the OLPHP found in this experiment with those who did the same experiment before. Tests were conducted with ethanol for the OLPHP operating at both vertical and horizontal orientations. Nature of the pulsating action were observed and compared with findings of others. Significant similarities of pulsating actions were found with the results of others finding. The experimental results show that the system presented better performance when operating at vertical orientation at higher heat load level and at horizontal orientation in lower heat load level as lower evaporation section temperatures were achieved at vertical orientation at higher heat load level and lower evaporator section temperatures were observed at horizontal orientation at lower heat load level.

KEYWORDS: *Pulsating Heat Pipe, Thermal Conductance.*

1. INTRODUCTION

An alternative to the capillary heat pipe is the pulsating heat pipe, which consists of one continuous channel that meanders back and forth between the evaporation and condensation regions. The channel can be closed (close looped) or open (open looped). The channel diameter in the pulsating heat pipes is on the order of ~1mm hydraulic diameter so that stratified flow is prevented and a vapor plug and liquid slug is formed.

Pulsating heat pipes (PHPs) are passive 2-phase thermal control devices first introduced by Akachi et al. [1]. PHPs consist of a capillary tube bent into several turns to form parallel passages. Reduced diameter is used here. The vapor plugs generated by the evaporation of liquid push the liquid slugs toward the condensation section and this motion causes flow oscillations that guide device operation [2]. Considering the sections of a PHP, it presents evaporation and a condensation section and may also present an adiabatic section. The tube doesn’t present a wick structure. Heat is acquired from the source through the evaporation section transferring it to the working fluid where the slug/plug pumping action will be generated. The fluid then flows through adiabatic to condensation section. In the open loop

PHP it is believed that a counter-current liquid-vapor flow occurs to promote proper device operations [3].

The pulsating action (plug/slug) is the motion force for the PHP, which is directly influenced by the inner tube diameter. The factors that influence the plug/slug formation in reduced diameters must be observed for this application, such as the correct working fluid selection, surface tension and shear stress effects, etc. Without this pumping action, the device will operate as a solid bar conducting heat from one end to another. As an important parameter for the proper PHP operation, the critical bubble diameter is directly related to the selected working fluid and can be estimated from the Bond number as

$$B_o=d_c\,[g\,(\rho_l-\rho_v)/\sigma]^{0.5} \qquad \text{where } B_o\leq 2.0 \qquad (1)$$

This variable should be used as an upper limit for the maximum tube inner diameter, as an important parameter for the vapor plug formation. If the conditions for the vapor plug formation are satisfied, the PHP would present a satisfactory operation. Another factor that directly influences the PHP performance is the number of turns, as the increase of this parameter will increase the PHP performance [4] and thus higher heat fluxes could be dissipated. For the proper working fluid selection, the Clausius Clayperon relation

$$(\,dP/dT)_{Tsat} = i_{lv}/(T_{sat}v_{lv}) \qquad (2)$$

could be applied, where high values for the magnitude of the derivative $(dP/dT)_{Tsat}$ (slope) must be achieved. A comparison of this parameter related to several working fluids was presented by Khandekar et al. [5]. This represents that a small change in the saturation temperature will result in a large influence in the saturation pressure, which will directly affect the pumping forces of the PHP during its operation. Other important parameters should also be evaluated, such as latent heat of vaporization (i_{lv}): high values of i_{lv} are desirable and important regarding the Clausius- Clayperon relation, which can reflect little temperature drop driving force. On the other hand, this parameter should present a reduced value in order to result in faster bubble generation and collapse; the PHP process is more likely to be due to sensible heat [2, 5]; Surface tension: it is desirable that the working fluid presents a low surface tension, although this parameter in conjunction with dynamic contact angle hysteresis may generate additional pressure drop [5]. Looking at the Bond number definition, low surface tension fluids are only possible for PHPs with small diameters to have the slug/plug distribution, in which this parameter should be used as a guide when selecting the proper working fluid.

Following the above mentioned parameters, an experimental apparatus was built to test a PHP configured as an open loop. The device was tested for ethanol as the working fluid. The results were gathered to compare the thermal performance of the PHP for vertical and horizontal orientations.

2. EXPERIMENTAL SETUP

The device used during the experimental tests is shown by Fig. 1. A pulsating heat pipe configured as an open loop was built using a capillary copper tubing with 3.20 mm OD, 1.65 mm ID, 4.2 m long to form 13 parallel channels with 12 curves. The critical diameter (d_c) of ethanol is 3.6 mm. The apparatus was placed on a support that allowed its adjustment on vertical and horizontal orientations.

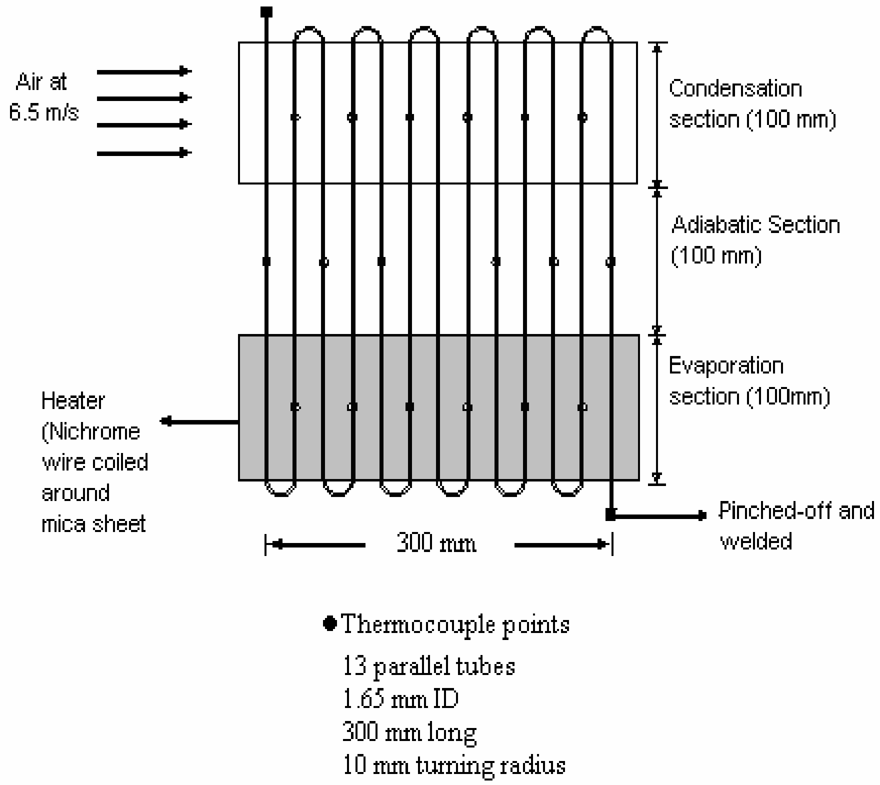

Fig.1 Experimental Set-up

The OLPHP was built with 3 regions: evaporation, adiabatic and condensation, each one being 100 mm long and 300 mm wide. For the tests under vertical orientation, the evaporation section was always below the condensation section. For the tests under horizontal orientation, all sections were at the same plane. Both evaporation and adiabatic sections were thermally insulated, while the condensation section was open to the surrounding air. The condensation section was forced air, using a fan able to deliver air at a velocity of 6.5 m/s. The tests were conducted in a controlled room environment, with temperature ranging between 27-29^{o}C. The evaporation section was in contact with nichrome wire which is coiled around two mica sheets to deliver the desired heat load. The heat loads were administered by an AC power supply. Eighteen K-type thermocouples were used to monitor the device performance during the tests. A total of 6 thermocouples were located at each section. The thermocouples were connected to a temperature controller to monitor all temperatures. The Temperatures were recorded at every 5 minutes. The filling ratio was 50%. All experimental tests were performed on a heat load profile basis, where the perspective was to evaluate the behavior of OLPHP related to the orientation and applied power.

3. RESULTS AND DISCUSSION

For the startup of the OLPHP, the expected behavior was similar to the other 2-phase thermal control devices such as capillary pumped loops and loop heat pipes. After initiating the administration of the heat load, an increase on the evaporation section temperature would be expected with consequent drop, indicating that the slug/ plug pumping action had been initiated, which would result in temperature oscillations. With the increase in heat load, the oscillations become more intensive and it can be detected by slight temperature decreasing. This behavior was detected by Khandekar et al. [5] during flow observation through transparent tubes in their experiment.

The behavior of OLPHP startup at different power level for ethanol as the working fluid under vertical orientation is shown in the Fig. 2(a). Up to power of 35W, the OLPHP was operating with minor flow oscillations at evaporator section. At 10W first oscillation occurred and when 35W power was applied intensive oscillation started and at 45W it turned into a drastic mode. At this particular case the oscillation can be up to 10°C. In adiabatic and condenser section oscillation started at 25W. Experimental result of Roger R. Riehl [6], with OLPHP of 1.5 mm ID shown in Fig. 2(b) is considered here for comparison. Figures indicate that for this OLPHP experimental results at vertical orientation are almost similar to [6]. In experiment of Roger R. Riehl [6], the first oscillation started at 25W at evaporator and the maximum oscillation was observed at 45W at adiabatic section.

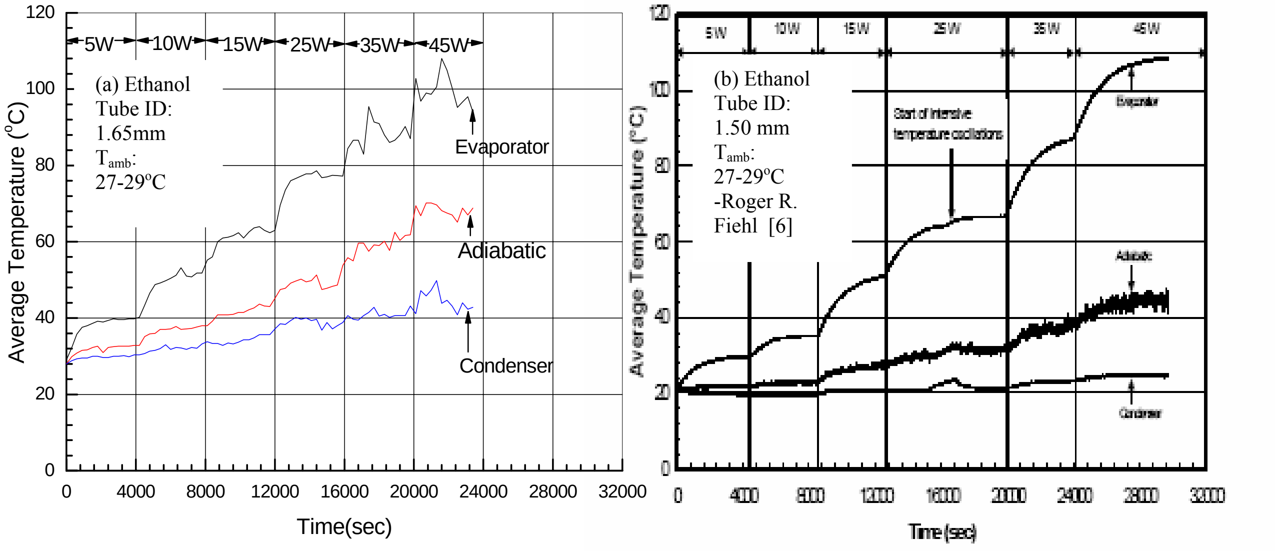

Fig. 2 OLPHP vertical test with ethanol

Upon testing the OLPHP under horizontal orientation as shown in Fig.2, it could be noticed that higher evaporation section temperatures were achieved for the same heat load levels. At lower heat load levels up to 15W, the vertical and horizontal orientation showed same temperature increment characteristics, but at higher heat loads the temperature was lower for vertical orientation which indicates that OLPHP could operate at high power levels. The OLPHP showed equivalent behavior for both orientations, where pulsations were captured by the thermocouples.

For ethanol, temperature oscillation started occurring from 10W power, but intensive oscillations were observed from 35W power as observed in the figure 3(a). For 45W, great perturbations were verified which indicated instabilities during the OLPHP operation without any tendency of dry out in the evaporator section. The same phenomenon was also observed by Roger R. Riehl [6] as shown in Fig. 3(b).

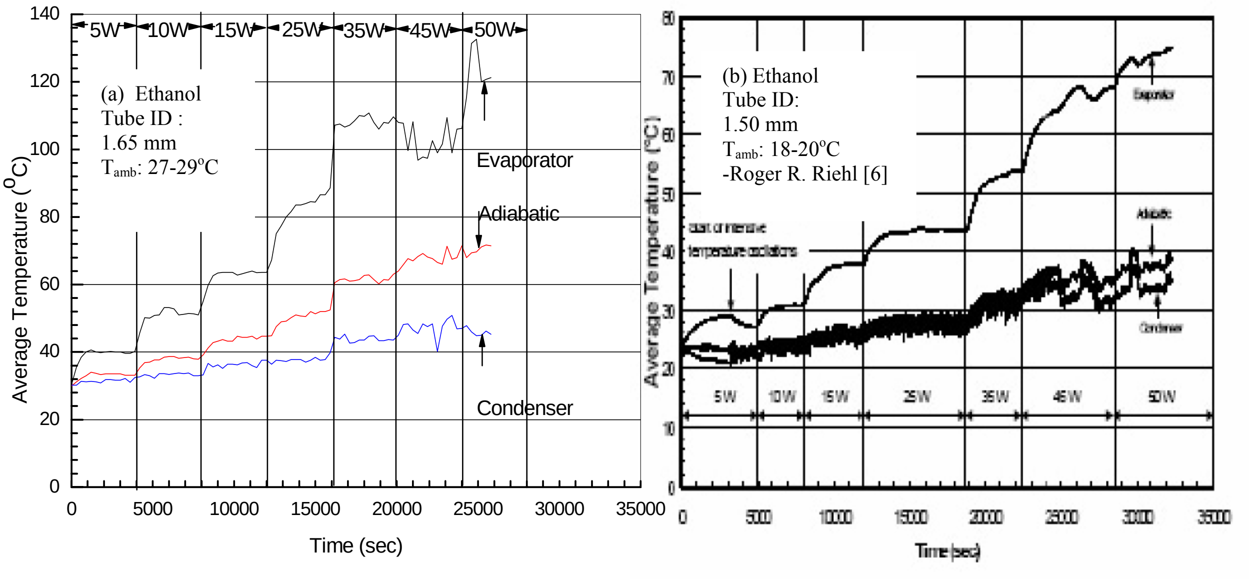

Fig.3 OLPHP horizontal test with ethanol

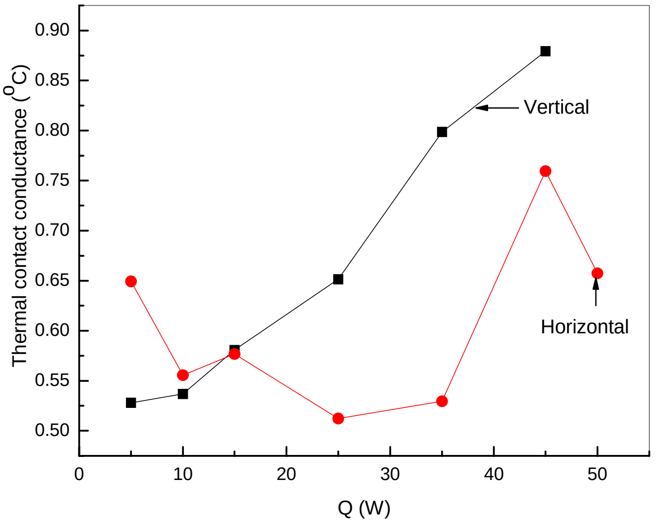

Fig. 4 Thermal contact conductance of OLPHP

Figure 4 presents the results for the thermal conductance based on the evaporation and condensation sections, for the OLPHP operating at vertical and horizontal orientations respectively. The value of the thermal conductance was determined by the following formula,

$$G = Q/ (T_E - T_C) \tag{3}$$

The value of the thermal conductance was greater for horizontal orientation at the beginning, but later this value decreased. For vertical orientation the value of the conductance gradually increased but for horizontal orientation the nature was fluctuating. Though fluctuations were observed, it can be observed that at first the value decreased slightly and then increased again. Nature of the increment of the value of the thermal contact conductance for horizontal orientation was similar to the nature for vertical orientation.

4. CONCLUSION

This paper presents an experimental investigation of an open loop pulsating heat pipe in which tests were performed for ethanol at both vertical and horizontal orientations. The conclusions that can be drawn from the investigation are as follows:

1. Lower temperature at evaporator was observed for vertical orientation for same heat load levels.
2. The value of the thermal conductance for the horizontal orientation was greater for low heat load. And at higher heat load thermal conductance is greater for the vertical orientation. A gradual increase in the value of thermal conductance was observed for vertical orientation but for horizontal case the values decreased at first and then increased again.
3. The beginning of the pulsation occurred almost at the same heat load for both orientation and pulsation was more drastic for horizontal orientation.

5. NOMENCLATURE:

A	Area ,m^2	Q	Heat load, W
d	Critical bubble diameter, m	T_C	Average condenser temperature, ^{o} C
g	Gravity acceleration, m/s^2	T_E	Average evaporator temperature, ^{o} C
i_{lv}	latent heat of evaporation, J/kg	T_{sat}	Saturation temperature, ^{o} C
G	Thermal conductance, W/^{o} C	T_{amb}	Ambient temperature, ^{o} C
Greek letters			
ρ_l	Liquid density, kg/m^3	σ	Surface tension, N/m
ρ_v	Vapor density, kg/m^3		

6. REFERENCE

[1] Akachi, H., Polášek F., Štulc P., "Pulsating Heat Pipes", Proceedings of the 5th International Heat Pipe Symposium, 1996, pp.208-217, Melbourne Australia.
[2] Zhang, Y., Faghri, A., "Heat Transfer in a Pulsating Heat pipe with an Open End", *International Journal of Heat and Mass Transfer,* Vol. 45, 2002, pp. 755-764.
[3] Riehl, R. R., "Evaluation of the Thermal-Hydro- Dynamics Behavior of an Open Loop Pulsating Heat Pipe", National Institute for Space Research (INPE)
Report,2003, 35p.
[4] haroensawan, P., Khandek ar, S., Groll, M., Terdtoon, P., "Closed Loop Pulsating Heat Pipes Part A: Parametric Experimental Investigations", *Applied Thermal Engineering,* 2003, Vol. 23, pp. 2009-2020.
[5] Khandekar, S., Dollinger, N., Groll, M., "Understanding Operational Regimes of Closed Loop Pulsating Heat Pipes: An Experimental Study" 2003, *Applied Thermal Engineering,* Vol. 23, pp. 707-719.
[6] Roger R. Riehl, "Characteristics of an Open Loop Pulsating Heat Pipe", SAE paper #2004-01-2509.

Proceedings of the 4th BSME-ASME International Conference on Thermal Engineering
27-29 December, 2008, Dhaka, Bangladesh

AIDING AND OPPOSING MECHANISMS OF DOUBLE DIFFUSIVE MIXED CONVECTION IN A TWO-SIDED LID-DRIVEN SQUARE CAVITY

Sumon Saha, Bidyut Baran Saha, Shigeru Koyama

Department of Energy and Environmental Engineering, Interdisciplinary Graduate School of Engineering
Sciences, Kyushu University, 6-1 Kasuga-koen, Kasuga-shi, Fukuoka 816-8580, Japan
E-mail: sumon@phase.cm.kyushu-u.ac.jp

ABSTRACT

The present study has been conducted to numerically investigate the heat and mass transport mechanism of laminar mixed convection in a shear- and buoyancy-driven cavity subjected to differential heating and differential species concentration. The focus is on the interaction of the forced convection induced by the moving sidewalls with the natural convection induced by the buoyancy. Two orientations of the direction of the moving walls at the cavity are considered in order to simulate the aiding and opposing buoyancy mechanisms. The two-dimensional transport equations for continuity, momentum, energy and species transfer are solved using the finite element formulation based on the Galerkin method of weighted residuals. Parametric studies of the effect of the mixed convection parameter, Richardson number on the fluid flow and heat and mass transfer have been performed. It is found that both Richardson number and the direction of moving walls affect the fluid flow and heat and mass transfer in the cavity. In addition, the predicted results for the average Nusselt and Sherwood numbers are presented and discussed for various parametric conditions.

Key words: *Double-diffusive flow; Heat and mass transfer; Lid-driven; Numerical simulation.*

1. INTRODUCTION

The structure of the fluid flow in a cavity driven by moving lid is a classical problem that has been the subject of widespread research for last three decades. Such prominent interest can be attributed due to its direct relevance in industrial applications. Secondly, it is a prototype problem in which many of the flow features with closed flow patterns can be studied. The motive behind the present study is to reveal the complex phenomena which results due to the interaction of the combined buoyancy forces of heat and mass transfer with the shear force of the moving lids. The most important investigation in a double-diffusive mixed convection process is the effect of thermal and solutal buoyancy on the forced convection transport rates. Depending on their relative directions to the direction of inertia-driven flow, the buoyancy forces may aid or oppose the forced flow, causing an increase or decrease in heat and mass transfer rates.

A review of literature shows that some studies in past were associated with side driven differentially-heated enclosures, where one wall or both vertical walls move with a constant velocity. Combination of buoyancy forces due to temperature difference and forced convection due to shear, results in a mixed convection heat transfer. Arpaci and Larsen [1] have presented an analytical treatment of the mixed convection heat transfer in tall cavities, which had one vertical side moving and vertical boundaries at different temperatures with adiabatic horizontal boundaries. Aydin [2] studied numerically and revealed the mechanisms of aiding and opposing forces in shear and buoyancy driven cavity. He carried out the parametric study for Gr/Re^2 from 0.01 to 100 with $Pr = 0.71$. He pointed that the range of Gr/Re^2 for opposing flow is wider than aiding-buoyancy case, although he did not present any quantitative information regarding these regimes and heat transfer characteristics. Later, Aydin and Yang [3] numerically studied mixed convection heat transfer in a two-dimensional square cavity with downwardly moving isothermal side walls. Guo and Sharif [4] then performed numerical simulation for the same mixed convection problem replacing the isothermal heat source by the isoflux heat source at the bottom wall. Oztop and Dagtekin [5] performed numerical analysis of mixed convection in a square cavity with moving and differentially heated sidewalls for three different configurations depending on the direction of moving walls. Kuhlmann *et al.* [6] conducted a numerical and experimental study on steady flow in rectangular two-sided lid-driven cavities. They found that the basic two-dimensional flow was not always unique.

The subject of mixed convection for double diffusion in cavities has also been studied extensively [7-10]. Yet, most work done considers flow through open or vented cavities [7-9]. In some applications, such as crystal growing, float glass production, metal casting, it is more appropriate to model the process of heat and mass transfer in closed lid-driven cavities, which is the subject of the present work. The present study extends the previous work of Oztop and Dagtekin [5] to include the effects of mass transfer. To obtain the characteristics of double diffusive mixed convection inside a lid-driven square cavity, numerical calculations are performed over a wide range of governing parameter.

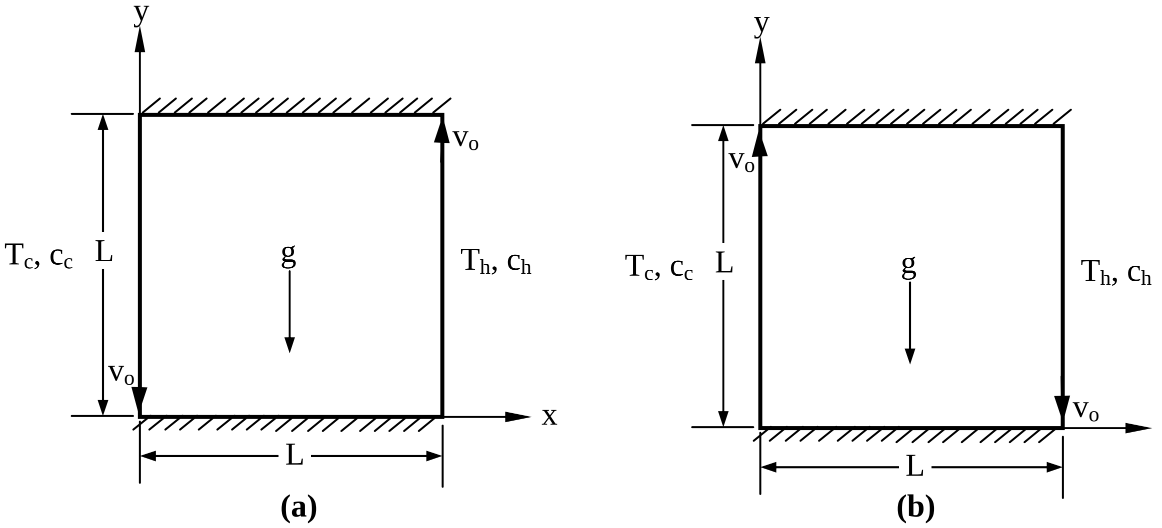

Fig. 1 Schematics of the problem with (a) aiding and (b) opposing flow configurations

2. PROBLEM DEFINITION

The domain under analysis is, as sketched in Fig. 1, a square, two-dimensional cavity of length L × L, suffering the influence of a gravitational field with a fluid which contains a pollutant concentration. The vertical walls are maintained at constant different levels of temperature and concentration as well as different direction of sliding constant velocity (v_o), thus giving rise to a double-diffusive mixed convection problem. The top and bottom surfaces are assumed to be adiabatic and impermeable.

3. MATHEMATICAL MODEL

The governing mass, momentum, energy and species conservation equations for double-diffusive mixed convective flows driven by the combined effect of the internal buoyancy induced from temperature and concentration differences and the external mechanical-driven forced flow through the moving lids under steady-state condition are given as dimensionless forms:

$$\frac{\partial U}{\partial X}+\frac{\partial V}{\partial Y}=0 \tag{1}$$

$$U\frac{\partial U}{\partial X}+V\frac{\partial U}{\partial Y}=-\frac{\partial P}{\partial X}+\frac{1}{\mathrm{Re}}\left(\frac{\partial^2 U}{\partial X^2}+\frac{\partial^2 U}{\partial Y^2}\right) \tag{2}$$

$$U\frac{\partial V}{\partial X}+V\frac{\partial V}{\partial Y}=-\frac{\partial P}{\partial Y}+\frac{1}{\mathrm{Re}}\left(\frac{\partial^2 V}{\partial X^2}+\frac{\partial^2 V}{\partial Y^2}\right)+\mathrm{Ri}\left(\Theta-\mathrm{N}C\right) \tag{3}$$

$$U\frac{\partial \Theta}{\partial X}+V\frac{\partial \Theta}{\partial Y}=\frac{1}{\mathrm{Re\,Pr}}\left(\frac{\partial^2 \Theta}{\partial X^2}+\frac{\partial^2 \Theta}{\partial Y^2}\right) \tag{4}$$

$$U\frac{\partial C}{\partial X}+V\frac{\partial C}{\partial Y}=\frac{1}{\mathrm{RePrLe}}\left(\frac{\partial^2 C}{\partial X^2}+\frac{\partial^2 C}{\partial Y^2}\right) \tag{5}$$

where, the dimensionless variables are

$$\left(X,Y\right)=\frac{\left(x,y\right)}{L},\ \left(U,V\right)=\frac{\left(u,v\right)}{v_o},\ P=\frac{p}{\rho v_o^2},\ \Theta=\frac{T-T_c}{T_h-T_c},\ C=\frac{c-c_c}{c_h-c_c}$$

and the dimensionless parameters are Reynolds number, Grashof number, Richardson number, Prandtl number, Lewis number and the buoyancy ratio which are defined as follows:

$$\mathrm{Re}=\frac{v_o L}{\upsilon},\ \mathrm{Gr}=\frac{g\beta_T\left(T_h-T_c\right)L^3}{\upsilon^2},\ \mathrm{Ri}=\frac{\mathrm{Gr}}{\mathrm{Re}^2},\ \mathrm{Pr}=\frac{\upsilon}{\alpha},\ \mathrm{Le}=\frac{\upsilon}{D}\ \text{and}\ \mathrm{N}=\frac{\beta_c\left(c_h-c_c\right)}{\beta_T\left(T_h-T_c\right)}$$

The heat and mass transfer rates on the surfaces of heat and contaminant sources are described by the average Nusselt and Sherwood numbers, respectively as follows

$$Nu=\int_0^1 -\left(\frac{\partial \Theta}{\partial X}\right)\Big|_{X=1} dY \tag{6}$$

$$Sh=\int_0^1 -\left(\frac{\partial C}{\partial X}\right)\Big|_{X=1} dY \tag{7}$$

4. NUMERICAL PROCEDURE

The solution of the governing equations along with the boundary conditions is obtained through the Galerkin finite element formulation. In this method, the solution domain is discretized into finite element meshes which are composed of triangular elements. Then the nonlinear governing partial differential equations i.e., mass, momentum, energy and concentration equations are transferred into a system of integral equations by applying Galerkin weighted residual method.

5. RESULTS AND DISCUSSION

The effect of the Richardson number Ri on the steady-state streamline, temperature and concentration distributions as well as the average Nusselt and Sherwood numbers (Nu and Sh) are presented for the following constant governing parameters: Pr = 0.7, N = 1 and Le = 1. To vary Ri from 0.01 to 100, Gr is fixed at 10^4 while changing Re through the lid-velocity, v_o. The influence of varying Ri on the transport phenomena is shown in Fig. 2 for aiding flow configuration. The Richardson number provides a measure for the importance of the thermal natural convection relative to the lid-driven forced convection effect.

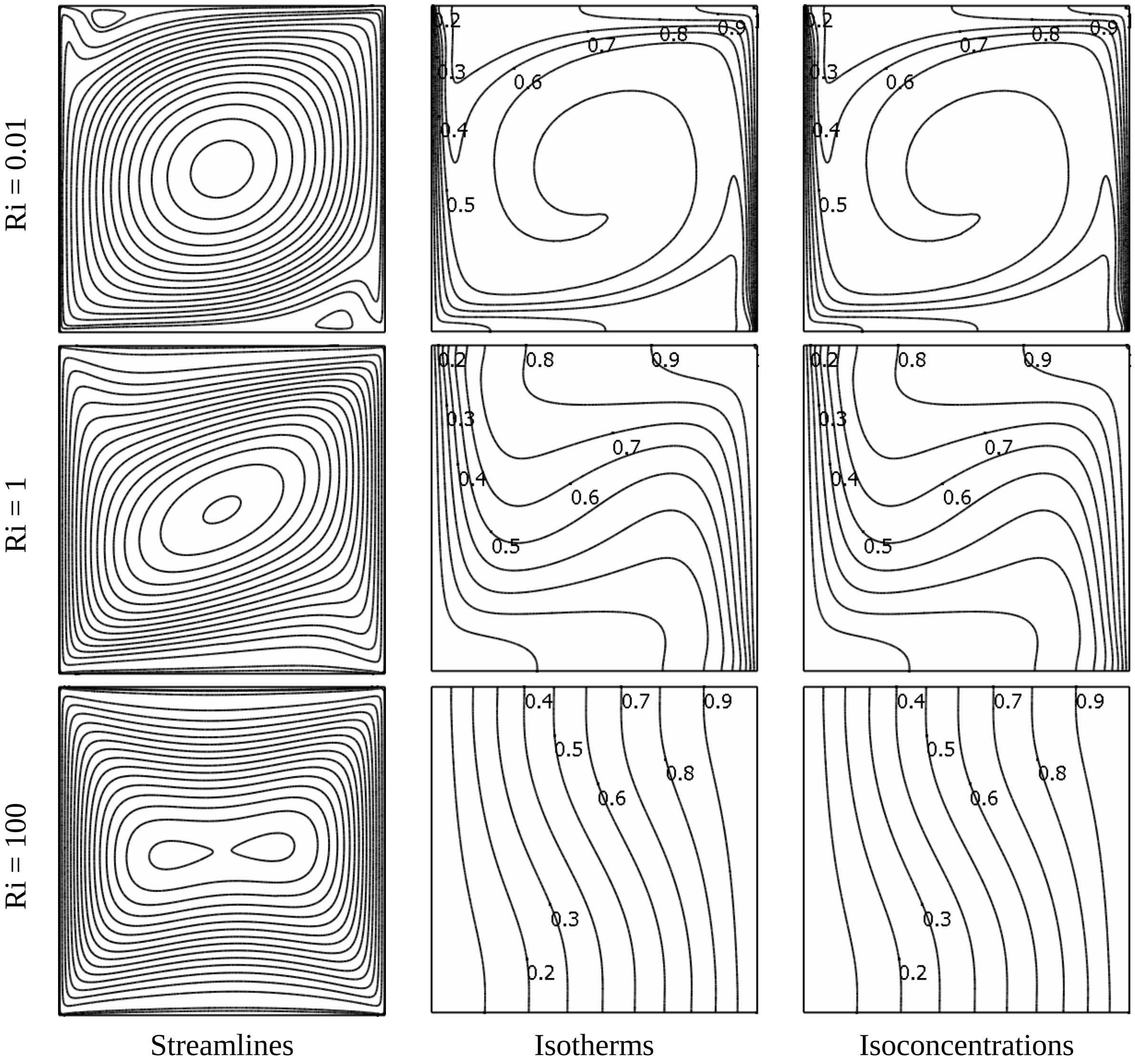

Fig. 2 Effect of Richardson number on the streamlines, isotherms and isoconcentrations for aiding flow configuration

The similar diffusion characteristics for both heat and mass transfer are observed as Le = 1 and N = 1 for fixed Pr = 0.7. The top row of Fig. 2 shows that the forced convection plays a dominant role and the counter-clockwise recirculation flow is mostly generated only by moving lids. Some perturbations in the streamlines are also observed in the upper left and lower right corners due to impingement of fluid to the horizontal wall. The middle row of Fig. 2 shows streamlines, isotherms and isoconcentrations for Ri = 1, in which case forced and natural convection heat transfer as well as mass transfer are comparable. There is less significant effect of the moving lids on the flow patterns. Since Gr = 10^4 in the present problem, at high Richardson number (Ri = 100), the buoyancy effect can be observed in the last row of Fig. 2, but not so dominant compare to forced flow situation. From the isotherm and isoconcentration patterns, it is clearly visible that the change in flow patterns make the heat and mass transfer rates lower as those lines become almost parallel horizontally.

In the opposing flow configuration case, the left vertical wall is moving upwards while the right wall downwards. The streamlines, isotherms and isoconcentrations for all Ri as shown in Fig. 3 represent a mirror image of those in Fig. 2 with circulation direction changing from counter-clockwise to clockwise due to moving plate directions.

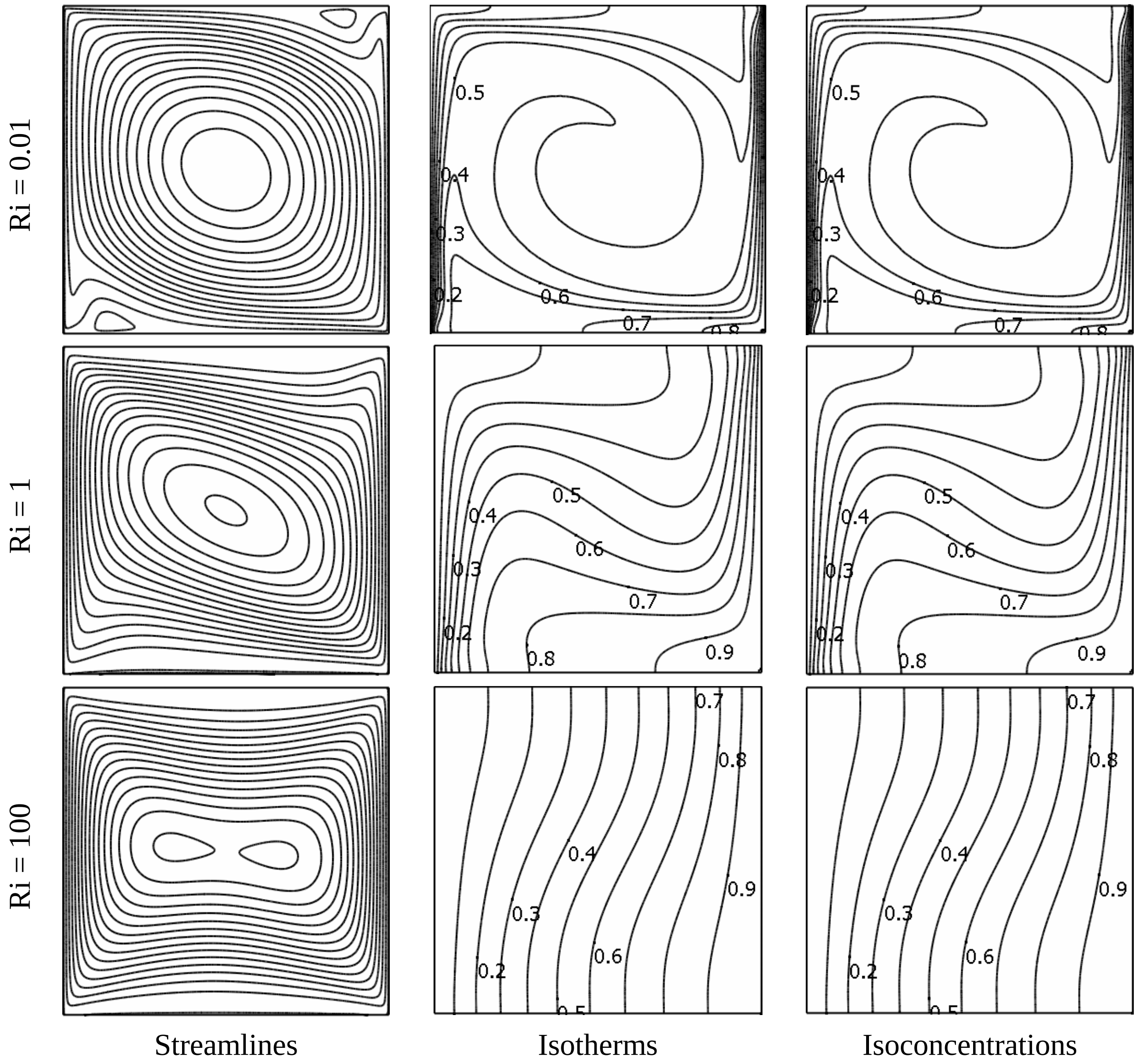

Fig. 3 Effect of Richardson number on the streamlines, isotherms and isoconcentrations for opposing flow configuration

Table. 1 Average Nusselt and Sherwood number with the variation of Richardson number for aiding and opposing flow configurations

Ri	Average Nusselt and Sherwood number	
	Assisting Flow	Opposing Flow
0.01	16.048	16.014
0.1	8.850	8.840
1	4.624	4.620
10	1.888	1.887
100	1.109	1.109

The average Nusselt and Sherwood numbers for both configurations are listed in Table 1 as a function of Richardson number. Both average Nusselt and Sherwood numbers are equal value due to same physical data and boundary conditions considered for the case of heat and mass transfer equations in the present problem. It is found that for higher Richardson number

(Ri > 1), average Nusselt and Sherwood numbers are lower but almost same for both configurations. However, aiding flow situation always gives greater value of average Nusselt and Sherwood numbers compare to opposing case as observed in lower Richardson number. Moreover, when Ri < 1, both average Nusselt and Sherwood number are much higher because of the dominant forced flow and weaker buoyancy effect.

6. CONCLUSIONS

This study has been concerned with the numerical modeling of double diffusive mixed convection in two-sided lid-driven differentially heated and concentrated cavities. The governing parameter is Richardson number, which characterizes the heat and mass transfer regime in double diffusive mixed convection. For Ri < 1, the flow, heat and mass transfer is dominated by forced flow, for Ri > 1, it is dominated by buoyancy arises due to temperature and concentration gradients and for Ri = 1, it is a mixed regime. For Ri > 1, the average Nusselt and Sherwood number relatively low and has the almost same order of magnitude for the two flow configurations. For Ri < 1, the forced flow becomes dominant, the buoyancy effect becomes relatively weaker, as a result of which both Nu and Sh are relatively higher. But the aiding flow configuration shows larger heat and mass transfer compare to the opposing flow configuration in that regime.

REFERENCES

[1] Arpaci, V. S., Larsen, P. S., Convection Heat Transfer, Prentice-Hall, 1984.

[2] Aydin, O., Aiding and Opposing Mechanisms of Mixed Convection in a Shear and Buoyancy Driven Cavity, *International Communication in Heat and Mass Transfer*, 26 (1999), pp. 1019-1028.

[3] Aydin, O., Yang, W. J., Mixed Convection in Cavities with a Locally Heated Lower Wall and Moving Sidewalls, *Numerical Heat Transfer, Part A*, 37 (2000), pp. 695-710.

[4] Guo, G., Sharif, M. A. R., Mixed Convection in Rectangular Cavities at Various Aspect Ratios with Moving Isothermal Sidewalls and Constant Flux Heat Source on the Bottom Wall, *International Journal of Thermal Science*, 43 (2004), pp. 465–475.

[5] Oztop, H. F., Dagtekin, I., Mixed Convection in a Two-Sided Lid-Driven Differentially Heated Square Cavity, *International Journal of Heat and Mass Transfer*, 47 (2004), pp. 1761-1769.

[6] Kuhlmann, H. C., Wanschura, M., Rath, H. J., Flow in Two Sided Lid-Driven Cavities: Non-Uniqueness, Instabilities, and Cellular Structures, *Journal of Fluid Mechanics*, 336 (1997), pp. 267-299.

[7] Brown, N. M., Lai, F. C., Correlations for Combined Heat and Mass Transfer from an Open Cavity in a Horizontal Channel, *International Communication in Heat and Mass Transfer*, 32 (2005), pp. 1000-1008.

[8] Deng, Q. H., Zhou, J., Mei, C., Shen, Y. M., Fluid, Heat and Contaminant Transport Structures of Laminar Double-Diffusive Mixed Convection in a Two-Dimensional Ventilated Enclosure, *International Journal of Heat and Mass Transfer*, 47 (2004), pp. 5257-5269.

[9] Saha, S., Saha, B. B., Numerical Simulation on Double Diffusive Mixed Convection inside a Vented Square Cavity, Proceedings of the 2nd International Forum on Heat Transfer, Tokyo, Japan, September 17-19, 2008.

[10] Al-Amiri, A. M., Khanafer, K. M., Pop, I., Numerical Simulation of Combined Thermal and Mass Transport in a Square Lid-Driven Cavity, *International Journal of Thermal Sciences*, 46 (2007), 7, pp. 662-671.

Proceedings of the 4th BSME-ASME International Conference on Thermal Engineering
27-29 December, 2008, Dhaka, Bangladesh

OPTIMIZATION OF FLOW RATE AND PRESSURE OF HIGH PRESSURE COOLANT IN TURNING AISI-4320 STEEL: TEMPERATURE, CHIP REDUCTION COEFFICIENT AND SURFACE ROUGHNESS

I. SULTANA, M. M. H. CHOWDHURY and N. R. DHAR

Department of Industrial & Production Engineering
Bangladesh University of Engineering & Technology (BUET)
Email: nrdhar@ipe.buet.ac.bd

ABSTRACT

Machining materials is associated with the generation of large amount of heat and cutting temperature. Additionally, high production machining inherently produce high cutting zone temperature. Determination of the maximum temperature and temperature distribution at the chip- tool interface zone is of particular importance because of its detrimental influence on tool life, as well as, the quality of the machined part. On the other hand, determination of optimal cutting parameters is another important element in any process planning of metal parts. This paper deals with a view to optimize the pressure (P) and flow rate (Q) of high pressure coolant to obtain improved machining performances in turning AISI-4320 steel by uncoated carbide insert in respect of cutting temperature, chip reduction co-efficient and surface roughness. In this study, optimization has been carried out with the help of Design of Experiment (DOE) along with Multiple Attribute Decision Making (MADM) method and multiple graphical plots. The results show that the optimal combinational effect of average chip-tool interface temperature, chip reduction co-efficient and surface roughness can be achieved by optimizing cutting speed, feed rate along with the pressure and flow rate of HPC coolant jet. Other significant effects such as the interaction between the process parameters are also investigated.

KEYWORDS: *HPC, MADM, DOE, Weighted product model, temperature, chip, surface roughness.*

1. INTRODUCTION

Generation of heat is an inherent character of metal cutting process. The heat generated during machining also raises the temperature of the cutting tool tips and the work-surface near the cutting zone. Due to such high temperature and pressure the cutting edge deforms plastically and wears rapidly which lead to dimensional inaccuracy, increase in cutting forces and premature tool failure. On the other hand, the cutting temperature, if it is high and is not controlled worsens the surface topography and impairs the surface integrity by oxidation and introducing residual stresses, micro-cracks and structural changes [1].

Cutting fluids are widely used in machining operations to obtain accuracy of part dimensions, longer tool life and in some cases better surface finish. But in the high speed-feed machining, which inherently generates high cutting zone temperature, cutting fluid can't reach to the chip-tool interface to reduce the temperature [2]. The machining costs (labor and overhead) in the US alone are estimated to be $300 billion/year [3]. The cost estimated with the use of cutting fluids is estimated to be about 16% of the manufacturing costs [4,5] which is much more times than the labor and overhead figures quoted above. Moreover, like other manufacturing activities, machining also leads to environmental pollution mainly because of using cutting fluids [6].

Dry machining is becoming increasingly popular as a means of reducing production costs while protecting the environment. Most problems associated with dry machining are related to heat. Deformation occurs earlier, degrading tool life. Thermal expansion of the work piece makes it hard to hold tight dimensional tolerances. Particularly in ferrous materials, an increase in cut temperature produces softer, more ductile chips. Chip control can quickly become difficult. In the absence of lubrication, surface finish can deteriorate quickly.

Some works have recently been done on cryogenic cooling by liquid nitrogen jet in machining and grinding some steel of common use [7]. It has also been reported that though the machining of steel with liquid nitrogen improves the machinability index, it is not used in industrial practices due to high cost of liquid nitrogen. Minimum quantity lubrication machining in particular has been accepted as a successful semidry application because of its environmentally friendly characteristics. Some good results have been obtained with this technique [8]. Possibilities of controlling high cutting temperature in high production machining by high-pressure coolant (HPC) has been reported also. Cutting forces and temperature were found to reduce while machining steel with tribologically modified carbide inserts. HPC injection technique not only provided reduction in cutting forces and temperature but also reduced the consumption of cutting fluid by 50% [9].

Optimization in metal cutting processes is carried out since many days in order to optimize the cutting or process parameters to achieve cost effective machining. In the manufacturing sector, it is very important to optimize process parameters for improving product quality, shortening processing time, reducing production cost and increasing product competitiveness [10]. In the cases involving multiple criteria, ad hoc methods such as multiple plots or engineering heuristics have been used to estimate the optimum [11]. Elsayed and Chen [12] presented an approach that lists all possible values of performance measures in a table and directly selects the optimized levels (or settings). Mayers et al. [13] briefly mentioned the use of multiple criteria optimization in the analysis of multi-response experiments.

In this study, a detailed experimental investigation has been carried out based on design of experiment to examine the effect of high-pressure coolant (HPC) as well as to find out the most influential factors affecting machining response in turning AISI 4320 steel with carbide tool. The process attributes, cutting temperature (θ), chip reduction coefficient (ζ), surface roughness (R_a) are then analyzed by implementing multiple attribute decision making method and then extending it by graphical method to find out the optimum values of pressure and flow rate.

2. EXPERIMENTAL INVESTIGATION

The experiment was carried out by turning of AISI 4320 steel rod having initial diameter 192 mm and length 520 mm in a CNC lathe (10 hp, Okuma, LB15) by using uncoated carbide insert (SNMG 120408 TTR) at different cutting velocities (V_c) and feed rates (S_o) under high-pressure coolant (HPC) condition having various pressure and flow rates. The photographic view of the experimental set-up is shown in Fig.1.Depth of cut was kept fixed at 1.5 mm. The Experimental conditions are given in Table-1.

Table-1 Experimental conditions

Machine tool	: CNC lathe (Okuma LB15), 7.5 kW
Work materials	: AISI 4320 Steel (φ192 X 520 mm)
Cutting insert	: Carbide, SNMG 120408 (P30 grade ISO specification), WIDIA
Tool holder	: PSBNR 2525 M12 (ISO specification), WIDIA
Working tool geometry	: -6°,-6°,6°,15°,75°,0.8 mm
Process parameters	
Cutting velocity, V_c	: 104, 148, 211 and 296 m/min
Feed, S_o	: 0.10, 0.14, 0.18, 0.22 mm/rev
Depth of cut, t	: 1.5 mm
High-pressure Coolant	: Pressure: 30, 50, 70 and 90 bar Coolant flow rate: 3, 4, 5 and 6 l/min through external nozzle having 0.5 mm tip diameter.
Environment	: High-pressure coolant

The application of high-pressure coolant jet is expected to affect the various machinability characteristics mainly by reducing the cutting temperature. Simple but a reliable tool–work thermocouple technique with proper calibration was used to measure the average cutting temperature under high-pressure coolant condition [7]. Chips are collected for each velocity-feed combination under high-pressure coolant conditions. Then thickness of the chips at different position is measured by a digital slide calipers for calculating the chip reduction coefficient (ξ). The surface roughness was monitored by a Talysurf (Surtronic 3^+, Rank Taylor Hobson) using a sampling length of 0.8mm.

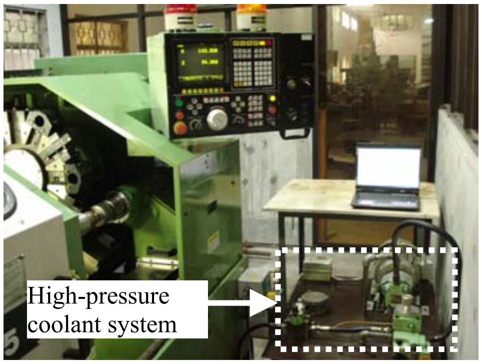

Fig.1 Photographic view of the experimental set-up

3. EXPERIMENTAL RESULT AND DISCUSSION

Heat generation is a very common phenomenon in metal cutting processes. During machining, the maximum heat is generated at the chip-tool interface. Hence the temperature generated at the chip-tool interface has been used in this research work to indicate machinability and defined as average chip-tool interface temperature (θ). The main justification for considering cutting temperature is its detrimental effects on chip formation, cutting forces, tool life, dimensional accuracy and surface integrity of the workpiece. In order to control this increased temperature, High pressure coolant jet has been applied at optimized pressure and flow rate to improve the aforesaid machinability indices.

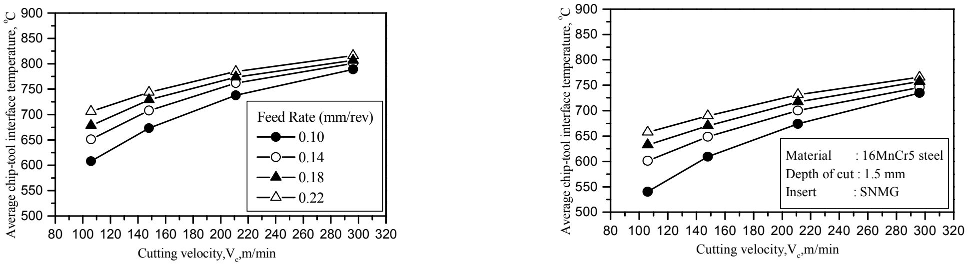

(a) 30 bar and 3 liter/min (b) 90 bar and 6 liter/min

Fig.2 Variation of average chip-tool interface temperature at different pressure and flow rate

The nature of variation in cutting temperature during turning at different V_c, S_o, P and Q under HPC condition is shown in Fig.2. Two things are very clear from the following graphs. The first one is θ always follows an increasing trend with the increase of V_c as well as S_o. This is mainly due to increased energy input at higher V_c and S_o. Secondly, changing the parameters of HPC lubrication system has a high impact on temperature reduction during machining. It is clear from the Fig.2 that approximately 6~10% temperature reduction is carried out by changing P & Q from 30 bar to 90 bar and 3 l/m to 6 l/m respectively. This is due to the action of HPC as both lubricant and coolant. Increased values of P& Q reduce the friction at the chip-tool interface resulting less heat generation.

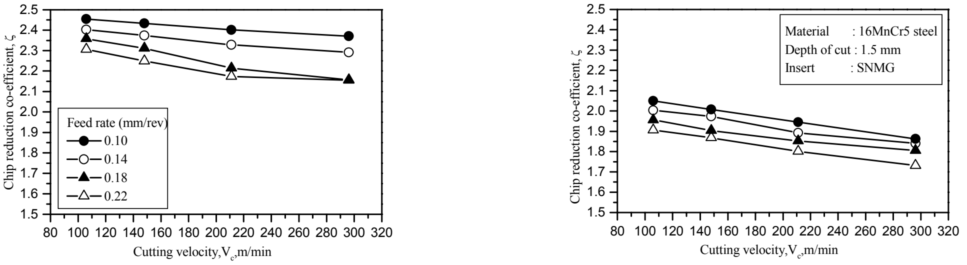

(a) 30 bar and 3 liter/min (b) 90 bar and 6 liter/min

Fig.3 Variation of ξ at different pressure and flow rate

Chip reduction co-efficient is an important response of machining process which not only reflects the influences on the chip thickness but also signifies the amount of cutting force implied on work material by cutting tool and hence the amount of cutting power consumption. Fig.3 clearly shows the nature of variation of ζ at different values of V_c and S_o along with changing P & Q. It is clear from the Fig.3 that ζ usually decreases with the increase of V_c and S_o particularly at its lower range due to plasticization and shrinkage of the shear zone for reduction in friction and built up edge formation at the chip-tool interface. This may due to built up edge which changes the effective rake angle of the cutting tool.

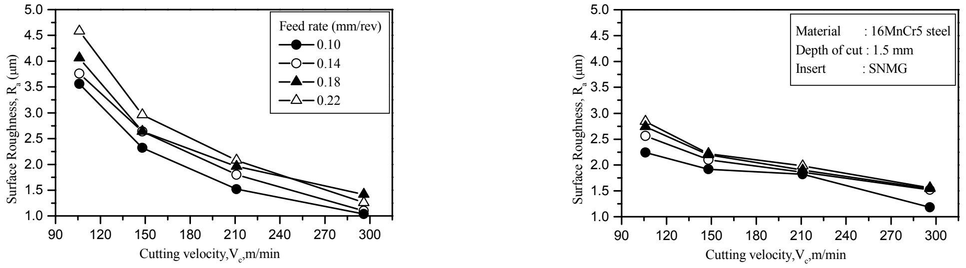

(a) 30 bar and 3 liter/min (b) 90 bar and 6 liter/min

Fig.4 Variation of surface roughness at different pressure and flow rate

Surface finish is also another important factor which signifies the extent of performance and service life of the machined part. Though good surface finish is achievable by finishing operation but it is highly desirable to obtain a good surface finish during machining as much as possible to reduce the machining cost.

Fig.4 shows the variation of surface roughness with respect to different cutting speeds and feed rates, pressure and flow rate. It is clear from Fig.4 that the roughness decreases with the increase in V_c and with the decrease of S_o. It is distinct from the Fig.4 that changing the pressure (P) and flow rate (Q) can affect the R_a at the lower velocity ranges for all feed values. At industrial speed-feed conditions, approximately 3~20% reduction in R_a is achievable by changing P and Q. This phenomenon can be explained by the fact that increasing pressure and flow rate of HPC jet is able to enter into the chip-tool interface which enhances the chip breakability resulting smooth surface finish on the machined component.

4. DESIGN OF EXPERIMENT (DOE)

Design of experiment (DOE) is a very effective statistical method by which it is possible to determine the most influential factors affecting the output among many factors. There are three responses θ, ζ, and R_a controlled by four design factors, V_c, S_o, P and Q. Among many other methods of DOE, 2^k factorial design method has been conducted here where K signifies the four design factors having two levels each. Therefore, 16 experiments have been carried out under 2^4 factorial design. Table-2 presents the 4 design factors with their 2 levels (maximum and minimum).

Table 2: factors and levels selected:

Level	V_c (m/min)	S_o (mm/rev)	P (bar)	Q (liter/min)
maximum	104	0. 10	30	3
Minimum	296	0. 22	90	6

Table 3 represents the design matrix containing observations of the 16 trial experiments. Here, A, B, C, D denote feed rate, cutting speed, pressure and flow rate respectively. Again, AB or ACD etc. indicate the interaction effect of feed and speed and feed, Pressure & flow rate respectively. From this table it is clear that the most influential factors are different for different responses. It can be concluded from the table that

i. The most influential factors affecting θ are V_c, S_o, P, interactions effect of Vc and S_o and Q which are ranked from 1 to 5 as shown in Table-3. It can be seen that flow rate has a minor effect on θ compared to others.

ii. Interestingly, in case of chip reduction co-efficient, the most influential factor is Q. Again, three factor interaction effects (V_c, Q and P) has come into consideration to affect ζ. The contributing factors, Q, S_o, P, V_c, interactions among V_c, Q and P which are of 27.5%, 21%, 18.4%, 17%, 3.67% respectively.

iii. Alike cutting temperature scenarios, Vc and So are the two influential factors to affect Ra. The other three factors are Q, interaction of V_c and P as well as P and Q having 10.3%, 8.4%, & 7.9% effects on R_a respectively.

Table-3 Design of Experiment

cell	**main effects**				**interaction factors**											**output**		
	A	**B**	**C**	**D**	**AB**	**AC**	**AD**	**BC**	**BD**	**CD**	**ABC**	**ABD**	**ACD**	**BCD**	**ABCD**	**θ**	**ξ**	**Ra**
1	-1	-1	-1	-1	1	1	1	1	1	1	-1	-1	-1	-1	1	608	2.454	3.56
2	1	-1	-1	-1	-1	-1	-1	1	1	1	1	1	1	-1	-1	706	2.306	4.58
3	-1	1	-1	-1	-1	1	1	-1	-1	1	1	1	-1	1	-1	789	2.371	1.04
4	1	1	-1	-1	1	-1	-1	-1	-1	1	-1	-1	1	1	1	815	2.155	1.26
5	-1	-1	1	-1	1	-1	1	-1	1	-1	1	-1	1	1	-1	545	2.381	2.80
6	1	-1	1	-1	-1	1	-1	-1	1	-1	-1	1	-1	1	1	658	2.165	3.50
7	-1	1	1	-1	-1	-1	1	1	-1	-1	-1	1	1	-1	1	738	2.205	1.18
8	1	1	1	-1	1	1	-1	1	-1	-1	1	-1	-1	-1	-1	775	1.948	1.84
9	-1	-1	-1	1	1	1	-1	1	-1	-1	-1	1	1	1	-1	600	2.278	1.90
10	1	-1	-1	1	-1	-1	1	1	-1	-1	1	-1	-1	1	1	696	2.052	3.44
11	-1	1	-1	1	-1	1	-1	-1	1	-1	1	-1	1	-1	1	780	2.122	0.88
12	1	1	-1	1	1	-1	1	-1	1	-1	-1	1	-1	-1	-1	813	1.901	1.28
13	-1	-1	1	1	1	-1	-1	-1	-1	1	1	1	-1	-1	1	541	2.050	2.24
14	1	-1	1	1	-1	1	1	-1	-1	1	-1	-1	1	-1	-1	654	1.906	2.84
15	-1	1	1	1	-1	-1	-1	1	1	1	-1	-1	-1	1	-1	736	1.863	1.18
16	1	1	1	1	1	1	1	1	1	1	1	1	1	1	1	765	1.732	1.56
rank	**2**	**1**	**3**	**5**	**4**													
θ	545	1203	395	49	295	39	3	29	2.99	8.99	25	1.01	13	11	17			
rank	**2**	**4**	**3**	**1**									**5**					
ξ	1.6	1.3	1.4	2.1	0.1	0.06	0.12	0.2	0	0.2	0.03	0.13	0.28	0.1	0			
rank	**2**	**1**		**3**				**5**	**4**									
Ra	5.52	15	0.8	4.4	2.2	0.8	0.32	3.4	3.6	1.44	1.68	0.5	1.1	1.7	0.16			

Overall one decision is certain from the DOE that interaction effects are not dominant here for any machining response. Therefore, optimizing main effects should be given higher priority.

5. MULTIPLE ATTRIBUTE DECISION MAKING METHOD

Design of Experiment of this present research work contains 16 runs in order to find out the influencing or dominant design factors. These 16 combinations of the four process parameters and each combination provide an alternative for decision making. The three responses, θ, ζ and R_a are regarded as the three attributes of the attributive matrix under the Weighted Product Model (WPM). Different weights are assigned to θ, ζ and R_a according to different machining requirement. Hence, in this research paper, a complete spectrum of weights is presented [10]. WPM has been carried out for the attribute matrix where the sensitivity study of the model is done by assigning a series of weights to the attributes. Table 4 lists the optimized solutions under different weight scenarios.

Table 4: Optimal solutions from WPM

Weight allotted to θ (%)	Weight allotted to ζ (%)	Weight allotted to R_a (%)	Optimal set of solutions
33.33	33.33	33.34	{15},{16, 13}
25	25	50	{15}, {11}
25	50	25	{15, 16}
50	25	25	{13},{9}
75	12.5	12.5	{13}
100	0	0	{13}
12.5	75	12.5	{16}, {15}
12.5	12.5	75	{11}, {15}
0	100	0	{16}
0	0	100	{11},{13}
0	50	50	{15, 16}
25	75	0	{16}, {14}

It can be found that for maximum weight range, the optimized solution set contains 13, 15, 16 trial runs. This indicates that this three solution set are robust against the weight change of θ, ζ and R_a. This also indicates that the increased level of P & Q from 30 bar and 3 liter/min respectively will provide effective machining.

6. OPTIMIZATION OF PRESSURE AND FLOW RATE

In conventional machine tools, changing the values of V_c and S_o is limited to manufacturers' specifications. On the other hand, changing the pressure (P) and flow rate (Q) of the coolant is free from this limitation and almost any required values of P and Q can be provided. Multiple Objective Decision Making method can be used to optimize the pressure and flow rate. In this paper, optimization is carried out by plotting the normalized weightage matrix done under weighted product model (WPM) along with the findings of DOE. It is distinct from the DOE table that V_c and S_o are the common dominant factors in all the three responses and optimizing V_c and S_o definitely return much better output than optimization of pressure and flow rate alone. Therefore, graphs of weighted normalized attributes at different V_c & S_o are plotted first to get the optimum values. The intersection or the minimum points of these graphs will return the optimized P and Q values. Fig.5 presents a graph of equally weighted normalized θ, ζ and R_a with respect to V_c and S_o.

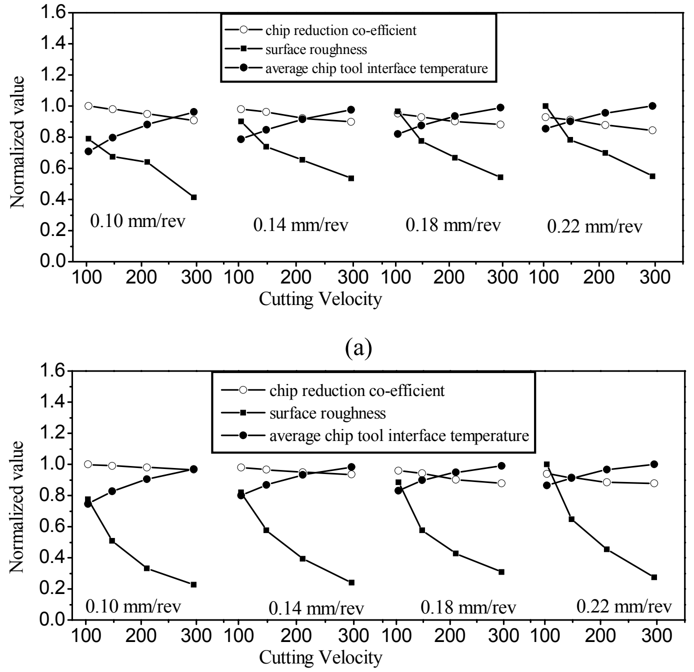

(a)

(b)

Fig.5 Optimization of cutting speed & flow rate at (a) 30 bar & 3 liter/min (b) 90 bar & 6 liter/min

It is clear from the graph that the intersection point returns the optimal set of {V_c, S_o} which are {180, 0.18} and {148, 0. 22}. {211,0.14} set also shows better result. Next, normalized θ, ζ, and R_a values are plotted again with respect to different flow rates for any one of the optimal sets of V_c and S_o.

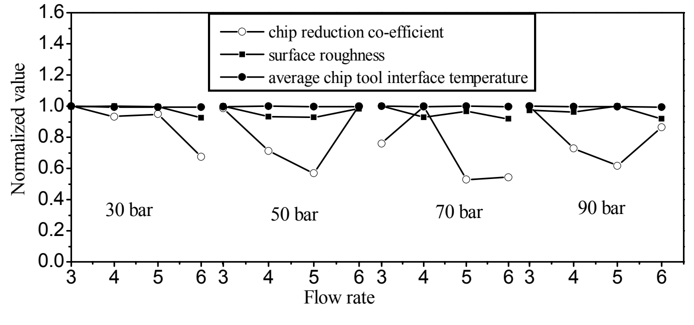

Fig.6 Optimization of pressure and flow rate at 211 m/min & 0.14 mm/rev

The entire problem is a minimization problem where all the three attributes are non-beneficial. Hence, the minimum normalized value derived from the function: (1/3) θ + (1/3) ζ + (1/3) R_a is the clear indication of the effective combinational effect of the three responses. Fig. 6 shows the trends of θ, ζ, and R_a with respect to different flow rates at 30, 50, 70, 90 bars respectively. It is distinct from the graph that the minimum normalized value is found in the third panel at 70 bar and 6 liter/min.

7. CONCLUSION

The optimized results of the pressure and flow rate of the HPC coolant jet along with the experimentally observed effect of the HPC in turning AISI 4320 steel by uncoated carbide insert may be summarized as follows:

i. Average cutting temperature at the chip-tool interface is highly influenced by mainly cutting speed, V_c along with S_o and P. In case of chip reduction co-efficient, flow rate plays the key role along with feed rate and pressure. On the other hand, surface roughness is highly influenced by the cutting velocity along with feed rate.

ii. In case of conventional machine tools, where range of cutting speed and feed rate entirely depends on manufacturers' specification, MADM approach can successfully draw optimal set of solutions of process parameters. It can be concluded by applying WPM approach is that changing the weights of θ, ζ, and R_a does not dramatically change the optimal set of process parameters rather in all cases high pressure and flow rate of the HPC jet is desirable to get effective combinational effect.

iii. In this research, it is evident that turning AISI 4320 by uncoated carbide insert is optimized at 148 m/min and 0. 22 mm/rev as well as 180 m/min and 0.18 mm/rev where optimized pressure and flow rate of the HPC jet is 70 bar at 6 liter/min.

8. ACKNOWLEDGEMENT

This research work has been funded by Directorate of Advisory Extension and Research Services, BUET, Dhaka, Bangladesh. The authors are also grateful to the Department of Industrial and Production Engineering, BUET for providing the facilities to carryout the experiment.

9. REFERENCE

[1] Chao, B. T. and Trigger, K.J., "Temperature Distribution at the chip-tool interface in metal-cutting", *Trans. of the ASME*, 1995, Vol.77,1107

[2] Dhar, N.R., Paul, S., Chattopadhyay, A.B., (2002), "Role of Cryogenic Cooling on cutting Temperature in Turning Steel", *J. of Manufacturing Science and Engineering*, 124 (1), 146-154

[3] Komanduri, R. and Desai, J., (1983), "Tool Materials", *Encyclopedia of Chemical Technology*, 3rd Edition, John Wiley & Sons, NY, 23: pp.273-309

[4] Byrne, G. and Scholta, E., "Environmentally Clean Machining Process - A Strategic Approach", *Annals of CIRP*, Vol.42/1, pp.471-474, (1993)

[5] Bennett, E.O. and Bennett, D.L., "Occupational Airway Diseases in the Metal-Working Industry", *Tribology International*, 18/3, pp.169-176, 1985

[6] Peter, C. R., Steven, C., and David, L., "Evaporation of Polydisperse Multi Component Oil Droplets", *American Industrial Hygiene Association*, 1996

[7] Dhar, N.R., Paul, S. and Chattopadhyay, A.B., (2002), "Role of Cryogenic Cooling on Cutting Temperature in turning steel", *Transaction of the ASME*, Vol. 123, pp. 146- 154

[8] Dhar, N.R., Islam, M.W., Islam, S., and Mithu, M.A.H. (2006), "The influence on Minimum Quantity Lubrication (MQL) on cutting temperature, chip and dimensional accuracy in turning AISI- 1040 steel", *Journal of Materials Processing Technology*, 17 1(1), pp.93-99

[9] Dhar, N.R., Islam, M.W., Islam, S., and Mithu, M.A.H. (2006), "The influence on Minimum Quantity Lubrication (MQL) on cutting temperature, chip and dimensional accuracy in turning AISI- 1040 steel", *Journal of Materials Processing Technology*, 17 1(1), pp.93-99

[10] SUN W.P., PEI Z.J., LEE E.S., "Optimization of Process Parameters in Manufacturing: An Approach of Multiple Attribute Decision Making**"**, *conference of NAMRC THIRTY-THREE*, May 24-27, 2005

[11] Greenall, R., (1989), "A Taguchi Optimization of the Manufacturing Process for an Injection Molded Housing," *Taguchi Methods: Applications in World Industry*, A. Bendell, J. Disney and W.A. Pridmore, Eds. New York: IFS Publications and Springer-Verlag

[12] Elsayed, E.A., and A. Chen, (1993), "Optimal Levels of Process Parameters for Products with Multiple Characteristics," *International Journal of Production Research*, Vol. 31, No. 5, pp1117-1132.

[13] Mayers, R.H., A.I. Khuri, and W.H. Carter, (1989), "Response Surface Methodology: 1966-1988," *Technometrics*, Vol. 31, pp. 137-157.

Proceedings of the 4th BSME-ASME International Conference on Thermal Engineering
27-29 December, 2008, Dhaka, Bangladesh

ANALYSIS OF THERMAL STRESSES IN A ROTATING FGM CIRCULAR DISK BY FINITE ELEMENT METHOD

A. M. AFSAR, J. GO, J. I. SONG

Department of Mechanical Engineering, Changwon National University, Changwon, 641-773, South Korea
email: mdafsarali1967@yahoo.com

ABSTRACT

This study concerns the analysis of thermal stresses in a thin rotating functionally graded material (FGM) circular disk having a concentric hole and subjected to a thermal load. The material distribution varies in the radial direction only. The Young's modulus, coefficient of thermal expansion (CTE), and density of the disk are assumed to vary exponentially while the Poisson's ratio is assumed to be constant. The incompatible eigenstrain developed in the material due to nonuniform coefficient of thermal expansion is taken into consideration. Based on the two dimensional thermoelastic theories, the axisymmetric problem is reduced to the solution of a second order ordinary differential equation. Using the variational approach and Ritz method, the differential equation is converted to a system of algebraic equations which is solved by Gauss elimination method. Some numerical results of stresses are presented for an Al_2O_3*/Al FGM disk for different prescribed temperature profiles. It is found that the stresses are significantly influenced by the hole size, angular speed, and difference between outer surface and inner surface temperatures which can be controlled to control the thermal stresses.*

KEYWORDS: *Functionally graded material, Circular disk, Thermal stress, Finite element method, Thermoelasticity*.

1. INTRODUCTION

Functionally graded materials (FGMs) consist of two or more distinct material phases and have a continuous gradient in material distribution. Consequently, these materials have continuously varying mechanical and thermal properties. Usually, a ceramic is used at one surface to resist severe environmental effect such as high temperature, wear, and corrosion and a metal is used at the other surface to ensure high toughness and thermal conductivity. Therefore, an FGM is a promising candidate for many engineering applications where a high temperature gradient field exists. Although the original purpose of these materials was to use as thermal barrier coatings, their unique properties have stimulated the interests of researchers towards the development of new potential structural applications. Nonlinearly distributed in-plane edge load [1] and uniaxial load [2] were considered for the analysis of buckling characteristics and bi-axial tensile load [3] was considered for the analysis of elastic field in FGM rectangular plates.

Geometrically nonlinear analysis was carried out for FGM plates and shells by Kim et al. [4]. All the studies mentioned above were concerned with the mechanical load acting on the FGM plates or shells. As the FGMs have continuously varying coefficient of thermal expansion, an eigenstrain [5] is developed in the materials when they undergo a change in temperature. The incompatibility of the eigenstrain has substantial effect on the overall thermal stresses. Therefore, the incompatible eigenstrain should be taken into account while designing with an FGM body. The effect of incompatible eigenstrain was considered in a study of an FGM circular plate [6] for the analysis of stresses due to thermal load. In another study, Afsar and Anisuzzaman [7] analyzed the stress intensity factor for two diametrically opposed edge cracks in a thick walled FGM cylinder by taking into account the incompatible eigenstrain.

Recently, FGMs have found their applications in the field of cutting and grinding tools because of their superior characteristics in comparison with those of conventional monolithic materials. A circular disk type cutter or a grinding disk is one of such type of tools. It experiences a higher temperature at the cutting edge or grinding surface, when it rotates and comes in contact with an object, and a lower temperature at the central region of the disk. Further, the cutting edge or grinding surface of this tool should possess high wear resistance while the central part should be tougher. These properties in a disk can be achieved by designing the disk with FGMs. However, to properly design this tool with FGMs, it is necessary to understand and quantify the thermal stresses in the tool. In an attempt to achieve this goal, this study is aimed at analyzing the thermal stresses in a rotating FGM circular disk with a concentric hole. Based on the two dimensional thermoelastic theories, the problem is reduced to the solution of a second order differential equation. The solution is obtained by using the variational approach of the finite element method.

2. STATEMENT OF THE PROBLEM

Figure 1 shows a rotating FGM circular disk with a concentric hole. The constituent materials of the FGM disk are denoted by A and B which are, respectively, represented by the dark and white colors as shown in the figure. The distribution of each material continuously varies along the radial direction only. The inner and the outer radii of the disk are designated by a and b, respectively. Further, the angular velocity of the disk is denoted by ω. As the material

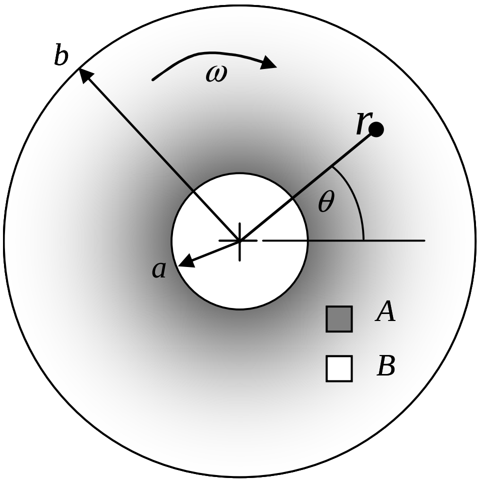

Fig. 1 Analytical model of the problem.

distribution is the function of r only, all the properties of the FGM disk are also functions of r only which reduces it to the axisymmetric problem. The Young's modulus E, coefficient of thermal expansion α, and the density ρ of the FGM disk are assumed to vary exponentially as

$$E = E_0 e^{\beta r} \quad ; \quad \alpha = \alpha_0 e^{\gamma r} \quad ; \quad \rho = \rho_0 e^{\mu r} \tag{1}$$

Applying the boundary conditions of the hole and the outer surfaces of the disk to Eq. (1), the constants in Eqs. (1) can be determined as

$$E_0 = E_A e^{-\beta a} \quad ; \; \alpha_0 = \alpha_A e^{-\gamma a} \quad ; \quad \rho_0 = \rho_A e^{-\mu a} \tag{2}$$

$$\beta = \frac{1}{a-b}\ln(E_A / E_B)\,; \quad \gamma = \frac{1}{a-b}\ln(\alpha_A / \alpha_B)\,; \; \mu = \frac{1}{a-b}\ln(\rho_A / \rho_B) \tag{3}$$

The subscripts A and B of a variable denote the properties of the constituent materials A and B, respectively, while the non-subscripted variables are used to represent the properties of the FGM. As the thickness of the disk is small, the analysis is carried out under plane stress condition.

3. THERMOELASTIC FORMULATION

Eigenstrains [5] are nonelastic strains or free expansion strains that are develop in a body due to various reasons such as phase transformation, precipitation, temperature change, etc. In the present study, the eigenstrain is associated with the thermal expansion that occurs when the FGM disk undergoes a change in temperature. Since the material of the FGM disk is isotropic, the thermal eigenstrain at a point is same in all directions and can be given by

$$\varepsilon^* = \alpha(r)T(r) \tag{4}$$

where $T(r)$ is the change in temperature at any point r. The total strain is the sum of the elastic strain and the eigenstrain. Thus, the components of total strain are given by

$$\varepsilon_r = e_r + \varepsilon^* \,; \; \varepsilon_\theta = e_\theta + \varepsilon^* \tag{5}$$

where ε_r and ε_θ are the radial and tangential components of the total strain and e_r and e_θ are the radial and tangential components of elastic strain. It is noted that the shear strain component does not come into the scenario due to symmetric deformation of the disk. The elastic strains are related to stresses by Hooke's law. Thus,

$$\varepsilon_r = (1/E)(\sigma_r - \nu\sigma_\theta) + \varepsilon^* \,; \; \varepsilon_\theta = (1/E)(\sigma_\theta - \nu\sigma_r) + \varepsilon^* \tag{6}$$

where σ_r and σ_θ are the radial and tangential stress components, respectively. The inertia force due to the rotation of the disk is the only body force. Thus, the two dimensional equilibrium equation and strain-displacement relations for symmetric condition reduce to

$$\frac{d}{dr}(r\sigma_r) - \sigma_\theta + \rho\omega^2 r^2 = 0 \tag{7a}$$

$$\varepsilon_r = \frac{du_r}{dr}\,; \; \varepsilon_\theta = \frac{u_r}{r} \tag{7b}$$

The combination of Eqs. (6) and (7) and making use of the substitution $F = r\sigma_r$ yield

$$\frac{d^2F}{dr^2} + \left(\frac{1}{r} - \beta\right)\frac{dF}{dr} + \frac{1}{r}\left(\beta\nu - \frac{1}{r}\right)F = \rho\omega^2 r(\beta r - \mu r - \nu - 3) - E\alpha\left(\gamma T + \frac{dT}{dr}\right) \tag{8}$$

$$\sigma_\theta = \frac{dF}{dr} + \rho\omega^2 r^2 \tag{9}$$

4. FINITE ELEMENT FORMULATION

As the analytical solution of Eq. (8) is quite involved, the finite element method is adopted to obtain its solution numerically. Following the variational approach and applying the Ritz method, Eq. (8) is converted into the following system of algebraic equations:

$$\sum_{j=1}^{2} K_{ij}^{e} F_{j}^{e} = L_{i}^{e} \tag{10}$$

where $K_{ij}^{e} = B(\phi_i^e, \phi_j^e)$; $L_i^e = l(\phi_i^e)$; $\phi_1^e = \dfrac{r_{e+1} - r}{r_{e+1} - r_e}$; $\phi_2^e = \dfrac{r - r_e}{r_{e+1} - r_e}$, and

$$B(w,F) = \int_{r_e}^{r_{e+1}} \frac{dw}{dr}\frac{dF}{dr}dr - \int_{r_e}^{r_{e+1}} (\frac{1}{r} - \beta) w \frac{dF}{dr} dr - \int_{r_e}^{r_{e+1}} \frac{1}{r}(\beta\nu - \frac{1}{r}) wF dr \tag{11a}$$

$$l(u) = \int_{r_e}^{r_{e+1}} wf(r)dr + w(r_{e+1})\frac{dF}{dr}(r_{e+1}) - w(r_e)\frac{dF}{dr}(r_e) \tag{11b}$$

The superscript *e* refers to the element number. Equation (10) is a system of algebraic equations, which can be used to form a global system of algebraic equations by satisfying the continuity condition $F_2^e = F_1^{e+1}$. The global system of algebraic equations is then solved by Gauss elimination method.

5. RESULTS AND DISCUSSION

To present some numerical results of stresses, an Al_2O_3/Al FGM disk is considered as an example, where *A* and *B* denote the constituent materials Al and Al_2O_3, respectively. The mechanical and thermal properties of the constituent materials used in the calculations are: E_A = 71 GPa, E_B = 380 GPa, $\alpha_A = 23.1\times10^{-6}$/°C, $\alpha_B = 8\times10^{-6}$/°C, ρ_A = 2.7 g/cm^3, and ρ_B = 0.961 g/cm^3.

Figure 2 shows five different prescribed temperature distributions along the radial distance of the disk. For these prescribed temperature distributions, the corresponding results of radial and tangential stress components are, respectively, presented in Figs. 3 and 4 for ω = 1 rad/s and *b/a* = 10. It is seen that the uniform temperature distribution yields the compressive radial stress while the other distributions of temperature produce tensile radial stress in the disk (Fig. 3). Further, the uniform temperature distribution causes the maximum peak value of this stress. However, for any temperature distribution, the stress is zero at the inner and outer surfaces of the disk that satisfies the boundary conditions of the problem. The tangential stress component as

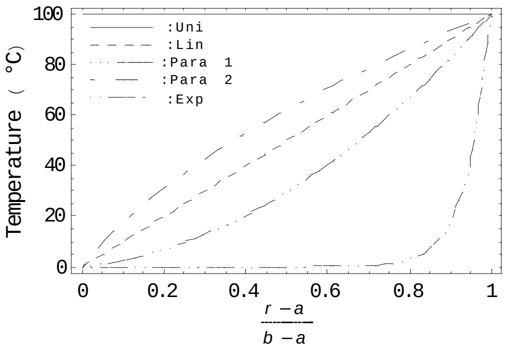

Fig. 2 Prescribed temperature distributions.

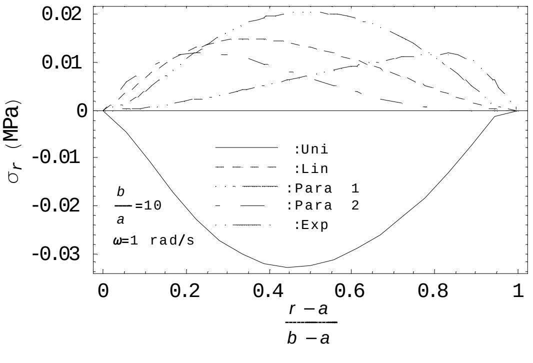

Fig. 3 Effect of temperature distribution on radial stress.

shown in Fig. 4 has different characteristics than those of radial stress component. For any temperature distribution, the tangential stress is compressive over a part of the radial dimension and tensile over the other part of it. Over the inner region of the disk, the value of tangential stress is maximum for uniform temperature distribution while its value is maximum for exponential temperature distribution over the outer region of the disk.

The effects of the ratio *b/a* (a measure of the hole size) on the distribution of stresses are illustrated in Figs. 5 and 6 which are plotted for the linear temperature distribution of Fig. 2 and angular speed $\omega = 1$ rad/s. It is found that the value of both the components of stress increases with the increase of the hole size, *i.e.*, with the decrease of the ratio *b/a*. This is due to the fact that the temperature varies linearly from its fixed minimum value (0°C) at the inner surface to its fixed maximum value (100°C) at the outer surface. Thus, the gradient in temperature increases as the hole size increases, *i.e.*, the ratio *b/a* decreases. This higher gradient in temperature indicating higher thermal load causes the stress to increase as the ratio *b/a* decreases.

Shown in Figs. 7 and 8 are the distribution of stresses as a function of angular velocity ω of the disk. The results correspond to the linear temperature distribution of Fig. 2 and $b/a = 10.0$. Although the tangential stress varies significantly with the variation of ω, the radial stress is almost uninfluenced by the angular speed ω of the disk.

The effect of the inner surface and outer surface temperature difference on the radial stress is depicted in Fig. 9. At higher temperature difference, the radial stress is positive throughout the disk. As the temperature difference is reduced, the radial stress transforms from tensile to compressive as shown in Fig. 9.

6. CONCLUSIONS

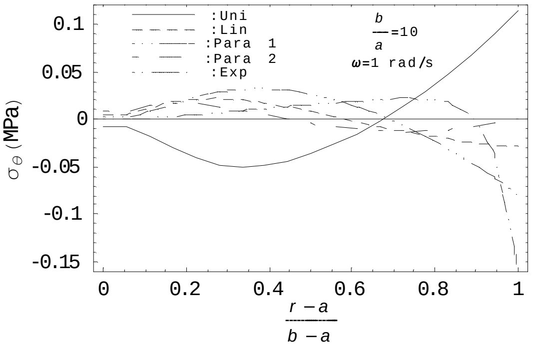

Fig. 4 Effect of temperature distribution on tangential stress.

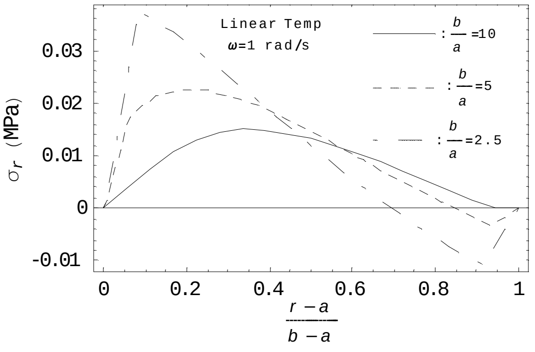

Fig. 5 Effect of hole size on radial stress.

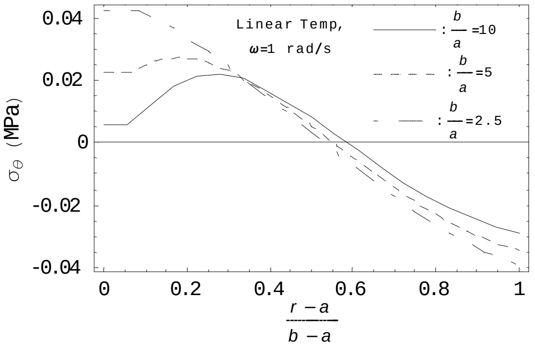

Fig. 6 Effect of hole size on tangential stress.

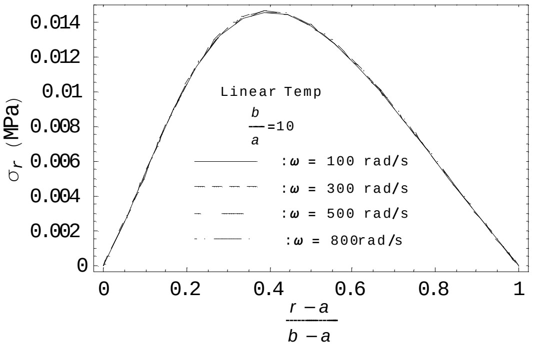

Fig. 7 Effect of angular speed on radial stress.

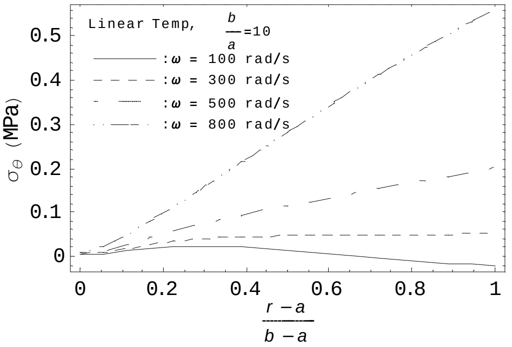

Fig. 8 Effect of angular speed on tangential stress.

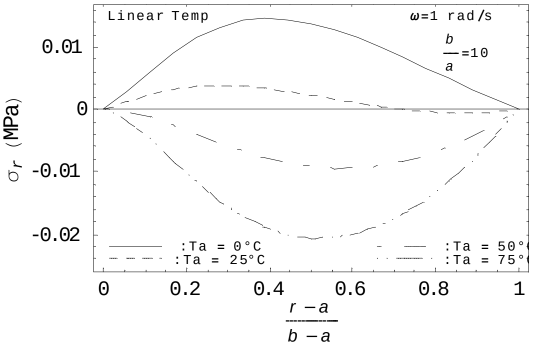

Fig. 9 Effect of temperature difference on radial stress.

A finite element model is developed for the analysis of thermal stresses in a rotating FGM circular disk with a concentric hole by taking into account the effect of incompatible eigenstrain developed in the disk due to nonuniform coefficient of thermal expansion. The finite element model is demonstrated for an Al_2O_3/Al FGM disk. The results show that the thermal stresses developed in the disk can be controlled by controlling the hole size, angular speed, and the inner and outer surface temperature difference.

ACKNOWLEDGEMENT

This work was partially supported by Brain Korea 21 (BK-21) Projects Corps. of the second phase.

REFERENCES

[1] Chen, X. L., Liew, K. M., Buckling of Rectangular Functionally Graded Material Plates Subjected to Nonlinearly Distributed In-Plane Edge Loads, *Smart Materials and Structures*, 13 (2004), pp. 1430-1437.

[2] Feldman, E., Aboudi, J., Buckling Analysis of Functionally Graded Plates Subjected to Uniaxial Loading, *Composite Structures*, 38 (1997), pp. 29-36.

[3] Afsar, A. M., Rahman, R., Wang, Y. Q., Shi, Y., Song, J. I., Finite Difference Solution of Stress and Strain in an FGM Plate, Proceedings, 16th International Conference on Composites/Nano Engineering, Kunming, China, July 20-26, 2008.

[4] Kim, K. D., Lomboy, G. R., Han, S. C., Geometrically Non-Linear Analysis of Functionally Graded Material (FGM) Plates and Shells Using a Four Node Quasi-Conforming Shell Element, *Journal of Composite Materials*, 42 (2008), 5, pp. 485-511.

[5] Mura, T., 1987, Micromechanics of Defects in Solids, Martinus Nijhoff Publishers, Dordrecht, 1987.

[6] Afsar, A. M., Farhana, L., Masheed, A., Wang, Y. Q., Song, J. I., Finite Difference Analysis of Elastic Field in a Functionally Graded Material Circular Plate under Thermal Load, Proceedings, Korean Society for Mechanical Engineers 2008 Spring Annual Meeting, Changwon, Korea, June 20-21, 2008, pp. 617-622.

[7] A. M. Afsar, M. Anisuzzaman, Stress Intensity Factors of Two Diametrically Opposed Edge Cracks in a Thick-Walled Functionally Graded Material Cylinder, *Engineering Fracture Mechanics*, 74 (2007), pp. 1617-1636.

Proceedings of the 4th BSME-ASME International Conference on Thermal Engineering
27-29 December, 2008, Dhaka, Bangladesh

PERFORMANCE STUDY OF ADSORPTION CHARACTERISTICS OF SILICA GEL-WATER AND ACTIVATED CARBON-*n*-BUTANE SYSTEMS

Sumon Saha, Anutosh Chakraborty, Bidyut Baran Saha, Shigeru Koyama

Interdisciplinary Graduate School of Engineering Sciences, Kyushu University, 6-1 Kasuga-koen, Kasuga-shi,
Fukuoka 816-8580, Japan
E-mail: sumon@phase.cm.kyushu-u.ac.jp

ABSTRACT

The adsorption characteristics of pure water vapor on to RD type silica gel and n-butane on pitch based activated carbon (type Maxsorb III) at temperatures ranging from 298 to 338 K and at different equilibrium pressures between 0.5 and 300 kPa have been experimentally measured by a volumetric technique. The porous properties such as, the density, Brunauer-Emmett-Teller (BET) surface area, pore size, pore volume along with pore size distribution (PSD) of these two different adsorbents have been determined. The Tóth and Dubinin-Astakhov (DA) adsorption isotherm models describe all of the isotherm experimental data within the acceptable error ranges for silica gel-water and activated carbon-n-butane systems, respectively. The isosteric heat of adsorption (ΔH_{ads}) of water on silica gel and n-butune on Maxsorb III is also determined in the present investigation.

Key words: *Activated carbon; Silica gel; Adsorption; Heat of adsorption; Thermodynamic properties.*

1. INTRODUCTION

The adsorption characteristics of water vapor on silica gel [1-4] and *n*-butane on pitch based activated carbon [5-9] are essential data in determining the energetic performance of adsorption chillers. From the fundamental basic for the design of adsorption chillers, the investigation of the adsorption isotherm is pertinent for the purpose of system modeling.

The adsorption performance of the assorted adsorbents and adsorption characteristics of adsorbent-refrigerant pair influence directly on the operating behaviors of adsorption processes as well as the porous properties of adsorbents. In terms of the adsorption chiller performance, the adsorbent must have good thermal conductivity as well as large specific area. Both Fuji Davison type RD silica gel and pitch based activated carbons (type Maxsorb III) fulfill these requirements. So these adsorbents are suitable for adsorption storage and cooling applications. The present study investigates experimentally the porous characteristics of Fuji Davison type RD silica gel and Maxsorb III along with adsorption isotherms, the isosteric heat of adsorption of the silica gel/water and Maxsorb III/*n*-butane pairs. The adsorption parameters are individually evaluated using Tóth and DA equations for silica gel/water and Maxsorb III/*n*-butane pairs respectively.

2. EXPERIMENTAL SECTION

Yeh *et al.* [2] carried out a comprehensive literature survey on physical properties of silica gel. In the present study, the microporous adsorbent Maxsorb III manufactured by Kansai Coke and Chemicals Co. Ltd., Osaka, Japan, has been used. Our experimentally determined porous properties are summarized in Table 1. The porosity, total pore volume, average pore diameter and surface area of the samples (silica gel and Maxsorb III) are measured by the adsorption isotherm of nitrogen at 77.4 K. Prior to the experiment, samples are degassed at a temperature 413 K for 48 h for silica gel and at a temperature 473 K for 3 h for Maxsorb III, to achieve the residual vacuum level in the sample tube to be not more than 10 mPa by using an Autosorb 1 MP machine. The analysis is performed using the system's built-in data reduction software. It measures the quantity of adsorbate (gas phase) adsorbed onto or desorbed from an adsorbent surface (solid surface) at an equilibrium vapour pressure by a static volumetric method.

Table 1. Porous properties of silica gel and Maxsorb III

Property	Value	
	RD type silica gel	Maxsorb III
BET Surface Area (m^2/g)	838 ± 3.8	3140
Micropore Volume (ml/g)	0.49	1.70
Total pore volume (ml/g)	1.00	2.01
Apparent Density (g/ml)	0.70	0.31
Residual Heat (%)	-	0.1
pH (-)	4.0	4.1
Mean pore diameter (nm)	2.2	2.008

The experimental adsorption data are analyzed using the nonlinear density functional theory (NLDFT) plus software (Mircromeritics Version 2.0) to determine pore volumes and pore size distributions. Figure 1 shows the pore size distributions for the two adsorbents investigated. It is found that the Maxsorb III is highly microporous.

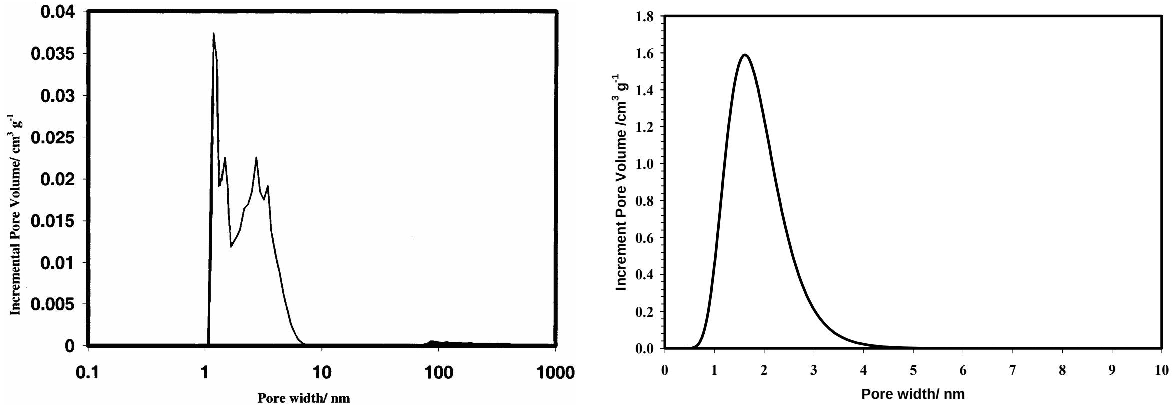

(a) (b)

Fig. 1 Pore size distribution of (a) RD type silica gel and (b) Maxsorb III for NLDFT method

The surface area is determined by the BET method from the N_2 adsorption isotherm data. The skeletal densities of dry silica gel and Maxsorb III are determined by the automated Micromeritics AccuPyc 1330 pycnometer at room temperature. In our experiments, each sample is regenerated at 413 K for 24 h and a dry mass sample is then introduced to the pycnometer.

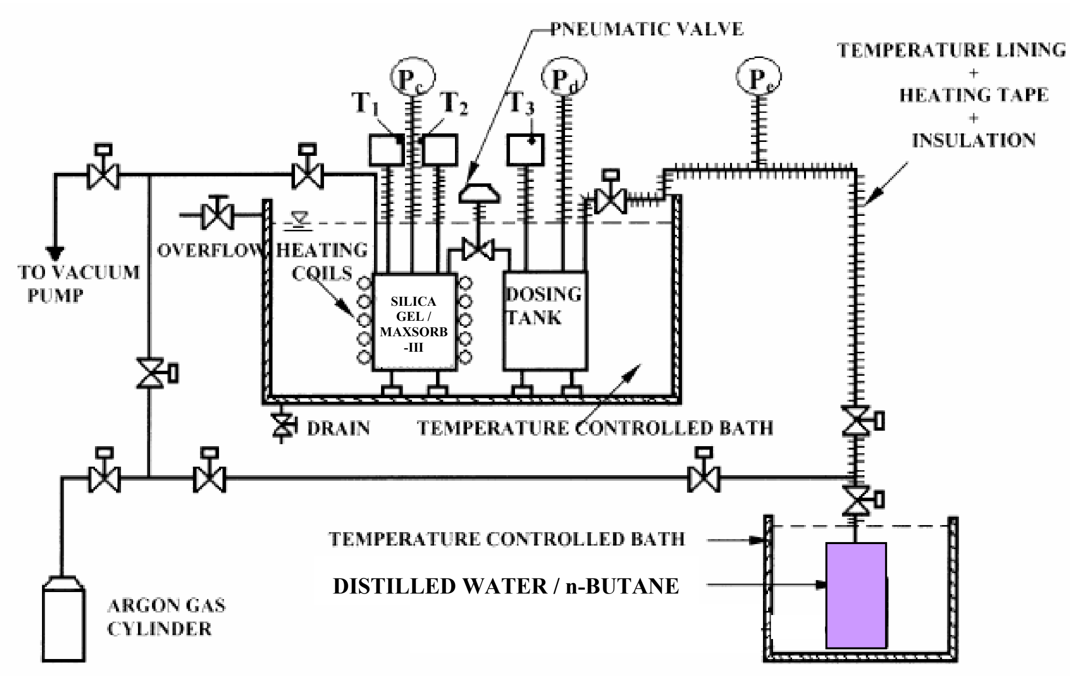

Fig. 2 Schematic diagram of the constant volume variable pressure (CVVP) test facility:T_1, T_2, T_3 = resistance temperature detectors or temperature sensors; P_s, P_d, P_e = pressure sensors

In the present study, the constant-volume variable pressure (CVVP) apparatus has been employed in order to measure the adsorption isotherms of two different adsorbent-adsorbate pairs as shown in Fig. 2. It is mainly comprised of a charging tank made of stainless steel (SS 304), a dosing tank also made of SS 304 and an evaporator flask. The charging tank is designed to have a high aspect ratio, so that the adsorbent could be spread on the large flat base. The volumes of the charging and dosing tanks are calibrated by charging helium gas with a purity of 99.9995% from a calibrated standard volume of (210.9 ± 0.2) cm^3. By measuring the pressures of the combined volumes at isothermal conditions, the volumes of both the charging and the dosing tanks are calculated using the ideal gas law. The pressures in the two tanks are measured with two calibrated pressure transducer while the temperatures are measured with three Pt 100 Ω Class A resistance temperature detectors (RTDs). The RTD for the charging tank, T_1 in Fig. 2, is designed to be in direct contact with either silica gel or Maxsorb III so that a more representative adsorbent temperature can be obtained. Except for the 3.175 mm vacuum adaptors used to seal the RTD probes, all other inter-connecting piping (SS 316), stainless steel vacuum fittings, and vacuum-rated stainless steel diaphragm valves (Nupro, Swagelok) are chosen to be 12.7 mm to ensure good conductance during evacuation. To maintain the system as isothermal, the two tanks are immersed in a temperature-controlled bath (precision of control ±0.01 K). To further reduce the measurement error caused by a temperature gradient along the piping, fittings, and valves, they are thermally jacketed. The exposed piping and fittings are then well insulated.

The CVVP setup is equipped with a two-stage rotary vane vacuum pump (Edwards bubbler pump) with a water vapor pumping rate of 315×10^{-6} m^3 s^{-1}. Argon, with a purity of 99.9995%, is sent through a column of packed calcium sulphate before being used to purge the vacuum system. Upon evacuation, a residual gas pressure of 100 Pa is found in the apparatus. The evaporator flask is immersed in a different temperature-controlled bath. All pressure and temperature readings are continuously monitored by a calibrated data acquisition unit. In the present test facility, the major measurement bottleneck lies in the measurement of the vapor pressure. The dry mass of silica gel and Maxsorb III is determined by the calibrated moisture balance (Satorious MA40 moisture analyzer; uncertainty 0.05% traceable to a DKD standard) at T = 413 K. For Fuji Davison type RD silica gel, a mass about 0.1-1.25 g is introduced into the charging tank whereas for Maxsorb III samples, it is typically in ranges from 2.0 g to 5.124 g.

The dosing and charging tanks along with all related piping systems are purged by purified and dried argon, and evacuated. Based on the measurement, there is no measurable interaction between the inert gas and the adsorbent, as the effect of the partial pressure of argon in the tanks is found to be small. The refrigerant is firstly charged into the dosing tank. The evaporator is isolated from the dosing tank soon after the equilibrium pressure is achieved inside the dosing tank. The mass of refrigerant is determined via pressure and temperature. Once the test system reaches thermodynamic equilibrium at a desired temperature, the pressurized interconnecting valve between the dosing and charging tank is opened, and both tanks are allowed to approach equilibrium. The temperatures of both tanks are adjusted to the desired temperature via the oil bath before pressure and temperature measurements are taken for both tanks. The test system is subsequently evacuated. The adsorbent is then regenerated, and the apparatus is purged with dried argon before the refrigerant at a given initial pressure is charged into the dosing tank to enable measurements to be made along an isotherm.

3. RESULTS AND DISCUSSION

From Table 1, one can observe the difference of the porous properties of these two different adsorbents. Moreover, these two different adsorbents possess significant difference in their corresponding refrigerant vapor uptake characteristics. In the present study, the temperatures and pressures investigated range from (303 to 338) K and (500 to 7000) Pa for silica gel and from (298 to 328) K and (20 to 300) kPa for Maxsorb III, respectively. The uncertainty of pressure ranges from (±10 to 200) Pa. Emphasis is placed on the conditions experienced in the adsorber because this is the range of conditions that directly determines the cooling capacity. From the equilibrium measurements of water vapor on RD silica gel and *n*-butane on Maxsorb III, the measured isotherms as graphical plots are shown in Fig. 3(a) and 3(b), respectively.

From Fig. 3(a), the isotherms of T = 304 K and 310 K for type RD silica gel-water system exhibit signs of onset of monolayer saturation at higher pressures. Tóth's equation [10, 11] is found to fit the experimental data of type RD silica gel-water system well and is therefore used to find the isotherm parameters and isosteric heats of adsorption. The form of Tóth's equation used is given as

$$q^{*} = K_{o}\exp\left[\Delta H_{ads}/\left(RT\right)\right]P/\left\{1+\left[K_{o}/q_{m}\exp\left(\Delta H_{ads}/\left(RT\right)\right)P\right]^{t}\right\}^{1/t} \qquad (1)$$

where q* is the adsorbed quantity of adsorbate by the adsorbent under equilibrium conditions, q_m denotes the monolayer capacity, P is the equilibrium pressure of the adsorbate in the gas phase, T is the equilibrium temperature of the gas-phase adsorbate, R is the universal gas constant, ΔH_{ads} is the isosteric enthalpies of adsorption, K_o is the preexponential constant, and t is the dimensionless Tóth constant. Using regression analysis, the derived monolayer capacity of the type RD silica gel is estimated to be 0.45 kg kg^{-1}. The other parameters such as K_o, ΔH_{ads}, t of Eq. (1) are found to be $(7.30\pm2)\times10^{-10}$ (kg $kg^{-1}kPa^{-1}$), $(2.693\pm0.1)\times10^{3}$ (kJ kg^{-1}) and 12, respectively. In addition to the choice of using Tóth's equation, we has considered the use of the Dubinin-Astakhov equation in describing the present isotherm data.

However, the Dubinin-Astakhov equation is found to be unable to provide a good description of the data to within the experimental uncertainties.

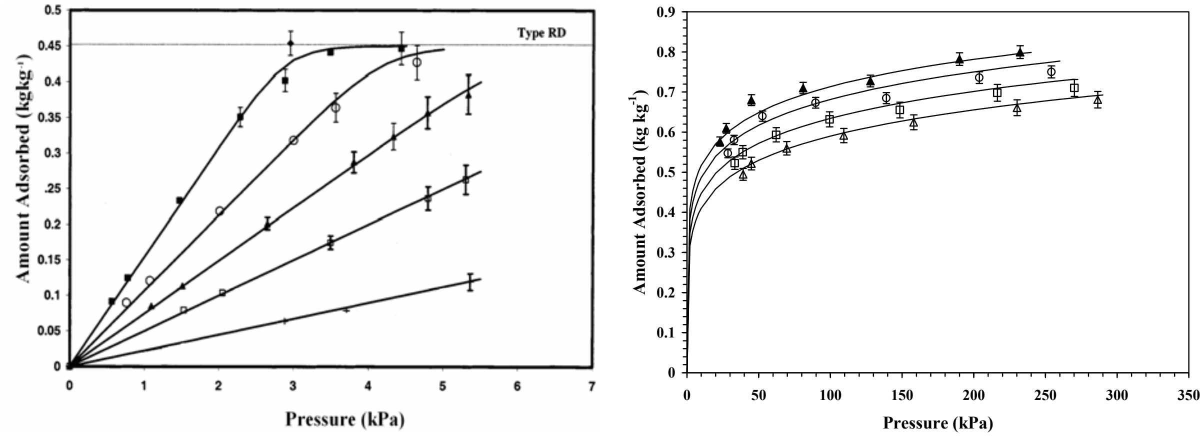

(a) (b)

Fig. 3 Isotherm data for (a) water vapor onto RD type silica gel: for experimental data points with (■) T = 304 K, (○) T = 310 K, (▲) T = 316 K, (□) T = 323 K, and (+) T = 338 K; for computed data points with solid lines for Tóth's equation and (b) *n*-butane on Maxsorb III: for experimental data points with (▲) T = 298 K, (○) T = 308 K, (□) T = 318 K, and (Δ) T = 328 K; for computed data points with solid lines for DA equation

As can be seen from Fig. 3(b), the isotherm of T = 298 K for Maxsorb III-*n*-butane pair exhibits signs of monolayer saturation at high pressure. For design purposes, the experimental data should be marched with an analytical expression that includes adjustable parameters as a function of pressure and temperature. The Maxsorb III is a highly microporous material and its pore size distribution is wide, which ranges from 0.4 to 3 nm. Therefore, Maxsorb III is considered to be a heterogeneous adsorbent. For the adsorption on carbon based heterogeneous adsorbents, the Dubinin–Astakhov (DA) isotherm equation [12, 13] is found suitable and hence the DA equation is used to correlate the experimental isotherm data. The DA equation can be written as:

$$q^* = q_m \exp\left[-\left\{\frac{RT}{E}\ln\left(\frac{P_s}{P}\right)\right\}^n\right] \tag{2}$$

The parameter, E denotes the activation energy and n is an exponential constant. Regressing experimental data, the parameters q_m, E, n of Eq. (2) are found to be 0.8 (kg kg^{-1}), 300 (kJ kg^{-1}) and 1.05, respectively.

From the experimentally measured adsorption isotherms, the isosteric heat of adsorption (ΔH_{ads}) as a function of loading (q^*) can be calculated by the following equation [14]:

$$\Delta H_{ads} = RT^2\left[\left(\frac{\partial(\ln P)}{\partial T}\right)_{m_a}\right] + Tv_g\frac{dP}{dT}(P,T) \tag{3}$$

Using the DA equation, equation (3) can be written as,

$$\Delta H_{ads} = h_{fg} + E\,ln\left(\frac{q*}{q}\right)^{\frac{1}{n}} + Tv_g\frac{dP}{dT}(P,T) \tag{4}$$

We have found that the isosteric heat of adsorption varies from 406 to 975 kJ kg^{-1} depending on the adsorbate loading.

4. CONCLUSION

Equilibrium studies of water vapor on Fuji Davison type RD silica gel and n-butane on Maxsorb III has been investigated experimentally. The nature of our experiments is very similar to the actual condition in adsorption chillers, and the ranges of pressure and temperature also covered the typical operating range of adsorption chillers. The derived monolayer capacities of RD type silica gel-water and Maxsorb III-n-butane pairs has been calculated to be about (0.45 and 0.8) kg,kg^{-1}, respectively. Tóth's and DA equations are found to be able to sufficiently describe the performance of the type RD silica gel with water vapor and Maxsorb III with *n*-butane, respectively.

REFERENCES

[1] Cho, S. H., Kim, J. N., Modeling of a Silica Gel/Water Adsorption-Cooling System, *Energy*, 17 (1992), pp. 829-839.

[2] Yeh, R. L.; Ghosh, T. K., Hines, A. L., Effects of Regeneration Conditions on the Characteristics of Water Vapor Adsorption on Silica Gel, *Journal of Chemical Engineering Data*, 37 (1992), pp. 259-261

[3] Saha, B. B., Akisawa, A., Kashiwagi, T., Silica Gel Water Advanced Adsorption Refrigeration Cycle, *Energy*, 22 (1997), 4, pp. 437-447.

[4] Saha, B. B., Alam, K. C. A., Akisawa, A., Kashiwagi, T., Ng, K. C., Chua, H. T., Two-Stage Non-Regenerative Silica Gel-Water Adsorption Refrigeration Cycle, Proceedings of the ASME Advanced Energy Systems Division, Orlando, 2000,Vol. 40, pp. 65-69.

[5] Fiani, E., Perier-Cambry, L., Thomas, G., Non-Isothermal Modelling of Hydrocarbon Adsorption on a Granulated Active Carbon, *Journal of Thermal Analysis and Calorimetry*, 60 (2000), pp. 557-570.

[6] Zhu, W., Groen, J. C., Kapteijn, F., Moulyn, J. A., Adsorption of Butane Isomers and SF6 on Kureha Activated Carbon: 1. Equilibrium, *Langmuir*, 20 (2004), 13, pp. 5277–5284.

[7] Garnier, C., Gorner, T., Razafitianamaharavo, A., Villiéras, F., Investigation of Activated Carbon Surface Heterogeneity by Argon and Nitrogen Low-Pressure Quasi-Equilibrium Volumetry, *Langmuir*, 21 (2005), 7, pp. 2838–2846.

[8] Walton, K. S., Cavalcante, Jr., C. L., Levan, M. D., Adsorption Equilibrium of Alkanes on a High Surface Area Activated Carbon Prepared from Brazilian Coconut Shells, *Adsorption*, 11(2005), pp. 107-111.

[9] El-Sharkawy, I. I., Saha, B. B., Koyama, S., Ng, K. C., A Study on the Kinetics of Ethanol-Activated Carbon Fiber: Theory and Experiments, *International Journal of Heat and Mass Transfer*, 49(2006), pp. 3104–3110.

[10] Suzuki, M., Adsorption Engineering, Elsevier: Amsterdam, The Netherlands, 1990.

[11] Tóth, J., State Equations of the Solid-Gas Interface Layers, *Acta Chim. Acad. Sci. Hung*, 69 (1971), pp. 311-328.

[12] Dubinin, M.M., Astakhov, V.A., Radushkevich, L.V., Cadenhead, D.A., Danielli, J.F., Rosenberg, M.D., Physical Adsorption of Gases and Vapours in Micropores, Progress and Membrane Science, Academic Press, New York, 1975.

[13] Akkimaradi, B. S., Prasad, M., Dutta, P., Srinivasan, K., Adsorption of 1,1,1,2-Tetrafluoroethane on Activated Charcoal, *Journal of Chemical and Engineering Data*, 46 (2001), 2, pp. 417–422.

[14] Chakraborty, A., Saha, B. B., Koyama, S., Ng, K. C., On the Thermodynamic Modeling of the Isosteric Heat of Adsorption and Comparison with Experiments, *Applied Physics Letters*, 89(2006), pp. 171901.

Proceedings of the 4th BSME-ASME International Conference on Thermal Engineering
27-29 December, 2008, Dhaka, Bangladesh

THERMAL PROPERTIES OF NATURAL FIBER REINFORCED PVC COMPOSITES

M. A. Gafur[1] , Halima Akter[2], Sangita Sharma[2] , and Abu Hassan Bhuiyan[2]
PP&PDC, BCSIR, Dhaka-120, Bangladesh
[1]Dept. of Physics, BUET, Dhaka-1000, and [2]PP&PDC, BCSIR, Dhaka-1205, Bangladesh

ABSTRACT

PVC-Natural fiber (palm fiber and sawdust) reinforced composites were fabricated using a simple hot press molding method. The effect of fiber addition on thermal properties were evaluated. The thermal stability of sawdust is greater than that of palm fiber resulting in greater thermal stability of PVC-sawdust composite than that of PVC-palm composites. There is an initial DTA peak for both palm fiber and composite due to water absorption, whereas PVC does not have that peak. Both the fiber have greater thermal stability than that of PVC. So, with the addition of fiber the thermal stability of composite increases.

Key words: Composites, DTA, TGA

1. INTRODUCTION

Governmental regulations and growing environmental awareness throughout the world have triggered a paradigm shift towards designing materials compatible with the environment. The use of palm fiber, derived from annually renewable source, as reinforcing fibers in both thermoplastic and thermosetting matrix composites provides positive benefits with respect to ultimate disposability and raw material utilization [1]. Recently natural fibers have been used as reinforcement-filler in low melting thermoplastic. Because of lower density, easy processibility, biodegradability and availability in nature, combined with a better cost-performance ratio, cellulosic materials show bright potentiality as a filler in thermoplastics [2,3]. The composites of engineering polymers combined with natural components like wood, flax, hemp, jute etc. are intensively studied due to the ecology and interesting physical properties of such natural cellulosic materials[4,5]. Natural fibers such as jute, coir, palm, wood fiber palm fiber, banana etc. are used as an alternative to synthetic fibers e.g. glass, aramid, carbon, etc. These fibers are used due to : their renewable character, acceptable specific strength properties, low cost, enhanced energy recovery, and biodegradability. Natural fiber reinforced polymer combine good mechanical properties with low specific mass. The palm fiber can be used as reinforcing agent in thermoplastics like polyethylene (PE), polypropylene (PP), poly vinyl chloride(PVC) etc. The use of palm fiber and their effects on properties are not well documented. The objective of the study is to find the effect of palm fiber addition on the properties of PVC-Palm fiber composites.

2. EXPERIMENTAL PROCEDURE

2.1 Raw Materials

Palm fiber were colleted in the following way – the palm leaves were cut from the tree, then the diving end of the middle hard part of the leaf are hammered, kept in water for 20 days.

After that the rotten materials are washed and fibers are collected and sun dried. From these fibers, short fibers having size of 2 mm are taken for composite preparation. Table 1 shows chemical composition of palm fiber.

Table 1 Chemical Composition of Sawdust

	Palm Fiber	Sawdust
Lignin	27.30	25.70
Hemicellulose	30.90	22.10
Alpha cellulose	38.40	42.40
Others	3.10	10.00

2.2 Fabrication

The composite preparation was done using a 450 KN Weber-Press. The press is consisted of pressing, heating and cooling system. Palm fiber and polymer are kept at 105^0C for 24 hours for drying. A blender was used to mix the PVC and palm fiber for 2 minute at 400 rpm. The mixtures were taken in die after using a little amount of mold releasing agent. The heating temperatures and initial pressure were set at 120^0 C and 50KN, respectively. After reaching the set temperature, the holding time was taken 1 hour 45 minutes. Then pressure was increased up to 100KN and stopped the heating system. Then the system was allowed to cool.

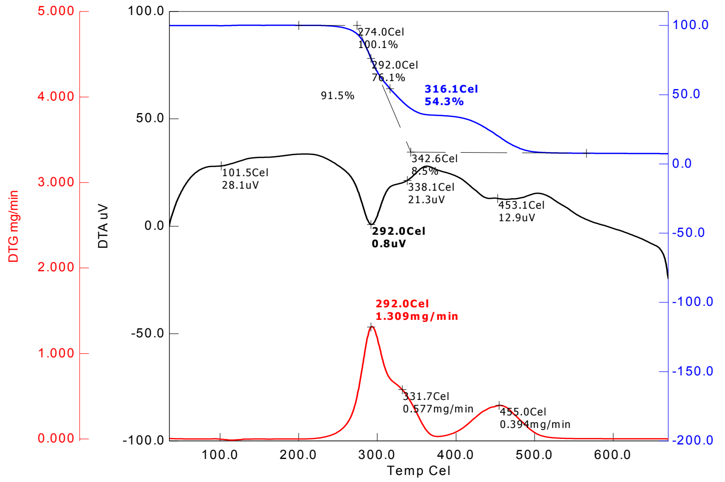

Fig. 1 TG%, DTA and of PVC

2.3 Measurement of properties

2.3.1 Thermal Analysis

Thermal analysis includes a group of techniques where some physical property of the sample is monitored under controlled conditions with variation of temperature at a programmed rate. When the mass change is monitored the results, which indicates chemical reactions, are called Thermogravimetry (TG). When heat absorption is monitored, the results indicate crystallization phase change etc. as well as reactions. This is called Differential Thermal analysis (DTA). Together, they are a powerful method of analysis. DTG stands for Differential Thermo Gravimetry. It is not the weight itself rather the first derivative of the sample weight with respect to time at constant temperature or with respect to temperature at constant value of heating is determined then this procedure is termed as DTG. Composites were taken using a computer controlled TG/DTA 6300 system controlled to an EXSTAR 6000 STATION, Seiko Instrument Inc., Japan. The TG/DTA module uses a horizontal system balance mechanism. The specifications of the instrument are: Heating rate;

0.01K/min. to 100.00 K/min., TGA measuring range: ± 200 mg (0.2 μg), DTA measuring range: ± 1000 μV (0.06 μV), Gas flow: ≤ 1000m/min.

3. RESULTS AND DISCUSSION

3.1 Thermal analyses

Figure 1 shows the TG, DTA nd DTG curves of PVC. The top one is the TG, bottom one is the DTG and middle one is the DTA curves of PVC. The TG curve shows two stage degradation. The onset set temperature, the 50% degradation temperatures are at 274.0°C and 292.0°C. A total 91.5% mass loss was obtained remaining 8.5% residue. The maximum slope was obtained at 316.1°C.DTA curve of PVC shows two endothermic peaks at 292.0^{0}C and 453.1^{0}C. DTG curve of PVC depicts two prominent peaks at 292.0°C and 455.0°C where the maximum degradation rate was 1.3 mg/min at 292.0°C. The two degradationstages are responsible for dehydrochlorination and deploymerization [6]. The initial degradation stage of TG curve is related to 1st endothermic DTA curve and 1st DTG peak. And the second DTA peak is related to 2nd DTA and 2nd DTG peak

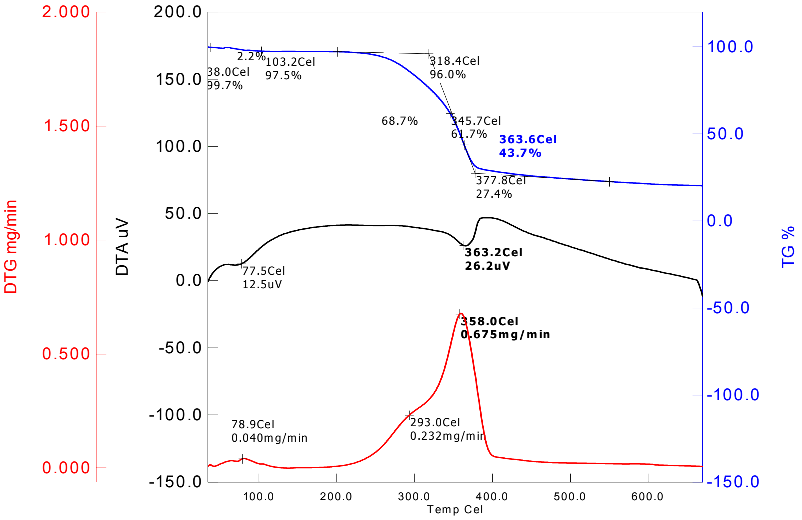

Fig. 2 TG%, DTA and of Palm Fiber

Figure 2 shows the TG, DTA nd DTG curves of palm fiber. The top one is the TG, bottom one is the DTG and middle one is the DTA curves of palm fiber. There is an initial weight loss(6.75%) due to moisture content of the fiber. The TG curve shows two stage degradation. The onset set temperature, the 50% degradation temperatures are at 294.0°C and 322.1°C. A total 48.1% weight loss was obtained remaining 27.4% residue. The maximum slope was obtained at 334.6°C. The initial endothermic DTA peak is obtained at 86.7°C which is related to moisture removal. DTA curve of palm shows two endothermic peaks at 296.4.0^{0}C and 377.1^{0}C. DTG curve of the fiber depicts two prominent peaks at 270.8°C and 336.10°C where the maximum degradation rate was 0.699 mg/min at 270.8°C. The two degradation stages are responsible for light (hemicellulose pectin etc.) and heavy material (cellulose, lignin, etc.). The two stage durations are 250-300°C and 310-375°C [7]. The initial degradation stage of TG curve is related to 1st endothermic DTA curve and 1st DTG peak. And the 2nd DTA peak is related to 2nd DTA and 2nd DTG peak

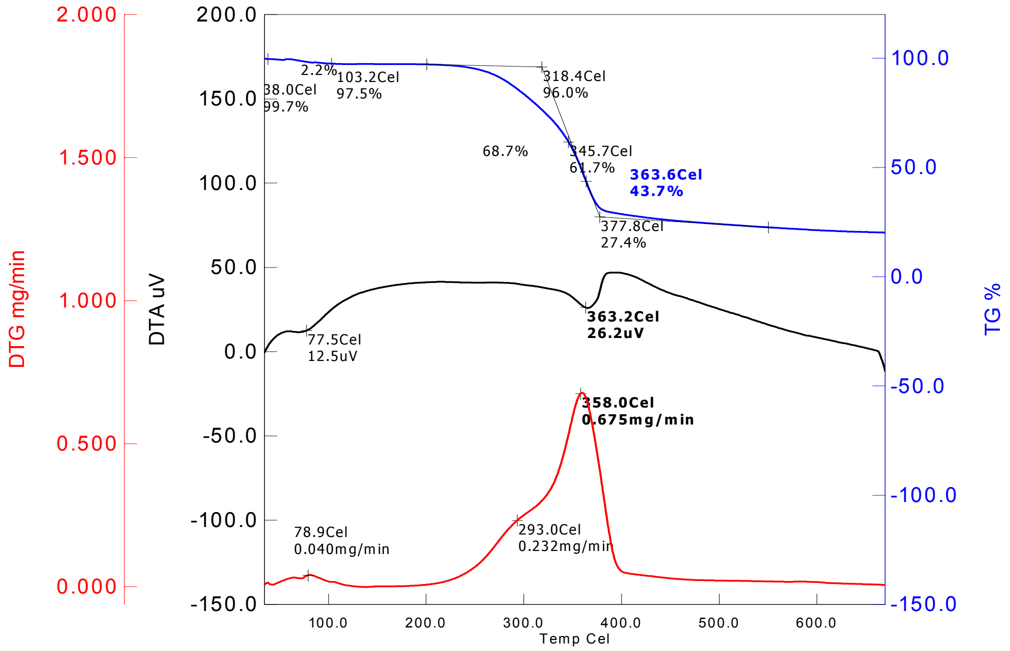

Fig. 3 TG%, DTA and DTG of Sawdust

Figure 3 shows the TG, DTA nd DTG curves of sawdust. The top one is the TG, bottom one is the DTG and middle one is the DTA curves of Palm fiber. There is an initial weight loss(2.20%) due to moisture content of the fiber. The TG curve shows two stage degradation. The onset set temperature, the 50% degradation temperatures are is 318.4^{o}C and 345.7^{o}C. A total 68.7% weight loss was obtained remaining 42.4% reside. The maximum slope was obtained at 363.3^{o}C. The initial endothermic DTA peak is obtained at 86.7^{o}C which is related to moisture removal. DTA curve of sawdust shows one endothermic peaks at 363.2^{o}C. DTG curve of the fiber depicts two prominent peaks at 293.0^{o}C and 358.0^{o}C where the maximum degradation rate was 0.675 mg/min. The two degradation stages are responsible for light (hemicelluloses, pectin, etc) and heavy material (cellulose, lignin, etc). The two stages duration are 250-300^{o}C and 310-375^{o}C (II). The initial degradation stage of TG curve is related to first DTG peak. And the second DTA peak is related to 2nd DTA and 2nd DTG peak The initial DTA peak is absent here.

Figure 4 shows the TG, DTA nd DTG curves of palm fiber reinforced PVC composites having 10%. palm. The top one is the TG, bottom one is the DTG and middle one is the DTA curves of composites. The TG curve shows two stage degradation. The onset set temperature, the 50% degradation temperatures are is 269.7^{o}C and 306.9^{o}C. A total 78.1% weight loss was obtained remaining 20% reside. The maximum slope was obtained at 291.1^{o}C. The initial endothermic DTA peak is obtained at about 80^{o}C which is related to moisture removal. DTA curve of composites shows two endothermic peaks at 289.6 and 454.6C. DTG curve of the fiber depicts two prominent peaks at 294.80^{o}C and 449.0^{o}C where the maximum degradation rate was 1.81 mg/min (294.8^{o}C). The initial degradation stage of TG curve is related to first DTA and DTG peak. And the second DTA peak is related to 2nd DTA and 2nd DTG peak The initial DTA peak is absent here. The first degradation is due to both the fiber and 1st stage of polymer and 2nd stage is due to 2nd stage of polymer as found figure 6.

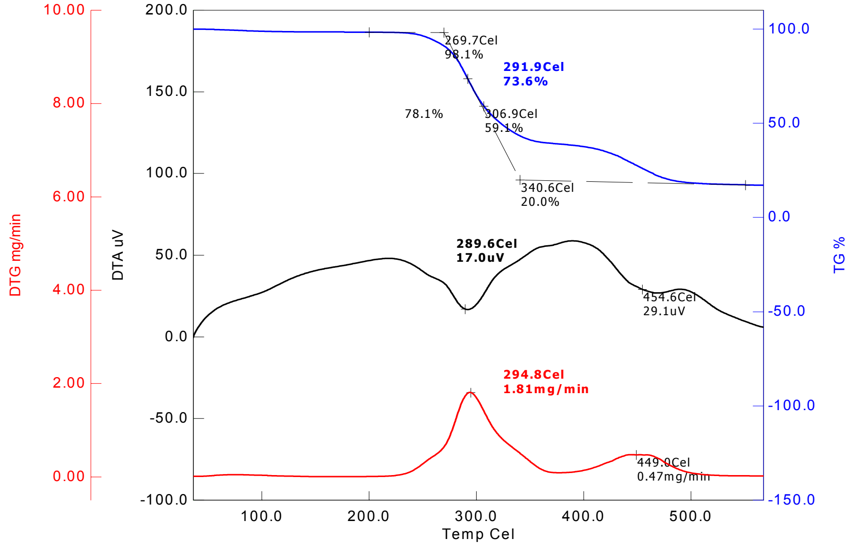

Fig. 4 TG%, DTA and DTG of Palm Fiber Reinforced Composites

Figure 5   shows the TG, DTA and DTG curves of sawdust fiber reinforced PVC composites having 10% sawdust. The top one is the TG, bottom one is the DTG and middle one is the DTA curves of Palm fiber. The TG curve shows two stage degradation. The onset set

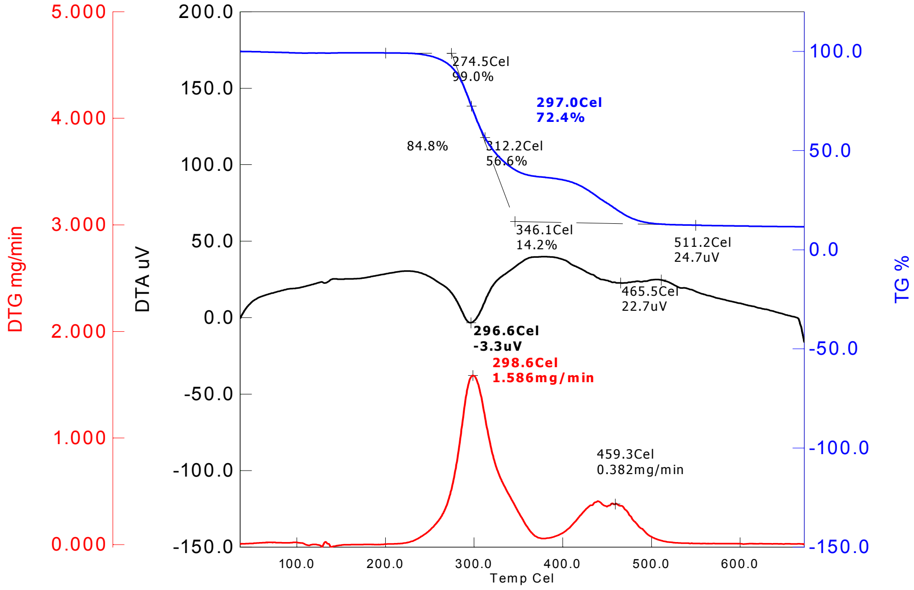

Fig. 5 TG%, DTA and DTG of Sawdust Reinforced Composites

temperature, the 50% degradation temperatures are is 274.50^{o}C and 312.0^{o}C. A total 84.1% weight loss was obtained remaining 14.2% residue. The maximum slope was obtained at 297.0^{o}C. DTA curve of composites shows two endothermic peaks at 296.6 and 465..6^{o}C. DTG curve of the fiber depicts two prominent peaks at 298.60^{o}C and 459.3^{o}C where the maximum degradation rate was 1.58 mg/min (298.6^{o}C). The initial degradation stage of TG curve is related to first DTA and DTG peak. And the second DTA peak is related to 2nd DTA and 2nd DTG peak The initial DTA peak is absent here. The first degradation is due to both the fiber and 1st stage of polymer and 2nd stage is due to 2nd stage of polymer as found figure 8.

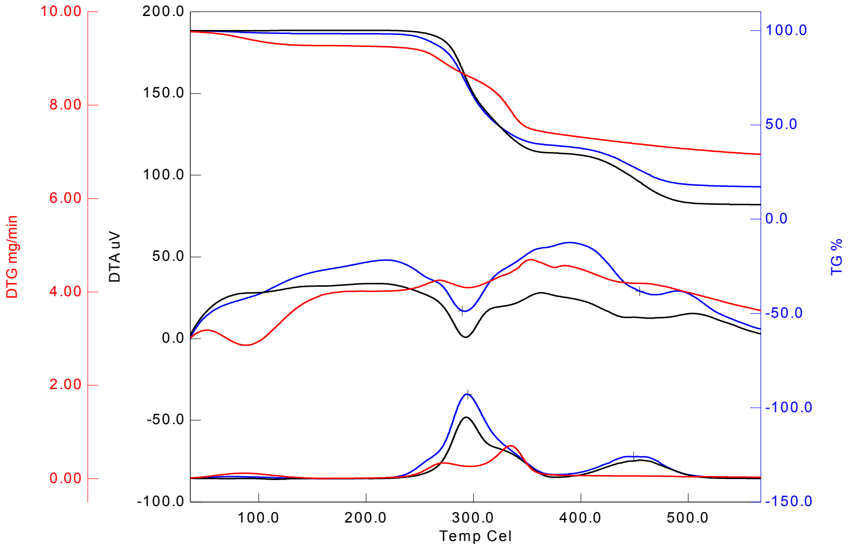

Fig. 6 TG%, DTA and DTG of PVC, Composite and Palm Fiber

Figure 6 shows the TG, DTA and DTG curves of PVC, palm fiber reinforced PVC composite and Palm fiber. The black curves are for PVC, blue curves are for composites and the red curves are for palm fiber. The figures depict that the curves for composite are the average of PVC and palm fiber. As the composite contain only 0% fiber, the properties of composites are dominated by the polymer.

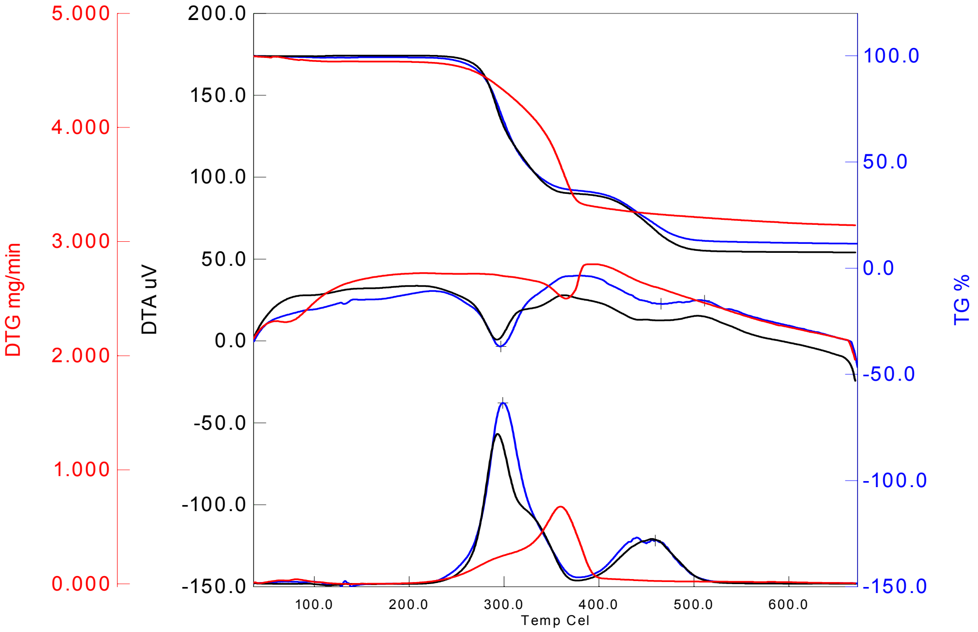

Fig. 7 TG%, DTA and DTG of PVC, composite and Sawdust

Figure 7 shows the TG, DTA and DTG curves of PVC, palm fiber reinforced PVC composite and sawdust. The black curves are for PVC, blue curves are for composites and the red curves are for palm fiber. The figures depict that the curves for composite are the average of PVC and palm fiber. As the composite contain only 0% fiber, the properties of composites are dominated by the polymer.

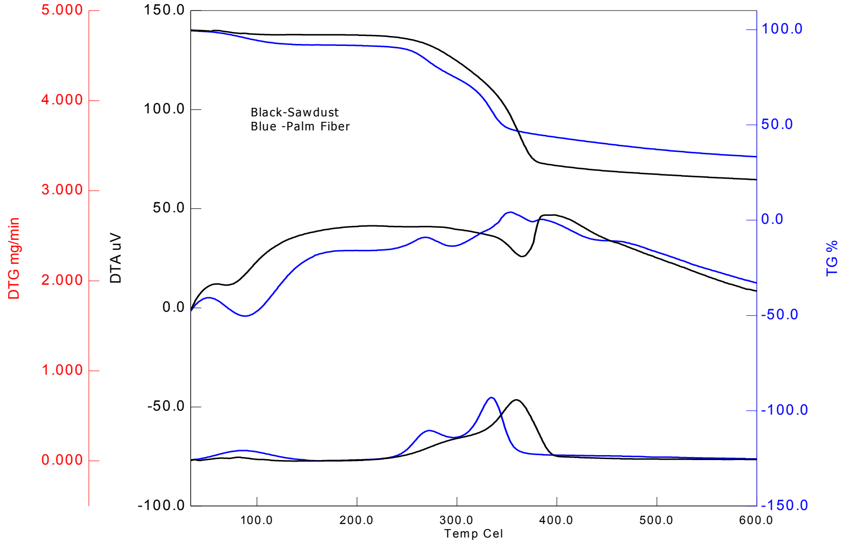

Fig. 8 TG%, DTA and DTG of Palm Fiber and Sawdust

Figure 8 shows the TG, DTA and DTG curves of palm fiber and sawdust. The blue curves and black curves are for palm fiber and sawdust, respectively. The TG curves shows lower % of moisture content and residue. The two stages are significant in sawdust, but in palm fiber one stage is more significant, The DTA curves greater DTA peak for palm fiber due to higher % of moisture content. The sawdust yields only one DTA peaks but the palm fiber have two endothermic peaks. The DTG peak of palm fiber for moisture is greater than that of sawdust due to higher % of moisture content. The palm fiber have two DTG degradation peaks whereas the sawdust has only one. Both the DTG degradation peaks are ahead of sawdust. This figure clearly depicts that sawdust is more thermally stable palm fiber.

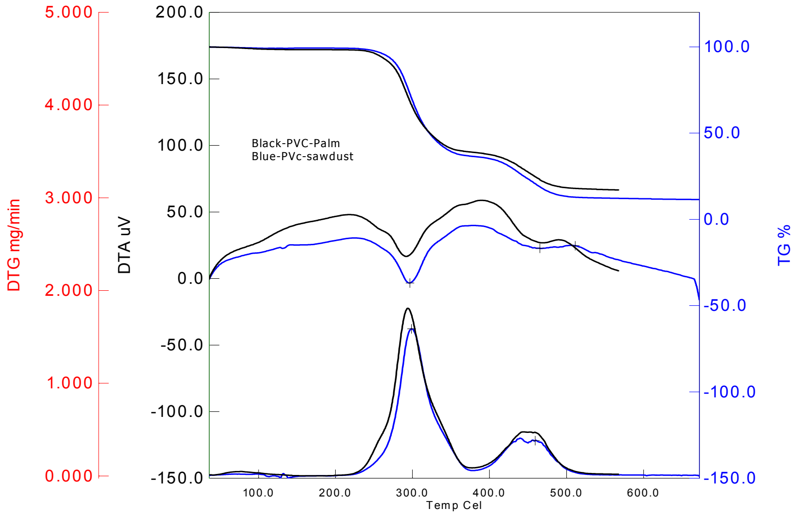

Fig. 9 TG%, DTA and DTG of Palm Fiber and Sawdust reinforced Composites

Figure 9 shows the TG, DTA and DTG curves of palm fiber and sawdust. The blue curves and black curves are for palm fiber and sawdust. reinforced PVC composites. The TG curve of sawdust clearly higher set and 50% degradation temperature. Both the DTA peak temperatures for both 1st and 2nd stage degradation are at higher temperature than those for palm. Both the DTG peak temperatures for both 1st and 2nd stage degradation are at higher temperature than those for palm. The sawdust reinforced composites is more thermally stable than the palm fiber reinforced composites due to higher thermal stability of sawdust.

Table 2 Different thermal properties of PVC, Palm, Sawdust, Palm Fiber Reinforced Composites, and Sawdust Reinforced Composites.

		PVC	**Palm Fiber**	**Sawdust**	**Palm Fiber reinforced Composites**	**Sawdust Reinforced**
TG	**Onset Temp.**	**274.0**	**294.0**	**318.4**	**269.7**	**274.5**
	50%degrad. temp	**292.0**	**322.1**	**345.7**	**306.90**	**312.6**
	Max. Slope	**316.1**	**334.0**	**363.3**		**297.0**
	Residue	**8.5%**	**27.4%**	**42.4%**	**20%**	**14.2%**
	Total wt. loss	**91.5%**	**48.1**	**68.7%**	**78.1%**	**84.1**
	Moisture	*****	**6.75**	**2.5**	**-**	**-**
DTA	**1st Degrad. Peak Temp.**	**292.0**	**296.4**	**-**	**294.8**	**298.6**
	2nd Degrad. Peak Temp.	**453.1**	**377.0**	**363.2**	**454.6**	**459.6**
DTG	**1st Peak**	**292.0**	**270.0**	**293.0**	**294.8**	**298.6**
	2nd Peak	**455.0**	**336.1**	**358.00**	**449.0**	**459.3**

Table 2 shows the comparative thermal characteristics of PVC, fibers and composites. From the table it reveals that the thermal parameters are are in the following order

Onset and 50% degradation

Sawdust >Palm fiber>Sawdust-PVC>Palm-PVC>PVC

Total Loss

PVC>Sawdust-PVC>Palm-PVC>Sawdust>Palm

Residue

Sawdust>Palm> Palm-PVC>Sawdust-PVC>PVC

1st Max. Degradation Rate Temp

Sawdust-PVC >Palm>Palm>PVC

2nd Max Degradation Rate Temp

Sawdust-PVC>PVC> Palm-PVC>Sawdust>Palm

CONCLUSIONS

TG, DTG and DTA curves of composites were found to be the average of fiber and of PVC. Due to higher thermal stability of sawdust than that of palm fiber, the thermal stability of sawdust-PVC is higher than that of palm-PVC.

REFERENCES

[1] Mohanty, A. K. , Mubarak, A. Khan, Shaoo, S. and G. Hinrichen, Effect of chemical Modification on the performance of Biodegradable jute yarn-Biopol composites, J. Material Science 35 (2000)2598.
[2] Woodhams, R.T., Thomas, G.and Rodgeers, D.K, Polym.Engi.Sci 24(15).1166-1171(1984).
[3] Mckenjie, A.W.and Yuritta ,J.P., Appita, 32(6), 460-465(1979).
[4] Bledzki, A.K., and Gassan, J., Natural fiber reinforced plastics in Handbook of Advanced Polymeric materials, Marcel Dekker Publishers, New Jersey(USA)1997.
[5] Quillin, D.T., Caulfield, D.F., and Koulsky, J.A, .J. Appl.Polym.Sci,(1993),50,1187
[6] Malcom P. Stevens Polymer Chemistery- An Introduction, University, Oxford University Press, 1999, p. 151.
[7] Md. Moniruzzaman, “Interface Modification and Mechanical Properties of Ligno_Cellulosic Okra fiber Reinforced Bakellite composites”, MSc Thesis, Islamic Univerdsity, of Kustia, Feb. 2008.

Proceedings of the 4th BSME-ASME International Conference on Thermal Engineering
27-29 December, 2008, Dhaka, Bangladesh

EXPERIMENTAL STUDY ON THE HEAT TRANSFER CHARACTERISTIC OF FeCrAl METALLIC FOAM

Pilhwan Kim[1], Meihua Jin[1], Youngjin Kim[1], Hyomin Jeong[2] and Hanshik Chung[2]

[1]Department of Mechanical and Precision Engineering, Gyeongsang National University, Tongyeong, 650-160, Korea,
[2]Department of Mechanical and Precision Engineering, Gyeongsang National University, Institute of Marine Industry, Tongyeong, Korea,
Email: pilani@naver.com

ABSTRACT

To enhancement heat transfer performance, the metallic foam as heat exchanger was studied rapidly. This was attributed to its high surface area to volume ratio as well as intensive flow mixing by tortuous flow passages. So the experimental study about the heat transfer characteristic of metallic foam is presented in this paper. Additionally, pressure drop inside the metallic foam was measured and also it was compared with the simulation results. The material in this experiment was used as FeCrAl which has density of 10 ppi, 20 ppi and 30 ppi respectively. And the results show the heat transfer is rise with permeability Reynolds number increase. The results show that the pressure drop metallic foam was increased with the ppi increase.

KEYWORDS: *Metallic foam, Porous medium, Heat transfer, Pressure drop, Nusselt number*

NOMENCLATURE

ε	porosity [%]
μ	coefficient of viscosity [N•s/m^2]
ρ	density [kg/m^3]
ΔP	Pressure drop [Pa]
L	Length of foam sample in flow direction [m]
K	Permeability [m^2]
U	Velocity of air [m/s]
Re_K	Pore Reynolds number
d_p	pore diameter
θ	Nondimensional temperature
X,Y	Nondimensional length of x or y Direction
H	Height of foam sample [m]
T_∞	Ambient temperature [^{o}C]
T_w	Wall temperature [^{o}C]
T_f	Fluid temperature [^{o}C]
q	Heat flux [W/m^2]

$k_{s,eff}$	Effective thermal conductivity of the metallic foam
$k_{f,eff}$	Effective thermal conductivity of the air
h_w	Coefficient of heat transfer
Nu	Nuselt number

1. INTRODUCTION

As a new material, metal foams are attracting increasing attention for a variety of applications. The advantages of porous medium lie on their low density, large surface area in a limited volume and high strength structure. Due to high manufacturing costs porous medium have until recently, mainly been used in the aerospace, ship building and defence industries. Heat transfer of a porous medium subject to oscillating flow has been investigated widely for a channel filled with spherical particles, granular beds or wire-screens[1]. Some research efforts have been made to obtain fundamental understanding of oscillating flow characteristics in a channel filled with particles or wire-screens[2] studied the oscillating flow characteristics of a Stirling engine regenerator made of wire-screens or sponge metals. They found that the prediction of pressure drop loss was possible by use of the hydraulic diameter as the representative length defined by the friction factor and Reynolds number[3] experimentally investigated oscillatory pressure drop characteristics in a packed column composed of three different sizes of woven screen and subjected to a periodically reversing flow of air. They showed that the oscillatory pressure drop factor increases with the kinetic Reynolds number and the fluid displacement and a correlation equation for the friction factor was obtained[4] studied the oscillating pressure drops and phase shift characteristics for regenerators filled with wire-screens under high frequency oscillation. They obtained values for the cycle-averaged pressure drop in the oscillating flow across the regenerator which are two to three times higher than that of a steady flow at the same Reynolds numbers based on the cross-sectional mean velocity.[5] Fourie et al(2002) studied pressure drop modelling in cellular metallic foams and they defined the model clearly the metallic foams for numerical analysis. And also they found that the experimental results for flow through isotropic, highly porous, cellular metallic foam clearly show that the morphological model and the representative hydraulic diameter concept introduced to complement the representative unit cell concept are capable of accurately predicting the pressure gradients in both Darcy and Forchheimer flows.[6] Boomsma et al[7] presented a new approach for modelling the flow through an intricately structured porous medium. This study was carried out experimental analysis about the temperature profile of metallic foam as heat exchanger and also numerical analysis about the pressure drop was carried out using FLUENT which commercial software. Finally, the results were compared with experiment results.

2. EXPERIMENT

2.1 Experiment device

Fig. 1 shows schematic diagram of the experiment device. Experiments were performed using metallic foam of 10 PPI. The fan was used to variable the velocity using controller. So the velocity can be control 0.4 m/s to 2.4 m/s. Pressure drop between inlet and outlet of foam was measured using micro manometer. Heating plate was installed at the bottom of the metallic foam and it was connected to slidac which can variable voltage to keep the constant heat flux. Consequently the heat flux was calculated by dividing the power by the surface area of the heater. The heat flux was 761 W/m^2 for each experiment.

Internal temperature measurements were performed inside the sample using T-type thermocouples. A total of thirty thermocouples were used at different points inside the sample as shown Fig. 1. And the thermocouples were attached to the channels of an automatic data acquisition system, which was connected to a computer, where the temperature readings were recorded every 2 second. The outside of the chamber on the test section was keep adiabatic condition using insulating material. The characteristics of the material which was used in this experiment are as follow Table 1.

Table 1 Metallic foam properties and experimental parameters

Material	ppi	ε	ρ (g/㎤)	$k_{s,eff}$(W/mK)
FeCrAl	10	0.88	7.1	2.54
	20	0.89		
	30	0.91		

In the Table 1, the ε mean porosity which can be calculates as follow:

$$\varepsilon = \frac{\text{weight of the metallic foam}}{\text{weight of pure meterial}} \tag{1}$$

2.2 Pressure drop numerical approaches

A wide variety of analytical and numerical models for porous media analysis have appeared in the literature. First of such models is the Darcy law, which was the first mathematical model of the pressure drop of a porous medium of length (L) and a permeability (K) to flow velocity (U) in porous medium based on experimental observations.[7]

$$\frac{\Delta P}{L} = \frac{\mu}{K} U \tag{2}$$

Dupuit's law(1863) includes a quadratic term, which important in higher flow velocity

$$\frac{\Delta P}{L} = \frac{\mu}{K} U + \frac{\rho c_F}{\sqrt{K}} U^2 \tag{3}$$

These two models is dependent on the Reynolds number of the flow as shown by Kaviany[8], Boomsma and Poulikakos[9-10]. In porous media, two methods of calculating the Re of a flow was difined by Boomsma and Poulikakos as shown below:

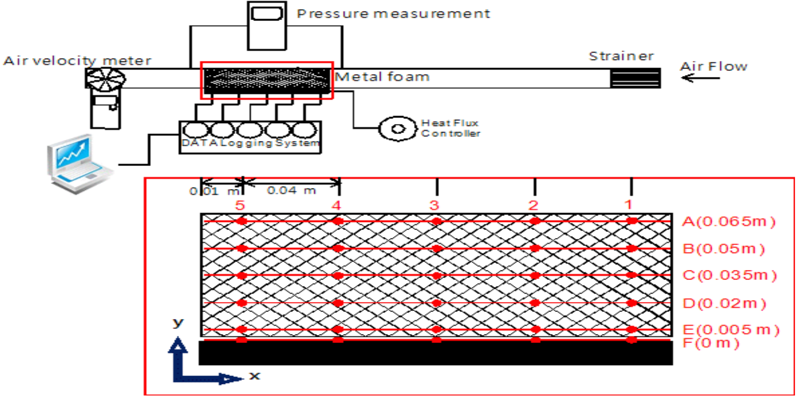

Fig. 1 Diagram of experiment apparatus

$$Re_K = \frac{\rho U K^{1/2}}{\mu} \tag{4}$$

$$Re_D = \frac{\rho U d_p}{\mu} \tag{5}$$

In equation (5), the square root of the permeability was replaced by pore diameter. It was specified that this method is better than first one to know the characterizing the flow in the metallic foam by Boomsma and Poulikakos[9-10]. The simulation about the pressure drop was performed using commercial software FLUENT.

3. RESULTS AND DISCUSSION

3.1 Pressure drop

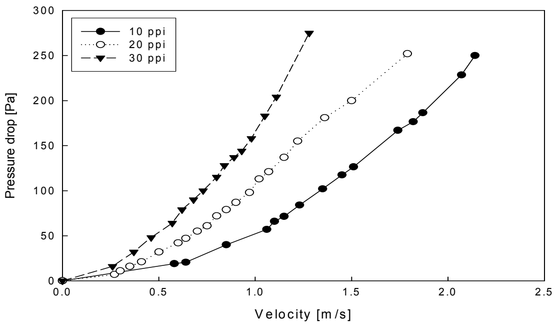

Fig. 2 Pressure drop with velocity

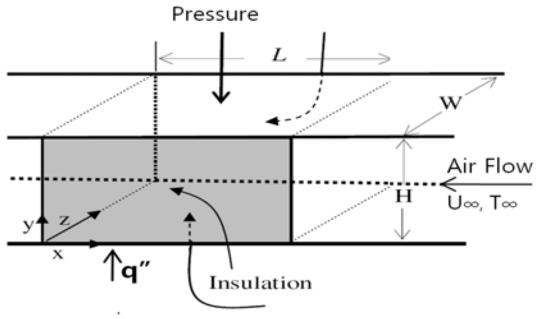

Fig. 3 Schematic of metallic foam in test

The experiment about pressure drop was performed within the range of velocity 0.2 to 2.2 m/s and the pressure drop was measured between inlet of material and outlet. Fig. 2 shows the results of comparison between three materials. The results show that the pressure drop is increase with velocity and density increasing. This is because that the air area in metal foam is decrease with density increase.

3.2 Temperature profile

The temperature measured in this experiment can be assumed that air temperature flow inside the metallic foam. To calibrate the error that occurring experiment process along outside condition change, non-dimensional temperature distribution was calculated as below:

$$\Theta(X, Y) = \frac{T - T_\infty}{q'' H / k_s,\mathrm{eff}} \tag{6}$$

$$X = x/L,\ Y = y/H \tag{7}$$

Fig. 4 shows the contours profile of temperature distribution for FeCrAl metal foam. This profiles show the heat from heat plate go up more with pore density is increase. It mean that the thermal conductivity of metal foam is affected by pore density. Fig. 5-7 show the experimental temperature profile in direction of the flow with pore density of 10 ppi, 20 ppi and 30 ppi respectively. The experimental data is given for the none-dimensional axial distances 0.05, 0.26, 0.47, 0.68 and 0.89 which correspond to the physical distances 1, 5, 9, 13 and 17 cm from the inlet of the each foam sample. From these figures, temperature distributions decrease with y length increase. The temperature of all the Y position in material drops down to the ambient temperature at an axial distance of about 0.85. And also the temperature difference between air inlet and outlet is decrease with pore density increase. This mean that the Nuselt number which define heat transfer characteristic defined as below

$$Nu = \frac{h_w H}{k_{f,eff}} \tag{8}$$

$$h_w = \frac{q_w}{T_w - < T_f >} \tag{9}$$

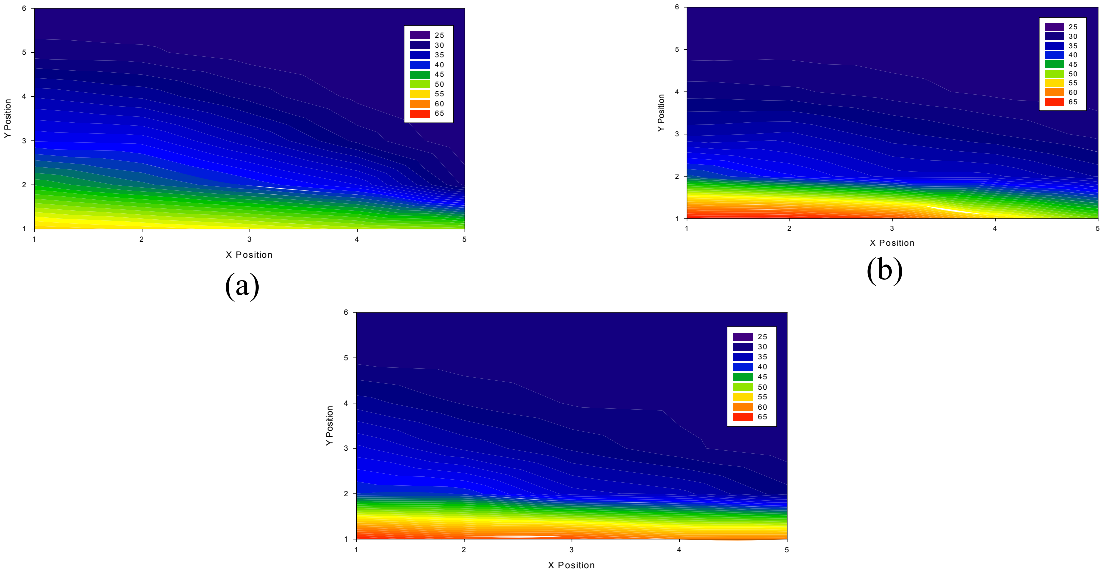

(a) (b) (c)

Fig. 4 Temperature profiles in the FeCrAl metal foam for the 10 ppi(a), 20 ppi(b), 30 ppi(c), respectively at the velocity of 1.2 m/s

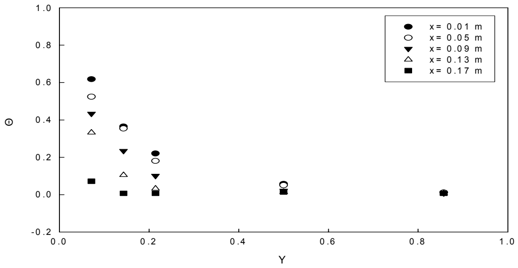

Fig. 5 None-dimensional Temperature distributions at the pore density is 10 ppi

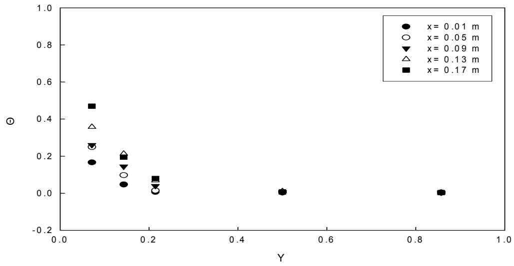

Fig. 6 None-dimensional Temperature distributions at the pore density is 20 ppi

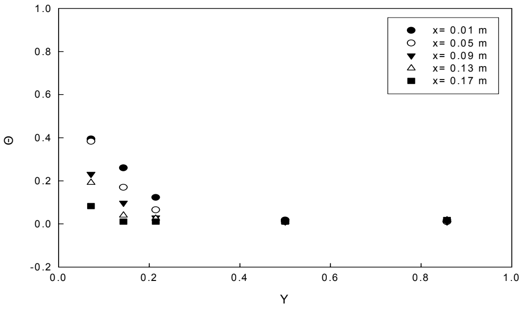

Fig. 7 None-dimensional Temperature distributions at the pore density is 30 ppi

Fig. 8 shows the Nuselt number with different pore Reynolds numbers. The results show overall heat transfer increase with Reynolds number increases. Because high Reynolds number leads to a higher local heat transfer coefficient, and in turn this enhances the heat transfer between the solid and fluid.

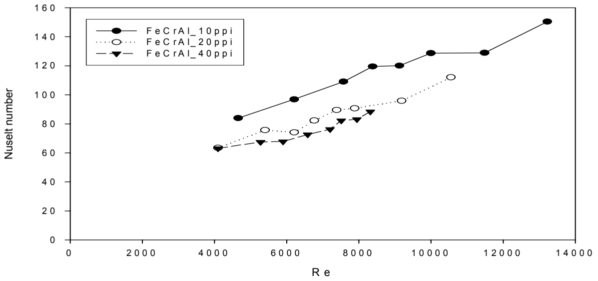

Fig. 8 Variation of Nusselt number with Reynolds

4. CONCLUSION

The pressure drop and heat transfer characteristic of FeCrAl metallic foam of 10 ppi was performed experimental study. The results show that pressure drop is increase with velocity and from comparison with the simulation results, average error range indicated within 5.5 %. From this results, it could confirm that the pressure drop depend on the permeability. The heat transfer characteristics show that Nuselt number is increase along pore Reynolds number increasing.

ACKNOWLEGEMENT

This research was financially supporting by the Ministry of Education Science Technology (MEST) and Korea Industrial Technology Foundation (KOTEF) through the Human Resource Training Project for Regional Innovation and Second-Phase of BK21 and NURI project, Korea

REFERENCES

[1] Sozen, M., Vafai, K., 1990. Analysis of oscillating flow compressible flow through a packed bed. Int. J. Heat Fluid Flow 12, 130–136.
[2] Tanaka, M., Yamashita, I., Chisaka, F., 1990. Flow and heat transfer characteristics of the Stirling engine regenerator in an oscillating flow. JSME Int. J. Ser. II 33, 283–289.
[3] Zhao, T.S., Cheng, P., 1996. Oscillatory pressure drops through a woven-screen packed column subjected to a cyclic flow. Cryogenics 36, 333–341.
[4] Ju, Y.L., Jiang, Y., Zhou, Y., 1998. Experimental study of the oscillating flow characteristics for a regenerator in a pulse tube cryocooler. Cryogenics 38, 649–656.
[5] K.C.Leong, L.W.Jin, 2006. Characteristics of oscillating flow through a channel filled with open-cell metal foam. International Journal of Heat and Fluid Flow 27, 144–153.
[6] J.G.Fourie, J.P.Du Plessis, 2002. Pressure drop modeling in cellular metallic foams. Chemical Engineering Science 57, 2781–2789.
[7] K. Boomsam, D. Poulikakos, Y. Ventikos, 2003. Simulations of flow through open cell metal foams using an idealized periodic cell structure. International Journal of Heat and Fluid Flow 24, 825–834.
[8] Kaviany, M., 1995. Principles of Heat Transfer in Porous Media. Springer-Verlag, New York.
[9] Boomsma, K., Poulikakos, D., 2002. The effects of compression and pore size variations on the liquid flow characteristics of metal foams. Journal of Fluids Engineering-Transactions of the ASME 124, 263～272.
[10] K. Boomsma, D. Poulikakos, F. Zwick, 2003, "Metal foams as compact high performance heat exchangers", Mechmat, 35, pp. 1161～1176.

Proceedings of the 4th BSME-ASME International Conference on Thermal Engineering
27-29 December, 2008, Dhaka, Bangladesh

CHARACTERISTICS OF HEAT TRANSFER AND FLOW DISTRIBUTIONS THROUGH A PLATE HEAT EXCHANGER CHANNEL

ZhenHua Jin[1], GiTae Park[1], XueSong Li[1], HanShik Chung[2] and HyoMin Jeong[2]

[1]Department of Mechanical and Precision Engineering, Gyeongsang National University,
Tongyeong, 650-160, Korea
[2]Department of Mechanical and Precision Engineering, Gyeongsang National University,
Institute of Marine Industry, Tongyeong, Korea
Email: jinzhenhua2001@yahoo.com.cn

ABSTRACT

Plate Heat Exchanger (PHE) have become popular in chemical, power, food and refrigeration industries due to the efficient heat transfer performance, extremely compact design and flexibility of extend or modify to suit changed duty. In present work, PHE aimed apply in the fresh water generator which installed in ship to desalinate seawater to fresh water use heat from engines. The experiment is proceeded to investigate the heat transfer between cold and hot fluid stream at different flow rate and supply temperature of hot fluid. Another target is the generated fresh water as outcome of the system. PHE is an important part of a condensing or evaporating system. One of common assumptions in basic heat exchanger design theory is that fluid is to be distributed uniformly at the inlet of each fluid side and throughout the core. However, in practice, flow mal-distribution is more common and can significantly reduce the heat exchanger performance. The main objective of this paper is discussing main conception of plate heat exchanger and applied in vacuum evaporator for product fresh water.

Key words: *plate heat exchanger, heat transfer, chevron type plate, fresh water*

1. INTTRODUCTION

Many countries in the world suffer from a shortage of nature fresh water. Increasing amounts of fresh water will be required in the future as a result of the rise in population rates and enhanced living standards, together with the expansion of industrial and agricultural activities. Most commercially applied technologies of desalination are based on the multistage flash distillation, multiple effect distillation and reverse osmosis processes. In distillation system it is no doubt heat exchanger as a key point that is extremely important. The importance of heat exchanger has increased immensely from the view point of energy conservation, conversion, recovery and successful implementation of new energy sources [1]. PHE was originally developed for use in hygienic applications such as pasteurization of liquid food products. However, the range of applications of this type of exchanger largely expanded in the last decades due to the continual design and construction improvements. Nowadays PHE widely use in different industries such as chemical, food and pharmaceutical process and refrigeration. The traditional concept, PHE consists of plates, gaskets, frames and some additional devices, such as carrying and guiding bars, support column, via ports. The heat transfer occurred between adjacent channels through plates as show in Fig.1. Alternate plates are assembled such that the corrugations on successive plates contact or cross each other to provide mechanical support to the plate pack through a large number of contact points. This resulting flow passages are narrow, highly interrupted and tortuous so that enhance the heat transfer flow and increasing the level of turbulence. True flexibility is unique to the plate heat exchanger both in initial design and after installation. In the initial design the basic size, geometry, total number and arrangement of standard plates can normally be selected to precisely fit the required duty. An existing plate heat exchanger can very easily be extended or modified to suit an increased or changed duty. Moreover, it is very compact and low in weight in spite of their compactness[2-5]. Plate patterns have great influence on both of thermal and hydraulic performance, the final design is certainly depends on the initial choice of plate pattern. Although many types have been used in the past, the chevron type plate has proved to be the most successful model during last decades. A comprehensive step of design method was presented by Shah and Focke[6]. The commonly used chevron angle varies between 30° to 60. This been verified by many researchers according to experimental results and simulations already. An analytical study has been made by Martin[7] to predict the performance of chevron type plate heat exchanger. The main objective of this paper is discussing main conception of plate heat exchanger applied in vacuum evaporator for product fresh water. Especially focus on the evaporating and condensing performance for product fresh water.

2. EXPERIMENTAL SETUP AND METHOD

A fresh water generator is increasingly used in desalination plants, typically located in coastal areas, which provide fresh drinking water to the local community. These have become very common in the Middle East, and are also in use in some other place. More desalination plants are likely to be built as a response to drought and concern over availability of water in growing cities. However, the costs involved in desalination plants are high and are considered by communities only when faced with water shortages from traditional sources.

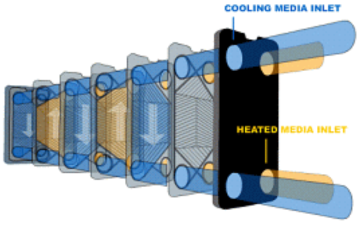

Fig.1 Flow arrangement in the plate heat exchanger

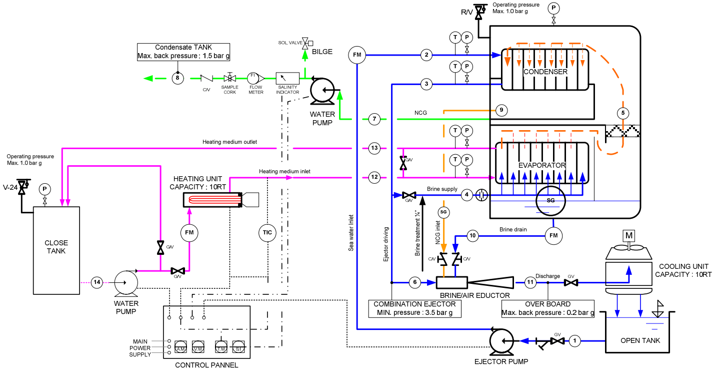

Fig.2 Diagram of the experimental facility of fresh water generator system

The concept of a fresh water generator is simple the sea water is evaporated using a heat source, separating pure water from salt, sediment and other elements. Fresh water generators often use the diesel engine jacket as a heat source, although steam can also be used as a heat source. Because freshwater generators often use existing heat to run, the cost of operation is low. There are two main elements in a fresh water generator, one heat exchanger evaporates the sea water and another one condenses the fresh water vapor into liquid phase for use. In the condenser element, the vapor is condensed through cooling, often simply using cold seawater. The heat transfer part contains corrugated plates with 60 degree of chevron angle which verified by many researchers and commonly apply. Moreover the plate package arranged with U type configuration. The air inside the evaporation chamber is evacuated to a near vacuum, so that the saturation point of water becomes lower much more. It then becomes possible to evaporate the seawater at a temperature around 60 ^{0}C. The diesel engine jacket cooling water is sufficiently hot to evaporate the seawater and it is commonly used. In present system can reach the vacuum between two dotted line shows in Fig.3. It means that for the saturation temperature located in 51^{0}C ~57 ^{0}C. Schematic diagram of fresh water generator experimental facility is shown in Fig.2. The system can be separate to two main circuits. One is cold water circuit that cold fluid is supplied to the heat exchanger where it receives heat from the hot fluid across the plates. Finally the cold water sent to cooling tower where temperature cool down and maintain at the inlet condition of heat exchanger. This experiment used city water and not installed on ship yet. However, in real state this system will be installed on ship so the cold water instead by seawater then cooling tower is unnecessary. Since it assumed that the seawater temperature is constant. In other hand, the hot fluid is flowing to the plate heat exchanger and fed back to hot water tank where is keep at a constant temperature using boiler instead of engine cooling water.

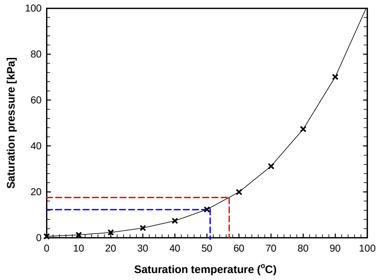

Fig.3 Saturation temperature and pressure

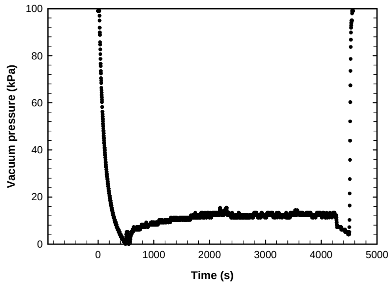

Fig.4 Vacuum pressure distribution inside of the vessel

For the procedure of experiment firstly operate cold fluid circuit to obtain near vacuum condition in the tank which contains the heat exchanger. Further step is operating hot water circuit to supply hot water to heat transfer with the cold fluid between alternate plate channels of heat exchanger. It should be notice that there is bypass line connected from outlet of cooling water to evaporator. The already heated cooling water provided to absorb heat from hot water so that can be evaporating much more quickly and use all the energy sufficiently. The temperature and pressure at inlet and outlet of fluids are recorded respectively till the steady state is reached. Same procedure has been repeated with different flow rate and supply temperature of hot fluid. As mentioned above the vessel contains two unit of exchanger is maintained with vacuum condition while the system is operating. The pressure variation in the inside of vessel is show as Fig.4. This is one of experimental results with operate system exactly operate ejector entrain the inside air so that pressure decrease rapidly within 10 minutes. At this condition flowing hot stream and cold stream to start to exchange heat. We can see inside pressure increase gradually since there are vapour occurred. However through some period it maintain at steady state along 12kPa vacuum pressure relatively. It showed sharp increasing at end of part this because stop ejector and it recovery to atmosphere condition. In this way one case of experiment is complete.

3. RESULTS AND DISCUSSION

According to above mentioned concept and procedure, the experiments conducted at the range of 60 ^{0}C, 65 ^{0}C and 70 ^{0}C for the setting temperature of hot fluid respectively. Meanwhile the flow rate of fluid is set at 3.0m^{3}/h and 3.5m^{3}/h. First look at pressure drop that it is calculated as approximately 1.5 times the inlet velocity head per pass. Since the entrance an exit losses in the core cannot be determined by experimentally, they are included in the friction for the given plate geometry. Although the momentum effect is negligibly small for liquids, it is also included in the following expression. The pressure drop or rise caused by elevation of change for liquids. Summing all contributions, the pressure drop on one fluid side in a plate heat exchanger is given by

$$\Delta P = \frac{1.5 G_p^2 n_p}{2 g_c \rho_i} + \frac{4 f L G^2}{2 g_c D_e}\left(\frac{1}{\rho}\right)_m + \left(\frac{1}{\rho_0} - \frac{1}{\rho_i}\right)\frac{G^2}{g_c} \pm \frac{\rho_m g L}{g_c}$$

$$f = 0.8 \mathrm{Re}^{-0.25}, \quad \mathrm{Re} = \frac{G D_e}{\mu}, \quad G_p = \dot{m}/(\pi/4) D_p^{\ 2}$$

Where Gp is the fluid mass velocity at the port and np is the number of passes in the given fluid side, De is the equivalent diameter of flow passages namely twice of pressing depth, ρ_o and ρ_i are fluid mass densities evaluated at local bulk temperature and mean pressure at outlet and inlet, respectively. The Reynolds number is based on hydraulic diameter of the corrugated channel which is equivalent to twice of pressing depth of the plate.Fig.5 shows the comparison of pressure drop between experiment and theoretical results based on the above equations. It is observed that there is difference for experimental results and calculation method which according to equation suggested by R. K. Shah. The calculation results ignored the third term of right hand side of equation since it is difficult to measure exact the density at each point. Additionally, in experiment friction loss through pipeline is inevitable. Therefore this may result into the gap compare to experimental results. Since the supply temperature is lower relatively. Hence, resulted into evaporating is not happened sporadically at this condition. Fig.6 shows the fresh water generation at each supply temperature of hot water and flow rate. The line depicts the effect of flow rate and supply temperature of hot water on the fresh produce. It is showed that compare two lines it clear that fresh water generation rate is increasing proportionately by increase of hot water supply temperature. For the different flow rate affect to the fresh water quantity is less at 65 ℃ and 70℃. However, the difference of fresh water quantity is become large at 60 ℃ of hot water temperature case. The reason for the difference might be due to when the hot water temperature is lower, the cold water outlet temperature will lower too so that for evaporating the temperature gap is large than other case at high temperature, similarly there need much more amount of heat and time to accumulate then it can be evaporated.

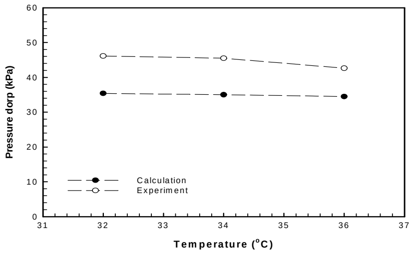

Fig.5 Comparison of pressure drop between experiment and calculation of cold water side

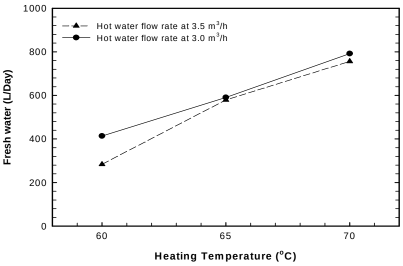

Fig.6 Fresh water generation rate with temperature and different flow rate

4. NUMERICAL ANALYSIS

A large number of optimization techniques are available from literature and quite a lot of commercial optimization software. CFD can provide another method approach to modeling and investigate performances. Moreover, there are a number of papers trying to approach other way namely numerical simulation like described in the articles[8-10]. In this paper, a CFD model taken to simulate flow distribution in the plate channel. The dimension of plate model in length of 400 and width of 100mm, equivalent diameter is 7mm and the port diameter is

24mm. The fluid domains were modelled with the properties of water. The simulation was solved use k-ε turbulence model. Simulation model is corrugated plate and 6 channel model with only plat shape as shown in Fig.7. In the simulation with corrugated model conduct 5 case which the Reynolds number increasing from 2000 to 6000. Fig. 8 shows pressure drop according to increasing of Reynolds number.

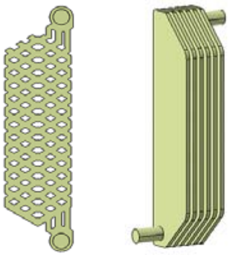

Fig.7 Corrugate plate & flat multi channel model

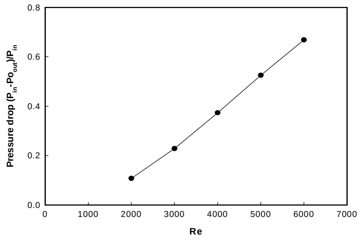

Fig.8 Pressure drop according to Re

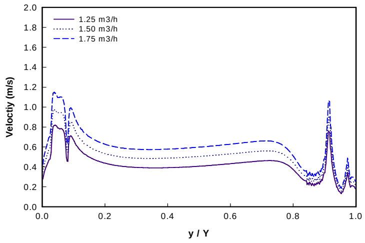

Fig.9 Velocity distributions at the last channel in 6 channel unit

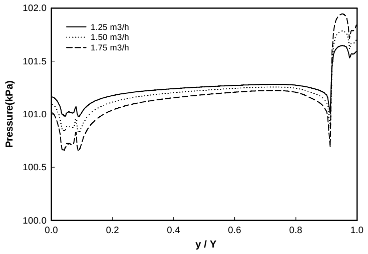

Fig.10 Pressure distributions at the last channel in 6 channel unit

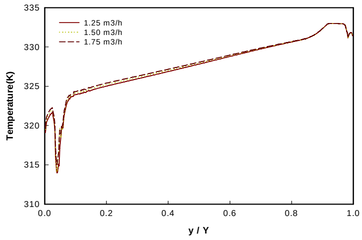

Fig.11 Temperature distributions at the last channel

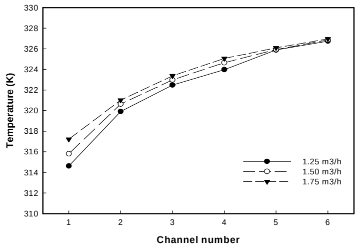

Fig.12 Temperature distributions in the each channel

From Fig.9 and Fig.10 we can see more detailed variation of velocity and pressure along y-direction cross port and plate channel. The y-axis distance means location from bottom of channel. This data represent the cross port section along y direction. The simulation results indicate that pressure and velocity varied sharply around port due to changing of flow area. However at other area the distribution of pressure and velocity is near uniform. Fig.11 shows the variation of temperature in the last channel. There is less influence of flow rate on the temperature distribution in this channel. However, Fig.12 shows a little difference of temperature when the flow approach to end of channels the influence is increasing.

5. CONCLUSIONS

In the present work, we discussed about fresh water generator system which used plate heat exchanger to evaporate and condense with vacuum conditions. Experiments have been carried out on the fresh water generating according to the supply temperature and flow rate of heating medium and show the influence on the performance of product fresh water as outcome of the system. Using a CFD tool can obtain the temperature and velocity distribution inside of PHE channel. In fact, it is very difficult to obtain experimental result for comparison with the simulation result. The experiment show that with higher hot water supply temperature can produce more quantity of fresh water. The flow rate of hot water supply temperature affect less to the produce of fresh water in the range of high temperature. However, it can achieve more fresh water at lower flow rate. Because at lower flow rate heat transfer sufficiently between hot medium and cold medium through adjacent plates. The simulation results indicate that pressure and velocity varied sharply around port due to changing of flow area. However at other area the distribution of pressure and velocity is near uniform state. It observed that pressure drop significant with increasing of Reynolds number. In the 6 channel model the flow rate is less effect on temperature but approach to end of channel the more the influence is increasing.

Unlike tubular heat exchangers for which design data and methods are easily available, PHE design continues to be proprietary in future. Extend detailed research with wide range of experimental condition will carried out in the near future in order to test and further improve the performance of system. That can contribute to the propagate application of PHE and it can be practice effective utilization of energy that conserve limited energy.

ACKNOWLEDGEMENT

This research was supported under the project (No.70002054) of ITEP in the Ministry of Knowledge Economy Ministry and the second-phase of Brain Korea 21 project and NURI project. The authors gratefully acknowledge the support from DAEWON heat plate Co., Ltd

REFERENCES

[1] Khawaji, A. D., Kutubkhanah, I. K. and Wie, J. M., Advances in seawater desalination technologies. *Desalination*. Vol 221(2008), pp.47-69.

[2] Zahid, H. A., Plate heat exchanger literature survey and new heat transfer and pressure drop correlations for refrigerant evaporators. *Heat Transfer Engineering*. Vol 24 (2003) No 5. pp.3-16.

[3] Bobbili, P. R., Sunden, B. and Das, S. K., An experimental investigation of the port flow maldistributon in small and large plate package heat exchangers. *Applied Thermal Engineering*. Vol 26 (2006), pp.1919-1926.

[4] Srihari, N. and Das, S. K., Transient response of multi-pass plate heat exchangers considering the effect of flow maldistribution. Chemical *Engineering and Processing*. Vol 47(2003), pp.695-707.

[5] Rao, B. P. Kumar, P. K. and Das, S. K., Effect of flow distribution to the channels on the thermal performance of a plate heat exchanger. *Chemical Engineering and Processing*. Vol 41 (2002), pp.49-58.

[6] Shah, R. K. and Focke, W. W., Plate heat exchanger and their design theory in heat transfer equipment design. Hemisphere.Washington. USA, 2003.

[7] Martin, H., A theoretical approach to predict the performance of chevron-type plate heat exchangers. *Chemical Engineering and Processing*. Vol 35 (1996), pp.301-310.

[8] Fernandes, C. S., Dias, R. P., Nobrega, J. M. and Maia, J. M., Laminar flow in chevron type plate heat exchangers: CFD analysis of tortusity, shape factor and friction factor, *Chemical Engineering and Processing*. Vol 46 (2007), pp.825-833.

[9] Zhang, G. M., Tian, M. C. and Zhou, S. J., Simulation and analysis of flow pattern in cross-corrugated plate heat exchanger. Journal of Hydrodynamics. Vol 18(2006), No 5. pp.547-551.

[10] Noh, S. J.,. Numerical study of heat transfer and pressure drop in chevron type plate heat exchanger. Thesis. 2004, pp.8-49.